Decoding splicing regulatory networks in cancer-relevant genes

---

Dissertation

Zur Erlangung des Grades

“Doktor der Naturwissenschaften”

am Fachbereich Biologie

Der Johannes Gutenberg-Universität Mainz

Mariela Cortés López
geb. am 21.09.1993 in, Mexiko

Mainz, October 2021

Dekan:

1. Berichterstatter:
2. Berichterstatter:

Tag der mündlichen Prüfung: 19.01.2022

Table of Contents

List of Tables

List of Figures

Preface

The results presented in this work have been published previously (Chapter 1 and 2) or submitted for publication and published as preprint (Chapter 3).

1. **Chapter 1**

   Braun, Simon, Mihaela Enculescu, Samarth T. Setty, **Mariela Cortés-López**, Bernardo P. de Almeida, F. X. Reymond Sutandy, Laura Schulz, et al. 2018. "Decoding a Cancer-Relevant Splicing Decision in the RON Proto-Oncogene Using High-Throughput Mutagenesis." *Nature Communications* 9 (1): 3315.

2. **Chapter 2**

   Schulz, Laura, Manuel Torres-Diz, **Mariela Cortés-López**, Katharina E. Hayer, Mukta Asnani, Sarah K. Tasian, Yoseph Barash, et al. 2021. "Direct Long-Read RNA Sequencing Identifies a Subset of Questionable Exitrons Likely Arising from Reverse Transcription Artifacts." *Genome Biology* 22 (1): 190.

3. **Chapter 3**

   Cortés-López, Mariela, Laura Schulz, Mihaela Enculescu, Claudia Paret, Bea Spiekermann, Anke Busch, Anna Orekhova, et al. 2021. "High-Throughput Mutagenesis Identifies Mutations and RNA-Binding Proteins Controlling CD19 Splicing and CART-19 Therapy Resistance." *bioRxiv*.

Each chapter contains a summary and statement of where I provide the details of my contributions. The work described in Chapters 2 and 3 involved the collaboration with members of the groups of Dr. Barash and Dr. Thomas-Tikhonenko. In Chapters 1 and 3, we teamed up with Prof. Legewie. Dr. Zarnack collaborated on all three manuscripts.

Zusammenfassung

Alternatives Spleißen ist ein hochgradig regulierter zellulärer Prozess, der für die Entstehung der Proteinvielfalt von Bedeutung ist. Elemente in der Sequenz der Transkripte regulieren das Spleißen in *cis*. Diese *cis*-Elemente werden von *trans*-wirkenden Faktoren gebunden, bei denen es sich in der Mehrzahl um RNA-bindende Proteine (RBPs) handelt. Die Interaktionen zwischen *cis*-Elementen und *trans*-wirkenden Faktoren definieren den Spleißcode. Derzeit werden Fehler in der Spleißregulierung häufig mit Krankheiten in Verbindung gebracht, was die Notwendigkeit unterstreicht, die Mechanismen und Folgen von falschem Spleißen zu verstehen.

Der erste Teil dieser Arbeit beschreibt die Entwicklung eines Hochdurchsatz-Mutagenese-Assays, mit dem wir die Auswirkungen einzelner Mutationen auf das Spleißen des Exons 11 im Proto-Onkogen *RON* untersuchen können. Dieser Assay deckt das Spleißnetzwerk des *RON*-Exons 11 auf und identifiziert HNRNPH als einen relevanten Regulator. Wir zeigen auch, wie HNRNPH das Spleißen des *RON*-Exons 11 in einer schalterähnlichen Weise kooperativ reguliert.

Im zweiten Teil dieser Arbeit stelle ich unechte Isoform vor, die als ex2Δpart bekannt ist. Diese Isoform ist ein Beispiel für ein exonisches Intron (Exitron), das sich als therapeutischer Marker eignen könnte. Wir zeigen, dass ex2Δpart stattdessen ein Artefakt der reversen Transkription (RT) ist. Mithilfe bioinformatischer Analysen beschreiben wir weitere Artefakte (sogenannte “Falsitrons”). Unsere Arbeit schlägt auch neue Strategien zur Verfeinerung der Isoform-Annotation vor.

Die vorherigen Kapitel dienen auch als Präzedenzfall für die zweite hier vorgestellte Hochdurchsatzstudie: die Mutagenese von *CD19* Exon 2. CD19 ist das Ziel der CART(Chimeric Antigen Receptor T)-19-Therapie, und ein falsches Spleißen seines zweiten Exons wurde mit Therapieresistenz in Verbindung gebracht. Hier stellen wir einen Hochdurchsatz-Mutagenese-Test vor, der die *cis*- und *trans*-Regulatoren in der Region zwischen den Exons 1-3 von CD19 charakterisiert. Die Studie liefert auch neue Informationen über das regulatorische Netzwerk des Spleißens von CART-19-Rückfallpatienten.

Zusammengenommen tragen die in dieser Arbeit beschriebenen regulatorischen Netzwerke zur Interpretation von Mutationen in zwei krebsrelevanten

Genen bei. Darüber hinaus stellt diese Arbeit auch eine Sammlung verschiedener Ansätze zur Verbesserung von Spleiß-Annotationen vor. Die hier beschriebenen Werkzeuge und Analysen können auf andere wichtige Mis-Splicing-Ereignisse ausgedehnt werden und helfen, den Spleißcode zu entschlüsseln.

Abstract

Alternative splicing is a highly regulated cellular process, relevant to the generation of protein diversity. Elements in the sequence of the transcripts regulate splicing in *cis*. These *cis*-elements are bound by *trans*-acting factors which, in their majority, are RNA binding proteins (RBPs). The interactions between *cis*-elements and *trans*-acting factors define the splicing code. Meanwhile, errors in splicing regulation have been frequently associated with diseases, highlighting the need to understand the mechanisms and consequences of mis-splicing.

The first part of this work describes the development of a high throughput mutagenesis assay that allows us to look at the impact of individual mutations in the splicing of the exon 11 in the proto-oncogene *RON*. This assay uncovered the splicing network of *RON* exon 11 and identified HNRNPH as a relevant regulator. We also show how HNRNPH cooperatively regulates RON exon 11 splicing in a switch-like manner.

During the second part of this work, I present the story of a spurious isoform, known as ex2Δpart. This isoform is an example of an exonic intron (exitron) with suggested potential as a therapeutic marker. We show how ex2Δpart is instead an artefact of reverse transcription (RT). Using bioinformatical analysis, we describe other artefacts (named "falsitrons"). Our work also suggests new strategies to refine isoform annotation.

The previous chapters also serve as a precedent for the second high-throughput study presented here: the mutagenesis of *CD19* exon 2. CD19 is the target of the CART(Chimeric Antigen Receptor T)-19 therapy, and mis-splicing of its second exon has been associated with therapy resistance. Here, we present a high-throughput mutagenesis assay that characterises the *cis*- and *trans*-regulators in the region between exons 1-3 of *CD19*. The study also provides new information on the regulatory network of splicing of CART-19 relapse patients.

Together, the regulatory networks described in this work contribute to interpreting mutations in two cancer-relevant genes. In addition, this work also presents a collection of distinct approaches to improve splicing annotations. The tools and analysis described here can be extended to other important mis-splicing events, helping to decipher the splicing code.

Introduction

Gene expression and RNA processing

Gene expression is the essential process that describes the generation of a copy of the DNA (desoxyribonucleic acid) encoded in a gene to generate a protein. The copy has the form of another biomolecule known as RNA (ribonucleic acid) which is composed of chemical bases similar to DNA. Subsequently to the descriptions of the chemical composition and structure of DNA, the next question to answer was the mechanism of the gene expression. In 1957, Francis Crick proposed the "central dogma of molecular biology" (Cobb 2017), stating that one gene originates a transcript (RNA) which then gives rise to a protein. The initial statement of Crick contemplated that the relationship from gene to protein was not one to one but was probably misunderstood in the community by the use of the word "dogma." Later on, Crick clarified the issue, and more evidence supported the importance of non-linearity of gene expression.

Splicing

Transcription is the process of generating RNA from DNA. The RNA serving as a template for protein production is known as messenger RNA (mRNA) and is far to be a perfect copy of the gene of origin. For an RNA to become an mRNA, several biochemical steps must take place. In general terms, parts of the sequence, known as introns, are removed from the initial transcript (pre-mRNA) and the remaining parts, known as exons, are then ligated. This process of removal and ligation in the pre-mRNA is known as splicing, and it was first described in 1977 by Philip Sharp (Berget et al. 1977) and Patrick Roberts (Chow et al. 1977) (Figure 1).

The splicing reaction is catalysed by the spliceosomal machinery, and it requires the precise recognition of signals in the sequence of the transcripts. The cleavage sites, named "splice sites" are highly conserved across eukaryotes and are located at the 5´ and 3´ of an intron. The 5´splice site (5´ss) is defined by the GU dinucleotide, whereas the 3´splice site (3´ss) is usually an AG. Additional conserved sequence elements that are also located in the sequence and share a

high degree of conservation are the branch point, defined as an adenosine (A), and the polypyrimidine tract. In chemical terms, the splicing reaction consists of two *trans*-esterification reactions (Newman 1998) the first one, is the attack by the 2'-OH of the branch point A to the phosphate of the 5´ss, creating a lariat intermediate (Figure 1). In the second part of the reaction, the 3'-OH of the 5´ss is ligated to the 3´ss liberating the lariat intermediate.

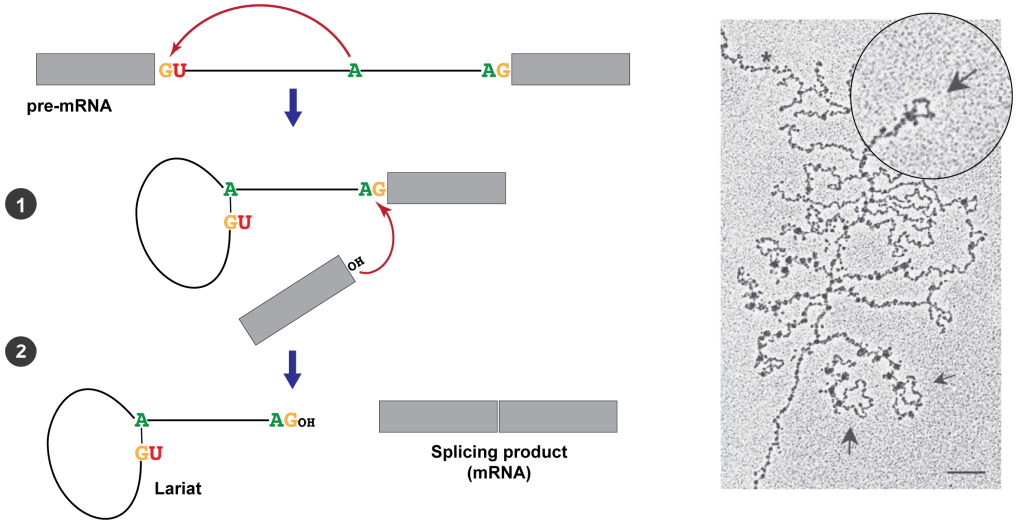

Figure 1: Splicing overview. Left: Main splicing reactions; Right: First observations of splicing from the Sharp Lab. Adapted from (Berget et al. 1977).

The recognition of the splice sites is mediated by the distinct subunits of the spliceosome. The spliceosomal subunits are composed of protein components and small nuclear RNAs (snRNA). Interactions between the snRNAs and the mRNAs are crucial to define the splicing boundaries. In eukaryotes, the process of splicing takes place through the successive formation of key intermediary complexes that favour the dynamics of the reactions (Figure 2). In the first reaction the U1-snRNP interacts with the 5´ss and additional protein factors recognise the 3´ss, forming the E complex. Subsequently, the U2 subunit recognises the branch point in the A complex, promoting its proximity to the 5´ss. Next, U4/U6.U5 tri-snRNP are recruited to generate the B complex. The catalytically active form of the B complex is known as the B* complex and it is characterised by the release of U1 and U4, here is when the first *trans*-esterification reaction takes place. Finally, in the C complex, the second reaction takes place, freeing the lariat and joining the exons.

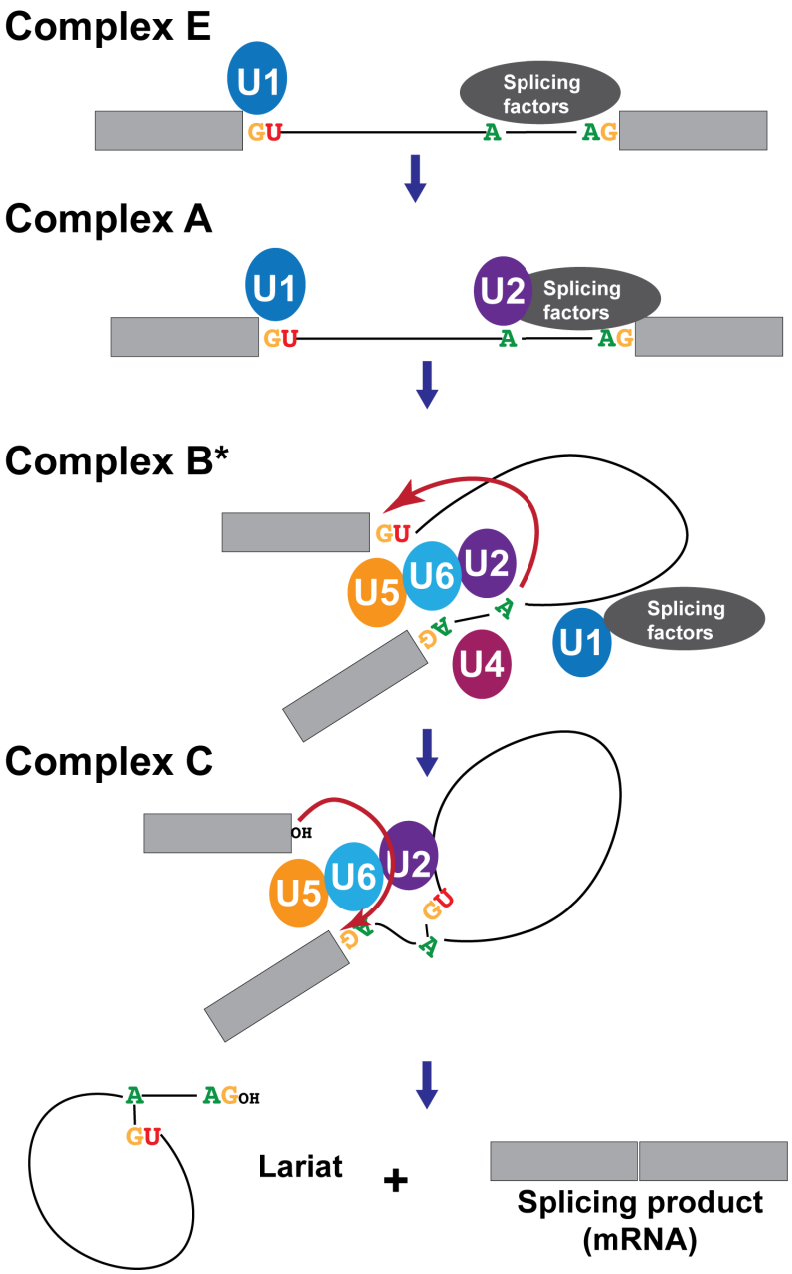

Figure 2: Spliceosome complexes performing the splicing reactions. Adapted from (El Marabti and Abdel-Wahab 2021).

Regulation of splicing goes beyond the recognition of canonical elements in the sequence by the spliceosome components. There are several examples of elements in the RNA sequence that inhibit or enhance splicing. Depending on their location, they can be labelled as exonic splicing enhancers (ESEs), or silencers (ESSs), and intronic splicing enhancers (ISEs) or silencers (ISEs) (Wang and Burge 2008). It has been discussed in the literature, how much the density of these short elements impact splicing and how the robustness to mutations of some splicing events could also be influenced by the presence of specific *cis*-elements that they host (Baeza-Centurion et al. 2020). The mechanism of action of these *cis*-elements is explained by their recruitment of *trans*-acting factors, mainly in the form of RNA-binding proteins (RBPs) (Ke et al. 2011) (Figure 3).

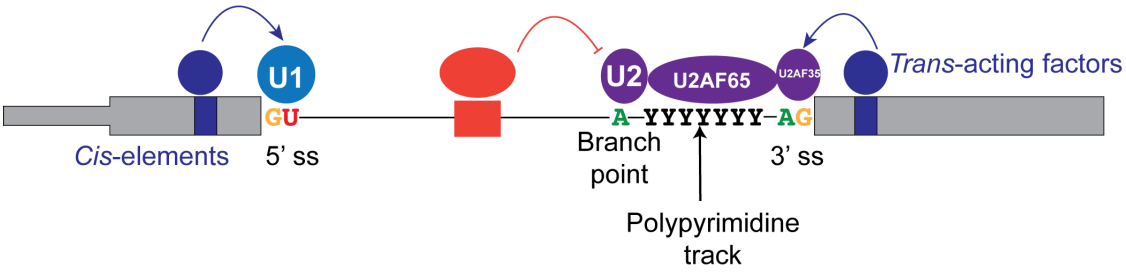

Figure 3: Splicing Code. Representation of the basic components of the splicing regulation.

Alternative splicing

Variation in the splicing regulatory mechanisms can generate distinct splicing outcomes from a single transcript. This process receives the name of alternative splicing of the pre-mRNA and it is an essential mechanism of diversification and organism complexity: it has been estimated to occur in approximately 95% of the multiexon genes (Pan et al. 2008). The majority of these alternatively spliced genes are protein-coding (Pan et al. 2008; Wang and Rio 2018). However, recent studies have also pointed out the importance and universality of alternative splicing in non-coding transcripts such as long non-coding RNAs (Deveson et al. 2018).

Types of alternative splicing

Alternative splicing involves many possibilities other than the shuffling of exons, creating an experimental challenge to study. It is possible to classify alternative splicing events into two major categories: classic examples and complex patterns (Park et al. 2018) (Figure 4). In the first class of events, we find the "cassette events" like exon skipping, the use of alternative 3´ or 5´ splice sites, exons that are mutually exclusive and retained introns. However, with the development of sequencing technologies, it has been possible to identify more complex alternative splicing patterns. Some of them are a result of extreme conditions in splicing efficiency while others, appear upon changes in consensus sequence recognition. Examples of these non-canonical splicing events are exonisations, where a new exon is born due to the use of cryptic splicing sites, microexon (extremely small exons) generation, exitrons (introns in a known exon), circular RNAs, chimeric RNAs and the use of atypical splicing sites, as a result of alternative compositions in the spliceosome (Sibley et al. 2016). In addition, these complex splicing patterns can appear in a combinatorial manner, generating a broad number of possibilities for the final mRNA sequence. For instance, a very extreme case of this is the *Dscam* gene in *Drosophila melanogaster*, which can express nearly 38,016 distinct mRNAs (Wojtowicz et al. 2004).

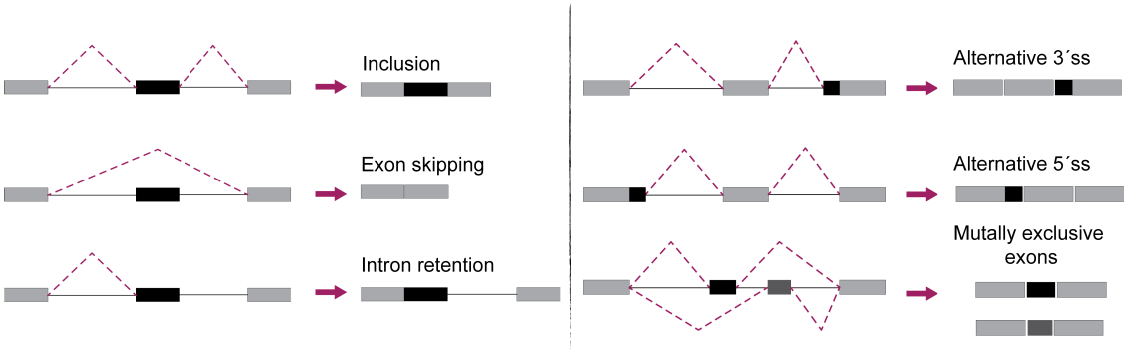

Figure 4: Basic types of alternative splicing in cassette exons.

Splicing regulatory networks

The key to alternative splicing control relies on the intrinsic communication of the *cis*-elements and *trans*-acting factors. Such communication receives the name of "splicing code" (Wang and Burge 2008; Barash et al. 2010) and it is maintained by conserved splicing regulatory networks. These networks are not isolated, but also communicate with other regulatory layers, such as those controlling transcription and genome organization (Han et al. 2017; Ruiz-Velasco et al. 2017). Furthermore, alternative splicing networks play critical roles in signalling or metabolic pathways (Jourdain et al. 2021). To understand the dynamics of the splicing regulatory networks it is necessary to look at the basic mechanisms that control splicing decisions and dissect how small interactions can change the outcomes.

Defining the splicing sites

The first challenge that the regulatory networks face is the definition of introns and exons. Currently, two models explain how the spliceosome interacts with the regulators to define the regions of the mRNA to be processed. Interestingly, both models could, in principle, being carried out by the same complexes (Li et al. 2019). The first model is the intron-definition and is the most abundant in invertebrates and small model organisms like yeast. The second model is exon-definition and explains the controlled splicing in long introns which are more common in vertebrates, like humans. What differentiates both models is the direction of the communication between the distinct splicing subunits. In the intron-definition, the communication takes place across the introns, bringing together the 5´ ss and the next downstream branch point (Figure 5). In contrast, for long introns (>250 bp), the spliceosome interacts first with the splice sites that define an exon to then engage with the next processing subunit and splice the exon (De Conti et al. 2012). Recent evidence also suggests that the processing

of long exons also could involve the usage of recursive splice sites (Wan et al. 2021), even in organisms with relatively short introns (Joseph and Lai 2021).

The role of RNA binding proteins in splicing decisions

Families of RNA binding proteins like the SR proteins, named after their repetitive serine and arginine repeats, have been described to act by regulating alternative splicing in a general manner. SR protein interactions act at different levels of the splicing process, for instance, it has been described that they can interact with the carboxyl-terminal domain (CTD) of the RNA polymerase (Pol) II, particularly when this is phosphorylated, influencing the formation of the spliceosomal complexes (Nojima et al. 2018).

Besides interacting with Pol II, SR proteins could be decisive in the splicing definition. Particularly, the distinct interactions of their RS disordered domains favours one model versus another. For instance, direct interactions with members of the U1-snRNP and U2 promote exon definition (Wu and Maniatis 1993) whereas interactions with other components of U1 and U2, like Rsd1 and Prp5, can shift the balance towards the intron definition (Shao et al. 2012) (Figure 5).

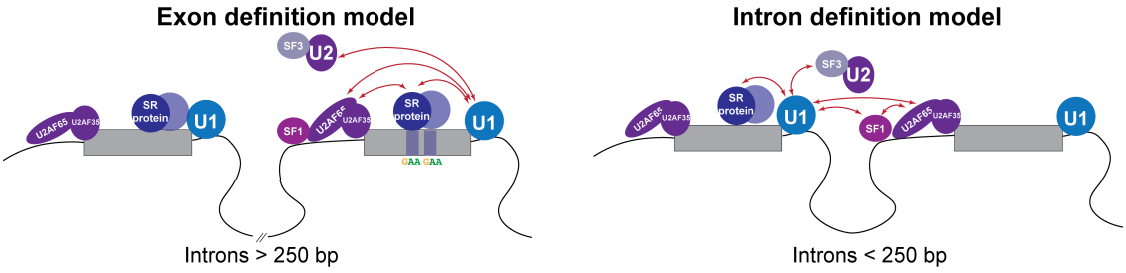

Figure 5: Models of exon and intron definition. The direction of the interactions is shown in the arrows.

Another set of proteins that can have an impact on the regulation of alternative splicing is the hnRNP (heterogeneous nuclear ribonucleoprotein) family. There are more than 20 well-characterized hnRNP members and some of them also have cytoplasmic functions, mostly controlling translation and RNA stability (Geuens et al. 2016). Their role in splicing has been described mostly as repressive (Okunola and Krainer 2009; Del Gatto-Konczak et al. 1999). However, there is increasing evidence that the outcome of their regulation depends on their binding position in relation with the splicing site (Erkelenz et al. 2012).

Evolution and mechanisms of the splicing regulatory networks

SR proteins are present across all eukaryotes, and it has been proposed that they might have a common ancestral origin, being as antique as alternative splic-

ing. Photosynthetic organisms contain twice as many SR proteins than animals, mostly with specialised functions (Richardson et al. 2011). On the other hand, several members of the hnRNP proteins are missing in plants (Busch and Hertel 2011) where orthologous proteins to the HNRNP1 group and simplified versions in the form of glycine-rich RBPs, perform similar splicing regulatory roles (Syed et al. 2012; Meyer et al. 2015). The co-evolution of these two main families of splicing factors with the increase in splicing complexity has suggested that specialisation probably provided of more flexibility to the core splicing signals. This idea is supported by the increased recognition of weak splicing signals in *Saccharomyces Cerevisiae* upon the introduction of mammalian SR proteins (Shen and Green 2006).

An important aspect of the RBPs in regulating splicing is their modularity: they tend to form complexes that interact with multiple *cis*-elements. Intrinsically disordered regions (IDRs) have been described as mediators of protein-complex formation. For example, hnRNP proteins can form complexes and bind cooperatively to exons to exert their regulatory functions. The key to recruitment of more splicing factors seems to be the IDRs, which are enriched in glycine and tyrosine residues (Gueroussov et al. 2017). IDR-containing proteins present high conservation in their regulated splicing patterns and interestingly, tend to associate with membraneless structures like stress granules (Protter et al. 2018). In fact, there is increasing evidence for the association of SR proteins and components of the spliceosome with nuclear speckles (Liao and Regev 2020), suggesting a physical compartmentalisation of the splicing process.

Another source of evolutionary divergence in splicing signals is provided by transposable elements. For instance, it has been described in several genes, how new *cis*-regulatory motifs can arise from repetitive elements like *Alu* or *LINE*s (Attig et al. 2018; Tajnik et al. 2015; Zarnack et al. 2013). With the presence of new splicing signals in repetitive elements, splicing factors have evolved to prevent the recognition of transposon-derived motifs. That is the case of HNRNPC in the *Alu* context (Zarnack et al. 2013) or MATR3 and PTBP1 in the *LINE*s (Attig et al. 2018). However, often these new splicing elements are preserved and even contribute to the generation of new regulatory domains, such as the case of the integration of transposase domains in the Krüppel-associated box (KRAB) transcriptional factors (Cosby et al. 2021).

Mis-splicing in cancer

Regulation on the post-transcriptional level, allows the cell to produce dynamic responses to maintain and regulate critical processes like growth, development, and differentiation. Thus, alterations in the splicing regulation can be relevant

during disease, especially in cancer. Cancerous cells can take advantage of errors in splicing and use them to their benefit. Additionally, other cancer types have a high frequency of splicing-factor mutations (Saez et al. 2017; Dvinge et al. 2016). These mutated factors then contribute to the generation of aberrant transcripts which increase the odds of escape from cellular control mechanisms and disturb proliferation.

Aberrations in splicing core components

With the increment of available high-throughput sequencing data, it has been possible to shed a light on the increased frequency of mutations in RBPs associated with splicing regulation. For instance, core components of the spliceosome like SF3B1 or U2AF1, both subunits of the U2 snRNP, appear to be frequently mutated in haematological malignancies (Tang et al. 2016; Wang et al. 2016; Ilagan et al. 2014), reaching a frequency >70% in certain subtypes (Papaemmanuil et al. 2011). In the case of the subunits from the U2 snRNP, it is expected that splicing-altering mutations lead the cancerous cells to have an improper function and affected proliferation. However, splicing alterations in the context of cancer have been observed to be advantageous. The mechanisms are diverse, for instance, the aberrant recognition of splice sites can contribute to the functional alteration of genes that contribute to oncogenic programs like the apoptotic modulation of Bcl-x (Stevens and Oltean 2019).

Global splicing alterations also have a relevant role in cancer progression, and they can be triggered by chemical compounds. In this regard, SF3B1 appears to be one of the most promising targets for splicing disruptions. Several natural compounds like the pladienolides, have shown to be effective in arresting the cell cycle (Webb et al. 2013) by altering the conformation of SF3B1, influencing its splicing activity (Lee and Abdel-Wahab 2016) and have been taken into clinical trials (Eskens et al. 2013). Recent evidence also points to the induction of specific signalling pathways as a result of major mis-splicing, such as the double-stranded RNA (dsRNA) response, which is normally activated under immune response to viruses (Bowling et al. 2021).

Changes in expression levels of RBP regulators

Not only the splicing patterns can be altered in cancer, but also the expression levels of the RBP regulators. Changes in expression can be a consequence of genomic rearrangements as well as other epigenetic factors. Some RBPs present a cancer-specific altered expression profile, for instance SRSF1 is constantly upregulated in solid tumours (Karni et al. 2007), while the mis-regulation of some

hnRNP proteins such as hnRNP A2/B2 results in poor prognosis in glioblastoma (Golan-Gerstl et al. 2011a).

Interestingly, MYC-driven tumours show sensitivity to splicing alterations (Koh et al. 2015; Phillips et al. 2020). As a transcription factor, MYC can directly alter the expression of splicing regulators. This is the case of hnRNP proteins like PTB (David and Manley 2010) and hnRNPA1/2 (Golan-Gerstl et al. 2011b). Another mechanism that could explain the impact of MYC on splicing regulation is that MYC-induced transcriptional changes may overload the splicing machinery, promoting vulnerability to splicing errors (Hegele et al. 2012).

Alternative splicing of *RON* exon 11

The proto-oncogene *RON*

The tyrosine kinase Recepteur d'origine nantais (RON) is a product of the gene *RON* (also known as *MST1R* or *MSP*) and it has a relevant function on cancer signalling, especially involved in migration, survival, angiogenesis and chemoresistance (Yao et al. 2013). Being expressed in epithelial cells, it is more frequently altered in solid tumours, such as breast, colon or lungs, where tumour-specific isoforms are produced (Mayer et al. 2015; Krishnaswamy et al. 2018). Out of the different protein isoforms that have been identified, RON$\Delta 165$ has been intensively studied due to its relevance in inducing an invasive phenotype in gastric cancer (Collesi et al. 1996).

The RON$\Delta 165$ transcript isoform is a result of an alternative splicing event involving the skipping of the exon 11 in *RON*. The exon 11 is flanked by two particularly small introns (<300 bp) (Figure 6) and previously it has been proposed that its splicing regulation could be mediated by the interactions of SRSF1 with an ESE located in the downstream exon 12 (Ghigna et al. 2005). However, knockdown experiments of other splicing factors have also uncovered other potential regulators of *RON* splicing, such as HNRNPH proteins (Papasaikas et al. 2015).

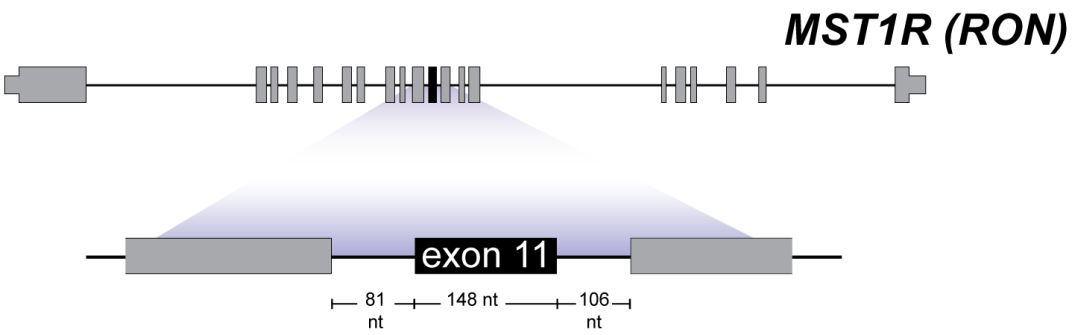

Figure 6: Schematic of the *RON* gene, with details on the exon 11 region.

HNRNPH proteins and their splicing role in cancer

HNRNP H/F proteins are an important subfamily of splicing regulators. Its members include HNRNPF, hnRNP H1 (H), H2 (H´) and H3 (2H9) (Han et al. 2010) and they are characterized by the presence of three poorly conserved quasi RNA recognition motifs (qRRMs) and two Glycine(Gly)-rich domains (Geuens et al. 2016). The qRRM domains allow the specific recognition of poly(G) sequences (G-tracks) (Dominguez 2006). These signals act frequently as splicing enhancers, especially when located close to intermediate strength 5´ splice sites (Xiao et al. 2009). On the other hand, Gly domains seem to mediate long-range interactions by bringing the splice sites of long introns in close proximity. The interactions between the motifs can also be influenced by post-transcriptional modifications, which can modulate the protein localization and communication with other proteins (Van Dusen et al. 2010). In fact, HNRNPH1/H2 are located preferentially in the nuclei whereas HNRNPHF is mostly cytoplasmic (Han et al. 2010).

The expression of HNRNPF presents low specificity, whereas HNRNPH1/H2 can be more abundant in the prostate gland but low in the liver or pancreas (Honoré et al. 2004). Across the main HNRNP H1/H2 splicing-regulated targets we can find neurological specific targets like c-src (Chou et al. 1999) or BACE1 (Fisette et al. 2012) as well as genes involved in the regulation of invasion and apoptosis, like MADD (LeFave et al. 2011) or Bcl-x (Garneau et al. 2005). There are indications of the role of HNRNPH1 in regulating the splicing of spliceosome-associated genes. This is supported by the observation of strong fluctuations in protein abundance upon depletion of HNRNPH (Uren et al. 2016). It is possible that HNRNPH plays a central role in rewiring splicing networks.

A cancer-relevant target: the case of *CD19*

B-cell Acute Lymphoblastic Leukaemia and CART-19

Acute lymphoblastic leukaemia (ALL) is a haematological malignancy usually manifested as an arrest in development of lymphoid precursor cells with subsequent proliferation of the immature cells, being more frequent in children but with a worse long-term prognosis in adults (Roberts 2018). The most common type of ALL is the B cell ALL (B-ALL), accounting for more than 80% of the ALL cases and ~30% of all childhood cancers (Huang et al. 2020). In Germany alone, according to the Childhood Cancer Registry, approximately 600 children develop ALL every year (Grabow et al. 2011). The standard treatment for B-ALL patients is risk-directed therapy, this means that there is a constant assessment of the minimal residual disease at defined points of the treatment, giving more intense chemotherapy to patients at higher risk (St. Jude Hospital 2021; NCI 2016).

In search of precision, directed therapies have arisen and one of the most successful developments against B-ALL is the chimeric antigen receptor (CAR) T-19 therapy. This therapy consists in the engineering of T-cells to make them express a new receptor, the CAR, which contains an intracellular signalling domain attached to a tumour antigen binding domain (Pehlivan et al. 2018). In the case of B-ALL, the CAR recognises the CD19 receptor, a 95 kDa transmembrane protein, that is a common marker of normal and neoplastic B cells (Wang et al. 2012) (Figure 7). The first successful CARs against CD19 appeared in April 2012 (Grupp et al. 2013) and subsequent data showed that although 67%-87% initially of the patients achieved complete remission, the following studies showed a high relapse rate of up to 50% may occur (Nie et al. 2020).

The mechanisms of CART-19 relapse are not completely understood, but more studies are hinting towards two major classes of the patients that relapse: the CD19 positive relapses ($CD19^{+}$) and the CD19 negative relapses ($CD19^{-}$) (Li and Chen 2019). These classifications are based on whether the CD19 receptor appears or not on the surface of cancerous B cells. The loss of CD19 can be attributed to three main reasons: a) the existence of a $CD19^{-}$ clone that proliferates under therapy (Weiland et al. 2016), b) a lineage switch from lymphoid to myeloid as a result of a reprogramming involving the B cell transcriptional factors (Gardner et al. 2016) and c) aberrations in CD19 copy number or transcript production and processing (Sotillo et al. 2015).

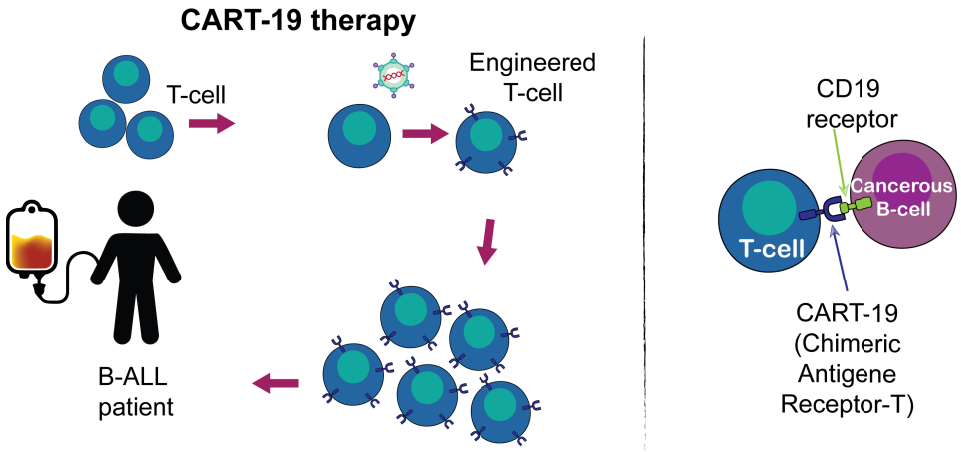

Figure 7: The CART-19 therapy. Left: Production. T-cells taken from patients are engineered to express a CAR. After proliferation, they are re-inserted into the B-ALL patient.; Right: Mechanism of interaction. CART-19 cells recognise the CD19 receptor, located in the surface of the B cells.

Alternative splicing of *CD19* exon 2

Located in the short arm of the chromosome 16, in humans, *CD19* is the gene that encodes for the CD19 receptor, which is specifically expressed from the earliest stages of B cell development until plasma cell terminal differentiation (Schroeder et al. 2019). The main function of CD19 is to act as a signal transducer which is done mainly by forming complexes with other relevant actors of B cell signalling like CD21 and the B cell receptor (BCR), playing a major role in the antigen-independent development, critical for an optimal immune response (Wang et al. 2012). Five different transcript variants have been annotated in ENSEMBL for this gene, with two showing protein support. However, in recent years, several alternative spliced isoforms have been associated with CART resistance, highlighting the importance of alternative splicing as a mechanism of loss of CD19.

Paediatric ALL are characterised by a low mutational burden (Zamora et al. 2019). Nonetheless, new genomic studies have described an increased mutation (hypermutation) associated with relapse cases (Waanders et al. 2020). *CD19* has not been shown to be frequently mutated in patients, but there is some evidence that relapse-associated mutations impact splicing of the gene, in particular exon 2, leading to the production of an aberrant isoform, CD19ΔExon2. This isoform potentially affects the recognition of the CD19 receptor by the CART (Sotillo et al. 2015). Mutations in exon 2 may hinder the binding of SRSF3, a splicing factor relevant for inclusion and thus increase exon skipping (Sotillo et al. 2015). Finally, CD19ΔExon2 may affect the recognition of the CD19 receptor by the CART (Sotillo et al. 2015)

Beyond CD19ΔExon2, three other isoforms have been reported to contribute

to relapse (Figure 8). The first one is Δex5-6, which seems to be present in patients upon therapy, and it is of interest given that affects the transmembrane and cytosolic domains of CD19 (Fischer et al. 2017). A second isoform, which seems to be more abundant in relapsed patients, is intron 2 retention, this isoform could result in an unproductive transcript or truncated protein (Asnani et al. 2019). The third isoform, ex2Δpart is not very well explored yet: it misses part of the exon 2 and does not contain conventional splicing sites. This isoform seems to be present before the disease (Fischer et al. 2017) but also has been suggested as potential marker of therapy resistance in adult B-ALL (Zhao et al. 2021). Given all that diversity of isoforms, it seems necessary to characterise the range in which mutations affect splicing and its consequences for therapy.

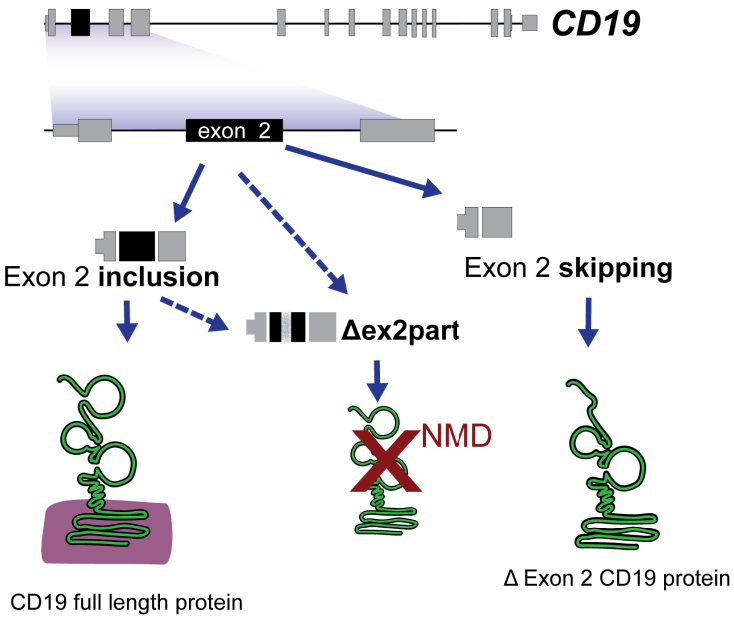

Figure 8: *CD19* genomic loci with focus on the region of exon 2. Isoforms derived from exon 2 are shown with their predicted consequences in CD19 production.

Methodologies to study splicing

Studying RNA splicing variants can be challenging as most of the RNA in cells comes from a small set of very abundant RNA species, such as ribosomal RNA (rRNA). Thus, the majority of protocols rely on optimizing ways to capture transcripts followed by subsequent amplification. The standard amplification procedure consists in using the reverse transcription polymerase chain reaction (RT-PCR), where RNA is converted to the much more stable DNA by means of a reverse transcriptase enzyme. Combining this technique with measurable signalling molecules, like fluorescently labelled nucleotides, generates a form of quantitative RT-PCR named RT-qPCR, which then allows for quantitative estimation of the

RNA in the sample.

Alternative splicing events are usually validated by using RT-PCR. This involves the design of primer sequences that target the flanking sequences of the region where the event occurs. Ideally, those regions will be constitutive exons, so that the fluctuation in the signal will come from the assayed event. While it is possible to create panels to assay several splicing events at a time a high throughput solution will usually involve sequencing.

Massive parallel assay reporter screens

Minigene system serve as a minimal set-up to study splicing. Briefly, minigene systems consist of an expression plasmid that contains an exon of interest flanked by its constitutive exons (Harvey and Cheng 2016). Minigene systems can help to address questions regarding the role of *cis*-regulatory elements as well as *trans*-acting factors that regulate an event, particularly when combined with perturbations in the form of knockdowns or knockouts of RBPs (Cooper 2005).

Table 1: Massive parallel assays for single events

Splicing event(s)	Minigene design	Assayed Variants	Reference
FAS/CD95 exon 6	*FAS* exons 5-7 in HEK293 cells.	All possible single mutants in the exon (189) plus double mutants.	Julien et al. (2016)
WT1 exon 5	WT1 exon 5 surrender by the exonic and intronic sequences of the Chinese hamster *dhfr* gene, in HEK293 cells.	Dinucleotides contained in the exonic positions 2-47.	Ke et al. (2017)
BRCA2 intron 17, *SMN1* intron 7 and *IKBKAP* intron 20	*BRCA2* introns 16-17, *SMN1* intron 6-8 and *IKBKAP* intron 19-21, in HeLa cells.	32,768 possible 9-nt GU and GC 5´ss sequences.	Wong et al. (2018)

Splicing event(s)	Minigene design	Assayed Variants	Reference
RON exon 11 [included in this work]	*RON* exons 10-12 in HEK293, MCF7 and HeLa cells.	All possible single mutations, including the intronic regions.	Braun et al. (2018)
SMN1 exon 7	Exon 1 with barcode, *SMN1* exon 7 and downstream exon, in HEK293 and HeLa.	180 single and 470 double exonic mutants.	Souček et al. (2019)
FAS exon 6, ancestral sequence	*FAS* exons 5-7 in HEK293, HeLa and COS-7 cells.	3,072 genotypes, reflecting the evolution of the exon 6.	Baeza-Centurion et al. (2019)
PSMD14 exon 11	*PSMD14* exon 11 using upstream *FAS* exon 5 and downstream *FAS* exon 7, in HEK293.	All single nucleotide exonic changes.	Baeza-Centurion et al. (2020)
CD19 exon 2 [included in this work]	*CD19* exons 1-3 in NALM-6 cells.	All possible single mutations, including the intronic regions.	Cortés-López et al. (2021)

In recent years, with the increase of accessibility of Next Generation Sequencing (NGS) technologies, several groups have developed massive parallel screens to characterise the effect of individual variants in disease-relevant exons. These experiments (described in Table 1) consist of the generation of minigene variants that contain distinct mutations, often characterising all possible mutants in a region or mutations with previous indications of medical relevance. These minigenes are then transfected into cells and sequenced. The variants often contain a unique barcode that serves as an identification tag of all the transcripts generated

upon mutation.

Table 2: Massive parallel assays for multiple events

Library design	Cell line	Model or pipeline derived	Reference
5´ss library: introns with two competing splicing donors separated by 44 nt. 3´ss library: similar to 5´ss but with a degenerate region overlapping the first splice acceptor branch point.	HEK293	SPANR	Rosenberg et al. (2015)
4,964 exonic mutant - WT pairs reported in the Human Gene Mutation Database (HGMD).	HEK293T	MaPSy	Soemedi et al. (2017)
2,059 human genetic variants spanning 110 alternative exons.	K562 and HepG2	Vex-seq	Adamson et al. (2018)
27,733 human variants across 2,198 exons assaying splicing outcome by fluorescence.	HEK293	MFASS	Cheung et al. (2019)
Libraries comprising library-specific common primers, a unique barcode and a 147–162 nt long variable region with native splice site contexts spanning a wide range of splicing ratios. No minigene but an insertion in AAVS1 loci.	K562	Splicing_MPRA	Mikl et al. (2019)
33,317 unique sequences across 259 exons to study 355 distinct splicing regulatory elements potentially bound by RBPs.	K562 and HepG2	Vex-seq RBP	Adamson et al. (2021)

The second type of massive parallel assays involves the experiments where, instead of looking at a single splicing event at the time, several splicing events and variants are assayed (listed in Table 2). Together with the single-gene assays, they have become helpful to generate splicing regulatory models (Cheng et al. 2019; Baeza-Centurion et al. 2020) and, in some cases to dissect the splicing function

for mutations with uncertain significance. However, one of the major limitations is that one of the major limitations is that splicing is highly tissue-specific, and the observed effects may thus not be transferable to other cellular contests. In addition, the integration of results of different assays results challenging due to the technical differences between protocols.

Third-generation sequencing technologies

One of the game-changers in recent years in the methodologies to study RNA has been the development of long-read technologies. Especially for splicing, long-reads have uncovered a myriad of new isoforms across organisms, tissues and cells. Two companies are the current leaders in the field, developing approaches for the distinct needs of their customers: Pacific Biosciences (PacBio) and Oxford Nanopore (ONT).

PacBio

PacBio uses the single-molecule, real-time DNA sequencing (SMRT) technology, which consists of the use of an immobilised DNA polymerase that, with a DNA molecule as a template, uses fluorescently labelled deoxyribonucleoside triphosphates (dNTPs) for the synthesis and produces a signal with every incorporation event (Eid et al. 2009). The main advantage of PacBio is its high accuracy, achieved through the generation of high-fidelity (HiFi) reads that provide a $>$ 99.9% read accuracy by circularising the DNA molecule and reading it several times, generating a circular consensus sequence (CSS) (Wenger et al. 2019) (Figure 9).

Since DNA single molecules are the templates of PacBio, RNA applications require first reverse transcription to generate a cDNA (complementary DNA). Iso-Seq is the isoform detection of PacBio, which differs from standard RNA-seq by including a size-selecting rather than a fragmentation step. This is then followed by the addition of the SMRTbell adapters, which are the key for the CSS generation (Gonzalez-Garay 2015). Alternatively, there are variations of the protocol that involve a targeted sequencing for when only a few transcripts are of interest (Dainis et al. 2019; Sheynkman et al. 2020).

Oxford Nanopore

ONT has developed pocket-size devices that are based on the detection of current shifts when a molecule passes through a nanoscale pore, allowing the direct read-out of single RNA or DNA molecules (Deamer et al. 2016). In the last years, several groups are also pushing for proteins (Brinkerhoff et al. 2021; Howorka

and Siwy 2020). In the case of RNA, ONT provides sample preparation protocols for sequencing cDNA molecules but also native (direct) RNA (ONT 2019) (Figure 9). Perhaps the major limitations are the input material necessary (up to 500 nanograms for direct RNA) as well as the initially medium accuracy of the reads. However, However, in recent years, accuracy has been pushed to > 99% via improvement in the real-time calling algorithms and the chemistry of the pores (Karst et al. 2021).

Regarding ONT applications in the RNA field, there is a growing number of reports of new transcriptomes uncovering more unknown isoforms. Moreover, taking advantage of the direct RNA sequencing, it is possible to detect certain modified ribonucleotides like m6A (Liu et al. 2019) and others (Pratanwanich et al. 2021). Another important limitation is that currently, only polyadenylated sequences can be sequenced, which limits the analysis of non-coding transcripts or other RNA species like tRNAs. However, creative solutions are being developed in the community (Thomas et al. 2021; Rahimi et al. 2021) that could improve the technology and extend its use in the following years.

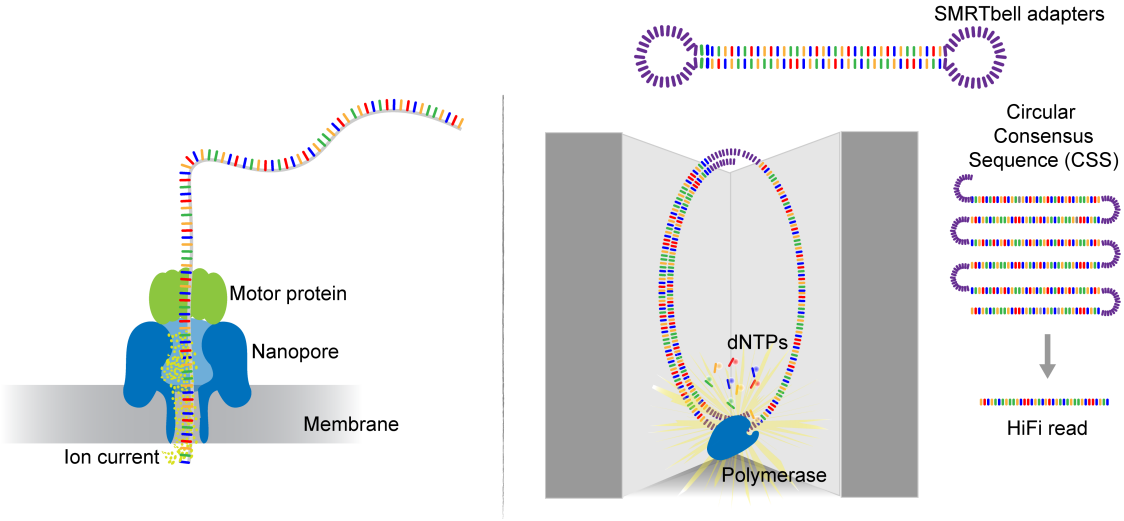

Figure 9: Long-read technologies. Left: Nanopore; Right: PacBio and HiFi read production.

Bioinformatic approaches to study splicing

How to measure splicing?

Detection of transcript isoforms is challenging but so is also its quantification. Even though many big databases are constantly curating the annotations of transcript isoforms, the dynamic and condition-specific nature of splicing requires the development of tools that allow accurate detection and quantification of new splicing events.

Differential splicing analysis results from a comparison of the splicing out-

comes between conditions, usually trying to identify those splicing events that appear when the context is perturbed. Using RNA-seq data we can approach this type of analysis in three methodological ways: an exon-centric, an event-centric and an isoform-centric view. The first and second could be preferred when analysing splicing mechanisms and regulation (Dvinge et al. 2016), while the latter is now approachable and, it will become more precise in the years to come, with the development of long-read technologies.

When analysing single splicing events, a common metric to use is the percent splice-in (PSI or ψ) which reflects the splicing efficiency of an event, ranging from 0 to 100%, with higher values meaning that the measured event is always present (Schafer et al. 2015). PSI values can be measured per condition and then compared, indicating this value as $\Delta\psi$. Some tools that have used this approach are rMATS (Shen et al. 2014), SUPPA2 (Trincado et al. 2018) and MISO (Katz et al. 2010). PSI can be a useful measurement, but it is not always appropriate for more complex splicing events, thus, other strategies have been proposed in the form of measuring local splicing variations like in MAJIQ (Vaquero-Garcia et al. 2016) or defining splicing clusters such as in LeafCutter (Li et al. 2017). A recent study concluded that, comparing more than ten tested methods, MAJIQ and rMATS perform best, but also showed the increased variability in the differentially spliced transcripts reported (Mehmood et al. 2019).

How to predict splicing?

One of the most ambitious goals of studying splicing is to be able to predict the effects of disruptions using the information that we have developed by using experiments. Perhaps the most reductionist approaches are the ones based solely on making inferences based on the nucleotide sequence of the genes. On the other hand, in recent years there has been an increase in algorithms that use machine learning techniques to improve splicing site prediction and effects.

Early predictive tools were developed by deducing metrics from the comparisons of the nucleotide conservation across the canonical splicing elements. Having the genomic sequence of an organism the first task is to know where the splicing machinery will decide that something looks like a 3´or a 5´ss. Initially some algorithms considered an approach based on positional weight matrices (PWMs), scoring the sequences according to their similarities with the nucleotide position and contribution in the reference matrix (Jian et al. 2013). These kinds of approaches can be easily biased by the initial data used to build the PWMs. For this reason, approaches with more flexibility were developed in the early 2000s.

Maximum Entropy distribution (MED) is an of approach that models short sequence motifs only assuming the consistency with the features of the empiri-

cal distribution from available data, allowing to generate different models and compare them (Yeo and Burge 2004). This algorithm can be accessed on-line in two variants, the 5´ss and the 3´ss predictions, each uses a 9 nt or 23 nt input sequence, respectively, to calculate what is known as the MaxEnt score. The interpretability of the score, as suggested in a publication involving the *ATM* (Eng et al. 2003), is: *"The higher the score, the higher the probability that the sequence is a true splice site..."* or *"the higher scoring sequence has a higher likelihood of being used"*.

MED based methods have the disadvantage of being constrained to a defined window of positions, making it more difficult to infer effects in splicing from long-distance *cis*-elements. Therefore, many other algorithms have been developed afterwards, giving also more importance to the dissection of the effect of single nucleotide variants (SNPs or other mutations) in the splicing outcome. With the recent popularity of deep neural networks (DNN), there have been splicing prediction algorithms build on these principles such as SPANR/Spidex (Xiong et al. 2014), MMSplice (Cheng et al. 2019) and SpliceAI (Jaganathan et al. 2019). The last two have gained special interest given that they take as input the genome sequence but are able to predict long range effects with high accuracy (especially SpliceAI-10K).

SpliceAI has been tested by other groups in diverse datasets showing a high variability of accuracy ranging from 33 to 94% (Lord and Baralle 2021). Difference in performance might be due to the specific cellular context. This issue has been addressed by extending MMSplice into MTSplice (Multi-tissue Splicing) which adds an extra component which models tissue-specific sequences (Cheng et al. 2021). First, MTSplice provides a prediction of PSI values while SpliceAI only gives information about the probability of usage for a certain splice site, upon mutation. Eventually, with the tissue-specific module of MTSplice site, it has been possible to make predictions of *de novo* variants in the context of autism. This demonstrates the advent of tissues specific splicing models providing more detailed predictions (Jha et al. 2017).

Scope of this work

The complexity of the splicing regulation requires the integration of different strategies that help to interpret the communication between *cis*- and *trans*-regulatory signals. It is necessary to understand what elements in a sequence define a splicing event, but also which sequences enhance or decrease the observed splicing patterns upon interaction with distinct protein factors. The dissection of the splicing code can begin at a more reduced level, approaching individual splicing events of relevance under a controlled system. This work aims to disentangle the critical components of the splicing regulatory networks from two cancer-relevant events: *RON* exon 11 and *CD19* exon 2.

In the first part of this thesis, a new massive parallel reporter assay is presented, which interrogates the effects of every potential mutant contained in the region defined by exons 10-12 of *RON*. The assay is comprehensive as it characterises intronic mutations beyond the splice site-neighbouring nucleotides. Using protein binding predictions, we search for the *trans*-regulators of the event. To clarify the link between *cis*-elements and *trans*-acting factors the mutagenesis screen is also conducted in the context of a knockdown of an important regulator, HNRNPH.

The accuracy of isoform detection and identification plays a major role in the description of the functions of alternative transcripts. Therefore, it is necessary to be cautious when interpreting the different splicing patterns observed from the experiments. Following this logic, the Chapter 2 this thesis explores the existence of artefactual isoforms, based on the *CD19* exonic intron ("exitron") ex2Δpart. Using distinct long-read RNA sequencing protocols, the bioinformatical analysis aims to characterise false exitrons ("falsitrons") which share characteristics with *CD19* ex2Δpart.

Given that some splicing events have a higher tissue or cell specificity, there is still a need to expand the characterisation of variants in more restrictive backgrounds. *CD19* exon 2 splicing provides a good example of a clinically relevant splicing event with a high cell specificity. Thus, based on the high-throughput mutagenesis assay that we generated in Chapter 1, Chapter 3 of this thesis describes a similar mutagenesis screen performed in the region of *CD19* exons 1-3. The *CD19* minigene has an increased length compared to *RON*, therefore, long-

read technology is implemented to characterise the introduced mutations in the minigene variants with high precision. We also use NALM-6 cells (B-ALL derived cells) to preserve the specificity of *CD19* expression. Similarly, we implement knockdown assays, guided by bioinformatic predictions from RBP regulators that use state-of-the-art tools.

These three chapters apply modern techniques to study splicing and discuss their reach and limitations. Together, the work presented in this thesis seeks to expand our understanding of the splicing code in the disease context, providing a detailed view of the splicing networks and their interactions.

Chapter 1

Decoding a cancer-relevant splicing decision in the RON proto-oncogene using high-throughput mutagenesis

Summary

Alternative splicing is a conserved step of gene expression. Several studies have shown that specific RNA sequence elements can be recognised by RNA-binding proteins (RBPs) with high specificity, playing an important role as the effectors of splicing regulation. Here, we describe the *cis*-regulatory landscape of an alternatively spliced cancer-relevant exon in the gene that encodes the MST1R (RON) receptor kinase. Using a new high-throughput mutagenesis approach, we identified positions in the sequence that influence *RON* exon 11 splicing. We combined *in silico* predictions of several RBP binding sites with the experimental data from the mutagenesis screening. We thereby defined potential regulatory hotspots as well as important RBPs involved in the regulation of the alternative splicing event. Interestingly, for one of the most important regulators, HNRNPH, we observed a good correlation of the predicted binding sites with the *in vivo* binding, assessed by iCLIP experiments, confirming the accuracy and precision of our system. Synergy analysis of HNRNPH uncovered the key binding sites involved in the splicing decisions but also highlighted a potential cooperative mechanism of splicing control in *RON* exon 11 which presents a switch-like behaviour. We demonstrate how high-throughput approaches can be used to study alternative splicing and the combination with RBP binding specificity allowed us to develop a better understanding of the regulation of disease-relevant loci.

Zusammenfassung

Alternatives Spleißen ist ein konservierter Schritt der Genexpression. Mehrere Studien haben gezeigt, dass spezifische RNA-Sequenzelemente von RNA-bindenden Proteinen (RBPs) mit hoher Spezifität erkannt werden können und eine wichtige Rolle als Effektoren der Spleißregulation spielen. Hier beschreiben wir die *cis*-Regulationslandschaft eines alternativ gespleißten krebsrelevanten Exons in dem Gen, das für die Rezeptorkinase MST1R (RON) kodiert. Mithilfe eines neuen Hochdurchsatz-Mutagenese-Ansatzes haben wir Positionen in der Sequenz identifiziert, die das Spleißen von *RON* Exon 11 beeinflussen. Wir haben *in silico* Vorhersagen verschiedener RBP-Bindungsstellen mit den experimentellen Daten aus dem Mutagenese-Screening kombiniert. Auf diese Weise definierten wir potenzielle regulatorische Hotspots sowie wichtige RBPs, die an der Regulierung des alternativen Spleißvorgangs beteiligt sind. Interessanterweise beobachteten wir für einen der wichtigsten Regulatoren, HNRNPH, eine gute Korrelation der vorhergesagten Bindungsstellen mit der *in vivo* Bindung, bewertet durch iCLIP-Experimente, was die Genauigkeit und Präzision unseres Systems bestätigt. Die Synergieanalyse von HNRNPH hat die wichtigsten Bindungsstellen aufgedeckt, die an den Spleißentscheidungen beteiligt sind, aber auch einen potenziellen kooperativen Mechanismus der Spleißkontrolle in *RON* Exon 11 aufgezeigt, der ein schalterähnliches Verhalten zeigt. Wir zeigen, wie Hochdurchsatzansätze zur Untersuchung des alternativen Spleißens verwendet werden können. Die Kombination mit der RBP-Bindungsspezifität ermöglichte uns ein besseres Verständnis der Regulierung krankheitsrelevanter Loci.

Statement of contribution

This project was part of the main doctoral work of Simon Braun and Samarth T. Setty. Since joining the project, in February 2017, I participated in all paper-related meetings and discussed ideas directly with the main authors. I contributed the binding site predictions (depicted in Figure 3e) and all the subsequent analyses shown in Figure 4a and Figure 5c,d. I generated all the previously mentioned figures, as well as Figure 6a. In addition, I generated the final versions of the Supplementary Data 1-4 and 6. I contributed to the main text with the description of the methodology used in the RBP binding site analysis and synergistic analysis.

Supervisor confirmation: _____

nature COMMUNICATIONS

ARTICLE

DOI: 10.1038/s41467-018-05748-7 OPEN

Decoding a cancer-relevant splicing decision in the *RON* proto-oncogene using high-throughput mutagenesis

Simon Braun[1], Mihaela Enculescu[1], Samarth T. Setty[2], Mariela Cortés-López[1], Bernardo P. de Almeida[3,4], F.X. Reymond Sutandy[1], Laura Schulz[1], Anke Busch[1], Markus Seiler[2], Stefanie Ebersberger[1], Nuno L. Barbosa-Morais[3], Stefan Legewie[1], Julian König[1] & Kathi Zarnack[2]

Mutations causing aberrant splicing are frequently implicated in human diseases including cancer. Here, we establish a high-throughput screen of randomly mutated minigenes to decode the *cis*-regulatory landscape that determines alternative splicing of exon 11 in the proto-oncogene *MST1R* (*RON*). Mathematical modelling of splicing kinetics enables us to identify more than 1000 mutations affecting *RON* exon 11 skipping, which corresponds to the pathological isoform RONΔ165. Importantly, the effects correlate with *RON* alternative splicing in cancer patients bearing the same mutations. Moreover, we highlight heterogeneous nuclear ribonucleoprotein H (HNRNPH) as a key regulator of *RON* splicing in healthy tissues and cancer. Using iCLIP and synergy analysis, we pinpoint the functionally most relevant HNRNPH binding sites and demonstrate how cooperative HNRNPH binding facilitates a splicing switch of *RON* exon 11. Our results thereby offer insights into splicing regulation and the impact of mutations on alternative splicing in cancer.

[1] Institute of Molecular Biology (IMB), Ackermannweg 4, 55128 Mainz, Germany. [2] Buchmann Institute for Molecular Life Sciences (BMLS), Goethe University Frankfurt, Max-von-Laue-Str. 15, 60438 Frankfurt, Germany. [3] Instituto de Medicina Molecular João Lobo Antunes, Faculdade de Medicina da Universidade de Lisboa, Av. Prof. Egas Moniz, 1649-028 Lisboa, Portugal. [4] Departamento de Ciências Biomédicas e Medicina, Universidade do Algarve, Campus Gambelas, 8005-139 Faro, Portugal. These authors contributed equally: Simon Braun, Mihaela Enculescu, Samarth T. Setty. Correspondence and requests for materials should be addressed to S.L. (email: s.legewie@imb-mainz.de) or to J.Kön. (email: j.koenig@imb-mainz.de) or to K.Z. (email: kathi.zarnack@bmls.de)

Alternative splicing constitutes a major step in eukaryotic gene expression. More than 90% of human genes undergo alternative splicing[1,2], which allows the production of distinct protein isoforms with different functionalities[3,4] and plays a critical role in development and tissue identity[5]. Strikingly, tumour suppressor genes and proto-oncogenes are particularly susceptible to splicing defects. Moreover, abnormally expressed splicing factors can have oncogenic properties[6], and changes in alternative splicing contribute to key processes in cancer initiation and progression[7–9]. A detailed characterisation of splicing mechanisms is therefore fundamental to our understanding of human biology and disease.

Splicing is an important step in the maturation of nascent transcripts that comprises excision of introns and joining of exons. During alternative splicing, certain exons can be either included or excluded, thus leading to different transcript isoforms. Splicing is catalysed by the spliceosome, a multi-subunit complex that recognises the 5′ and 3′ splice sites and flanking sequence elements in the pre-mRNA. The latter include the polypyrimidine tract (Py-tract) and the branch point upstream of each exon[10]. In addition to these core splice signals, multiple *cis*-regulatory elements reside in exons and flanking introns which can be primary RNA sequence elements as well as RNA secondary structures. The recognition of *cis*-regulatory elements by *trans*-acting RNA-binding proteins (RBPs) guides the spliceosome and ultimately determines the splicing decision at each alternative exon. Altogether, the information in the pre-mRNA sequence and how it is interpreted by RBPs is commonly referred to as the splicing code[11–13].

Despite many efforts to understand the molecular rules of splicing, our knowledge about *cis*-regulatory elements and *trans*-acting factors in most cases remains far from complete. Recent bioinformatic studies aimed to decipher the splicing code by predicting the impact of sequence variants on alternative splicing decisions[14,15]. Moreover, mutagenesis screens were employed to map sequence determinants of alternative splicing. However, these studies were limited to targeted mutagenesis of synthetic reporter constructs or short exonic regions[16–18].

Recepteur d'origine nantais (RON) is a receptor tyrosine kinase encoded by the proto-oncogene *MST1R* (also referred to as *RON*). Under normal conditions, the protein is cleaved to form a functional receptor. Skipping of *RON* alternative exon 11 results in the isoform RONΔ165, which remains as a single-chain protein. Spontaneous oligomerisation of RONΔ165 results in constitutive phosphorylation[19] that promotes epithelial-to-mesenchymal transition and contributes to tumour invasiveness[20–23]. Consistently, RONΔ165 is frequently upregulated in solid tumours, including ovarian, pancreatic, breast and colon cancers[21,24,25]. On the molecular level, previous studies identified a handful of mutations that influence *RON* exon 11 splicing[26,27]. Moreover, several RBPs were reported to regulate *RON* splicing[7,26,27]. For instance, heterogeneous nuclear ribonucleoprotein H (HNRNPH; collectively referring to HNRNPH1 and its close paralogue HNRNPH2 which are 96% identical at the amino acid level[28]) was found to repress *RON* exon 11 inclusion via binding within the alternative exon. While these studies suggested that *RON* splicing is heavily regulated, most *cis*-regulatory elements remain unknown.

Here, we establish a high-throughput mutagenesis approach to comprehensively characterise the regulatory landscape of *RON* exon 11 splicing. Starting from a library of almost 5800 randomly mutated minigenes, we employ a mathematical model of the splicing kinetics to detect more than 1000 point mutations that significantly affect *RON* alternative splicing. Importantly, the deduced single mutation effects correlate with the splicing levels in cancer patients bearing the same mutations. Moreover, we comprehensively characterise how HNRNPH acts as a key regulator of healthy and pathophysiological *RON* splicing by recognising multiple *cis*-regulatory elements in a cooperative fashion. Our mutagenesis screening approach promises insights into the splicing effects of mutations in humans and the mechanisms of alternative splicing regulation in general.

Results

Random mutagenesis introduces 18,000 mutations. To systematically study the *cis*-regulatory sequence elements that control *RON* alternative splicing, we designed an in vivo screening approach based on random mutagenesis of a splicing reporter minigene (Fig. 1a). The minigene harbours *RON* exon 11 together with the complete flanking introns and the constitutive exons 10 and 12 (Supplementary Fig. 1a). We confirmed that the minigene gives rise to the same transcript isoforms as the endogenous gene in human HEK293T cells (Supplementary Fig. 1b). Moreover, mutations in a known *cis*-regulatory element led to increased *RON* exon 11 skipping as reported previously[7] (Supplementary Fig. 1c). We next amplified the minigene with error-prone PCR to spread mutations randomly across all exons and introns. A 15-nt barcode sequence was introduced downstream of constitutive exon 12 via a randomised sequence in the reverse primer to uniquely identify each mutated minigene variant. Upon vector ligation and amplification, we pooled ~6000 clones into a minigene library (Supplementary Fig. 1d). As an internal reference, the library was supplemented with wild-type (wt) minigene variants that carry distinct barcode sequences but no mutations.

To map the introduced mutations, we sequenced the minigene library with 300-nt paired-end reads and five overlapping amplicons. The 15-nt barcode included in each read pair enabled us to assign and reconstruct the complete sequence of all minigene variants in the library (Supplementary Fig. 2a). Using a custom-tailored analysis pipeline (Supplementary Fig. 2b), we capture a total of 5791 unique minigene variants (see Methods), including 5200 with randomly introduced mutations as well as 591 with the wt sequence (Supplementary Data 1). Mutation calling identified 18,948 point mutations with an average frequency of 3.6 mutations per minigene variant. The mutations are randomly spread across the *RON* minigene, such that 97% of the positions are mutated at least ten times within the library (average 28 times per position; Supplementary Fig. 2c–e). We validated the accuracy of mutation calling with Sanger sequencing of 59 randomly selected minigene variants, confirming all 169 mutations without additional false positives.

Targeted RNA-seq quantifies alternative splicing outcome. To measure the splicing outcome, we transfected the library as a pool into human HEK293T cells where the minigenes are transcribed and spliced. We devised a targeted RNA-seq strategy based on 300-nt paired-end reads, which allows us to assemble the complete sequence of all splice products including the 15-nt barcode sequence that is present in all read pairs (Supplementary Fig. 2f, g). A total of 5598 (97%) minigene variants were captured in all three independent biological RNA-seq replicates (Supplementary Fig. 2h and Supplementary Data 1). From the RNA-seq data, we could reconstruct and quantify 163 distinct splice isoforms. The most abundant isoforms reflect the canonical splicing events, i.e., alternative exon (AE) inclusion and skipping, as well as partial and full intron retention (IR) (Fig. 1b, g and Supplementary Fig. 2g). In addition, we detected non-canonical splicing events at 82 and 71 cryptic 3′ and 5′ splice sites, respectively, which are collectively referred to as 'other' (Fig. 1c). For instance, mutations disrupting the 3′ splice site of the downstream constitutive exon 12 trigger activation of a cryptic AG (marked by one asterisk in

Fig. 1b, g). While the overall abundance of the cryptic isoforms in the RNA-seq libraries is low, they can dominate the splice products of individual minigene variants (Fig. 1b).

For the wt minigenes, i.e., in the absence of mutations, the frequency of the AE inclusion isoform (i.e., the ratio of AE inclusion over the sum of all measured isoforms) shows little variance, supporting the notion that confounding effects of the barcode sequences are negligible (Fig. 1d). In contrast, almost half of the mutated minigenes (2248, 45%) show more than 10% deviation in AE inclusion, suggesting that many introduced mutations strongly affect the splicing outcome (Fig. 1d). As expected, any mutation within the splice sites of *RON* exon 11 completely abolishes AE inclusion (Fig. 1d, f). We validated the accuracy of the RNA-seq quantification using individual RT-PCR measurements of the 59 Sanger-sequenced minigene variants (Fig. 1e and Supplementary Data 8). We conclude that the random mutagenesis approach enables precise high-throughput quantification of alternative splicing.

Linear regression modelling infers single mutation effects. Since each mutated minigene variant carries several mutations, the measured splicing changes are an overlay of multiple effects.

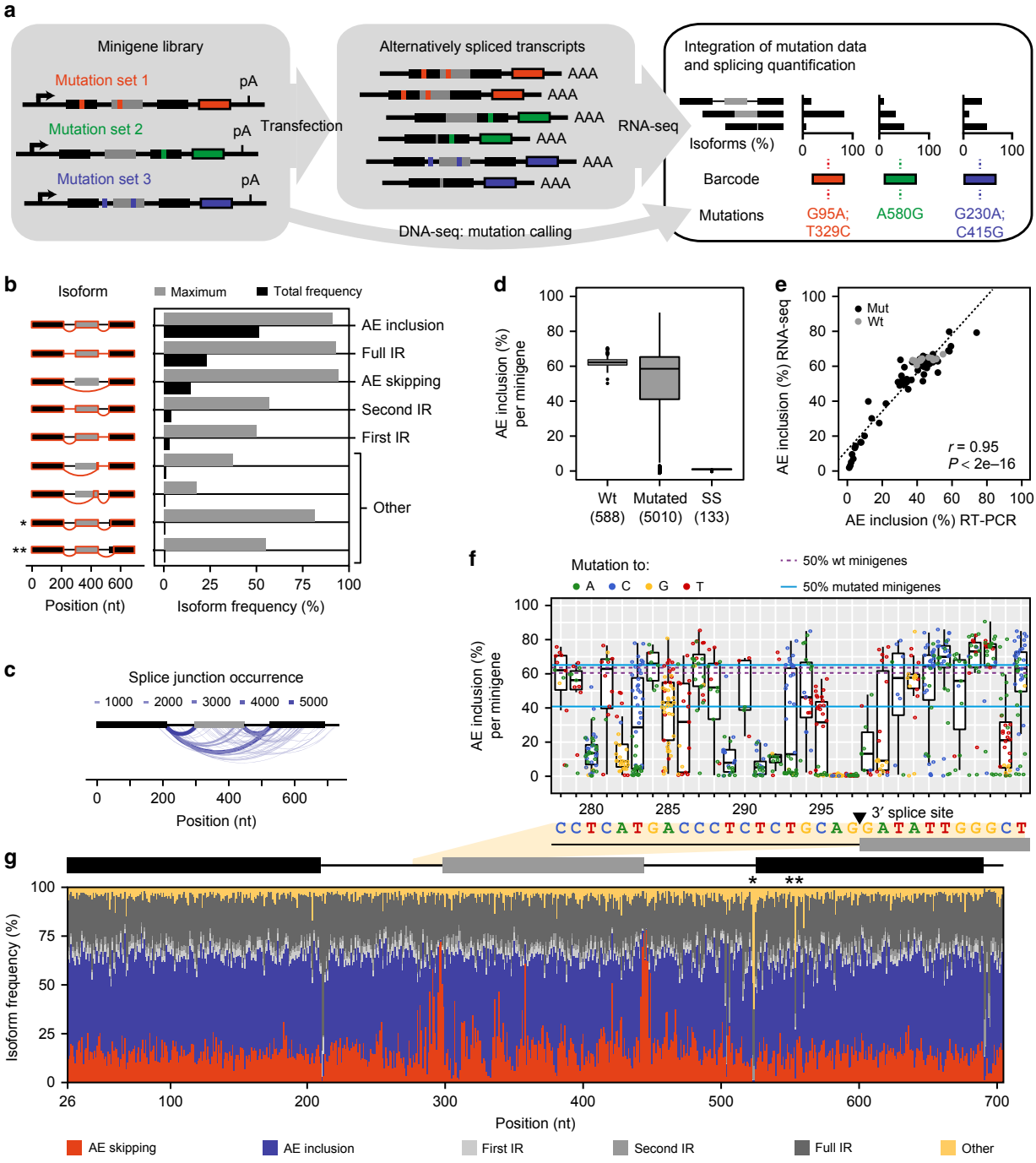

Consequently, a set of minigenes that share a given mutation displays a certain degree of variation in their splicing behaviour (Fig. 1f and Supplementary Data 2). To extract the impact of individual mutations, we made the simplifying assumption that mutations affect splicing independently and derived a linear regression-based mathematical modelling approach. In the linear regression model, the splicing change of each minigene relative to wt is described as the sum of single mutation effects (Fig. 2a). By fitting this model to the measured combined mutation effects, the underlying single mutation effects can be inferred.

To assess whether additivity of mutation effects can indeed be assumed, we analysed a reaction network representing splicing of the *RON* minigene using kinetic modelling (Supplementary Note 1 and Supplementary Fig. 3a). Model analysis shows that only when we consider splice isoform ratios (i.e., ratios of two measured isoform frequencies), mutation effects do not depend on the presence of other mutations in a minigene. Thus, for splice isoform ratios, mutation effects add up in log-space and a linear regression can be performed. In contrast, at the level of individual splice isoform frequencies (or related metrics such as percent spliced-in, PSI), mutation-induced fold changes depend on the mutational background and are thus not additive in log-space. We directly confirmed the additive behaviour of isoform ratios for mutations that are present as single mutation minigenes and simultaneously occur as combinations in double/triple mutation minigenes (Supplementary Fig. 4).

To integrate the full mutation information available in the data set, we formulated five separate regression models, each expressing the splicing outcome as a ratio of one splice isoform relative to the reference AE inclusion isoform. By simultaneously fitting the complete set of linear equations, each reflecting one minigene, to the experimental data, we were able to estimate 1800 single mutation effects. Based on the regression results, we could infer the frequency of five canonical splice isoforms for each of these single mutations, or combinations thereof (Supplementary Table 1 and Supplementary Data 3). The models fit the data with high accuracy, as judged by the excellent correlation between model fit and experimental data (Pearson correlation coefficient, $r = 0.99$, P value $< 2e{-}16$; Fig. 2b and Supplementary Fig. 5a, b). This supports our assumption that mutations affect splicing independently and can be described as a sum of single mutation effects (Supplementary Figs. 3b and 4a).

To test for ability of the model to infer novel combined mutations, we employed tenfold cross-validation, in which the model was fitted to 90% of the minigenes and used to predict the splicing outcome for the remaining 10%. The excellent cross-validation accuracy (Pearson correlation coefficients $r =$ 0.96–0.97, P value $< 2e{-}16$; Supplementary Fig. 6) outperformed alternative regression model variants that were fitted directly to the measured splice isoform frequencies (Supplementary Note 2 and Supplementary Fig. 7a, b). The inference power of the model for novel single mutation effects was assessed by separately leaving out one of >500 single-mutation minigene variants and fitting the model to the remaining data, or to subsets, in which further occurrences of the considered mutation were left out. This procedure revealed that the inference error for a single mutation effect decays with increasing occurrence of a mutation in our data set as $(E \sim 1/\sqrt{\text{occurrence}})$ (see Supplementary Note 2, Fig. 2c and Supplementary Fig. 5c). For mutations with occurrences >5 (i.e., present in more than five minigene variants), the estimated standard deviation of the inference error levels around 6%, suggesting that at sufficiently high occurrence the model inference accuracy is close to the experimental variation for wt minigene variants (3% standard deviation). We compared the cross-validation results to a simpler proxy in which single mutations effects are estimated from the median splice isoform frequencies over all minigenes containing a particular mutation. Even though the latter approach should average out the effect of accompanying mutations when enough minigenes are present, the regression model outperforms the median-based estimation across all occurrence levels (Fig. 2c and Supplementary Fig. 5c, d).

To independently validate the modelling results, we generated 26 minigene variants with individual mutations for which the model predictions substantially differed from the simpler median-based estimation of single mutations effects. Using RT-PCR to assess splicing outcomes, we find a strong correlation with the splice isoform frequencies inferred by the model (Fig. 2d, Supplementary Fig. 4b and Supplementary Data 8). The gain in accuracy by the model is particular apparent for mutations with a low frequency, i.e., appearing in only few minigenes. We conclude that the regression model offers a reliable method to quantify the impact of single mutations on *RON* alternative splicing.

Numerous positions contribute to *RON* alternative splicing. Using the model inference for HEK293T cells, we find a total of 778 mutations that significantly alter the frequency of at least one isoform (henceforth called splicing-effective mutations; >5% change in isoform frequency, 5% false discovery rate, FDR; Fig. 2e–g, Supplementary Fig. 8 and Supplementary Table 2). At the 5′ splice site of *RON* exon 11, we observe a good correlation between AE inclusion levels and in-silico-predicted splice-site

Fig. 1 High-throughput mutagenesis screen provides quantitative splicing information across the *RON* minigene. **a** High-throughput detection of splicing-effective mutations. Mutagenic PCR creates mutated minigene library (left) that gives rise to alternatively spliced transcripts (middle). Mutations and corresponding splicing products are characterised by DNA and RNA sequencing, respectively, and linked by unique 15-nt barcode sequence in each minigene (coloured boxes). Black and grey boxes depict constitutive and alternative exons, respectively. **b** Nine most frequent isoforms found in HEK293T cells. Bar diagram shows total frequency in RNA-seq library (black) and maximal frequency for any individual minigene variant (grey). Asterisks mark non-canonical isoforms from cryptic 3′ splice site usage upon mutations at positions marked in **g**. AE, alternative exon, IR, intron retention, other, non-canonical isoforms. **c** Occurrence of distinct splice junctions in HEK293T cells. Line thickness and colour represent number of minigene variants producing a given junction (only junctions accounting for ≥1% of all junctions for a given minigene). **d** Boxplot showing distribution of AE inclusion frequencies (as % of all isoforms) for all wild-type (wt) and mutated minigenes and a subset with mutations in splice sites (ss) of *RON* exon 11. Boxes represent quartiles, centre lines denote 50th percentile, and whiskers extend to most extreme values within 1.5× interquartile range (IQR). **e** Validation of AE inclusion frequencies for 59 randomly selected minigene variants. Scatterplot compares the RNA-seq quantification to semiquantitative RT-PCR for individual minigene variants in HEK293T cells. *r*, Pearson correlation coefficient and associated *P* value. **f** Mutational landscape around the 3′ splice site of *RON* exon 11. Boxplot of AE inclusion frequencies in HEK293T cells for all minigenes with mutation at indicated positions (*x*-axis). Box representation as in **d**. Colours illustrate inserted nucleobase (see legend). Blue and purple lines indicate IQR of AE inclusion frequencies for all mutated and wt minigenes, respectively. Sequence of wt *RON* minigene given below. **g** Isoform frequencies arising from mutations along *RON* minigene. Stacked bar chart shows median frequency of six isoform categories for all minigenes with mutation at a given position. Average of three biological replicates in HEK293T cells. Asterisks highlight positions where mutations lead to non-canonical isoforms depicted in **b**

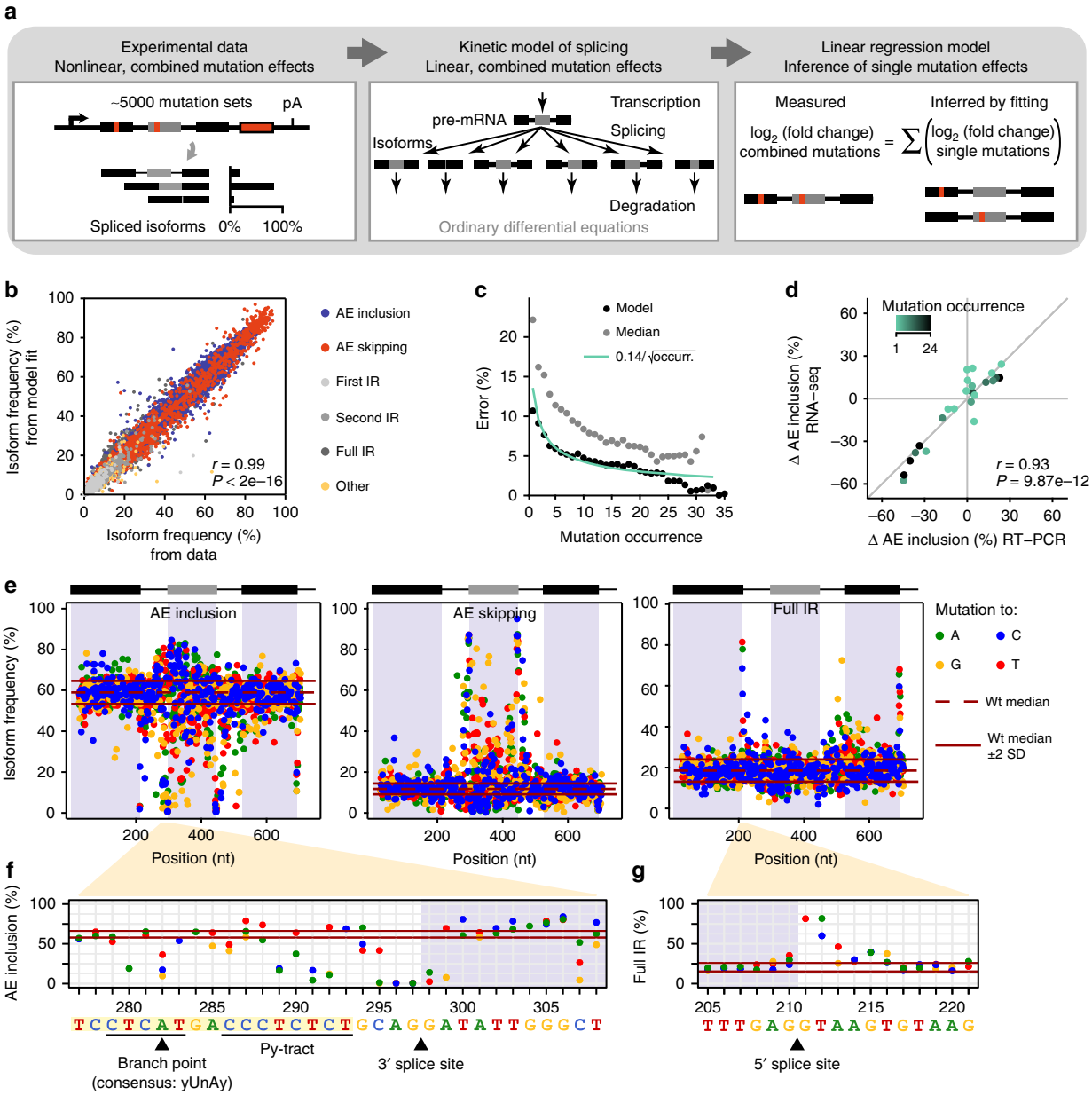

Fig. 2 A linear regression model determines more than 1900 single mutation effects. **a** Model-based inference of single mutation effects. Isoform quantifications from RNA-seq for 5598 unique minigene variants, each harbouring multiple mutations, are used as input. A kinetic model of splicing reactions reveals that splice isoform ratios show linear mutation effects, irrespective of other mutations. A linear regression model is used to infer single mutation effects in a system of 5010 linear equations, one per mutated minigene variant. **b** Regression model describes experimental measurements with high correlation (Pearson correlation coefficient $r = 0.99$, P value <2e−16). Scatterplot shows frequencies of distinct splice isoforms (see legend; separately shown in Supplementary Fig. 5a) for combined mutations calculated from fitted model against one biological replicate (see Supplementary Note 2). **c** The model more accurately infers frequently occurring single mutation effects. Cross-validation by separately excluding single-mutation minigenes (and permutations of other minigenes containing this mutation). Inference is expressed as standard deviation of inference error in AE inclusion (y-axis) and analysed for different permutations containing mutation at different frequencies (x-axis). Inference power of model (black dots) matches theoretical expectation (green line) and outperforms median-based estimation (grey dots; see Supplementary Note 2). **d** Experimental validation of model-inferred single mutation effects. Semiquantitative RT-PCR measurements of AE inclusion (other isoforms in Supplementary Fig. 4b) for targeted single-mutation minigenes that were not used for model fitting. Discrepancies between model and data appear if mutation infrequently occurs in the library (colour-coded). r, Pearson correlation coefficient and associated P value. **e** Model-inferred landscapes of 1747 single mutation effects on AE inclusion, AE skipping and full IR in HEK293T cells. Each mutation effect is indicated as a coloured dot (inserted nucleobase, see legend). Red lines indicate median (dashed) ± 2 standard deviations (SD; solid) for wt minigenes. **f**, **g** Zoom-in landscapes of single mutation effects on AE inclusion around 3′ splice site of *RON* exon 11 (**f**) and on full IR around 5′ splice site of constitutive exon 10 (**g**). Black lines and arrowheads mark splicing signals, including branch point, polypyrimidine tract (Py-tract) and splice sites. Visualisation as in **e**

strength upon mutation[29] (Spearman correlation coefficient $r = 0.89$, P value = 2.36e−08; Supplementary Fig. 9a). In contrast, predictions for 3′ splice site strength capture the effects of Py-tract composition, but fail to detect branch point mutations and other sequence contributions (Spearman correlation coefficient $r = 0.62$, P value = 4.02e−07; Supplementary Fig. 9b). As expected, transitions between pyrimidines within the Py-tract upstream of *RON* exon 11 act neutrally, whereas transversions into purines reduce inclusion, illustrating that the screen allows to discriminate base-specific effects (Fig. 2f). Consistent with the exon definition model of splicing, we find that disrupting the 5′ splice site of constitutive exon 12 (not spliced in the minigene context) also changes AE inclusion (Fig. 2e, Supplementary Table 2 and Supplementary Data 4), underlining that flanking constitutive exons can distally influence alternative splicing[11,30].

Notably, 91% of all positions within *RON* exon 11 (134/147 nt) harbour at least one splicing-effective mutation, revealing that the alternative exon is densely packed with *cis*-regulatory elements (Fig. 2e and Supplementary Fig. 8). Moreover, neighbouring positions or even different base substitutions in the same positions often affect different isoforms or change splicing in opposite directions (e.g., regions 404–429 nt or 565–567 nt, respectively, in Supplementary Data 4). The resulting patterns likely resemble footprints of the RNA sequence specificity of the interacting RBPs (see below) or RNA secondary structures. In addition to disrupting existing *cis*-regulatory elements, some mutations may also generate new elements, which further increases the complexity of the observed regulatory landscape.

The widespread occurrence of splicing-regulatory effects in *RON* exon 11 highlights that the majority of exonic positions mediate splicing regulation and thus harbour a second layer of information beyond their protein-coding function. As previously described[16], splicing-regulatory effects occur with similar frequency and effect sizes for synonymous and non-synonymous mutations (Supplementary Fig. 9e, f). Moreover, we detect substantial effects in the flanking introns and constitutive exons (50–82% splicing-effective positions per region; Supplementary Table 2). Albeit less frequent, the splicing-effective mutations within introns show comparable effect sizes to those in the alternative exon (Supplementary Fig. 9d). Globally, mutations in and around the alternative exon primarily affect the AE inclusion and skipping isoforms, whereas mutations in the downstream constitutive exon strike a balance between AE inclusion and full intron retention (Supplementary Fig. 8).

In line with a pathological relevance, we find that splicing-effective positions within introns are more conserved than non-effective positions, evidencing an evolutionary selection pressure towards maintaining the splicing-effective positions[31] (Supplementary Fig. 9c). In contrast, within exons both splicing-effective and non-effective positions show high conservation but no difference, likely reflecting constraints on amino acid composition that may overrule conservation of splicing signals. A total of 135 (25%) of splicing-effective mutations within the three exons are synonymous with respect to the encoded RON protein and would hence not be interpreted as potentially deleterious variants when considering protein sequence only. Importantly, our results clearly indicate that albeit preserving the protein sequence, such synonymous mutations may contribute to disease by changing alternative splicing patterns[32,33].

Splicing-effective positions are mutated in human cancers. Since altered *RON* splicing is involved in cancer progression[21,25], we repeated the splicing measurements in the human breast cancer cell line MCF7. Compared to HEK293T cells, the wt minigene shows lower AE inclusion in MCF7 cells, supporting a shift towards the pathophysiological state (Supplementary Fig. 1b). Nevertheless, the measured mutation effects are highly consistent between both cell lines, underlining the robustness of our screening approach (Pearson correlation coefficient $r = 0.96$, P value = 2.2e−16; Fig. 3a).

In order to address the physiological relevance of the mutations, we compared our data to the Catalogue of Somatic Mutations in Cancer (COSMIC). Out of 33 COSMIC entries within the region of the *RON* minigene, 20 coincide with splicing-effective mutations and seven of these are synonymous with respect to the encoded RON protein (Fig. 3b). It is thus conceivable that their splicing-regulatory function rather than their protein-coding role is involved in cancer progression. Prompted by this observation, we analysed patient data from The Cancer Genome Atlas (TCGA) (https://cancergenome.nih.gov/) to investigate *RON* splicing in human cancers. We identified 153 patients, from 19 different cohorts (representing different cancer types), that carry mutations in the *RON* minigene region specifically in their tumour samples, but not in their matched normal samples (Supplementary Data 5). We next quantified the difference in *RON* exon 11 splicing (in PSI), per cohort, between tumour samples of mutation-bearing and non-bearing patients. Strikingly, we observe a good correlation between *RON* splicing changes in mutated TCGA tumour samples and the single mutation effects determined by our approach (Pearson correlation coefficient $r = 0.62$, P value = 4.8e−05; Fig. 3c). Strongest *RON* exon 11 skipping associates with a splice site mutation (G297A; identified in a patient with thyroid carcinoma, THCA). Of note, the second largest effect is found for mutation G370T (head–neck squamous cell carcinoma, HNSC), which introduces a missense mutation at the level of the encoded protein (Fig. 3d, see Discussion). The correlation between our screen and the TCGA data is reduced if these two strongest sites are removed from the analysis (Pearson correlation coefficient $r = 0.27$, P value = 0.12; Fig. 3c), most likely because the remaining effects are weaker and compromised by experimental variation. In conclusion, our high-throughput screen recapitulates strong in vivo splicing changes in human cancer patients.

***cis*-Regulatory elements in *RON* are targeted by multiple RBPs.** In MCF7 cells, a total of 1022 mutations across the minigene affect *RON* alternative splicing, pointing towards the presence of multiple *cis*-regulatory elements (Supplementary Data 6). We used the ATtRACT database[34] to identify putative RBP binding sites, thereby predicting RBPs that recognise these *cis*-regulatory elements. In order to focus on sites that are actively involved in splicing regulation, we retained only RBP motifs if at least 60% of the positions therein showed a mutation effect on at least one splice isoform (referred to as splice-regulatory binding sites, SRBS). The analysis recovers two previously reported *cis*-regulatory elements in the alternative and the downstream constitutive exon that are targeted by HNRNPH[26] and SRSF1[21], respectively. In total, we identify 76 potential RBP regulators (Fig. 3e and Supplementary Fig. 10), suggesting that *RON* splicing is extensively controlled by multiple RBPs. To prioritise among them, we overlaid our data with a large-scale knockdown (KD) screen which tested the KD effect of 31 RBPs from our list on *RON* exon 11 splicing in HeLa cells[35]. Notably, 17 of these RBPs showed a substantial impact on *RON* splicing, with HNRNPH and SRSF2 being the strongest repressor and activator, respectively (Fig. 3e).

In a complementary approach, we investigated the expression of 190 RBPs which were identified as putative regulators of *RON* splicing by our ATtRACT analyses and/or by the published RBP KD screen[35] using matched RNA-seq data sets for 4514 TCGA

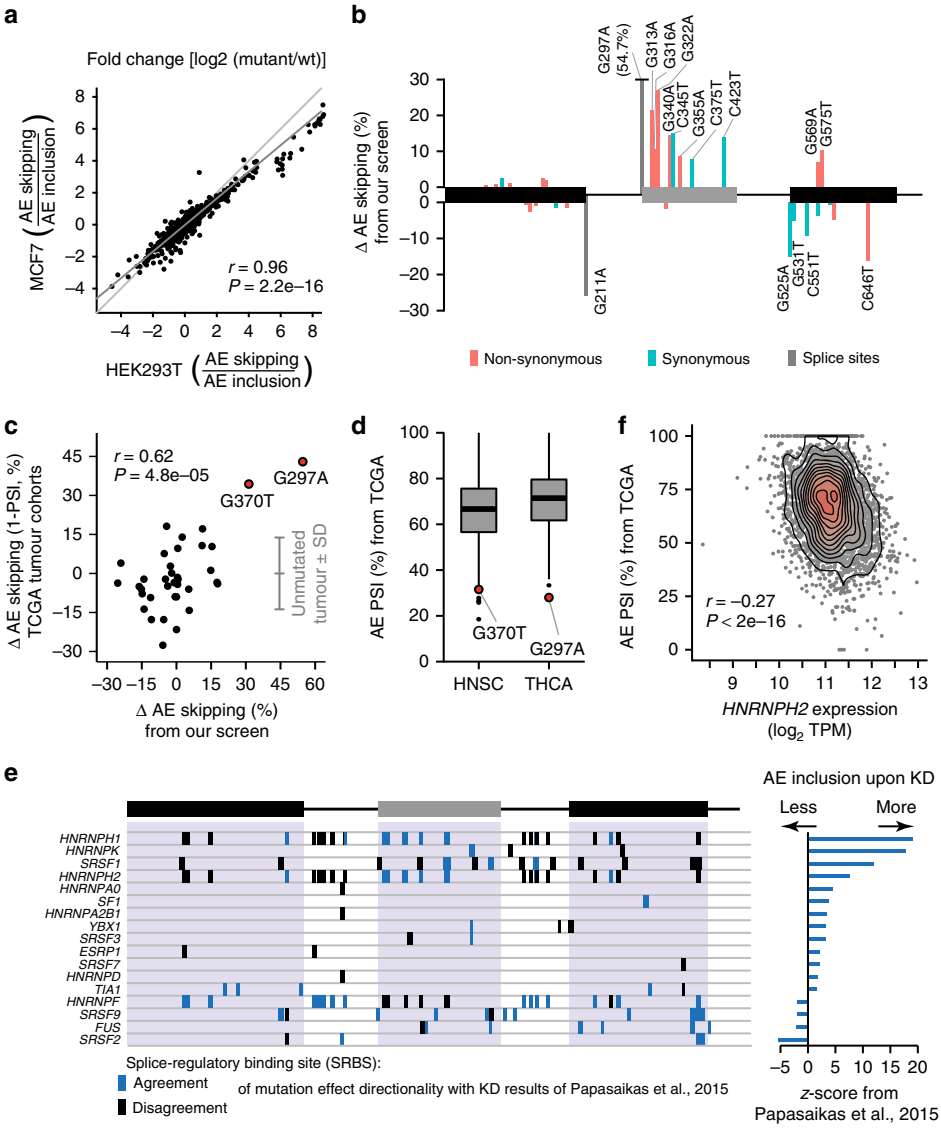

Fig. 3 Mutation effects are recapitulated in human cancer patients and point to regulatory RNA-binding proteins. **a** Model-inferred single mutation effects are consistent between HEK293T and MCF7 cells. Scatterplot compares changes in splice isoform ratios for mutations along *RON* minigene. Light and dark grey lines correspond to diagonal and linear regression, respectively. *r*, Pearson correlation coefficient and associated *P* value. **b** Somatic mutations in cancer can cause significant splicing effects. Bar diagram displays changes in AE inclusion for 33 mutations from COSMIC database. Mutations with significant effect on AE skipping are labelled ($n = 16$). Orange, blue and grey indicate non-synonymous, synonymous and splice site mutations, respectively. Mutation G297A extends beyond visualised range. **c** Mutation effects from our screen recapitulate altered splicing in cancer patients. Scatterplot compares *RON* AE skipping between mutated and non-mutated TCGA tumour samples (percent spliced-in, PSI) from 117 cancer patients (with 36 different mutations in 14 cohorts) to mutation-induced change in AE skipping in MCF7 cells. Grey lines indicate mean and standard deviation of unmutated tumour samples. *r*, Pearson correlation coefficient and associated *P* value. $r = 0.27$, *P* value = 0.12 without two mutations with strongest impact (G370T and G297A). **d** Tumour samples from mutation-bearing patients show strong *RON* exon 11 skipping. Boxplot summarises *RON* exon 11 inclusion (PSI) in head–neck squamous cell carcinoma (HNSC) and thyroid carcinoma (THCA) cohort. Box represents quartiles, centre line denotes 50th percentile and whiskers extend to most extreme data points within 1.5× interquartile range. Tumour samples with mutations G370T and G297A are labelled. **e** In silico predictions for RNA-binding proteins (RBPs) identify splice-regulatory binding sites (SRBS; predicted binding sites that show substantial mutation effects, see Methods). Boxes indicate SRBS for 17 putative RBP regulators that overlap with published data on *RON* exon 11 splicing upon RBP KD[35]. Colour code indicates whether majority of mutation effects within SRBS agree with direction of published RBP KD effect (*z*-scores; right panel). **f** *HNRNPH2* shows strongest correlation of expression levels with *RON* exon 11 splicing across 27 tumour cohorts. Density scatterplot shows *HNRNPH2* expression (in transcripts per million, TPM) and *RON* exon 11 PSI across all TCGA tumour samples. *r*, Spearman correlation coefficient and associated *P* value

cancer patient samples from 27 different cancer types. We detect 140 RBPs whose transcript levels significantly correlated with *RON* exon 11 inclusion (FDR for Spearman correlation <5%; Supplementary Fig. 11a–c and Supplementary Data 7). Compared to all annotated RBPs or all protein-coding genes, the 190 pre-selected RBPs significantly enriched among the most highly correlated (gene set enrichment analysis, *P* value = 0.04 or 0.003, respectively).

Strikingly, the strongest association in the TCGA data set is observed for *HNRNPH2*, whose expression shows a significant negative correlation with *RON* exon 11 inclusion (Spearman

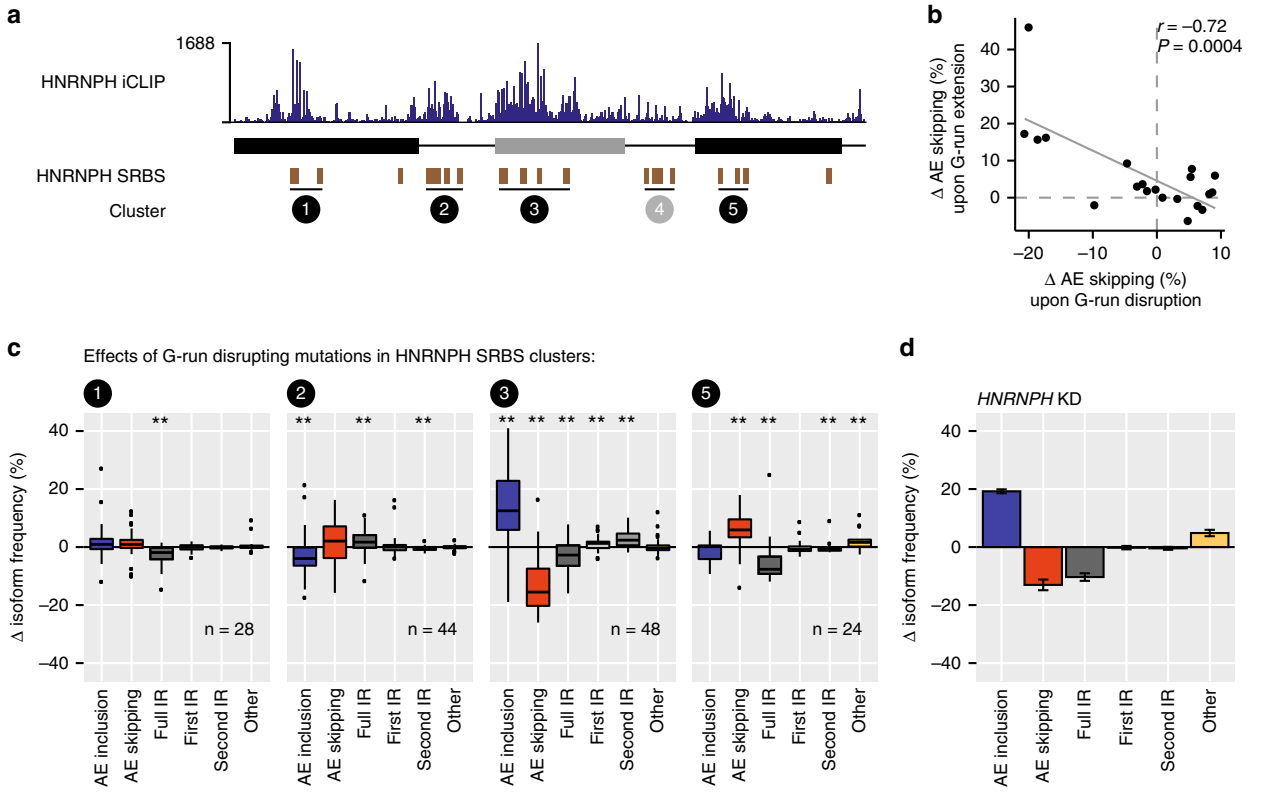

Fig. 4 HNRNPH controls *RON* exon 11 splicing via multiple intronic and exonic binding sites. **a** HNRNPH iCLIP validates HNRNPH binding to predicted splice-regulatory binding sites (SRBS). Bar diagram shows the number of HNRNPH crosslink events from HEK293T cells on each position along the wt *RON* minigene. HNRNPH SRBS (brown boxes) were assigned to five SRBS clusters (circled numbers). iCLIP data show HNRNPH binding to four out of the five SRBS clusters. **b** Extending or disrupting G-runs results in opposite splicing effects. Scatterplot shows inverse correlation of median changes in AE inclusion (average of three biological replicates) of all mutations per SRBS that extend or disrupt the G-run (see Methods) with linear regression line. *r*, Spearman correlation coefficient and associated *P* value. **c** Exonic and intronic HNRNPH binding exerts distinct effects on *RON* exon 11 splicing. Boxplots summarise the change in frequencies of each isoform in MCF7 cells (mean, $n = 3$) for all G-run-disrupting mutations within HNRNPH SRBS of different clusters (circled numbers). Box represents quartiles, centre line denotes 50th percentile and whiskers extend to most extreme data points within 1.5× interquartile range. Number of considered mutations for each cluster given below. *P value < 0.05, **P value < 0.01, one-sample Wilcoxon test against population mean of zero. **d** Bar diagram shows the changes in isoform frequency of wt *RON* minigenes upon *HNRNPH* KD in MCF7 cells. Error bars indicate standard error of the mean from three biological replicates

correlation coefficient $r = -0.27$, P value < 2e−16; Fig. 3f). This behaviour is consistent with the previously described function of HNRNPH as a repressor of *RON* exon 11 inclusion[26]. Differentiating into the 27 TCGA cohorts, we observe a significant correlation in 11 individual cancer types (FDR for Spearman correlation < 5%; Supplementary Table 3), all negative, suggesting that HNRNPH2-mediated repression of *RON* exon 11 commonly occurs in human cancers. Notably, we find a similar association in RNA-seq data of 24 healthy human tissues from the Genotype-Tissue Expression (GTEx) Project[36] (Spearman correlation coefficient $r = -0.12$, P value = 5.7e−11; Supplementary Fig. 11d). Comparing GTEx and TCGA samples, we observe consistently lower *RON* exon 11 inclusion levels in the tumour samples (mean PSI 76% vs. 67%, P value < 2.2e−16, Mann–Whitney–Wilcoxon test), supporting an increased expression of the constitutively active RONΔ165. Accordingly, *HNRNPH2* expression is increased in cancer (mean transcripts per million [TPM] 57.88 vs. 46.29, P value < 2.2e−16; Mann–Whitney–Wilcoxon test). Together, these observations suggest that HNRNPH is a major determinant of *RON* alternative splicing in healthy human tissues and cancer.

HNRNPH binding can both activate and repress *RON* splicing. Within the *RON* minigene, we predict 22 SRBS for HNRNPH (Fig. 4a), all of which harbour the G-rich sequences (G-runs) recognised by HNRNPH[37]. The HNRNPH SRBS occur across all transcript regions and arrange into five clusters, each containing at least three SRBS (clusters 1–5, Fig. 4a). Individual-nucleotide resolution UV crosslinking and immunoprecipitation (iCLIP; Supplementary Fig. 12a) in HEK293T cells confirms that endogenous HNRNPH significantly binds at the predicted HNRNPH SRBS clusters (Fig. 4a and Supplementary Fig. 12b), with the exception of cluster 4. The strongest iCLIP signal locates in the alternative exon (Supplementary Fig. 12b).

Consistent with HNRNPH's sequence preference towards G-runs, mutations within the binding sites show opposing impact when either disrupting or generating G-runs in the RNA sequence (Fig. 4b). The direction and the most susceptible isoform depend on the position of the HNRNPH SRBS. Most prominently, mutations within SRBS cluster 3 in the alternative exon promote inclusion (Fig. 4c). A similar splicing pattern is observed for the wt *RON* minigene upon *HNRNPH* KD (Fig. 4d),

indicating that cluster 3 plays an important role in HNRNPH-mediated repression of *RON* exon 11. Mutations in the intronic clusters 2 reduce AE inclusion, whereas mutating cluster 5 in the downstream constitutive exon 12 leads to decreased intron retention, accompanied by increased AE skipping. These observations cumulate into a complex regulatory scenario, in which HNRNPH acts via multiple binding sites that have activating or repressing effects on *RON* splicing.

Synergy analysis identifies predominant HNRNPH sites. In order to identify which sites are most relevant for HNRNPH-dependent regulation, we tested the splicing response of the minigene library upon *HNRNPH* KD. We hypothesised that mutations that either weaken or reinforce an HNRNPH binding site would display positive or negative synergy with the *HNRNPH* KD. For instance, a reduced KD response compared to the wt minigene would be expected if an important HNRNPH binding site is compromised by a mutation (negative synergy).

In order to test this idea, we performed siRNA-mediated *HNRNPH* KD in MCF7 cells expressing the minigene library and used targeted RNA-seq to measure the splicing outcome. As previously reported[26,35], *HNRNPH* KD results in a strong increase in *RON* exon 11 inclusion for both wt and mutated minigene variants in the library. In line with synergy, a subset of minigene variants reproducibly show a weaker or stronger KD response compared to the remainder of the library. For instance, minigenes harbouring mutations G305A or G310A within cluster 3 consistently show elevated control AE inclusion levels, but a reduced KD response, suggesting that HNRNPH regulation is partially abolished due to these mutations (Fig. 5a).

To comprehensively identify synergistic interactions, we again turned to linear regression modelling and inferred the single mutation effects in control and KD conditions (Fig. 5b). We then calculated a *z*-score, in which the difference in the KD effect between wt and mutant is normalised by the experimental variation of the wt minigenes. Using our model based on isoform ratios (Supplementary Note 3 and Supplementary Fig. 13), we estimate that the *HNRNPH* KD on average has a 2.4-fold effect on the AE skipping-to-inclusion isoform ratio. Importantly, this effect is largely independent of the mutational background and hence the AE inclusion frequency which a minigene exhibits under control conditions (Fig. 5b, right). The exception are very strong mutations that on their own completely abolish splicing, i.e., prevent the KD from having additional measurable effects (Supplementary Fig. 7f, g). In contrast, at the level of individual splice isoform frequencies, the KD effect of all mutations strongly depends on the starting isoform level and thereby introduces systematic biases (Fig. 5b, left, and Supplementary Fig. 7e). Since such biases can be minimised by modelling splice isoform ratios, our approach allows to reliably estimate synergy.

By modelling the splice isoform ratios, we derive landscapes of synergistic interactions between *HNRNPH* KD and distinct mutations in the *RON* minigene sequence (Fig. 5c, Supplementary Fig. 12c and Supplementary Data 6). For the vast majority of point mutations, no significant synergistic interaction is observed (1428 out of 1786, 80%; Supplementary Table 2). Importantly, 354 mutations (20%) in 278 positions show significant synergy for at least one splice isoform ($|z\text{-score}| > 2$, adjusted P value < 0.001, Stouffer's test). These are significantly enriched in the SRBS in cluster 3 in the alternative exon, in which 64% of mutations (93% of positions) display synergy with *HNRNPH* KD (Fig. 5d and Supplementary Fig. 12c, d). This observation suggests that the SRBS in the alternative exon are most relevant for HNRNPH-dependent regulation. This is further supported by the fact that 42% of the strongest synergistic interactions that affect AE skipping ($|z\text{-score}| > 5$) fall into SRBS cluster 3 (Fig. 5c). Consistent with the known sequence preference of HNRNPH, we observe that the disruption of G-runs in cluster 3 leads to a weaker KD response (negative synergy; Fig. 5d and Supplementary Fig. 14). Instead, synergistic interactions at clusters 1 and 5 in the constitutive exons frequently reinforce HNRNPH-dependent regulation by creating new or extending existing G-runs, leading to a stronger-than-average KD response (positive synergy; Supplementary Fig. 14). Hence, while the HNRNPH SRBS clusters outside *RON* exon 11 do not prevail under the tested conditions, they can become more important when HNRNPH binding for these sites is increased.

In order to validate the functional relevance of SRBS cluster 3, we generated ten minigene variants with individual point mutations disrupting G-runs within HNRNPH SRBS from the five clusters (Supplementary Data 8), and tested their splicing under *HNRNPH* KD conditions using semiquantitative RT-PCR. Indeed, single mutations in cluster 3, for which the model had inferred the strongest synergistic interactions, almost completely cancel out the KD response (Fig. 5e). In contrast, minigenes with mutations in other clusters still respond to the *HNRNPH* KD, in agreement with their less pronounced synergistic interaction with HNRNPH. In summary, the synergy analysis allows to link an RBP to its functionally most relevant *cis*-regulatory elements.

Cooperative HNRNPH binding establishes a splicing switch. We find that individual G-run-disrupting point mutations within the alternative exon (e.g., G305A, G331C and G348C) are sufficient to almost completely abolish the response to *HNRNPH* KD (Fig. 5e). This suggests that the corresponding SRBS cooperatively recruit HNRNPH. In line with this notion, our linear regression model which does not consider cooperativity, on average provides a worse fit to minigenes containing simultaneous mutations in two HNRNPH SRBS in the alternative exon (Supplementary Fig. 15e). In order to test for interdependent HNRNPH binding, we repeated the HNRNPH iCLIP experiments in the context of mutated *RON* minigenes harbouring point mutations within three different SRBS of cluster 3. In line with cooperative binding, the resulting drop in HNRNPH crosslinking is not limited to the site of the point mutation, but spreads to several further SRBS in *RON* exon 11 (Fig. 6a).

Cooperative HNRNPH binding to multiple SRBS would imply that HNRNPH regulates splicing with a steep, sigmoidal dose–response curve. To test this, we performed gradual *HNRNPH* KD and *HNRNPH1* overexpression experiments, in which we transfected MCF7 cells with increasing amounts of HNRNPH-specific siRNA and *HNRNPH1* overexpression construct, respectively. Notably, we observe a switch-like splicing response of *RON* exon 11 from the minigene as well as the endogenous *RON* gene. Indicative of strong cooperativity, we find that the dose–response curves can be described by high Hill coefficients for the endogenous *RON* gene (nH = 17.4, confidence interval (CI) [10.8,35.2]) as well as the transfected wt *RON* minigene (nH = 13.8, CI [10.4,17.7]; Fig. 6b and Supplementary Figs. 15a–d, 16). Consistently, we observe that *HNRNPH2* shows the steepest regression slope among the 190 RBPs tested for expression correlation in the TCGA data (Figs. 3f and 6c). Even though *HNRNPH2* expression in the TCGA data is not variable enough to reach plateaus in splicing, the steep slope further supports a switch-like behaviour of *RON* exon 11 inclusion.

Based on these observations, we conclude that *RON* exon 11 splicing is extensively regulated via multiple interdependent HNRNPH binding sites that exert strong cooperativity. This enables switch-like splicing with small changes in HNRNPH concentration causing large changes in splicing (Fig. 6d), potentially explaining why *HNRNPH* expression is a strong predictor of *RON* exon 11 splicing in cancer cells.

Discussion

Systems approaches combined with mathematical modelling are required to fully comprehend the complex regulation of alternative splicing. Our work builds on previous approaches to measure the effect of mutations in defined regions of splicing-reporter minigenes[16–18,38]. Central to our analytical framework is the mathematical splicing model which allows us to predict the

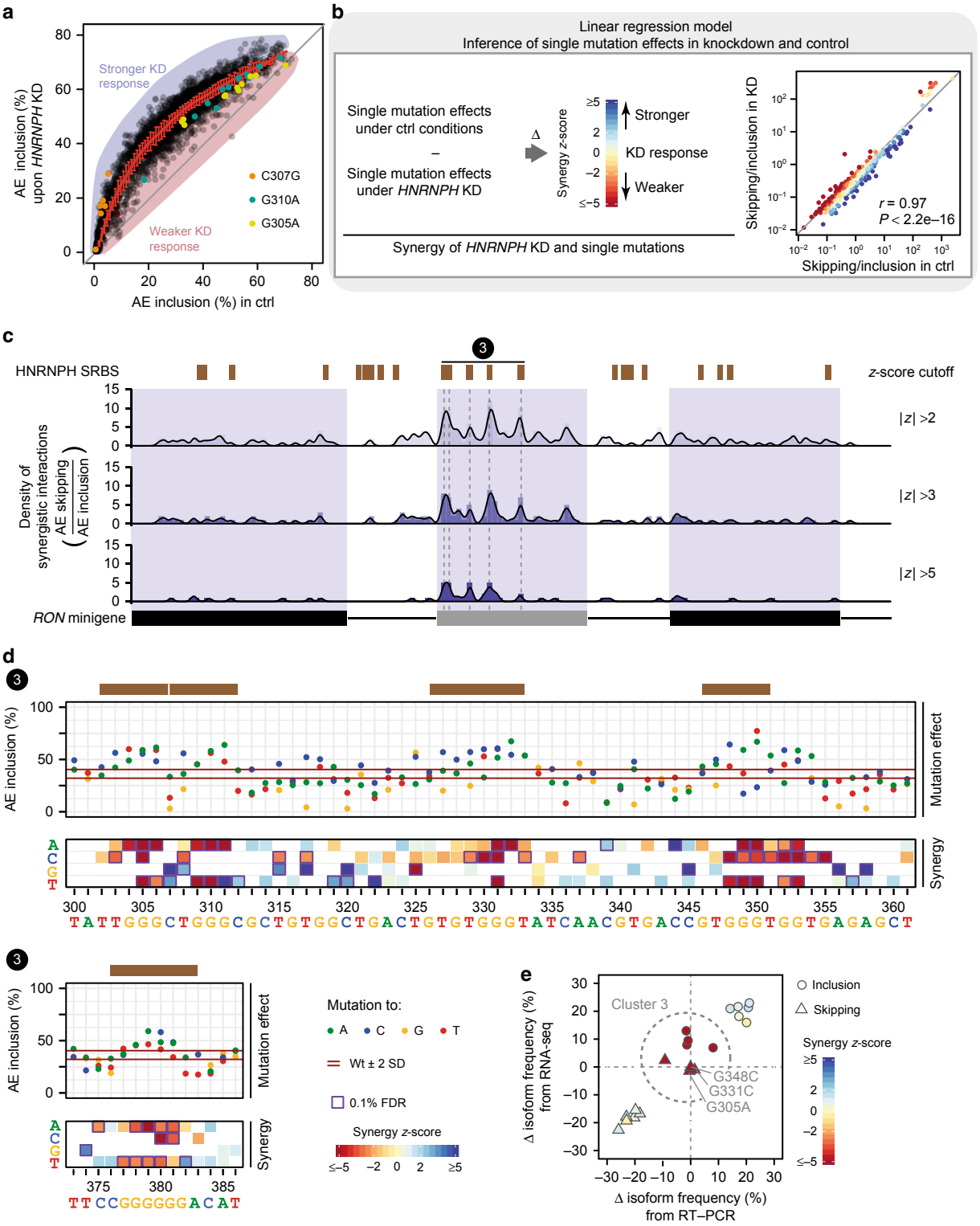

effects of individual mutations based on measurements of combined mutation effects. We employ linear regression modelling to disentangle these effects, and validate the predictive power of this approach using cross-validation, targeted single mutations and by relating *RON* mutations to splicing outcomes in cancer patients.

To formulate the linear regression model, we investigated how mutation effects cumulate in minigenes exhibiting several mutations. We termed a mutation effect linear if a mutation induces the same fold change in splicing irrespective of the mutational background (i.e., other mutations being present). If linearity holds true, the mutation effects add up in log-space and a linear regression can be performed to infer single mutation effects from the measured combined mutations. Using a kinetic model reflecting *RON* alternative splicing, we found that splice isoform ratios show the desired linear behaviour (Supplementary Note 1 and Supplementary Fig. 7e). Accordingly, the isoform ratio-based regression model fitted the complete minigene library with high accuracy. In line with our approach, Rosenberg et al. quantitatively modelled the contribution of randomised *k*-mer sequences in 25-nt regions of a synthetic minigene using an additive model that was based on the AE inclusion-to-skipping ratio[18]. In contrast, direct linear regression using the splice isoform frequencies decreases the accuracy and inference power of the model (Supplementary Note 2 and Supplementary Fig. 7b), possibly indicating nonlinear interactions between mutations at this level. Therefore, care needs to be taken when interpreting the interplay of mutations and/or other perturbations directly based on the abundance of certain splice isoforms (e.g., percent spliced-in/PSI, or equivalent metrics), as each perturbation shifts the operating point of the system. As a global trend, we observe that minigenes showing inclusion frequencies around 50% are most sensitive to perturbations such as *HNRNPH* knockdown (Fig. 5a). However, after transformation to isoform ratios, *HNRNPH* knockdown elicits linear, context-independent changes (Fig. 5b). Thus, isoform ratios are superior when analysing the interplay of multiple treatments or mutations, while isoform frequencies are essential for judging the physiological impact of splicing changes.

Our conclusion that combined mutations can be accurately described as a linear combination of single point mutations implies that synergistic interactions between mutations have only a minor impact on *RON* splicing outcomes. Intriguingly, our data suggest that even simultaneous mutations in two *cis*-regulatory elements mostly elicit linear, independent effects: across more than 100 minigenes containing two or more simultaneous mutations in any HNRNPH SRBS, 93% of the splice isoform frequencies can be explained within 5% deviation from the measured value using the linear regression approach (Supplementary Fig. 15e). Thus, the goodness of fit of this subset is comparable to the complete minigene population, suggesting that *cis*-regulatory elements in many cases act independently on *RON* alternative splicing.

Despite most mutations acting independently, we observe cooperative effects for adjacent HNRNPH binding sites in the alternative exon (see below). Such nonlinear effects are not captured by our model, but are in line with previous work showing that splicing-relevant mutations can amplify each other in combination, thereby showing cooperative interactions[11,16]. That such nonlinear effects are more prevalent in a previous screen by Julien et al.[16] may result from the fact that their study systematically screened double mutations in close vicinity. However, when relating the goodness of fit of our linear regression model to the nearest distance between two splicing-effective mutations, we found no clear effect of the mutation proximity on the fitting error (Supplementary Fig. 7c, d). This suggests that also nearby mutations typically act independently of each other and agrees well with results from a recent saturation mutagenesis study of a 51-nt region in the alternatively spliced exon of the *WT1* gene[17]. Since our data set does not exhibit enough coverage to comprehensively detect cooperative interactions of nearby mutations, it remains possible that adjacent sites mutually influence each other, whereas distal *cis*-regulatory elements act independently. Such a scenario would be consistent with a local assembly of ribonucleoprotein complexes that act as independent regulatory units.

Our high-throughput mutagenesis screen uncovers a highly complex *cis*-regulatory landscape, with >80% of all positions affecting *RON* alternative splicing. Within this set, we recover mutations in all previously identified *cis*-regulatory elements[7,21,26,27,39]. Within the alternative *RON* exon 11, we find that 91% of all positions show a significant impact on *RON* splicing. Conceptually, these splicing-effective mutations either disrupt existing *cis*-regulatory elements at the RNA sequence or structure level or generate novel elements, thereby further increasing the complexity of *RON* splicing regulation. Even though the newly generated *cis*-regulatory elements do not occur under normal conditions, they may be relevant in cancer when mutations accumulate. A similar density of effective mutations was also reported for *FAS* exon 6[16]. Our study demonstrates that other than previously suggested, such a densely packed

Fig. 5 Synergistic interactions highlight the functionally most relevant HNRNPH binding sites. **a** Minigene variants are differentially spliced upon *HNRNPH* knockdown (KD). Scatterplot compares AE inclusion under control (ctrl) and *HNRNPH* KD conditions for all minigene variants. Average behaviour illustrated by running mean and standard deviation (red). Shadings schematically highlight stronger/weaker-than-average KD response. Minigenes with mutations C307G, G310A and G305A in HNRNPH splice-regulatory binding sites (SRBS) cluster 3 are highlighted. **b** Quantification of synergistic interactions by linear regression modelling. Single mutation effects are determined separately for ctrl and *HNRNPH* KD using linear regression and subtracted to estimate KD responses compared to wt (*z*-score based on standard deviation of wt minigenes, colour-coded; see Supplementary Note 3). Right graph shows model-inferred AE skipping-to-inclusion isoform ratios of single mutations in ctrl vs. KD. Regression line indicates average KD effect. Consideration of isoform ratios, as compared to isoform frequencies (**a**), leads to linearisation of KD response in line with predictions of kinetic splicing model (Supplementary Fig. 3a). **c** Model-inferred synergistic interactions accumulate in *RON* exon 11. Bar diagrams quantify significant synergistic interactions affecting AE skipping-to-inclusion isoform ratio using different *z*-score cutoffs in adjacent 5-nt windows. Line indicates density in 5-nt sliding window. Splice sites ± 2 nt were excluded. Predicted HNRNPH SRBS (brown) are given above. **d** Mutations in HNRNPH SRBS cluster 3 lead to increased AE inclusion and reduced *HNRNPH* KD response. Dot plots (top) display single mutation effects (inserted nucleobase, see legend) on AE inclusion (mean, $n = 3$). Red lines indicate median isoform frequency of wt minigenes ± 2 standard deviations (SD). HNRNPH SRBS (brown) are given above. Heat maps (bottom) show *z*-scores as measure of synergy (mean, $n = 3$) per inserted nucleobase. White or grey fields indicate mutations that were not present or filtered out, respectively (see Methods). Purple boxes highlight significant synergistic interactions (0.1% FDR). **e** Consistent with strong synergistic interactions (colour-coded), mutations in cluster 3 almost completely abolish the *HNRNPH* KD response in MCF7 cells. Scatterplot compares model-inferred estimates with semiquantitative RT-PCR measurements of AE inclusion (circles) and AE skipping (triangles) upon *HNRNPH* KD (mean, $n = 3$) for ten targeted mutations in HNRNPH SRBS (Supplementary Data 8)

arrangement is not exclusive to short exons such as *FAS* exon 6[16] (63 nt) or *SMN1* exon 7[38] (54 nt), as *RON* exon 11 (147 nt) is around the average length of human cassette exons[40].

A major advance of our study is that we detect *cis*-regulatory elements along the entire minigene, including introns and flanking constitutive exons. In the constitutive exons, the effect sizes are generally smaller, possibly due to an accumulation of partially redundant exonic splicing enhancers (ESEs) that ensure constitutive splicing[13]. Notably, we find that mutations not necessarily trigger intron retention, but can also specifically swap between AE inclusion and skipping (such as T581G or G686C; Supplementary Data 6). These distal effects agree with previous observations from positional splicing maps (RNA-maps), showing that RBP binding at flanking constitutive exons can regulate the inclusion of neighbouring alternative exons[41].

Our ATtRACT analysis together with a previous study[35] suggest that splicing of *RON* exon 11 is controlled by a multilayered network of at least 17 *trans*-acting RBPs. Many of these RBPs are linked to multiple binding sites in different regions, further increasing the regulatory complexity. Importantly, significant correlations in our TCGA analyses suggest that many of the regulatory relationships are functional in humans in vivo. A multilayered regulation of alternative splicing events has also been suggested by a recent high-throughput screen for RBP KD

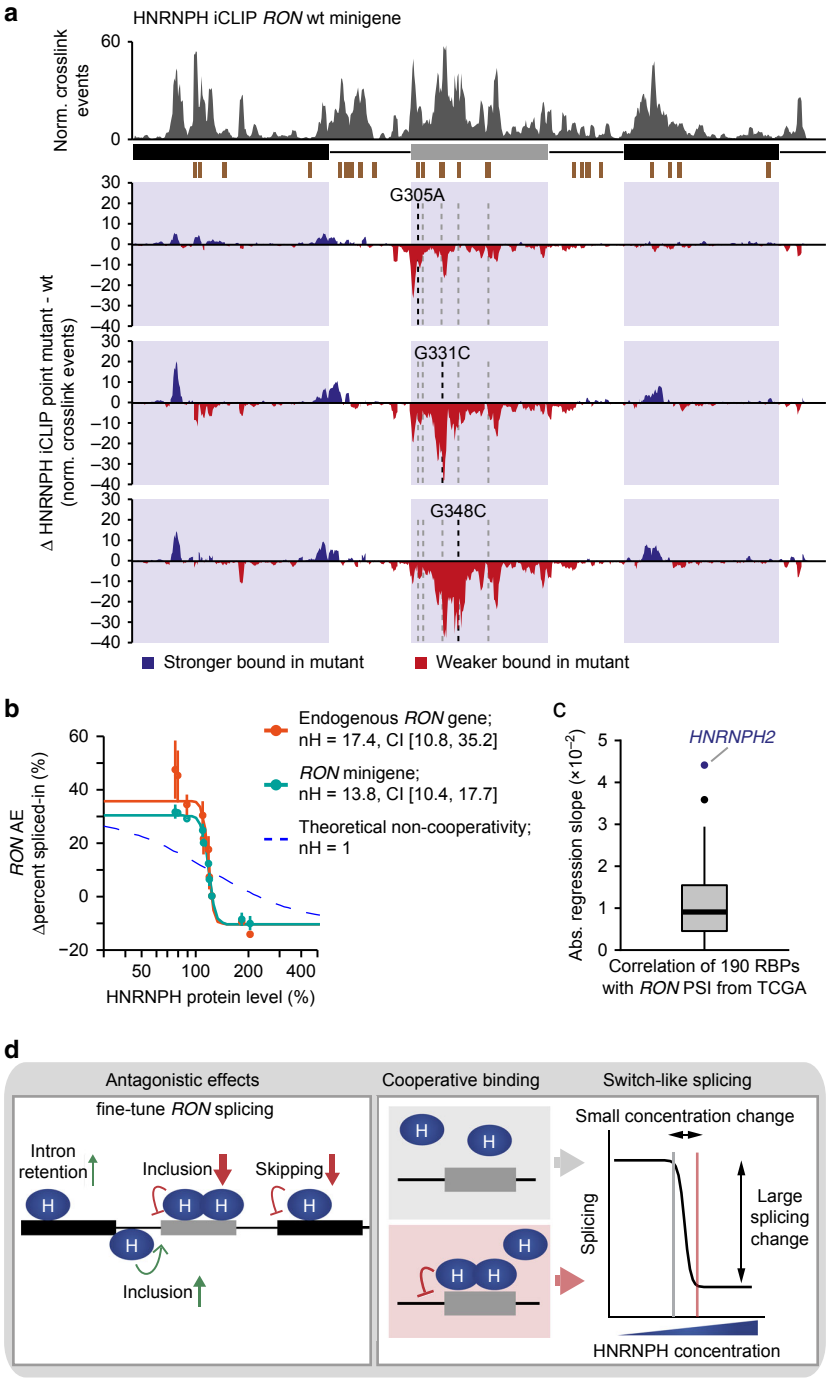

effects[42]. We extend beyond this view by directly identifying synergistic interactions between sequence mutations and RBP KD.

Our study highlights HNRNPH as a key regulator of *RON* exon 11 splicing. Using mutational analysis and iCLIP, we demonstrate that it acts via five clusters of intronic and exonic SRBS that antagonistically affect *RON* splicing (Fig. 6d). In line with previous global splicing maps[37,43,44], we observe that HNRNPH binding in the alternative exon represses AE inclusion, whereas binding in the flanking introns increases AE inclusion. Synergy analysis pinpoints the SRBS in the alternative exon as the functionally most relevant sites. We speculate that this interwoven arrangement of antagonistic SRBS may allow to fine-tune *RON* splicing. More generally, tightly regulated exons might benefit from modulating not just one but several competing splicing reactions in order to achieve an optimal adjustment of alternative splicing under changing physiological conditions.

Other than previously suggested for intronic HNRNPH sites[44], we find strong indications for cooperative binding of HNRNPH to multiple SRBS within the alternative exon. One possible mechanism for the observed cooperativity would be oligomerisation of HNRNPH via its glycine/tyrosine (GY)-rich domain. It was recently shown that other hnRNP proteins form multimeric assemblies via GY-rich domains to regulate splicing[45]. Moreover, HNRNPH binding sites might fold into G-quadruplex structures[46–49], which could contribute to the observed cooperativity through sequestering and simultaneously releasing G-runs. The cooperative HNRNPH binding renders *RON* splicing sensitive to individual mutations in HNRNPH SRBS or to small changes in HNRNPH protein expression.

Extensive changes in alternative splicing are characteristic for many human cancers[50], and it has been estimated that about half of all synonymous driver mutations change splicing[51]. The skipping of *RON* exon 11 results in a ligand-independent, constitutively active variant of the encoded RON receptor tyrosine kinase, RONΔ165[20]. Contrary to initial reports[52], we and others detect RONΔ165 expression also in healthy human tissues[21], suggesting that the encoded protein could play a role under physiological conditions. However, overexpression of RONΔ165 was shown to trigger increased cell motility and invasive tumourigenesis[20]. Consistent with this oncologic potential, abnormal RONΔ165 accumulation has been described in breast and colon cancers, among others[25].

With the help of our mutagenesis screen, we identify many mutations that trigger a strong skipping of *RON* exon 11. Importantly, the mutation effects in our screen are reflected in cancer patients bearing the same mutations. Several of the mutations are synonymous with respect to the encoded protein, suggesting that mutation-induced splicing changes can have deleterious impact in cancer[51,53–55]. In addition, we also identify numerous non-synonymous mutations that have a strong, and in some cases a surprising, impact on splicing regulation: for instance, the nonsense mutation G370T found in a head–neck squamous cell carcinoma (HNSC) patient also triggers *RON* exon 11 skipping (Fig. 3c, d). Intriguingly, this splicing change inverts the physiological consequence of the mutation, as the majority of mature *RON* transcripts will exclude the mutated exon and thereby translate into a constitutively active rather than a prematurely truncated RON protein.

Due to their prevalence in cancers, altered *RON* isoforms represent a promising target for intervention[56]. For instance, clinical trials assessed the therapeutic potential of monoclonal antibodies targeting RON to block the binding of its ligand MSP (MST1)[57] (ClinicalTrials.gov Identifier: NCT01119456; antibody RON8, Narnatumab, ImClone; phase-I discontinued). However, tumours expressing the constitutively active isoform RONΔ165 can specifically escape this kind of therapies, as this protein no longer requires ligand-dependent activation[24]. A detailed knowledge of mutations that promote this isoform might therefore allow a personalised therapy in the future.

Methods

Cloning of the *RON* wt minigene. To generate the *RON* wt plasmid, a segment of the *MST1R* gene was amplified by polymerase chain reaction using Phusion DNA polymerase (NEB) with the forward primer 5′- CCCAAGCTTTGTGAGAGGCA GCTTCCAGA-3′ and the reverse primer 5′- CAGTCTAGANNNNNNNNNNN NNNGGATCCGCCATTGGTTGGGGGTAGGGGCTGATTAAAGGTAGG-3′ at 65 °C annealing temperature with human genomic DNA (Promega) as a template (Supplementary Table 4). The 779 bp DNA product was gel-purified with the QIAquick Gel Extraction Kit (QIAGEN) and then digested using *Hin*dIII and *Xba*I restriction endonucleases (NEB). The cut DNA fragment was purified using a PCR purification kit (QIAGEN) prior to ligation into the pcDNA 3.1 (+) vector (Invitrogen). To raise AE inclusion in the *RON* wt minigene comparable to endogenous levels, the first nucleotide of the alternative exon was exchanged to a guanine.

Plasmids harbouring point mutations were generated using the Q5 Site-Directed Mutagenesis Kit (NEB) according to the manufacturer's instructions.

Mutagenic PCR and library construction. For the mutagenesis of the *RON* minigene, we used the GeneMorph II Random Mutagenesis Kit (Agilent) according to the manufacturer's instructions. Aiming for an average mutation rate of 3.5 mutations/minigene, three libraries were independently generated and finally fused. To this end, 8 and 4 µg of the unmutated *RON* wt plasmid were amplified with 30 cycles, and 0.8 µg of the unmutated *RON* wt plasmid were amplified with 20 cycles. The primers used to amplify the mutagenic fragments were 5′-CCCAA GCTTTGTGAGAGGCAGCTTCCAGA-3′ (forward primer) and 5′-CAGTCTAG ANNNNNNNNNNNNNNNGGATCCGCCATTGGTTGGGGGTAGGGGCTGA TTAAAGGTAGG-3′ (reverse primer) (Supplementary Fig. 1a and Supplementary Table 4). The PCR products were purified using the QIAquick Gel Extraction Kit (QIAGEN). Purified DNA was cut with *Hin*dIII and *Xba*I (NEB) restriction endonucleases for 45 min at 37 °C and subsequently purified using a PCR

Fig. 6 Cooperative HNRNPH binding establishes a splicing switch of *RON* exon 11. **a** A single point mutation in an HNRNPH splice-regulatory binding site (SRBS) results in reduced HNRNPH binding in HEK293T cells also at neighbouring SRBS in *RON* exon 11. Bar diagrams show the number of HNRNPH iCLIP crosslink events on the wt *RON* minigene (top) and the difference in normalised crosslink events on wt and mutated *RON* minigenes (mutations G305A, G331C and G348C in different SRBS within cluster 3, marked by dashed lines; bottom) in a sliding 5-nt window along the wt *RON* minigene. HNRNPH SRBS (brown boxes) indicated below. **b** Splicing response to gradual *HNRNPH* KD and overexpression suggests cooperative regulation of *RON* exon 11 by HNRNPH. Scatterplot shows semiquantitative RT-PCR quantifications of *RON* exon 11 inclusion (in percent spliced-in/PSI, Supplementary Fig. 15a, b) from endogenous *RON* gene (orange) and wt *RON* minigene (blue) against corresponding HNRNPH protein levels (Supplementary Fig. 15c, d). Degree of cooperativity is quantified by fitting Hill equation (solid lines) and compared to theoretical fit for non-cooperativity (dashed line). Error bars denote standard deviation of three biological replicates. **c** Steep regression slope for *HNRNPH2* supports cooperative HNRNPH regulation and switch-like splicing of *RON* exon 11. Boxplot shows distribution of regression slopes for expression correlations of 190 RBPs with *RON* exon 11 inclusion in TCGA samples (Supplementary Data 7). Box represents quartiles, centre line denotes 50th percentile and whiskers extend to most extreme data points within 1.5× interquartile range. *HNRNPH2* is highlighted. **d** HNRNPH acts as key regulator of *RON* splicing by recognising multiple *cis*-regulatory elements in a cooperative fashion. Schematic model summarises position-dependent effects of HNRNPH on *RON* exon 11, indicating most strongly effected isoform for each site (left panel). Multiple interdependent HNRNPH binding sites within *RON* exon 11 exert strong cooperative control on the alternative exon, resulting in a splicing switch upon small changes in HNRNPH abundance (right panel)

purification kit (QIAGEN). The digested plasmid DNA and mutagenic fragments were ligated for 5 min at room temperature in a volume of 21 µl containing 50 ng of plasmid and 21 ng of insert (3:1 ratio of insert to plasmid DNA), 10 µl of 2× Quick Ligation Reaction Buffer and 1 µl Quick T4 DNA ligase (NEB). Transformations were carried out via $CaCl_2$ transformation of *Escherichia coli* DH5-alpha strain with 2 µl of the ligated DNA. Bacteria were plated in low density to allow the formation of similar-sized colonies and determination of the number of transformants by counting of the colonies. Sixteen hours after the transformation, ~2000 colonies per transformation were washed off the plates into lysogeny broth (LB) medium and plasmids were extracted using the Plasmid Plus Midi Kit (QIAGEN). In addition, 200 wt plasmids were generated to be used as a spike-in to the above-mentioned libraries by using the same primers and template wt plasmid but non-mutagenic amplification with Phusion DNA Polymerase (NEB) and the following conditions: 98 °C for 30 s, 30 cycles of [98 °C for 10 s, 61 °C for 20 s, 72 °C for 20 s] and final extension at 72 °C for 5 min. Note that the remainder of wt minigenes in the library represent the proportion of error-free minigenes within the product pool of the mutagenic PCR. Purification, digestion and transformation were performed as described above. Mutagenesis and wt libraries were pooled together to yield a library of ~6000 plasmids. To obtain single plasmids of the library for benchmarking via Sanger Sequencing and validation via RT-PCR, a re-transformation of the library was carried out and plasmids of resulting colonies were extracted using QIAprep Spin Miniprep Kit (QIAGEN).

Semiquantitative RT-PCR. Semiquantitative RT-PCR was used to quantify isoform ratios of individual plasmids and endogenous *RON* mRNA. To this end, reverse transcription was carried out in a volume of 20 µl using 500 ng of total RNA, 1 µl $(dT)_{18}$ primer (100 µM), 1 µl dNTPs (10 mM) and 1 µl RevertAid reverse transcriptase (Fermentas) by heating 70 °C for 5 min, 25 °C for 5 min, 42 °C for 60 min, 45 °C for 10 min, and 70 °C for 5 min. Subsequently, 1 µl of the cDNA was used as a template for the PCR reaction with the condition as follows: 94 °C for 30 s, 24 cycles (minigene) or 35 cycles (endogenous) of [94 °C for 20 s, 52 °C (minigene) or 62 °C (endogenous) for 30 s, 68 °C for 30 s] and final extension at 68 °C for 5 min. The primers used to amplify the minigene-derived isoforms anneal to the upstream constitutive exon and a region located downstream of the random barcode but upstream of the polyadenylation site: 5′- TGCCAACCTAGTTCCAC TGA-3′ (forward primer) and 5′- GCAACTAGAAGGCACAGTCG-3′ (reverse primer). The primers to amplify endogenously derived isoforms were 5′-CCTGA ATATGTGGTCCGAGACCCCCAG-3′ (forward primer) and 5′-CTAGCTGCT TCCTCCGCCACCAGTA-3′ (reverse primer; Supplementary Table 4). The TapeStation 2200 capillary gel electrophoresis instrument (Agilent) was used for isoform quantification of the PCR products.

Cell culture and transfection of plasmids and siRNAs. HEK293T and MCF7 cells were grown in Dulbecco's modified Eagle medium (DMEM) supplemented with 10% foetal bovine serum at 37 °C with 5% CO_2. Standard *HNRNPH* KD was carried out using single small interfering RNA (siRNA) against *HNRNPH*[58] (5′-GGAGCUGGCUUUGAGAGGA[dT][dT]-3′, Sigma-Aldrich) or non-targeting control siRNA (5′-UGGUUUACAUGUCGACUAA[dT][dT]-3′, Sigma-Aldrich) at a final concentration of 20 nM. KD efficiencies were assessed by western blot analyses. For gradual *HNRNPH* KD, the siRNA concentration was varied between 0.05 nM and 10 nM. One day prior to transfection, 2×10^5 HEK293T cells were seeded in a 6-well plate to result with ~20% confluence at the day of transfection. MCF7 cells were seeded 3 days prior to transfection with 0.5×10^5 cells per well of a 6-well plate. The transfection mix was prepared by incubating 3 µl RNAiMax (Invitrogen) with 2 µl siRNA (20 µM) in 200 µl OPTI-MEM (Invitrogen) for 20 min, and the mix was added in a dropwise manner to the cells. For transfection of plasmids 24 h later, a mixture of 2 µg minigene plasmid DNA and 20 µg polyethylenimine MW ~2500 transfection reagent (Polysciences, Inc.) in 100 µl OPTI-MEM (Invitrogen) was prepared and incubated for 20 min before it was added to the cells. Cultures were harvested another 24 h later. For the HNRNPH1 overexpression, 4×10^5 MCF7 cells were seeded in a 6-well plate 1 day prior to transfection. Transfection was carried out using Lipofectamine 2000 (Invitrogen) and 1 or 2.5 µg pcDNA 3.1 (+)-HNRNPH1 overexpression construct or pcDNA 3.1 (+) empty vector control. The minigene plasmid was transfected 24 h later as described above and cells were harvested another 24 h later. RNA was extracted using the RNeasy Plus Mini Kit (QIAGEN) according to the manufacturer's protocol. For semiquantitative RT-PCR analysis of splicing isoforms without KD conditions, 7×10^5 HEK293T cells were seeded and transfected the next day with plasmid DNA under the above-mentioned conditions.

No cell line used in this paper is listed in the database of commonly misidentified cell lines maintained by ICLAC. HEK293T (CRL-3216) and MCF7 cells (HTB-22) were purchased from ATCC (Manassas, VA) without further authentication. Cell lines were tested for mycoplasma contamination on a monthly basis.

Library preparation and high-throughput sequencing. For preparation of high-throughput RNA sequencing (RNA-seq) libraries, the total RNA obtained from transfected HEK293T cells or MCF7 cells was enriched for mRNA by performing polyA selection of 20 µg of total RNA using Dynabeads® Oligo $(dT)_{25}$ beads (Invitrogen) according to the manufacturer's protocol. Reverse transcription was carried out using 500 ng of enriched mRNA under the above-mentioned conditions. To prevent the formation of chimeric amplicons, the libraries were amplified using emulsion PCR[59], with Phusion DNA Polymerase (NEB) and either cDNA derived from polyA-selected RNA in the case of RNA-seq or plasmid DNA of the minigene library in the case of high-throughput DNA sequencing (DNA-seq). To amplify fragments for RNA-seq, the following primers containing Illumina sequencing adaptors were used (Supplementary Fig. 2g): 5′-CAAGCAGAA-GACGGCATACGAGATCGGTCTCGGCATTCCTGCTGAA CCGCTCTTCCGATCTNNNNNNNNNNGTTCCACTGAAGCCTGAG-3′ (forward primer) and 5′-AATGATACGGCGACCACCGAGATCTACACTCTTTC CCTACACGACGCTCTTCCGATCTNNNNNNNNNNNATAGAATAGGGCCCT CTAGA-3′ (reverse primer) under the following PCR conditions: 98 °C for 30 s, 15 cycles of [98 °C for 10 s, 56 °C for 20 s, 72 °C for 60 s] and final extension at 72 °C for 5 min. For the DNA-seq library amplification, the same PCR conditions and 18 cycles with different primer combinations were used (Supplementary Fig. 2a and Supplementary Table 4). Following amplification, the DNA-seq PCR products were cleaned using the GeneRead Size Selection Kit (QIAGEN) according to the manufacturer's instructions. Products intended for RNA-seq were purified using Agencourt AMPure XP beads (Beckman Coulter). Purified products were first analysed with the TapeStation 2200 capillary gel electrophoresis instrument (Agilent) and then fluorimetrically quantified using a Qubit fluorimeter (Thermo Scientific). RNA-seq and DNA-seq were carried out on the Illumina MiSeq platform using paired-end reads of 300 nt length and a 10% PhiX spike-in to increase sequence complexity.

Western blot. Cell lysates were prepared with modified RIPA buffer (50 mM Tris HCl pH 7.5, 150 mM NaCl, 1 mM EDTA, 1% NP-40, 0.1% sodium deoxycholate, protease inhibitor cocktail; Roche). The following antibodies were used for western blot analyses: rabbit polyclonal anti-HNRNPH, 1:10,000 dilution (AB10374, Abcam) and mouse monoclonal anti-HNRNPA1, 1:10,000 dilution (R4528, Sigma-Aldrich).

iCLIP experiment and data processing. We used iCLIP to capture the binding pattern of HNRNPH on the *MST1R* transcript. iCLIP was performed according to a previously published protocol[60]. In brief, the iCLIP libraries were made from HEK293T cells 24 h after transfection of the *RON* wt minigene (in triplicates) or mutated *RON* minigenes carrying point mutations G305A (in triplicates), G331C or G348C (both in duplicates). The cells were irradiated with 150 mJ/cm^2 UV light at 254 nm. For the immunoprecipitation step, we used 7.5 µg of a polyclonal rabbit anti-HNRNPH antibody from Abcam (AB10374). RNase digestion was performed by adding 10 µl of 1/100 diluted RNase I (Ambion) to the sample of the wt minigene experiment shown in Supplementary Fig. 12a or 1/300 diluted RNase I (Ambion) to each sample of the experiment shown in Fig. 6a (comparison of the iCLIP landscape of the *RON* wt minigene with point mutation minigenes). Reverse transcription was carried out with RT primers listed in Supplementary Table 4. We performed the sequencing on an Illumina HiSeq 2500 for the *RON* wt minigene (51-nt single-end reads) and the *RON* wt/point mutant minigene comparison was sequenced on either Illumina MiSeq or NextSeq 500 with 75-nt single-end reads. Sequencing reads were first filtered for quality in the experimental and random barcode, and then the adaptor sequences were trimmed. Trimmed reads were mapped to the human genome (hg19/GRCh37) using STAR[61] resulting in ~49 million (HiSeq 2500), ~10 million (MiSeq) or ~121 million (NextSeq 500) uniquely mapping reads. In order to quantitatively compare HNRNPH iCLIP data for the *RON* wt and point mutation minigenes (Fig. 6a), crosslink events were normalised to the total number of crosslink events within the minigene region excluding *RON* exon 11. Normalised counts were averaged between replicates, counted into 5-nt sliding windows and then subtracted between conditions to determine differences in HNRNPH crosslinking.

DNA-seq data processing and mutation calling. The DNA-seq library was sequenced on Illumina MiSeq (300-nt paired-end) with a total of 40 million reads and analysed with a custom Python pipeline (version 2.7.9: Anaconda 2.2.0, 64-bit; Supplementary Fig. 2b). In detail, we used FastQC (fastqc_v0.11.3; https://www.bioinformatics.babraham.ac.uk/projects/fastqc/) for quality control and Trimmomatic[62] (version 0.33; parameters HEADCROP:20 SLIDINGWINDOW: 7:10 MINLEN:0) to remove excess sequence and trim low-quality bases (average Phred score < 10 in 7-nt window). After trimming, we filtered for a minimum length of 130 nt (read #1) and 90 nt (read #2). In order to extract the 15-nt barcode (read #1) which assigns the read pairs to an individual minigene variant, we used matchLRPatterns() from the R/Bioconductor package 'Biostrings' to search for the flanking restriction sites (Lpattern = TCTAGA, Rpattern = GGATCC, allowing one mismatch). We only retained read pairs with a Phred score ≥ 30 at all barcode positions. For each minigene variants with at least 640 read pairs, reads were mapped to the sequence of the *RON* wt minigene using NextGenMap[63] (version 0.4.12). A read was reported as mapped if >50% of its bases were mapped, the alignment had an identity >65%, and at least one stretch of 13 bp was identical to the reference. Mutations were called using the HaplotypeCaller tool (version 3.4.0) of the Genome Analysis Toolkit (GATK)[64] with -dt NONE. We recounted

overlapping reads using bam-readcount (https://github.com/genome/bam-readcount) and then manually filtered against single-nucleotide variants (SNV) with low penetrance based on reference (Ref) and alternative (Alt) allele frequencies: (i) Alt/(Alt + Ref) > 0.8, and (ii) (Alt + Ref)/total > 0.5 taking into account all other isoforms. The identified mutations include 18,948 point mutations as well as 608 short insertions and deletions. The latter were taken into account as independent sequence variants in the mathematical splicing model and are provided in addition to the point mutations in Supplementary Data 3. The final library contained 5791 minigene variants, including 591 wt and 5200 mutated minigenes. The accuracy of mutation calling was validated by Sanger sequencing of 59 randomly selected minigene variants, confirming the presence of all 169 GATK-called mutations without further false negatives.

RNA-seq data processing and splicing isoform quantification. RNA-seq libraries were sequenced on Illumina MiSeq (300-nt paired-end), yielding 17–22 million reads per sample (Supplementary Table 1), and analysed with a custom Python pipeline similar to DNA-seq (see above; Supplementary Fig. 2f). Briefly, we removed low-quality sequences (average Phred score < 20 in 6-nt window) and extracted the 15-nt barcode (read #1) as described above. Only reads originating from the 5791 minigene variants that were recovered from the DNA-seq library were considered for further analyses. Read pairs for each minigene variant were aligned to the *RON* wt minigene sequence using the splice-aware alignment algorithm STAR[61] (version 2.5.1b), allowing up to ten mismatches without input of prior knowledge of existing splice junctions. Only read pairs conferring splice isoform information (i.e., both mates extended at least 10 nt beyond the constitutive exon boundaries) were kept. Furthermore, all improperly or inconsistently mapped read pairs were removed from the analysis. Read pairs are referred to as improperly mapped if they map with a wrong orientation, while inconsistently mapped read pairs overlap and show a disagreement in their mapping patterns. Finally, only minigene variants which were covered by at least 100 remaining read pairs were used further, resulting in 5697, 5645 and 5623 minigene variants detected in RNA-seq replicates 1, 2 and 3 from HEK293T cells, respectively (Supplementary Fig. 2h and Supplementary Table 1).

Reconstruction and quantification of splicing isoforms. For each read pair, the underlying splicing isoform was reconstructed based on the CIGAR strings of the two mates. Isoforms which were supported by <1% of the read pairs or less than two read pairs in any plasmid were removed from the analysis. The frequency of each isoform for each minigene variant was calculated as the number of read pairs supporting this particular isoform in relation to the total read pairs for all detected isoforms for this particular minigene variant. All kept non-canonical isoforms derived from cryptic splice site activation were collected in the isoform category 'other'.

Dynamic model of splicing. We modelled the splicing dynamics using a set of ordinary differential equations, in which concentrations of RNA intermediates are determined by production and degradation terms (Supplementary Fig. 3a). The pre-mRNA precursor x_0 is produced at a constant rate c and spliced into five splice products with linear kinetics and rates r_i. All non-canonical isoforms are included in the model as one additional species produced at rate r_6. This leads to $\mathrm{d}x_0/\mathrm{d}t = c - (r_1 + r_2 + r_3 + r_4 + r_5 + r_6)x_0$. Six additional differential equations describe the dynamics of the canonical (AE inclusion, AE skipping, full IR, first IR and second IR) and non-canonical (other) splice isoforms. The concentration x_i of isoform i is described by $\mathrm{d}x_i/\mathrm{d}t = r_i x_0 - d_i x_i$, where d_i are RNA degradation rates.

The measured isoform frequencies correspond in the model to the concentration of transcripts x_i normalised by the total RNA concentration. These fractions can be calculated analytically from the steady state of the system (see Supplementary Note 1). As a result, we find that the frequency p_i of a certain isoform i has the form $p_i = K_i/(K_1 + K_2 + K_3 + K_4 + K_5 + K_6)$. Here, the splicing rates $K_j = r_j/d_j$, $j = 1,2,4,5,6$ are the ratios of production and degradation rates for the isoforms involving splicing, and $K_3 = 1 + r_3/d_3$ reflects the sum of the unspliced pre-mRNA (x_0) and full intron retention (x_3) isoforms, which cannot be discriminated experimentally. Thus, due to normalisation, a change in the production rate of one isoform due to a particular mutation will affect all isoform frequencies, and this effect depends in a nonlinear manner on the values of all splice rates K_i (i.e., on the mutational background). To infer the mutation effects from the data, it is instructive to consider the isoform ratio relative to the inclusion isoform ($p_i/p_1 = K_i/K_1$), as this no longer depends on all splice rates, and relates to K_i in a linear fashion.

Calculation of single mutation effects by linear regression. For the estimation of single mutation effects in HEK293T cells, we assumed that the combined log fold changes of multiple mutations on a splice isoform ratio can be written as the sum of individual log fold changes (see Supplementary Note 2). One such equation was formulated for each minigene, resulting in a system of 5621–5697 equations for each splice isoform ratio, depending on the amount of minigene variants that were detected in the RNA-seq replicates (Supplementary Table 1).

To support our assumption of additive mutation effects, we analysed how single mutation effects interact in minigenes containing several mutations. To this end, we analysed a subset of mutations that is contained in the library as single mutation minigenes (~600 minigene variants), and furthermore occur within double/triple mutation minigenes together with other mutations from the list (Supplementary Fig. 4a and Supplementary Table 1). For the majority of these mutations, we observed that the combined mutational effects on the splicing rates K_i are multiplicative, e.g., $K_i(m_1,m_2)/K_i(\mathrm{WT}) = K_i(m_1)/K_i(\mathrm{WT}) * K_i(m_2)/K_i(\mathrm{WT})$, where $K_i(\mathrm{WT})$, $K_i(m_1)$, $K_i(m_2)$ and $K_i(m_1,m_2)$ are the splicing rates of the wt minigene and of the minigenes including mutation m_1 or mutation m_2 or both mutations m_1 and m_2, respectively. In practice, we calculate the mutational effects $K_i(m_1,\ldots m_n)/K_i(\mathrm{WT})$ as a mutation-induced fold change of the splice isoform ratios p_i/p_1 (see above). By a log-transformation, the above multiplicative relationship transforms to a linear one that connects the measured cumulative mutation effects with the predominantly unknown single mutation effects (Supplementary Fig. 3a). For the whole pool of measured minigene variants, this constitutes a system of linear equations that can be solved for the single mutation effects in a least-square sense (see Supplementary Note 2 for details).

As an alternative approach to estimate the single mutation effects, we calculated the median isoform frequency across all minigene variants that harbour a given mutation, and compared these numbers to the estimation of the regression model (Supplementary Fig. 4b). If enough minigene variants with the mutation are present in the library, this procedure should average out the effect of accompanying mutations. The median isoform frequency for a mutation was independently calculated for each isoform category and treated as a representative measure of the splicing effect of this particular mutation.

Estimation of the inference accuracy of the model. The training data set contained about ~600 mutations that were measured also as single mutations in individual minigenes (Supplementary Table 1). We used these single mutation minigenes to estimate the inference accuracy of the model, and to assess the dependency of the inference accuracy on the occurrence of a mutation in the data set. For each such mutation, the following cross-validation procedure was repeated: The single mutation minigene was removed from the data set before fitting the regression model, and kept for the evaluation of the regression results. The remaining minigenes containing the particular mutation were removed from the data set successively and each time the effect of the mutation was assessed by regression and the estimation compared to the single mutation minigene value. In this way, we obtained estimates for the prediction error based on 1 up to $n-1$ minigenes containing a particular mutation, where n is the total occurrence of the mutation in the data set. In some cases, estimation of mutational effects was not possible from a reduced data set, e.g., the prediction error for a particular mutation was estimated only for occurrences between m and $n-1$, with $1 < m \le n-1$. Finally, the standard deviation of the inference errors for all mutations was estimated for each measured frequency (Fig. 2c).

Significant mutation effects and synergistic interactions. The estimated single mutation effects on splice isoform ratios as obtained by linear regression could be used to predict single mutation effects on each splice isoform frequency (p_i) (see Supplementary Note 2 for details). To quantify the effects of each individual mutation on each isoform frequency, we calculated a z-score value from the model-derived single mutation effects, using the mean and standard deviation of the 591 wt minigene variants: $\frac{\left(p_i^{\mathrm{mutation}} - \mathrm{mean}\left(p_i^{\mathrm{wt}}\right)\right)}{\mathrm{Standard\ deviation}\left(p_i^{\mathrm{wt}}\right)}$. The z-scores were independently calculated per replicate and later averaged. Only mutations present in all three replicates were kept for further analyses.

In order to combine the evidence from the three replicate experiments, we applied Stouffer's test to combine the z-scores[65]. The resulting standard-normally distributed metric was converted into a P value and subjected to multiple testing correction (Benjamini–Hochberg). We considered a mutation as significant for a given isoform if it displays (i) ≥5% change in isoform frequency compared to the mean of the 591 minigene variants (ΔIF ≥ 5%), and (ii) less than 5% false discovery rate (FDR, adjusted P value <0.05). Combining all six isoform categories, this approach identified 778 and 1022 splicing-effective mutations in HEK293T and MCF7 cells, respectively (Supplementary Table 2). These accumulated into 469 and 550 splicing-effective positions, i.e., nucleotide positions in the *RON* minigene where at least one out of three possible mutations shows a significant effect on at least one isoform.

To calculate z-scores for synergistic interactions between mutations and *HNRNPH* knockdown from the model-derived isoform ratios, we divided the log-transformed fold change in isoform ratios (KD over control condition) by the wt variation (standard deviation; see Supplementary Note 3). z-scores were calculated by replicates and then averaged, removing mutations that were not present in the three replicates under KD conditions. We then used Stouffer's test and multiple testing correction as above. Since the uncertainty of the synergy z-score (measured as the standard deviation between replicates) increases near 0% AE inclusion due to boundary effects (Supplementary Fig. 7g), we excluded the splice sites (positions 209–210, 298–299, 443–444, 523–524 and 689–690) mutations that on their own completely abolish splicing (<1% isoform frequency under control conditions). To identify significant synergistic interactions, we applied a cutoff at 0.1% FDR (adjusted P value <0.001). Additionally, we required a consistent directionality of the synergistic effects in all three replicates. Combining the five different isoform ratios, this approach identified 354 significant synergistic

interactions (|*z*-score| > 2) on 278 positions between mutations and *HNRNPH* knockdown in MCF7 cells (Supplementary Table 2). Applying more stringent cutoffs at |*z*-score| > 3 or >5 identified 222 or 66 significant synergistic interactions, respectively (Supplementary Table 2).

Characterisation of splicing-effective positions. Splice site strengths were predicted using the sequence analysis software MaxEntScan[29] for all mutations in the positions considered by MaxEntScan (278–300 nt and 442–450 nt for the 3′ and 5′ splice site, respectively; Supplementary Fig. 9a, b). PhyloP scores[66] were retrieved from the UCSC Genome Browser (http://genome.ucsc.edu/cgi-bin/hgTables; table: Mammal Cons, PhyloP46wayPlacental) for the genomic coordinates corresponding to the *RON* minigene (chr3:49933134–49933840, human genome version hg19; Supplementary Fig. 9c).

Annotation of splice-regulatory RBP binding sites (SRBS). We used the Scan Sequence tool of the ATtRACT database[34] to identify potential RBP binding sites along the *RON* wt minigene sequence. Duplicated records, e.g., due to overlapping database entries from different experimental methodologies, were removed. We retained only those binding sites for which ≥60% of positions were identified as splicing effective in our screen. This step was independently performed for each splice isoform. Within each RBP, these binding sites were then collapsed if they shared an overlap of ≥2 nt and still harboured ≥60% splicing-effective positions for at least one isoform after collapsing, if they did not fulfil this condition, they were kept unmerged. For the comparison in Supplementary Fig. 12b, the HNRNPH SRBS within each cluster were extended by 2 nt. Nucleotide positions in the two isolated SRBS in the constitutive exons were excluded from this analysis.

In order to connect mutation effects to HNRNPH's sequence specificity, G-run-disrupting mutations were defined as a G-to-H mutation at any position of the G-run (used in Fig. 4c), while the two possible H-to-G mutations in immediately neighbouring positions were counted as G-run-extending. Figure 4b compares the median splicing effect (average of three biological replicates) of all G-run disrupting versus extending mutations for the 22 predicted HNRNPH SRBS.

Analysis of TCGA and GTEx data. Normalised gene expression data for 11,688 post mortem samples from 30 human tissues, collected from 714 non-diseased human donors, were retrieved from the GTEx project[36] (v7). Normalised gene expression data from TCGA tumour samples (https://cancergenome.nih.gov/) were retrieved from Firebrowse (http://firebrowse.org/). Alternative splicing for both data sets was quantified using *psichomics* (version 1.2.1, https://github.com/nuno-agostinho/psichomics), using the default minimum coverage to calculate *RON* exon 11 PSI values. We quantified both gene expression and *RON* exon 11 PSIs for 2743 normal samples, from 24 healthy human tissues, and 4514 tumour samples, from 27 cancer types. The comparison of *HNRNPH2* expression between tumours from TCGA (9807 samples) and healthy tissues from GTEx (7851 samples) was done using TPM values calculated at Toil[67], which are already normalised for comparison.

Calculation of single mutation effects in cancer. Exome sequencing data from TCGA tumour samples were downloaded from Genomic Data Commons Data Portal (https://portal.gdc.cancer.gov/). We identified a total of 153 patients bearing 55 different mutations within the region of our *RON* minigene (Supplementary Data 5). The impact on splicing of each mutation in the TCGA tumour samples was quantified, per cohort, as the difference of *RON* exon 11 skipping (calculated as 1 − PSI) between mutated and non-mutated tumour samples. These differences were correlated with those derived from the skipping isoform frequencies observed in our screen for each mutation. Since we observed that the correlation was affected by the minimum read coverage used to calculate PSIs, we restricted the correlation analysis to cohorts with an average of more than 24 reads mapping to the involved splice junctions (resulting in 117 patients from 14 cohorts harbouring 36 different mutations; Fig. 3c). The intrinsic variability of *RON* exon 11 inclusion levels in TCGA patient samples was calculated as the standard deviation of *RON* exon 11 PSI in unmutated TCGA tumour samples (i.e., without a given mutation) from cohorts considered in Fig. 3c and with more than 24 reads mapping to the involved splice junctions.

Identification of candidate RBPs. A recent large-scale RBP KD screen tested the KD effect of >200 RBPs on splicing of *RON* exon 11 and other alternative exons in HeLa cells[35]. The study used *z*-scores calculated from the PSI upon siRNA treatment and the median absolute PSI deviation, divided by its standard deviation. A positive *z*-score indicates more AE inclusion upon RBP KD. Using a cutoff of |*z*-score| > 1.5, 125 RBPs showed a substantial effect on *RON* exon 11 splicing. These include 17 RBPs that also have predicted SRBS in the *RON* minigene.

In order to identify potential regulators of *RON* exon 11 splicing in humans, we searched for RBPs whose expression correlated with *RON* exon 11 splicing in cancer. The correlation analysis was performed with 190 pre-selected RBPs, consisting of 65 identified via ATtRACT, 108 identified in the previously published RBP KD screen[35] and 17 common to both approaches. The mRNA expression levels of the RBPs were Spearman-correlated with *RON* exon 11 inclusion levels across TCGA tumour samples (Supplementary Data 7 and Supplementary Table 3). The significance of those correlations (ranked by minus base-10 logarithm of the associated *P* value) was tested against those of all RBPs retrieved from[8] and of all protein-coding genes using Gene Set Enrichment Analysis (GSEA) tool[68,69]. RBPs and protein-coding genes were first restricted to the ones showing at least the same average expression value as the least expressed pre-selected RBP, known to be highly expressed in cancer, so that GSEA was not biased by gene expression ranges. Moreover, we performed linear regressions between the expression of each of the 190 pre-selected RBPs and *RON* exon 11 PSI in TCGA tumour samples, using the resulting slopes to quantitatively assess the relative magnitude of association between each RBP and *RON* exon 11 splicing.

Analysis of cooperativity and switch-like splicing behaviour. Changes in percent spliced-in (ΔPSI) data for *RON* exon 11 inclusion from the endogenous *RON* gene and the wt *RON* minigene measured at different *HNRNPH* knockdown (KD) and overexpression (OE) levels (Supplementary Fig. 15a–d, 16) were fitted using the Hill function

$$y(x) = y_{\max} - \frac{(y_{\max} - y_{\min})x^{n_H}}{x^{n_H} + \mathrm{EC50}^{n_H}},$$

with x and y being vectors of experimentally determined HNRNPH levels and corresponding splicing outcomes (ΔPSI), respectively (Fig. 6b). $y_{\min}$, $y_{\max}$, EC50, and n_H are fitted parameters. Fitting was done by minimising the residual cost function

$$\chi^2 = (\Delta\mathrm{PSI} - y(\mathrm{HNRNPH}))/\sigma_{\Delta\mathrm{PSI}},$$

where $\sigma_{\Delta\mathrm{PSI}}$ denotes the standard deviation of the PSI measurement. Minimisation was done using the Matlab nonlinear least-squares solver *lsqnonlin*. The parameter ranges used during fitting were $y_{\min} \in [-0.5,0]$, $y_{\max} \in [0,0.5]$, $\mathrm{EC50} \in [0.1,2]$ and $n_H \in [1,20]$. The optimal parameter values found were

1. for the endogenous *RON* gene: $y_{\min} = -0.11$, $y_{\max} = 0.36$, $\mathrm{EC50} = 0.93$, $n_H = 17.4$
2. for the wt *RON* minigene: $y_{\min} = -0.11$, $y_{\max} = 0.3$, $\mathrm{EC50} = 0.94$, $n_H = 13.8$

Confidence intervals were determined for all parameters by using a profile likelihood approach. For each fitted parameter θ, the following workflow was repeated: The parameter was assigned successively a number of values around its optimal value θ_0 listed above. While keeping this parameter at the fixed value, the remaining parameters were optimised and the value of the corresponding cost function was determined. Thus, the dependence of the cost function $\chi^2(\theta)$ on the parameter value around the minimum corresponding to the optimal value θ_0 was determined. The likelihood-based confidence interval for this parameter is defined by

$$\left[\theta, \chi^2(\theta) - \chi^2(\theta_0) < \chi^2(\alpha, 1)\right],$$

where α is the confidence level and $\chi^2(\alpha,1)$ is the χ^2 distribution with degree of freedom 1. For each parameter, the 95% confidence intervals were found by determining the values θ on both sides of θ_0, for which the likelihood $\chi^2(\theta)$ crosses the threshold $\chi^2(\theta_0) + \chi^2(0.95,1)$.

The 95% confidence intervals found for the endogenous *RON* gene were:

$$y_{\min} \in [-0.12, -0.1], y_{\max} \in [0.28, 0.43],$$
$$\mathrm{EC50} \in [0.89, 0.95], n_H \in [10.8, 35.2],$$

and for the wt *RON* minigene:

$$y_{\min} \in [-0.14, -0.08], y_{\max} \in [0.3, 0.31],$$
$$\mathrm{EC50} \in [0.93, 0.95], n_H \in [10.4, 17.7],$$

Code availability. Code that was used to generate the presented data is available from the corresponding authors upon request.

Data availability. The sequencing data generated in this study are available from ArrayExpress under the accession numbers E-MTAB-6216 and E-MTAB-6217 (RNA-seq), E-MTAB-6219 (DNA-seq), E-MTAB-6220 and E-MTAB-6221 (iCLIP). All other data supporting the findings of this study are available from the corresponding authors on reasonable request.

Received: 8 January 2018 Accepted: 19 July 2018
Published online: 17 August 2018

References

1. Pan, Q., Shai, O., Lee, L. J., Frey, B. J. & Blencowe, B. J. Deep surveying of alternative splicing complexity in the human transcriptome by high-throughput sequencing. *Nat. Genet.* **40**, 1413–1415 (2008).

2. Wang, E. T. et al. Alternative isoform regulation in human tissue transcriptomes. *Nature* **456**, 470–476 (2008).
3. Ellis, J. D. et al. Tissue-specific alternative splicing remodels protein-protein interaction networks. *Mol. Cell* **46**, 884–892 (2012).
4. Yang, X. et al. Widespread expansion of protein interaction capabilities by alternative splicing. *Cell* **164**, 805–817 (2016).
5. Baralle, F. E. & Giudice, J. Alternative splicing as a regulator of development and tissue identity. *Nat. Rev. Mol. Cell Biol.* **18**, 437–451 (2017).
6. Sterne-Weiler, T. & Sanford, J. R. Exon identity crisis: disease-causing mutations that disrupt the splicing code. *Genome Biol.* **15**, 201 (2014).
7. Bonomi, S. et al. HnRNP A1 controls a splicing regulatory circuit promoting mesenchymal-to-epithelial transition. *Nucleic Acids Res.* **41**, 8665–8679 (2013).
8. Sebestyen, E. et al. Large-scale analysis of genome and transcriptome alterations in multiple tumors unveils novel cancer-relevant splicing networks. *Genome Res.* **26**, 732–744 (2016).
9. Sveen, A., Kilpinen, S., Ruusulehto, A., Lothe, R. A. & Skotheim, R. I. Aberrant RNA splicing in cancer; expression changes and driver mutations of splicing factor genes. *Oncogene* **35**, 2413–2427 (2016).
10. Wahl, M. C., Will, C. L. & Luhrmann, R. The spliceosome: design principles of a dynamic RNP machine. *Cell* **136**, 701–718 (2009).
11. Barash, Y. et al. Deciphering the splicing code. *Nature* **465**, 53–59 (2010).
12. Fu, X. D. & Ares, M. Jr. Context-dependent control of alternative splicing by RNA-binding proteins. *Nat. Rev. Genet.* **15**, 689–701 (2014).
13. Wang, Z. & Burge, C. B. Splicing regulation: from a parts list of regulatory elements to an integrated splicing code. *RNA* **14**, 802–813 (2008).
14. Barash, Y. et al. AVISPA: a web tool for the prediction and analysis of alternative splicing. *Genome Biol.* **14**, R114 (2013).
15. Xiong, H. Y. et al. RNA splicing. The human splicing code reveals new insights into the genetic determinants of disease. *Science* **347**, 1254806 (2015).
16. Julien, P., Minana, B., Baeza-Centurion, P., Valcárcel, J. & Lehner, B. The complete local genotype-phenotype landscape for the alternative splicing of a human exon. *Nat. Commun.* **7**, 11558 (2016).
17. Ke, S. et al. Saturation mutagenesis reveals manifold determinants of exon definition. *Genome Res.* **28**, 11–24 (2018).
18. Rosenberg, A. B., Patwardhan, R. P., Shendure, J. & Seelig, G. Learning the sequence determinants of alternative splicing from millions of random sequences. *Cell* **163**, 698–711 (2015).
19. Zhang, K., Zhou, Y. Q., Yao, H. P. & Wang, M. H. Alterations in a defined extracellular region of the RON receptor tyrosine kinase promote RON-mediated motile and invasive phenotypes in epithelial cells. *Int. J. Oncol.* **36**, 255–264 (2010).
20. Collesi, C., Santoro, M. M., Gaudino, G. & Comoglio, P. M. A splicing variant of the RON transcript induces constitutive tyrosine kinase activity and an invasive phenotype. *Mol. Cell Biol.* **16**, 5518–5526 (1996).
21. Ghigna, C. et al. Cell motility is controlled by SF2/ASF through alternative splicing of the Ron protooncogene. *Mol. Cell* **20**, 881–890 (2005).
22. Wang, D., Shen, Q., Chen, Y. Q. & Wang, M. H. Collaborative activities of macrophage-stimulating protein and transforming growth factor-beta1 in induction of epithelial to mesenchymal transition: roles of the RON receptor tyrosine kinase. *Oncogene* **23**, 1668–1680 (2004).
23. Zhou, Y. Q., He, C., Chen, Y. Q., Wang, D. & Wang, M. H. Altered expression of the RON receptor tyrosine kinase in primary human colorectal adenocarcinomas: generation of different splicing RON variants and their oncogenic potential. *Oncogene* **22**, 186–197 (2003).
24. Chakedis, J. et al. Characterization of RON protein isoforms in pancreatic cancer: implications for biology and therapeutics. *Oncotarget* **7**, 45959–45975 (2016).
25. Mayer, S. et al. RON alternative splicing regulation in primary ovarian cancer. *Oncol. Rep.* **34**, 423–430 (2015).
26. Lefave, C. V. et al. Splicing factor hnRNPH drives an oncogenic splicing switch in gliomas. *EMBO J.* **30**, 4084–4097 (2011).
27. Moon, H. et al. A 2-nt RNA enhancer on exon 11 promotes exon 11 inclusion of the Ron proto-oncogene. *Oncol. Rep.* **31**, 450–455 (2014).
28. Nazim, M. et al. Competitive regulation of alternative splicing and alternative polyadenylation by hnRNP H and CstF64 determines acetylcholinesterase isoforms. *Nucleic Acids Res.* **45**, 1455–1468 (2017).
29. Yeo, G. & Burge, C. B. Maximum entropy modeling of short sequence motifs with applications to RNA splicing signals. *J. Comput. Biol.* **11**, 377–394 (2004).
30. Llorian, M. et al. Position-dependent alternative splicing activity revealed by global profiling of alternative splicing events regulated by PTB. *Nat. Struct. Mol. Biol.* **17**, 1114–1123 (2010).
31. Xing, Y. & Lee, C. Alternative splicing and RNA selection pressure–evolutionary consequences for eukaryotic genomes. *Nat. Rev. Genet.* **7**, 499–509 (2006).
32. Shabalina, S. A., Spiridonov, N. A. & Kashina, A. Sounds of silence: synonymous nucleotides as a key to biological regulation and complexity. *Nucleic Acids Res.* **41**, 2073–2094 (2013).
33. Xing, Y. & Lee, C. Evidence of functional selection pressure for alternative splicing events that accelerate evolution of protein subsequences. *Proc. Natl Acad. Sci. USA* **102**, 13526–13531 (2005).
34. Giudice, G., Sanchez-Cabo, F., Torroja, C. & Lara-Pezzi, E. ATtRACT-a database of RNA-binding proteins and associated motifs. *Database* baw035 (2016).
35. Papasaikas, P., Tejedor, J. R., Vigevani, L. & Valcárcel, J. Functional splicing network reveals extensive regulatory potential of the core spliceosomal machinery. *Mol. Cell* **57**, 7–22 (2015).
36. GTEx Consortium. Human genomics. The genotype-tissue expression (GTEx) pilot analysis: multitissue gene regulation in humans. *Science* **348**, 648–660 (2015).
37. Uren, P. J. et al. High-throughput analyses of hnRNP H1 dissects its multi-functional aspect. *RNA Biol.* **13**, 400–411 (2016).
38. Mueller, W. F., Larsen, L. S., Garibaldi, A., Hatfield, G. W. & Hertel, K. J. The silent sway of splicing by synonymous substitutions. *J. Biol. Chem.* **290**, 27700–27711 (2015).
39. Moon, H. et al. SRSF2 promotes splicing and transcription of exon 11 included isoform in Ron proto-oncogene. *Biochim. Biophys. Acta* **1839**, 1132–1140 (2014).
40. Savisaar, R. & Hurst, L. D. Estimating the prevalence of functional exonic splice regulatory information. *Hum. Genet.* **136**, 1059–1078 (2017).
41. Witten, J. T. & Ule, J. Understanding splicing regulation through RNA splicing maps. *Trends Genet.* **27**, 89–97 (2011).
42. Han, H. et al. Multilayered control of alternative splicing regulatory networks by transcription factors. *Mol. Cell* **65**, 539–553 (2017). e537.
43. Katz, Y., Wang, E. T., Airoldi, E. M. & Burge, C. B. Analysis and design of RNA sequencing experiments for identifying isoform regulation. *Nat. Methods* **7**, 1009–1015 (2010).
44. Xiao, X. et al. Splice site strength-dependent activity and genetic buffering by poly-G runs. *Nat. Struct. Mol. Biol.* **16**, 1094–1100 (2009).
45. Gueroussov, S. et al. Regulatory expansion in mammals of multivalent hnRNP assemblies that globally control alternative splicing. *Cell* **170**, 324–339 (2017). e323.
46. Conlon, E. G. et al. The C9ORF72 GGGGCC expansion forms RNA G-quadruplex inclusions and sequesters hnRNP H to disrupt splicing in ALS brains. *eLife* **5**, e17820 (2016).
47. Dardenne, E. et al. RNA helicases DDX5 and DDX17 dynamically orchestrate transcription, miRNA, and splicing programs in cell differentiation. *Cell Rep.* **7**, 1900–1913 (2014).
48. Decorsiere, A., Cayrel, A., Vagner, S. & Millevoi, S. Essential role for the interaction between hnRNP H/F and a G quadruplex in maintaining p53 pre-mRNA 3'-end processing and function during DNA damage. *Genes Dev.* **25**, 220–225 (2011).
49. Fisette, J. F., Montagna, D. R., Mihailescu, M. R. & Wolfe, M. S. A G-rich element forms a G-quadruplex and regulates BACE1 mRNA alternative splicing. *J. Neurochem.* **121**, 763–773 (2012).
50. Singh, B. & Eyras, E. The role of alternative splicing in cancer. *Transcription* **8**, 91–98 (2017).
51. Supek, F., Minana, B., Valcárcel, J., Gabaldon, T. & Lehner, B. Synonymous mutations frequently act as driver mutations in human cancers. *Cell* **156**, 1324–1335 (2014).
52. Lu, Y., Yao, H. P. & Wang, M. H. Multiple variants of the RON receptor tyrosine kinase: biochemical properties, tumorigenic activities, and potential drug targets. *Cancer Lett.* **257**, 157–164 (2007).
53. Gartner, J. J. et al. Whole-genome sequencing identifies a recurrent functional synonymous mutation in melanoma. *Proc. Natl Acad. Sci. USA* **110**, 13481–13486 (2013).
54. Gotea, V., Gartner, J. J., Qutob, N., Elnitski, L. & Samuels, Y. The functional relevance of somatic synonymous mutations in melanoma and other cancers. *Pigment. Cell Melanoma Res.* **28**, 673–684 (2015).
55. Jung, H. et al. Intron retention is a widespread mechanism of tumor-suppressor inactivation. *Nat. Genet.* **47**, 1242–1248 (2015).
56. Yao, H. P., Zhou, Y. Q., Zhang, R. & Wang, M. H. MSP-RON signalling in cancer: pathogenesis and therapeutic potential. *Nat. Rev. Cancer* **13**, 466–481 (2013).
57. O'Toole, J. M. et al. Therapeutic implications of a human neutralizing antibody to the macrophage-stimulating protein receptor tyrosine kinase (RON), a c-MET family member. *Cancer Res.* **66**, 9162–9170 (2006).
58. Rauch, J. et al. c-Myc regulates RNA splicing of the A-Raf kinase and its activation of the ERK pathway. *Cancer Res.* **71**, 4664–4674 (2011).
59. Williams, R. et al. Amplification of complex gene libraries by emulsion PCR. *Nat. Methods* **3**, 545-550 (2006).
60. Sutandy, F. X. R., Hildebrandt, A. & König, J. Profiling the binding sites of RNA-binding proteins with nucleotide resolution using iCLIP. *Methods Mol. Biol.* **1358**, 175–195 (2016).
61. Dobin, A. et al. STAR: ultrafast universal RNA-seq aligner. *Bioinformatics* **29**, 15–21 (2013).

62. Bolger, A. M., Lohse, M. & Usadel, B. Trimmomatic: a flexible trimmer for Illumina sequence data. *Bioinformatics* **30**, 2114–2120 (2014).
63. Sedlazeck, F. J., Rescheneder, P. & von Haeseler, A. NextGenMap: fast and accurate read mapping in highly polymorphic genomes. *Bioinformatics* **29**, 2790–2791 (2013).
64. Van der Auwera, G. A. et al. From FastQ data to high confidence variant calls: the Genome Analysis Toolkit best practices pipeline. *Curr. Protoc. Bioinformatics* **43**, 11–33 (2013). 11 10.
65. Whitlock, M. C. Combining probability from independent tests: the weighted Z-method is superior to Fisher's approach. *J. Evol. Biol.* **18**, 1368–1373 (2005).
66. Pollard, K. S., Hubisz, M. J., Rosenbloom, K. R. & Siepel, A. Detection of nonneutral substitution rates on mammalian phylogenies. *Genome Res.* **20**, 110–121 (2010).
67. Vivian, J. et al. Toil enables reproducible, open source, big biomedical data analyses. *Nat. Biotechnol.* **35**, 314–316 (2017).
68. Mootha, V. K. et al. PGC-1alpha-responsive genes involved in oxidative phosphorylation are coordinately downregulated in human diabetes. *Nat. Genet.* **34**, 267–273 (2003).
69. Subramanian, A. et al. Gene set enrichment analysis: a knowledge-based approach for interpreting genome-wide expression profiles. *Proc. Natl Acad. Sci. USA* **102**, 15545–15550 (2005).

Acknowledgements

The authors would like to thank the members of all participating labs for their support and discussion. We gratefully acknowledge the Institute of Molecular Biology Core Facilities for their support, especially the Genomics and the Bioinformatics Core Facilities, and the use of the Illumina NextSeq 500 instrument (INST 47/870-1 FUGG) as well as Teresa Maia (NMorais Lab, iMM) for assistance with TCGA data retrieval and analyses and Tina Han for help and technical support. We would like to thank Guiseppe Biamonti and Heiner Schaal for advice on the *RON* minigene. The results published here are in part based upon data generated by TCGA managed by the NCI and NHGRI. Information about TCGA can be found at http://cancergenome.nih.gov. This work was funded by a joint DFG grant (ZA 881/2-1 to K.Z., KO 4566/4-1 to J.K. and LE 3473/2-1 to S.L.). K.Z. was also supported by the LOEWE program Ubiquitin Networks (Ub-Net) of the State of Hesse (Germany) and the Deutsche Forschungsgemeinschaft (SFB902 B13). N. Barbosa-Morais' laboratory is supported by EMBO (Installation Grant 3057) and Fundação para a Ciência e a Tecnologia, Portugal (FCT Investigator Starting Grant IF/00595/2014). S.L. acknowledges support by the German Federal Ministry of Research (BMBF; e:bio junior group program, FKZ: 0316196). The Institute of Molecular Biology (IMB) gGmbH is funded by the Boehringer Ingelheim Foundation.

Author contributions

S.B. established the high-throughput screening approach and performed most experiments. S.T.S. performed most bioinformatics analyses. M.E. and S.L. designed the mathematical modelling approach and performed the analyses. M.C.-L. annotated putative RBP binding sites and analysed mutation effects and synergistic interactions. M. S. contributed to the RNA sequence annotation. B.P.d.A. and N.L.B.-M. performed the analyses of the TCGA and GTEx data sets. F.X.R.S. performed iCLIP experiments, and L. S. did validation experiments. A.B. performed iCLIP and RNA-seq data processing as well as splice isoform quantification. S.E. and K.Z. supervised the bioinformatics analyses. J.K. conceived the project and supervised the experimental work. S.B., S.L., J.K. and K.Z. wrote the manuscript with help and comments from all co-authors.

Additional information

Supplementary Information accompanies this paper at https://doi.org/10.1038/s41467-018-05748-7.

Competing interests: The authors declare no competing interests.

Decoding a cancer-relevant splicing decision in the *RON* proto-oncogene using high-throughput mutagenesis

SUPPLEMENTARY INFORMATION

Braun et al.

Content:

Supplementary Notes

In these Supplementary Notes, we describe how we used mathematical modelling to infer the effect of single mutations on the splicing outcome. We employed a two-step modelling strategy in which we first calculate changes in splicing reactions from the isoform frequency using a dynamical model (Supplementary Note 1). In the second step, we describe the splice change in each minigene variant harbouring multiple mutations as a linear combination of single mutation effects, and estimate these single effects using a regression approach (Supplementary Note 2). Finally, we compare single mutation effects for control and *HNRNPH* knockdown conditions to identify synergistic interactions between these two types of perturbations (Supplementary Note 3).

Supplementary Note 1: Dynamic model of splicing reactions

We modelled the dynamics of splicing using a set of ordinary differential equations, in which concentrations of transcript intermediates are determined by production and degradation terms. The precursor mRNA (pre-mRNA) x_0 is produced at a constant rate c and spliced into different splice products with linear kinetics and rates r_i, leading to

$$\frac{dx_0}{dt} = \mathrm{c} - (r_1 + r_2 + r_3 + r_4 + r_5 + r_6)x_0. \qquad (1)$$

Additional differential equations describe the dynamics of the spliced isoforms:

$$\frac{dx_i}{dt} = r_i x_0 - d_i x_i, i = 1,\ldots,6. \qquad (2)$$

where $x_1 \ldots, x_5$ are the number of transcripts representing the alternative exon (AE) inclusion, AE skipping, full intron retention (IR), first IR and second IR isoforms. The additional non-canonical isoforms that were also measured are integrated in the model together by the species x_6, collectively referred to as 'other'. Furthermore, d_i are the degradation rates of the different isoforms.

The steady state found by setting dx_i/dt to zero in Supplementary Equations 2 reads $x_i = (r_i/d_i)x_0$. The measured isoform frequencies p_i correspond in the model to the fractions of the transcripts x_i within the total mRNA:

$$p_i = \frac{x_i}{x_0+x_1+x_2+x_3+x_4+x_5+x_6}, i = 1,2,4,5,6. \qquad (3)$$

For the frequency p_3 of mRNA transcripts that exhibit the complete sequence, we sum up the number of mRNA transcripts with full intron retention x_3 and the number of unspliced pre-mRNA transcripts x_0, since these two species were experimentally not differentiated. Thus, we get

$$p_3 = \frac{x_0+x_3}{x_0+x_1+x_2+x_3+x_4+x_5+x_6}. \qquad (4)$$

At steady state, we obtain from Supplementary Equations 1-4

$$p_i = \frac{K_i}{K_1+K_2+K_3+K_4+K_5+K_6}, i = 1,\ldots,6. \qquad (5)$$

where we introduced the parameters $K_i = r_i/d_i$, $i = 1,2,4,5,6$ for the isoforms involving splicing and $K_3 = 1 + r_3/d_3$ for the unspliced full IR isoform.

We remark that due to the normalisation condition $\sum_{i=1}^{6} p_i = 1$, not all model parameters K_i can be determined from the experimental data, but only ratios of K_i with respect to a reference isoform. If we normalise all K_i by the AE inclusion rate, we can determine the ratios K_i/K_1, $i = 2,\ldots,6$ from the measured isoform frequencies via $K_i/K_1 = p_i/p_1$.

1.1 *In silico* simulation of competing splicing reactions

Supplementary Equation 5 reflects the non-linear nature of the splicing system: For example, a perturbation affecting the splicing parameter K_2 will affect all transcript isoform frequencies $p_i$if $K_2$is large compared to other parameters, but not otherwise. In contrast, the splice isoform ratios respond in the same way to a perturbation affecting the splicing parameter K_2, irrespective of the other parameter values.

We confirmed that perturbation-induced fold-changes in the isoform frequencies, but not isoform ratios, depend on the mutational background by numerically simulating the steady state of the splicing system (Supplementary Equations 1 and 2). Random mutagenesis (i.e., the varying mutational background) was mimicked by uniformly sampling parameters c, $r_i, d_i, i = 1, \ldots, 6$ in logarithmic space within the range [0.1,10], and calculating the steady state for 5,000 different realisations. Subsequently, each parameter set was additionally perturbed by decreasing the parameter r_2 at 20% of the sampled value (representing an additional mutation or knockdown), and the new steady state was calculated. As expected from the inspection of the steady states given in Supplementary Equation 5, the effect of the perturbation on splice isoforms frequencies is nonlinear and strongly depends on the specific parameter values, i.e., the mutational background (**Supplementary Fig. 7e**).

In contrast, the perturbation of r_2 has a linear effect on the splice isoform ratios in the sense that the fold-change between perturbed and unperturbed steady states is the same for all parameter sets (**Supplementary Fig. 7e**). Therefore, a mutation (or knockdown) affecting splicing kinetics induces the same fold change of an isoform ratio, irrespective of the presence of other mutations in the minigene. Thus, perturbation effects on splice isoform ratios show additive behaviour in log-space and are therefore more suitable for the regression approach described below.

Supplementary Note 2: Inference of single mutation effects

2.1 Calculation of single mutation effects by linear regression

By analysing the cumulative mutational effects in minigenes containing two or three mutations that are also present as single mutations in other minigenes, we found that the effects of single mutations on the above defined splicing rates are in general multiplicative (**Supplementary Fig. 4a**). Thus, we assume that the splicing parameter K_i for a minigene exhibiting a combination of several mutations is given by

$$K_i^{\text{mutated}} = K_i^{\text{wild type}} m_i^1 m_i^2 \dots m_i^n, \qquad (6)$$

where n is the number of the mutations in the minigene and m_i^k the effect of the k-th mutation on K_i.

Using the same normalisation to the AE inclusion isoform as in Supplementary Note 1, and taking the logarithm of Supplementary Equation 6 leads to

$$\sum_{k=1}^{n} \log \frac{m_i^k}{m_1^k} = \log \frac{p_i}{p_1} - \log \frac{p_i^{\text{wt}}}{p_1^{\text{wt}}}, i = 2, \dots, 6, \qquad (7)$$

where p_i and $p_i^{\text{wt}}, i = 1, \dots, 6$ are the isoform frequencies of the mutated and wild type (wt) *RON* minigenes, respectively. The isoform frequencies for the wt *RON* minigene were calculated as the median of the measured values across the minigenes exhibiting the wt sequence (586 minigene variants present in all RNA-seq replicates).

By considering all minigene variants together, we get a system of linear equations for the mutational effects $x_i(k) = \log\left(m_i^k / m_1^k\right), i = 2, \dots, 6, k = 1, \dots, N$, where N is the total number of mutations present in the dataset. For each of the five splice isoform ratios K_i/K_1, we get a separate system of linear equations which can be written in the matrix form:

$$A\mathbf{x}_i = \mathbf{b}_i, i = 2, \dots, 6. \qquad (8)$$

The entries of the matrix are $A(j,k) = 1/0$ if mutation k is present/absent in minigene variant j, respectively. The vectors $\mathbf{b}_i$ contain the experimental observations which are given by

$$b_i(j) = \log \frac{p_i^j}{p_1^j} - \log \frac{p_i^{\text{wt}}}{p_1^{\text{wt}}}, i = 2, \dots, 6, j = 1, \dots, m, \qquad (9)$$

with m being the number of unique combinations of mutations included in the calculation (between 4,467 and 4,771, depending on the cell line and replicate, see **Supplementary Table 1**).

Since any minigene contains only a few of the total unique 2,042 mutations present in the whole dataset (up to 18 mutations, with a mean of 3.7 mutations/minigene including insertions and deletions), the systems to be solved are sparse. To get the single mutational effects $x_i(k)$, we solved the systems in Supplementary Equations 8 in least square sense using Matlab subroutine lscov.

From the estimated mutational effects $x_i(k)$, a model prediction for the isoform frequencies p_i^k in a minigene containing the single mutation k can be made: For the single-mutation minigene, we would have

$$\frac{p_i^k}{p_1^k} = \frac{p_i^{\text{wt}}}{p_1^{\text{wt}}} \mathrm{e}^{x_i(k)}, i = 2, \dots, 6. \qquad (10)$$

By summing up Supplementary Equations 10 and using the normalisation condition $\sum_{i=1}^{6} p_i^k = 1$, we therefore get

$$\frac{1-p_1^k}{p_1^k} = \sum_{i=2}^{6} \frac{p_i^{\mathrm{wt}}}{p_1^{\mathrm{wt}}} \mathrm{e}^{x_i(k)}, \qquad (11)$$

which can be solved to find the AE inclusion isoform frequency p_1^k as a function of the single mutation effects:

$$p_1^k = \frac{1}{1+\sum_{i=2}^{6} \frac{p_i^{\mathrm{wt}}}{p_1^{\mathrm{wt}}} \mathrm{e}^{x_i(k)}} = \frac{p_1^{\mathrm{wt}}}{p_1^{\mathrm{wt}} + \sum_{i=2}^{6} p_i^{\mathrm{wt}} \mathrm{e}^{x_i(k)}}. \qquad (12)$$

Finally, the remaining isoform frequencies can be estimated via:

$$p_i^k = p_1^k \frac{p_i^{\mathrm{wt}}}{p_1^{\mathrm{wt}}} \mathrm{e}^{x_i(k)} = \frac{p_i^{\mathrm{wt}} \mathrm{e}^{x_i(k)}}{p_1^{\mathrm{wt}} + \sum_{i=2}^{6} p_i^{\mathrm{wt}} \mathrm{e}^{x_i(k)}}, i = 2, \ldots, 6. \quad (13)$$

Supplementary Equations 8 and 9 were used to infer the effects of single mutations from the data. Different replicates were treated separately, since both wt and mutated minigene variants showed systematic shifts in the measured frequencies between replicates. Thus, we always calculate mutational effects by comparing isoform frequencies of mutated and wt minigenes within the same replicate.

We note that the library also contains some minigenes with different barcodes but the same combination of mutations. We have included such combinations of mutations only once and attributed to them the median of the measured isoforms frequencies over the different minigenes with the same combination of mutations. Thus, the number of unique combinations of mutations is smaller than the number of mutated minigene variants (i.e. unique barcodes) in the dataset (**Supplementary Table 1**). Furthermore, we have excluded barcodes containing ambiguous mutations from the calculation.

The predictive power of our modelling approach was confirmed using cross-validation (also see Methods; **Supplementary Fig. 6**), and by comparing the inferred splicing outcome in response to single mutations (according to Supplementary Equations 11 and 12) to RT-PCR measurements of previously untested minigenes containing only these single mutations (see main manuscript; **Fig. 2d**).

It should be noted that certain minigenes had to be excluded from the linear regression procedure because they deviated from linear behaviour: (i) Minigenes simultaneously harbouring two splice site mutations: these minigenes show a very similar distribution of inclusion frequencies as minigenes containing only one of these mutations (**Supplementary Fig. 7f**). The median inclusion frequency of both, one- and two-splice-site-mutation minigenes, was non-zero (0.7%). The apparent lack-of-effect of secondary splice site mutations at non-zero inclusion frequencies contradicts their strong effect as isolated splice site mutations, and introduces strong inconsistencies and biases in linear regression. In our opinion, this observation hints to a constant background signal, e.g., due to leaky sequencing reads originating from other minigenes where inclusion is the predominant isoform. Therefore, we excluded minigenes exhibiting any two mutations at positions proximal to splice sites (positions 210-212, 295-297, 443-446, 522-524, 689-691). (ii) Minigenes with strong activation of cryptic splice sites: The activation of cryptic splice sites by mutations leads to the generation of a plethora of new splicing products ('other') which behave heterogeneously and cannot be considered in our model. Therefore, we performed first the regression on the complete dataset and subsequently excluded the minigenes containing

mutations that were predicted to exhibit an increased 'other' isoform frequency $p_6 > 4p_6^{\mathrm{wt}}$ in this first run. The threshold used for the exclusion of minigenes from the regression dataset was four times the median p_6^{wt} of the 'other' isoform frequency for the wt minigenes, and thus cell line and replicate-specific. The final calculation of mutational effects was performed on this reduced dataset (**Supplementary Table 1**). As an alternative approach to estimate the mutation effects of the excluded mutations, we calculated the median of isoform frequencies for all minigene variants harbouring the given mutation (**Supplementary Data 3**).

Depending on the replicate and cell line, between 3-9% of the unique combinations of mutations were excluded from the calculations based on the above criteria (**Supplementary Table 1**). Still, the effects of 94-97% of the mutations present in the library could be assessed by regression that covered almost the entire length of the minigene (all but 3-4 out of all 679 nucleotides in the minigene).

2.2 Comparative analysis of linear regression approaches

As described above, kinetic modelling suggested that fitting to splice isoform ratios is most suitable for linear regression. To support this claim, we tested two alternative regression approaches for the inference of single mutation effects, both of which were based on direct fitting to splice isoform frequencies. Reassuringly, our isoform ratio-based approach outperformed these alternative methods.

First, we assumed that the mutation effects add up at the level of splice isoform frequencies (not at the level of ratios). Thus, we used

$$\sum_{k=1}^{n} \log m_i^k = \log p_i - \log p_i^{\mathrm{wt}}, i = 1,\ldots,6 \qquad (14)$$

instead of Supplementary Equation 7 for the computation of the single mutation effects m_i^k. The corresponding isoform frequencies for the single mutation minigene k then read

$$p_i^k = p_i^{\mathrm{wt}} m_i^k, i = 1,\ldots,6. \qquad (15)$$

Supplementary Equation 14 was solved in least square sense using the Matlab subroutine fmincon with the constraint that all isoform frequencies in a single mutation background are bounded to unity, i.e., $\sum_{i=1}^{6} p_i^k = 1, k = 1,\ldots,N$. During cross-validation, predictions for new combinations of mutations were given by

$$p_i = p_i^{\mathrm{wt}} m_i^1 m_i^2 \ldots m_i^n, i = 1,\ldots,6, \qquad (16)$$

where $m_i^1,\ldots,m_i^n$ are the infered single mutation effects, and $1,\ldots,n$ the mutations present in the new combined minigene. We have compared the prediction performance of this method to the isoform ratio-based regression in 10-fold cross-validation and found that the use of isoform frequencies instead of ratios is inferior in terms of the prediction-data correlation. The corresponding Pearson correlation coefficients between model-predicted isoform frequencies and measured values for each predicted subset not used in fitting are visualised in **Supplementary Fig. 7b**. The predictions of the frequency-based model were in many cases also qualitatively wrong, as isoform frequencies of minigenes were not bounded to 1, thus leading to mispredictions $p_i > 1$, especially for the AE skipping isoform. In contrast, the calculation of isoform frequencies by renormalisation of the ratio-based regression results (Supplementary Equations 12 and 13) inherently prevents such biologically unreasonable mispredictions.

As a second alternative approach, we used multinomial logistic regression to infer the isoform frequencies in single-mutation minigenes. In this case, the dataset was categorised by introducing

six copies of each minigene and assuming as splicing output a different isoform for each of the copies. The data was weighted by the measured isoform frequencies, so each of the six samples corresponding to one minigene got as weight the measured frequency of its output isoform. We used the Python package scikit-learn with cross entropy loss and L2 regularisation to infer the probabilities for each splicing isoform for single-mutation minigenes and minigenes with new combinations of mutations. The prediction performance of this method in 10-fold cross-validation was also inferior to the isoform ratios-based regression, as shown in **Supplementary Fig. 7a**.

2.3 Estimation of the prediction error of the model

The prediction accuracy for a single mutation effect depends on the occurrence of the mutation in the minigene library. To quantitatively benchmark the accuracy of our model, we focused on ~600 mutations whose effects have been measured directly in our dataset as minigenes containing single mutations.

Benchmarking was done by eliminating the corresponding single-mutation minigenes from the dataset (separately for each of these mutations) and repeating the linear regression for the remaining data, or after removing further minigenes containing this mutation. This procedure allowed us to estimate how the prediction error depends on the occurrence of a mutation in the minigene library.

After calculating the single mutation effects, the isoform frequencies were estimated (Supplementary Equations 12 and 13) and the values for the mutations of interest were compared to the measured isoform frequencies of the single-mutation minigene. We find that the standard deviation of the prediction error (over all mutations and permutations) decreases with the occurrence of the mutation in the subset used in linear regression by $1/\sqrt{\text{occurrence}}$ (see main manuscript; **Fig. 2c**).

This relationship can also be proven analytically by exploiting the profile likelihood which characterises the measurement-compliant range for each parameter value in the model (Raue et al., 2009). The agreement of the experimental data $\mathbf{b}_i$ with the model simulations $\mathbf{x}_i$ is measured by the sum of squared residuals:

$$\chi_i^2(\mathbf{x}_i) = \|A\mathbf{x}_i - \mathbf{b}_i\|^2 = \sum_{j=1}^{m}[\sum_{k=1}^{N} A\,(j,k)x_i(k) - b_i(j)]^2. \qquad (17)$$

The optimal values $\widehat{\mathbf{x}_i}$ of the model parameters estimated by linear regression minimise the objective functions χ_i^2, thus we have

$$\boldsymbol{\nabla}\chi_i^2(\widehat{\mathbf{x}_i}) = 2(A\mathbf{x}_i - \mathbf{b}_i)^{\mathrm{T}}A = 0. \qquad (18)$$

The confidence interval for a certain parameter $x_i(k)$ can be derived from the curvature of the objective functions, for example by calculating the Hessian matrices $H_i = \boldsymbol{\nabla}^{\mathrm{T}}\boldsymbol{\nabla}\chi_i^2(\widehat{\mathbf{x}_i})$. We find

$$H_i = 2A^{\mathrm{T}}A. \qquad (19)$$

The matrix A indicates the presence/absence of a particular mutation in a particular minigene variant, i.e. $A(j,k) = 1$ if mutation k is found in minigene variant j and $A(j,k) = 0$ otherwise. We therefore get for the diagonal elements of $A^{\mathrm{T}}A$

$$(A^{\mathrm{T}}A)_{kk} = \sum_{j=1}^{m} A\,(j,k)A(j,k) = \text{occurrence}(k). \quad (20)$$

which is equal to the number of minigene variants that exhibit the mutation k. For the non-diagonal elements of $A^{\mathrm{T}}A$, we get

$$(A^T A)_{kl} = \sum_{j=1}^{m} A\,(j,k)A(j,l) = \text{occurrence}(k,l), k \neq l, \quad (21)$$

which is equal to the number of minigenes that simultaneously exhibit the mutations k and l.

Therefore, the Taylor expansion of the objective function χ_i^2 around the minimum $\chi_i^2(\hat{\mathbf{x}}_i)$ is up to the second order given by

$$\chi_i^2(\mathbf{x}_i) = \chi_i^2(\hat{\mathbf{x}}_i) + \sum_{k=1}^{N} \text{occurrence}\,(k)[x_i(k) - \hat{x}_i(k)]^2 + \sum_{k=1}^{N}\sum_{l=1,l\neq k}^{N} \text{occurrence}\,(k,l)[x_i(k) - \hat{x}_i(k)][x_i(l) - \hat{x}_i(l)]. \quad (22)$$

Supplementary Equation 22 can be used to find the confidence intervals for the model parameters calculated by regression. For a given value of the parameter $x_i(k_0) = \hat{x}_i(k_0) + \delta_0$, the remaining parameters $x_i(k \neq k_0)$ can be refitted. Introducing $x_i(k) = \hat{x}_i(k) + \delta_k, k \neq k_0$ and using Supplementary Equation 18 for $k \neq k_0$ leads to a reduced system of equations for $\delta_{k\neq k_0}$, that can be written in matrix form as

$$C_{k_0}\left(\delta_1,\ldots,\delta_{k_0-1},\delta_{k_0+1},\ldots,\delta_N\right)^{\mathrm{T}} = -\mathbf{c}_{k_0}^{\mathrm{T}}\delta_0. \quad (23)$$

Thereby, the symmetric matrix C_{k_0} is found by deleting the k_0th row and column from $A^{\mathrm{T}}A$, thus

$$C_{k_0} = (A^{\mathrm{T}}A)(k,l), k \neq k_0, l \neq k_0. \quad (24)$$

Furthermore, the vector $\mathbf{c}_{k_0}$ contains the nondiagonal elements of the k_0th row of $A^{\mathrm{T}}A$:

$$\mathbf{c}_{k_0} = [\text{occurrence}(k_0,1),\ldots.,\text{occurence}(k_0,k_0-1),\text{occurrence}(k_0,k_0+1),\ldots.,\text{occurrence}(k_0,N)]^T. \quad (25)$$

Solving Supplementary Equation 23 leads to the optimal values for the parameters $\delta_{k\neq k_0}$:

$$\left(\delta_1,\ldots,\delta_{k_0-1},\delta_{k_0+1},\ldots,\delta_N\right)^{\mathrm{T}} = -C_{k_0}^{-1}\mathbf{c}_{k_0}\delta_0. \quad (26)$$

Introducing these solutions in Supplementary Equation 22 and regrouping the terms gives us

$$\chi_i^2(\delta_0) = \chi_i^2(\hat{\mathbf{x}}_i) + \text{occurrence}(k_0)\delta_0^2 + \sum_{k=1,k\neq k_0}^{N} \text{occurrence}\,(k_0,k)\delta_0\delta_k + \sum_{k=1,k\neq k_0}^{N}\sum_{l=1,l\neq k_0}^{N} \text{occurrence}\,(k,l)\delta_l\delta_k. \quad (27)$$

By using the above notations in Supplementary Equations 23 and 25 as well as Supplementary Equation 26, we find

$$\sum_{k=1,k\neq k_0}^{N} \text{occurrence}\,(k_0,k)\delta_0\delta_k = \mathbf{c}_{k_0}^{\mathrm{T}}\delta_0\left[-C_{k_0}^{-1}\mathbf{c}_{k_0}\delta_0\right] = -\mathbf{c}_{k_0}^{\mathrm{T}}C_{k_0}^{-1}\mathbf{c}_{k_0}\delta_0^2 \quad (28)$$

and

$$\sum_{k=1,k\neq k_0}^{N}\sum_{l=1,l\neq k_0}^{N} \text{occurrence}\,(k,l)\delta_l\delta_k = \left(\delta_{k\neq k_0}\right)^{\mathrm{T}} C_{k_0}\left(\delta_{k\neq k_0}\right) = \left[C_{k_0}^{-1}\mathbf{c}_{k_0}\right]^T C_{k_0}C_{k_0}^{-1}\mathbf{c}_{k_0}\delta_0^2 = \mathbf{c}_{k_0}^{\mathrm{T}}C_{k_0}^{-1}\mathbf{c}_{k_0}\delta_0^2. \quad (29)$$

where we used the symmetry $C_{k_0}^{\mathrm{T}} = C_{k_0}$. Introducing Supplementary Equations 28 and 29 in Supplementary Equation 27 finally gives us the variation of the objective function with δ_0:

$$\chi_i^2(\delta_0) = \chi_i^2(\hat{\mathbf{x}}_i) + \text{occurrence}(k_0)\delta_0^2. \quad (30)$$

Supplementary Equation 30 defines a parable with the minimal value $\chi^2(\hat{\mathbf{x}}_i)$ having the curvature $2\text{occurrence}(k_0)$. Thus, the more frequent the mutation k_0 is in the dataset, the steeper is the

parable and more constrained is the model parameter corresponding to this mutation. Setting a confidence threshold th for the objective function, e.g. imposing $\chi_i^2(\mathbf{x}_i) < \chi_i^2(\widehat{\mathbf{x}}_i) + \mathrm{th}$, defines a confidence interval with respect to variation of the parameter $x_i(k_0)$ given by

$$|x_i(k_0) - \widehat{x}_i(k_0)| < \sqrt{\frac{\mathrm{th}}{\mathrm{occurrence}(k_0)}}, \qquad (31)$$

which confirms the result obtained numerically by validation with the single-mutation minigenes (see main manuscript; **Fig. 2c**).

Supplementary Note 3: Model analysis of *HNRNPH* knockdown effects

We compared the effect of *HNRNPH* knockdown (KD) on wt and mutant minigene variants to identify synergistic interactions between both types of perturbations that may hint to the strengthening or weakening of HNRNPH binding sites by mutations (**Fig. 5a**). Using linear regression, we sought to trace back these synergistic interactions between mutations and *HNRNPH* KD to the single mutation level.

We initially checked the validity of our splice rate model (**Supplementary Fig. 3a**; see Supplementary Note 1) for the *HNRNPH* KD data: In the primary data, the fold-change in each isoform frequency upon *HNRNPH* KD is not stable and depends on the baseline value of the mutated minigene variant under non-targeting control conditions (**Supplementary Fig. 13a**). This can be understood from Supplementary Equation 5, in which a KD affecting a splice rate K_i has a strong (linear) effect or a weak (less than linear) effect depending on how K_i relates to the other competing splice rates $K_{j\neq i}$. To correct for this effect and to facilitate linear regression modelling, we therefore employed ratios of splice isoform frequencies, which show a similar effect (fold-change) of the *HNRNPH* KD for the majority of minigenes (**Fig. 5b**, right, and **Supplementary Fig. 13b**). This can be explained as follows: If for all minigenes, the splice parameters in the *HNRNPH* KD $\bar{K}_i$ relate to the control splice parameters K_i by the same, isoform and KD-specific factors α_i

$$\bar{K}_i = \alpha_i K_i, i = 1,\dots,6, \qquad (32)$$

then the isoform ratios $\bar{p}_i/\bar{p}_1$ and p_i/p_1 in *HNRNPH* KD and control conditions will also be related by the factors α_i/α_1, independent of splice-rate competition effects. This suggests that the splice model is able to correct for nonlinearities in the data, thereby facilitating the identification of true synergistic interactions.

Large discrepancies from the linear behaviour in Supplementary Equation 32 imply that a particular minigene variant reacts differently than the majority of the library to the *HNRNPH* KD, pointing to a change in a binding site of HNRNPH itself or other means that enhance or repress its function (positive or negative synergy). We used modelling to identify such synergistic interactions of sequence mutations and *HNRNPH* KD at single-nucleotide resolution. Instead of calculating KD-induced fold-changes per minigene, we employed linear regression modelling to infer single mutation effects before comparing KD effects on wt minigenes and individual mutations.

By the linear regression setup (see Supplementary Note 2), we can determine the mutational effects of single mutations in control $x_i(k)$ and KD $\bar{x}_i(k)$ conditions. According to our model, we have

$$\frac{\bar{K}_i^k}{\bar{K}_1^k} = \frac{\bar{K}_i^{\mathrm{wt}}}{\bar{K}_1^{\mathrm{wt}}} \mathrm{e}^{\bar{x}_i(k)}, \frac{K_i^k}{K_1^k} = \frac{K_i^{\mathrm{wt}}}{K_1^{\mathrm{wt}}} \mathrm{e}^{x_i(k)}, i = 2,\dots 6, k = 1,\dots,N. \qquad (33)$$

Using Supplementary Equation and assuming the same KD factors α_i on both mutated and wt minigenes, we get

$$\frac{\bar{K}_i^k}{\bar{K}_1^k} = \frac{\alpha_i}{\alpha_1}\frac{K_i^k}{K_1^k}, \frac{\bar{K}_i^{\mathrm{wt}}}{\bar{K}_1^{\mathrm{wt}}} = \frac{\alpha_i}{\alpha_1}\frac{K_i^{\mathrm{wt}}}{K_1^{\mathrm{wt}}}, i = 2,\dots 6, k = 1,\dots,N. \quad (34)$$

From Supplementary Equations 33 and 34, we find

$$\frac{\bar{K}_i^k}{\bar{K}_1^k} = \frac{\bar{K}_i^{\mathrm{wt}}}{\bar{K}_1^{\mathrm{wt}}} \mathrm{e}^{\bar{x}_i(k)} = \frac{\alpha_i}{\alpha_1}\frac{K_i^{\mathrm{wt}}}{K_1^{\mathrm{wt}}} \mathrm{e}^{\bar{x}_i(k)}, \qquad (35)$$

and

$$\frac{\bar{K}_i^k}{\bar{K}_1^k} = \frac{\alpha_i}{\alpha_1}\frac{K_i^k}{K_1^k} = \frac{\alpha_i}{\alpha_1}\frac{K_i^{\mathrm{wt}}}{K_1^{\mathrm{wt}}}\mathrm{e}^{x_i(k)}. \qquad (36)$$

By comparing Supplementary Equations 35 and 36 we conclude that the mutation effects $x_i(k)$ should not change significantly between control and KD conditions, e.g.

$$\bar{x_i}(k) = x_i(k) \qquad (37)$$

should be valid for all mutations present in minigenes that react to the *HNRNPH* KD similarly to the wt minigenes. By contrast, above-average deviations from Supplementary Equation 37 are expected for mutations present in minigenes that react non-linearly to the KD.

We used *z*-scores to quantify to what extent a mutation shows different effects under control and *HNRNPH* KD conditions:

$$z_i^{\mathrm{kd}}(k) = \frac{x_i(k) - \bar{x_i}(k)}{\delta_i^{\mathrm{wt}}}, i = 2,\ldots,6, k = 1,\ldots,N. \qquad (38)$$

Due to the additivity of perturbation effects, this *z*-score can be interpreted to reflect differential *HNRNPH* KD effects in wt vs. single mutant backgrounds, allowing us to formulate positive and negative synergy as stronger or weaker KD responses in mutants compared to wt (see **Fig. 5b** and main text). In these *z*-scores, the difference between *HNRNPH* KD and control behaviour is normalised by the variation of KD effects in the wt minigenes to correct for experimental noise: Based on the wt minigenes present in both control and KD datasets, the standard deviation for the wt difference between control and KD conditions can be calculated by

$$\delta_i^{\mathrm{wt}} = \mathrm{STD}\left\{\log\frac{p_i^{\mathrm{wt}}}{p_1^{\mathrm{wt}}} - \log\frac{\bar{p}_i^{\mathrm{wt}}}{\bar{p}_1^{\mathrm{wt}}}\right\}, i = 2,\ldots 6. \qquad (39)$$

When calculating synergies between mutations and knockdowns using *z*-scores, the results may become unstable if one of the two perturbations already induces a close-to-maximal effect on the splice isoform frequencies. In fact, when analysing the variation of *z*-scores over the three replicates, we find that mutations that shift the inclusion frequency close to 0% increase the error in synergy *z*-score calculations and are thus potentially problematic. We show this effect in **Supplementary Fig. 7g**, in which we plot the uncertainty of the synergy *z*-score (standard deviation over the three replicates) against the (inferred) inclusion frequency in a single-mutation minigene.

Supplementary Tables 1 - 4

Supplementary Table 1: Information on the input and output data of the mathematical model on the different RNA-seq replicates.

	HEK293T			**MCF7 – control**			**MCF7 – *HNRNPH* KD**		
	Rep 1	Rep 2	Rep 3	Rep 1	Rep 2	Rep 3	Rep 1	Rep 2	Rep 3
General information									
Internal ID	imb_koenig_2015_13			imb_koenig_2016_07			imb_koenig_2016_08		
Initial reads	17,261,922	19,501,750	18,166,077	19,103,473	17,132,590	22,075,639	17,956,862	19,551,048	21,930,173
Minigenes	5,697	5,645	5,623	5,680	5,680	5,684	5,686	5,700	5,683
Wt minigenes	586	586	586	586	586	586	586	586	586
Unique mutation comb.	4,938	4,886	4,865	4,923	4,923	4,927	4,929	4,942	4,926
Model input									
Comb. used by model	4,571	4,467	4,472	4,672	4,678	4,650	4,763	4,771	4,739
Excluded comb.	367 (7%)	419 (9%)	393 (8%)	251 (5%)	245 (5%)	277 (6%)	166 (3%)	171 (3%)	187 (4%)
Singlets	606	603	603	612	608	609	613	613	613
Doublets	1,009	1,000	1,001	1,023	1,025	1,021	1,034	1,032	1,030
Triplets	869	859	858	891	888	886	910	909	905
Model output									
Mutations in dataset	2,042	2,033	2,032	2,038	2,040	2,041	2,039	2,042	2,040
Estimated mutation effects	1,942 (95%)	1,915 (94%)	1,915 (94%)	1,957 (96%)	1,956 (96%)	1,957 (96%)	1,972 (97%)	1,974 (97%)	1,974 (97%)
Positions in dataset	680	679	680	680	680	680	680	680	680
Estimated position effects	676 (99.4%)	675 (99.6%)	676 (99.4%)	677 (99.6%)	677 (99.6%)	677 (99.6%)	677 (99.6%)	677 (99.6%)	677 (99.6%)

For each RNA-seq replicate (Rep), the internal library identifier is given together with information on the number of total and wild type (wt) minigene variants detected in each dataset, the number of unique mutation combinations (differentiated into those used or excluded from the model analysis; see Supplementary Note 2) as well as the used single-/double-/triple-mutation combinations (singlets/doublets/triplets, respectively). Output information summarises the mutation and position effects that can be estimated by the model in relation to all mutations and mutated positions represented in each dataset.

Supplementary Table 2. Summary of splicing-effective mutations and synergistic interactions with *HNRNPH* knockdown per region in HEK293T and MCF7 cells.

		Exon 10	Intron 10	Exon 11	Intron 11	Exon 12	Intron 12	Total
HEK239T	**Mutations**	555	261	441	240	498	42	2037
	Measured	487 (87.7%)	224 (85.8%)	381 (86.4%)	190 (79.2%)	430 (86.3%)	35 (83.3%)	1747 (85.8%)
	Any isoform > 5%	**117** (24%)	**118** (52.7%)	**270** (70.9%)	**108** (56.8%)	**144** (33.5%)	**21** (60%)	**778** (44.5%)
	AE inclusion	100	111	263	87	92	19	672
	AE skipping	20	67	185	53	29	9	363
	First IR	2	6	3	0	4	2	17
	Second IR	0	1	0	3	6	10	20
	Full IR	70	74	107	79	113	16	459
	Other	0	0	2	4	1	0	7
	Any isoform > 10%	**26** (5.3%)	**66** (29.5%)	**159** (41.7%)	**54** (28.4%)	**45** (10.5%)	**12** (34.3%)	**362** (20.7%)
	Any isoform > 20%	**2** (0.4%)	**32** (14.3%)	**59** (15.5%)	**25** (13.2%)	**9** (2.1%)	**9** (25.7%)	**136** (7.8%)
	Positions	185	87	147	80	166	14	679
	Measured	184 (99.5%)	87 (100%)	147 (100%)	77 (96.2%)	166 (100%)	14 (100%)	675 (99.4%)
	Any isoform > 5%	**92** (50%)	**67** (77%)	**134** (91.2%)	**64** (83.1%)	**99** (59.6%)	**13** (92.9%)	**469** (69.5%)
	Any isoform > 10%	**25** (13.6%)	**42** (48.3%)	**97** (66%)	**33** (42.9%)	**39** (23.5%)	**7** (50%)	**243** (36%)
	Any isoform > 20%	**2** (1.1%)	**18** (20.7%)	**45** (30.6%)	**16** (20.8%)	**9** (5.4%)	**4** (28.6%)	**94** (13.9%)

(a) Splicing-effective mutations (top) and positions (bottom) in HEK293T cells. The total number of possible and measured mutations/positions are indicated first, followed by the number of significant effects when considering any isoform at three cutoffs (>5%, >10% and >20%). Mutation effects are additionally given for each individual isoform. AE - alternative exon; IR - intron retention. Related to Fig. 2e and Supplementary Fig. 8.

Supplementary Table 2 (continued). Summary of splicing-effective mutations and synergistic interactions with *HNRNPH* knockdown per region in HEK293T and MCF7 cells.

		Exon 10	Intron 10	Exon 11	Intron 11	Exon 12	Intron 12	Total
MCF7	**Mutations**	555	261	441	240	498	42	2037
	Measured	501 (90.3%)	229 (87.7%)	386 (87.5%)	196 (81.7%)	440 (88.4%)	35 (83.3%)	1787 (87.7%)
	Any isoform >5%	**150** (29.9%)	**149** (65.1%)	**300** (77.7%)	**137** (69.9%)	**264** (60%)	**22** (62.9%)	**1022** (57.2%)
	AE inclusion	81	115	260	99	91	16	662
	AE skipping	86	125	271	102	217	18	819
	First IR	5	14	5	3	6	0	33
	Second IR	1	2	12	7	15	11	48
	Full IR	79	63	62	82	185	16	487
	Other	3	2	8	14	13	0	40
	Any isoform > 10%	**41** (8.2%)	**88** (38.4%)	**202** (52.3%)	**76** (38.8%)	**100** (22.7%)	**14** (40%)	**521** (29.2%)
	Any isoform > 20%	**6** (1.2%)	**39** (17%)	**86** (22.3%)	**32** (16.3%)	**16** (3.6%)	**10** (28.6%)	**189** (10.6%)
	Positions	185	87	147	80	166	14	679
	Measured	185 (100%)	87 (100%)	147 (100%)	78 (97.5%)	166 (100%)	14 (100%)	677 (99.7%)
	Any isoform > 5%	**108** (58.4%)	**74** (85.1%)	**139** (94.6%)	**70** (89.7%)	**147** (88.6%)	**12** (85.7%)	**550** (81.2%)
	Any isoform > 10%	**36** (19.5%)	**52** (59.8%)	**112** (76.2%)	**48** (61.5%)	**74** (44.6%)	**8** (57.1%)	**330** (48.7%)
	Any isoform > 20%	**6** (3.2%)	**22** (25.3%)	**61** (41.5%)	**22** (28.2%)	**14** (8.4%)	**5** (35.7%)	**130** (19.2%)

(b) Splicing effective mutations (top) and positions (bottom) in MCF7 cells. Format as in (a).

Supplementary Table 2 (continued). Summary of splicing-effective mutations and synergistic interactions with *HNRNPH* knockdown per region in HEK293T and MCF7 cells.

		Exon 10	Intron 10	Exon 11	Intron 11	Exon 12	Intron 12	Total
MCF7 – synergistic interactions with *HNRNPH* knockdown	**Mutations**	555	261	441	240	498	42	2037
	Measured	501 (90.3%)	229 (87.7%)	385 (87.3%)	196 (81.7%)	440 (88.4%)	35 (83.3%)	1786 (87.7%)
	Any isoform $\|z\| > 2$	**70** (14%)	**35** (15.3%)	**135** (35.1%)	**51** (26%)	**58** (13.2%)	**5** (14.3%)	**354** (19.8%)
	AE skipping	37	21	100	17	39	1	215
	First IR	8	3	5	4	8	1	29
	Second IR	10	6	6	4	7	0	33
	Full IR	30	20	47	14	18	3	132
	Other	21	17	54	30	9	1	132
	Any isoform $\|z\| > 3$	**44** (8.8%)	**25** (10.9%)	**89** (23.1%)	**31** (15.8%)	**31** (7%)	**2** (5.7%)	**222** (12.4%)
	Any isoform $\|z\| > 5$	**10** (2%)	**3** (1.3%)	**35** (9.1%)	**7** (3.6%)	**11** (2.5%)	**0** (0%)	**66** (3.7%)
	Positions	185	87	147	80	166	14	679
	Measured	185 (100%)	87 (100%)	147 (100%)	78 (97.5%)	166 (100%)	14 (100%)	677 (99.7%)
	Any isoform $\|z\| > 2$	**61** (33%)	**28** (32.2%)	**93** (63.3%)	**38** (48.7%)	**54** (32.5%)	**4** (28.6%)	**278** (41.1%)
	Any isoform $\|z\| > 3$	**42** (22.7%)	**23** (26.4%)	**61** (41.5%)	**25** (32.1%)	**31** (18.7%)	**2** (14.3%)	**184** (27.2%)
	Any isoform $\|z\| > 5$	**10** (5.4%)	**3** (3.4%)	**27** (18.4%)	**7** (9%)	**11** (6.6%)	**0** (0%)	**58** (8.6%)

(c) Synergistic interactions between mutations (top) or positions (bottom) and *HNRNPH* knockdown in MCF7 cells. Same format as in (a). Interactions for any isoform are reported at different absolute *z*-score cutoffs ($|z|$ >2, >3 and >5). Note that synergistic interactions are calculated from ratios of a given isoform over AE inclusion, so no synergistic interactions are given for AE inclusion. Related to Fig. 5c and Supplementary Fig. 12c.

Supplementary Table 3: Association of *HNRNPH2* expression with *RON* exon 11 inclusion levels in different TCGA cohorts. Related to Fig. 3f.

TCGA cohort	# samples	Spearman correlation	*HNRNPH2* variance	*P*-value	FDR	Significance (FDR < 0.05)
BRCA	778	-0.28	0.24	1.5e-15	3.9e-14	TRUE
LUAD	485	-0.25	0.15	3.5e-08	4.6e-07	TRUE
COAD	323	-0.27	0.16	8.0e-07	6.9e-06	TRUE
READ	103	-0.41	0.16	2.0e-05	1.3e-04	TRUE
ESCA	181	-0.29	0.13	7.3e-05	3.8e-04	TRUE
PAAD	163	-0.29	0.08	2.2e-04	9.5e-04	TRUE
LUSC	315	-0.2	0.12	3.8e-04	1.4e-03	TRUE
CESC	248	-0.2	0.16	1.3e-03	4.2e-03	TRUE
STAD	414	-0.14	0.13	3.2e-03	9.2e-03	TRUE
HNSC	455	-0.13	0.16	4.3e-03	1.1e-02	TRUE
THYM	51	-0.37	0.10	7.0e-03	1.7e-02	TRUE
OV	178	-0.18	0.14	1.5e-02	3.3e-02	TRUE
KIRC	11	-0.56	0.25	7.0e-02	1.4e-01	FALSE
PRAD	10	-0.52	0.03	1.3e-01	2.4e-01	FALSE
TGCT	17	0.36	0.10	1.5e-01	2.6e-01	FALSE
BLCA	251	-0.086	0.17	1.7e-01	2.8e-01	FALSE
THCA	282	-0.077	0.04	1.9e-01	2.9e-01	FALSE
KIRP	47	-0.19	0.10	2.1e-01	3.0e-01	FALSE
CHOL	28	-0.2	0.09	3.1e-01	4.2e-01	FALSE
LIHC	24	-0.21	0.15	3.2e-01	4.2e-01	FALSE
SKCM	59	-0.11	0.14	4.0e-01	5.0e-01	FALSE
KICH	4	-0.6	0.18	4.2e-01	5.0e-01	FALSE
UCEC	61	-0.09	0.19	4.9e-01	5.5e-01	FALSE
SARC	19	0.076	0.37	7.6e-01	8.2e-01	FALSE
DLBC	3	0.5	0.04	1	1	FALSE
LAML	3	0.5	0.08	1	1	FALSE
GBM	1	NA	NA	NA	NA	NA

Cancer types: BLCA, Bladder Urothelial Carcinoma; BRCA, Breast Invasive Carcinoma; CESC, Cervical Squamous Cell Carcinoma and Endocervical Adenocarcinoma; CHOL, Cholangiocarcinoma; COAD, Colon Adenocarcinoma; DLBC, Lymphoid Neoplasm Diffuse Large B-cell Lymphoma; ESCA, Esophageal Carcinoma; GBM, Glioblastoma Multiforme; HNSC, Head-Neck Squamous Cell Carcinoma; KICH, Kidney Chromophobe; KIRC, Kidney Renal Clear Cell Carcinoma; KIRP, Kidney Renal Papillary Cell Carcinoma; LAML, Acute Myeloid Leukemia; LIHC, Liver Hepatocellular Carcinoma; LUAD, Lung Adenocarcinoma; LUSC, Lung Squamous Cell Carcinoma; OV, Ovarian Serous Cystadenocarcinoma; PAAD, Pancreatic Adenocarcinoma; PRAD, Prostate Adenocarcinoma; READ, Rectum Adenocarcinoma; SARC, Sarcoma; SKCM, Skin Cutaneous Melanoma; STAD, Stomach Adenocarcinoma; TGCT, Testicular Germ Cell Tumours; THCA, Thyroid Carcinoma; THYM, Thymoma; UCEC, Uterine Corpus Endometrial Carcinoma.

Supplementary Table 4: Oligonucleotides used in this study.

Name	Sequence (5'-3')	Purpose
minigene_cloning_fwd	CCCAAGCTTTGTGAGAGGCAGCTTCCAGA	Cloning of wt *RON* minigene
minigene_cloning_rev	CAGTCTAGANNNNNNNNNNNNNNNGGATCCGCCATTGGTTGGGGGTAGG-GGCTGATTAAAGGTAGG	Cloning of wt *RON* minigene
BamHI_HNRNPH1_fwd	catGGATCCaccatgatgttgggcacggaagg	Cloning of HNRNPH1 overexpression construct
XbaI_HNRNPH1_rev	cattctagactatgcaatgtttgattgaaaatc	Cloning of HNRNPH1 overexpression construct
RT-PCR_minigene_fwd	TGCCAACCTAGTTCCACTGA	RT-PCR for *RON* minigene
RT-PCR_minigene_rev	GCAACTAGAAGGCACAGTCG	RT-PCR for *RON* minigene
RT-PCR_endo_fwd	CCTGAATATGTGGTCCGAGACCCCCAG	RT-PCR for endogenous *RON* gene
RT-PCR_endo_rev	CTAGCTGCTTCCTCCGCCACCAGTA	RT-PCR for endogenous *RON* gene
RON A	CAAGCAGAAGACGGCATACGAGATCGGTCTCGGCATTCCTGCTGAACCGCTCTTCCGATCTNNNNNNNNNNCTATAGGGAGACCCAAGCTT	Illumina fwd sequencing primer for DNA-seq
RON B	CAAGCAGAAGACGGCATACGAGATCGGTCTCGGCATTCCTGCTGAACCGCTCTTCCGATCTNNNNNNNNNNGTTCCACTGAAGCCTGAG	Illumina fwd sequencing primer for DNA-seq and RNA-seq
RON C	CAAGCAGAAGACGGCATACGAGATCGGTCTCGGCATTCCTGCTGAACCGCTCTTCCGATCTNNNNNNNNNNAGCTGCCAGCACGAGTTC	Illumina fwd sequencing primer for DNA-seq
RON D	CAAGCAGAAGACGGCATACGAGATCGGTCTCGGCATTCCTGCTGAACCGCTCTTCCGATCTNNNNNNNNNNGAATCTGAGTGCCCGAGG	Illumina fwd sequencing primer for DNA-seq
RON E	CAAGCAGAAGACGGCATACGAGATCGGTCTCGGCATTCCTGCTGAACCGCTCTTCCGATCTNNNNNNNNNNctactggctggtcctcatga	Illumina fwd sequencing primer for DNA-seq
P5 SOLEXA RON	AATGATACGGCGACCACCGAGATCTACACTCTTTCCCTACACGACGCTCTTCCGATCTNNNNNNNNNNATAGAATAGGGCCCTCTAGA	Illumina rev sequencing primer for DNA-seq and RNA-seq
RT1	NNAATANNNAGATCGGAAGAGCGTCGTGGATCCTGAACCGC	RT primer HNRNPH iCLIP for wt replicate 1
RT2	NNTTTCNNNAGATCGGAAGAGCGTCGTGGATCCTGAACCGC	RT primer HNRNPH iCLIP for wt replicate 2
RT3	NNCGATNNNAGATCGGAAGAGCGTCGTGGATCCTGAACCGC	RT primer HNRNPH iCLIP for wt replicate 3
RT4	NNTTCTNNNAGATCGGAAGAGCGTCGTGGATCCTGAACCGC	RT primer HNRNPH iCLIP for G305A replicate 1
RT5	NNCTCGNNNAGATCGGAAGAGCGTCGTGGATCCT	RT primer HNRNPH iCLIP

	GAACCGC	for G305A replicate 2
RT6	NNACGCNNNAGATCGGAAGAGCGTCGTGGATCCT GAACCGC	RT primer HNRNPH iCLIP for G305A replicate 3
RT7	NNTTCTNNNAGATCGGAAGAGCGTCGTGGATCCT GAACCGC	RT primer HNRNPH iCLIP for G331C replicate 1
RT8	NNGGCGNNNAGATCGGAAGAGCGTCGTGGATCCT GAACCGC	RT primer HNRNPH iCLIP for G331C replicate 2
RT9	NNTGTGNNNAGATCGGAAGAGCGTCGTGGATCCT GAACCGC	RT primer HNRNPH iCLIP for G348C replicate 1
RT10	NNGTATNNNAGATCGGAAGAGCGTCGTGGATCCT GAACCGC	RT primer HNRNPH iCLIP for G348C replicate 2

Oligonucleotides were purchased either from Sigma-Aldrich or Integrated DNA Technologies.

Supplementary Figures 1 - 16

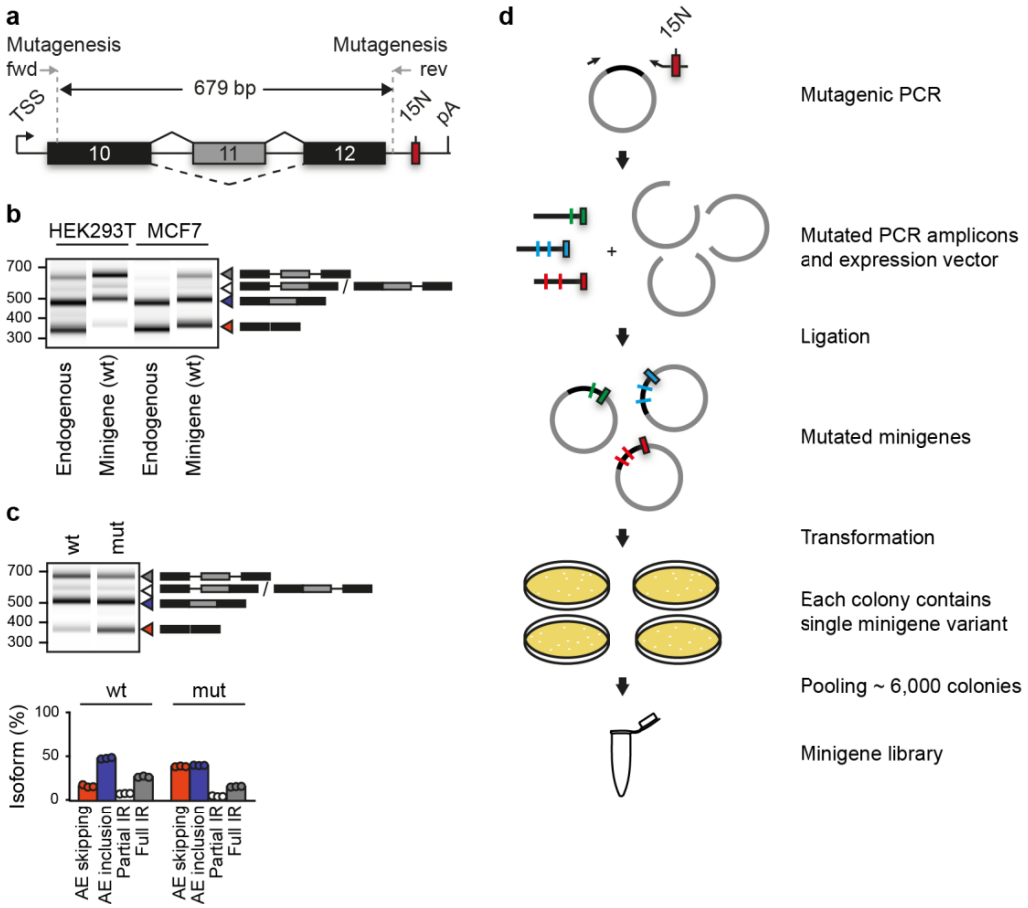

Supplementary Figure 1: Random mutagenesis generates a mutated *RON* minigene library. Related to Fig. 1a.

(a) The *RON* minigene harbours genomic sequence of the *RON* gene (*MST1R*, ENSG00000164078) including alternative exon 11 with the complete flanking introns and constitutive exons 10 and 12 (chr3: 49,933,098 - 49,933,837, GRCh37/hg19). Mutagenesis of a 679 bp region was performed using error-prone PCR and indicated forward (fwd) and reverse (rev) primers. TSS, transcriptional start site; pA, polyadenylation site; 15N, the 15-nt barcode as a unique identifier of each minigene variant.

(b) The wild type (wt) *RON* minigene gives rise to the same splicing isoforms as the endogenous *RON* gene in HEK293T and MCF7 cells. Gel-like representation of capillary electrophoresis of PCR products from semiquantitative RT-PCR monitoring *RON* exon 11 inclusion. Note that different primer combinations were used to differentiate between the endogenous *RON* gene and the *RON* wt minigene (**Supplementary Table 4**), resulting in a 52-bp difference in the RT-PCR products for the same isoforms.

(c) Introducing a previously published triple mutation[3] into the *RON* minigene (T565A, G566T, G569A; mut) triggers the expected splicing response. Gel-like representation of RT-PCR products from HEK293T cells as in (b). Bar diagram below shows quantification of isoform frequencies (in %) for alternative exon (AE) inclusion and skipping, as well as partial and full intron retention (IR). Individual data points from three independent biological replicates are displayed. Note that partial IR refers to the sum of first IR and second IR isoforms that cannot be discriminated in the RT-PCR analysis.

(d) Schematic overview of the experimental procedure to generate the mutated minigene library. Mutagenic PCR amplification of the wt *RON* minigene creates mutated amplicons that were ligated into the expression vector to obtain the mutated minigene library. The reverse primer used in the mutagenic PCR carries a 15-nt random sequence (15N) that is included as a unique identifier into each minigene variant. See Methods for details. Coloured vertical bars schematically indicate point mutations.

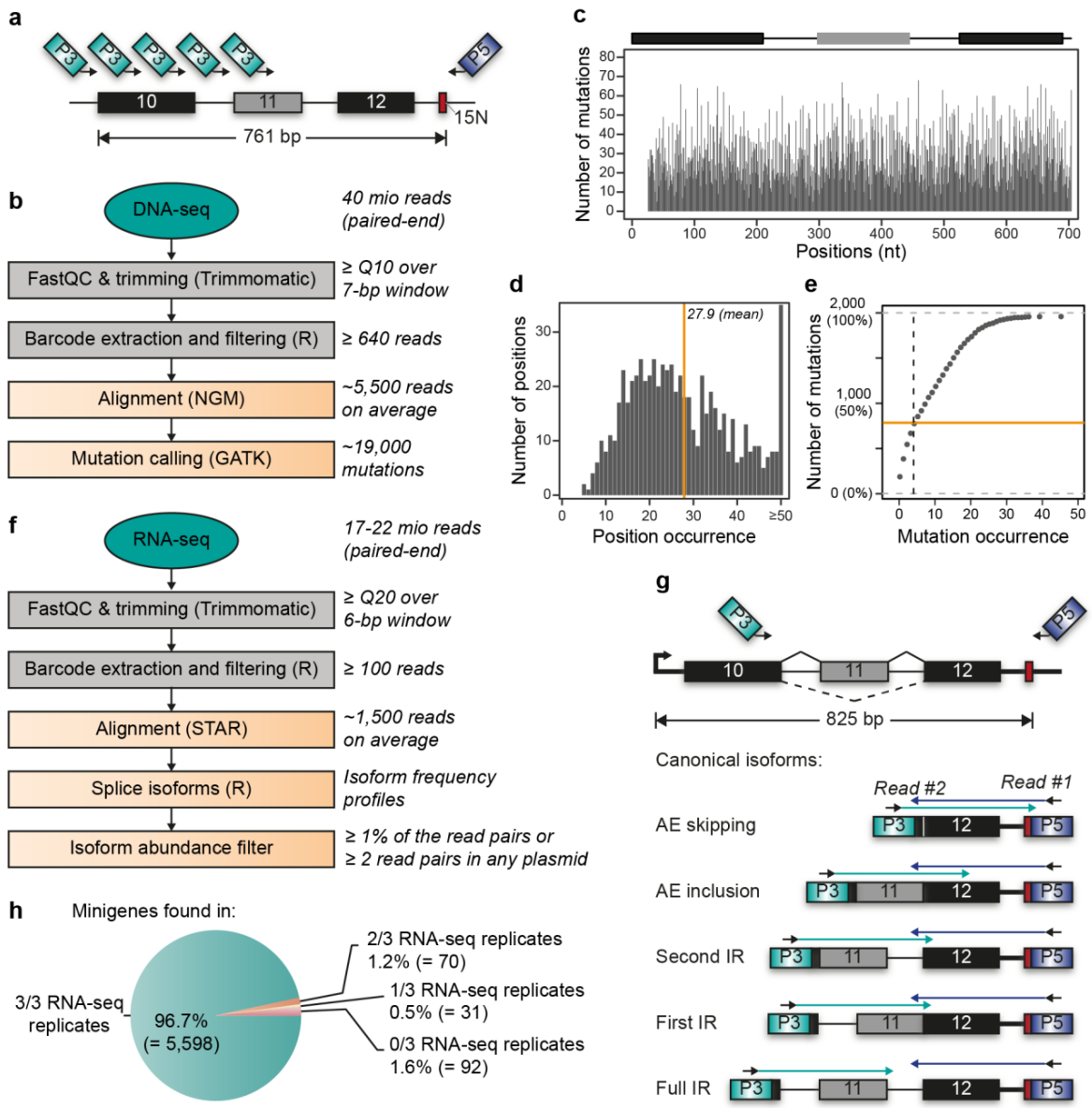

Supplementary Figure 2: Mutations and splicing products from the minigene library are characterised by high-throughput DNA and RNA sequencing. Related to Fig. 1.

(a) Schematic of amplicons for paired-end DNA sequencing. Reverse primer binds downstream of 15-nt barcode (15N, red box) and introduces Illumina sequencing adaptor P5 (Read #1). Five variants of the forward primer bind to subsequent positions resulting in five overlapping amplicons of the minigene. Forward primers introduce P3 (Read #2).

(b) Bioinformatics workflow for DNA-seq analysis to characterise mutations. Quality control and trimming was performed with FastQC and Trimmomatic, respectively, followed by custom scripts (in R) to extract 15-nt barcode and filter for minigenes with ≥640 read pairs. Reads were aligned to wt *RON* minigene sequence using NextGenMap (NGM), and mutation calling was done using HaplotypeCaller tool from Genome Analysis Toolkit (GATK). See Methods for details.

(c) 18,948 point mutations evenly distribute across the *RON* minigene. Bar diagram showing the number of minigene variants (out of 5,791) harbouring a mutation in a given position.

(d) Each position is on average mutated in 28 different minigene variants. Histogram summaries number of positions with a given mutation frequency. Orange line indicates mean mutation frequency across all positions.

(e) The majority of mutations occur in at least five different plasmid variants (labelled in orange). Cumulative distribution of mutations with a given mutation occurrence.

(f) Bioinformatics workflow for RNA-seq analysis to quantify splice isoforms. Upon quality control and filtering similar to (b), reads were aligned to wt *RON* minigene using splice-aware alignment software STAR. All isoforms present in RNA-seq library were reconstructed and filtered for minimum abundance using custom scripts (R). See Methods for details.

(g) Each canonical isoform is uniquely identified by paired-end RNA-seq. Read #1 starting from the P5 adaptor provides the 15-nt barcode information and the splice junction upstream of exon 12, while Read #2 from P3 reads the splice junction downstream of exon 10. For partial or full IR isoforms, both reads extend into the respective intron.

(h) The majority of minigene variants in the library is recovered in all three RNA-seq replicates from HEK293T cells. Pie chart displays the fraction of 5,791 minigene variants in the library that is recovered in 0-3 replicates.

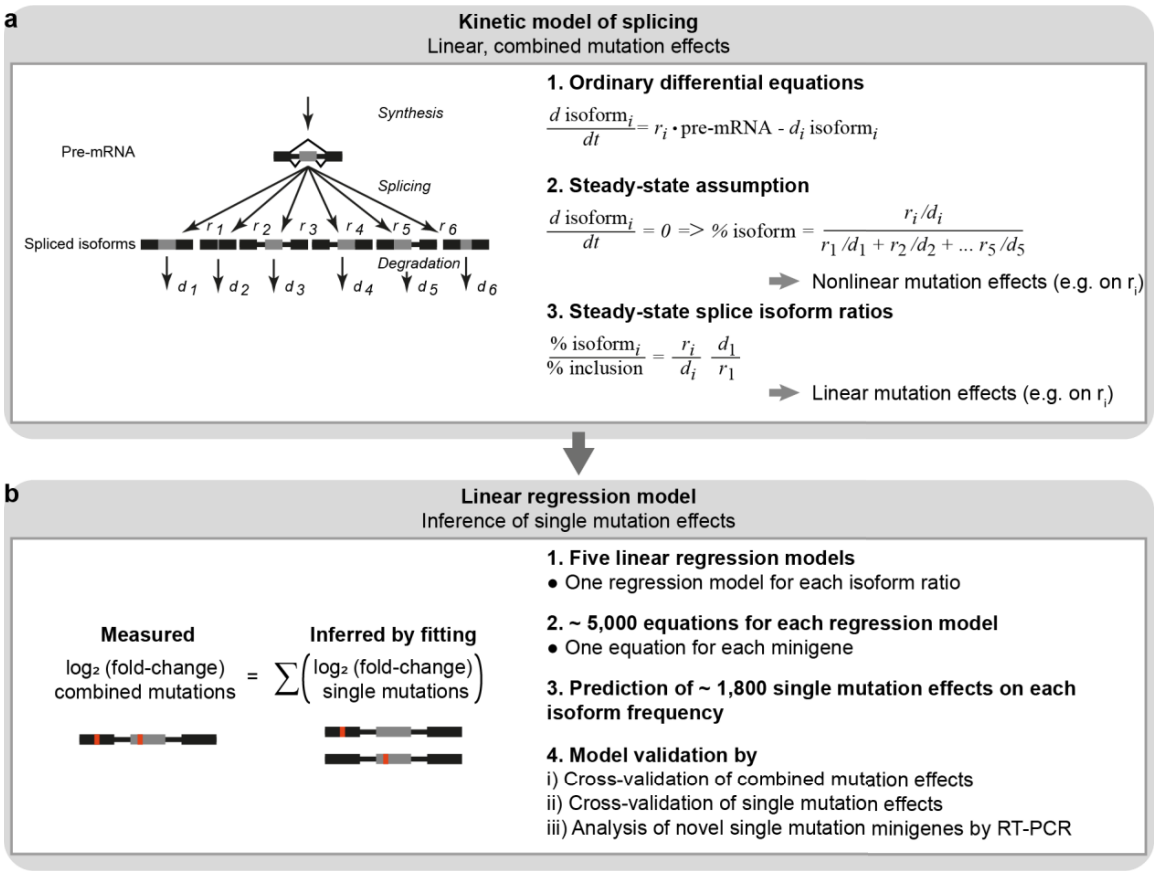

Supplementary Figure 3: Modelling workflow for the inference of single mutation effects. Related to Fig. 2a.

(a) Kinetic model of splicing linearises splicing effects. Pre-mRNA synthesis, splicing reactions and mRNA degradation (scheme) are described by a set of ordinary differential equations (1). At steady state, each isoform frequency is described by a Michaelis-Menten-type equation (2), leading to non-linear mutation effects (e.g., effect of a mutation-induced change in r_1 depends on other parameters, i.e. other mutations). Mutation effects (e.g., on r_1) have linear effects when splice isoform ratios relative to a reference isoform are considered (3). See **Supplementary Note 1** for details.

(b) Linear regression model infers single mutation effects. Effect of combined mutations (log fold-change) is formulated as sum of individual mutation effects. Five regression models (one per splice isoform), each containing ~5,000 equations (one per minigene), are formulated and fitted to the data. The models can be used to predict ~2,000 single mutation effects (700 nucleotides * 3 nucleotide exchanges) for each splice isoform. Model was subjected to cross-validation by leaving out 10% of the minigenes (i) or individual single mutation minigenes (ii) from the fit. Independent validation was performed by testing model predictions against RT-PCR for novel single mutation minigenes. See **Supplementary Note 2** for details.

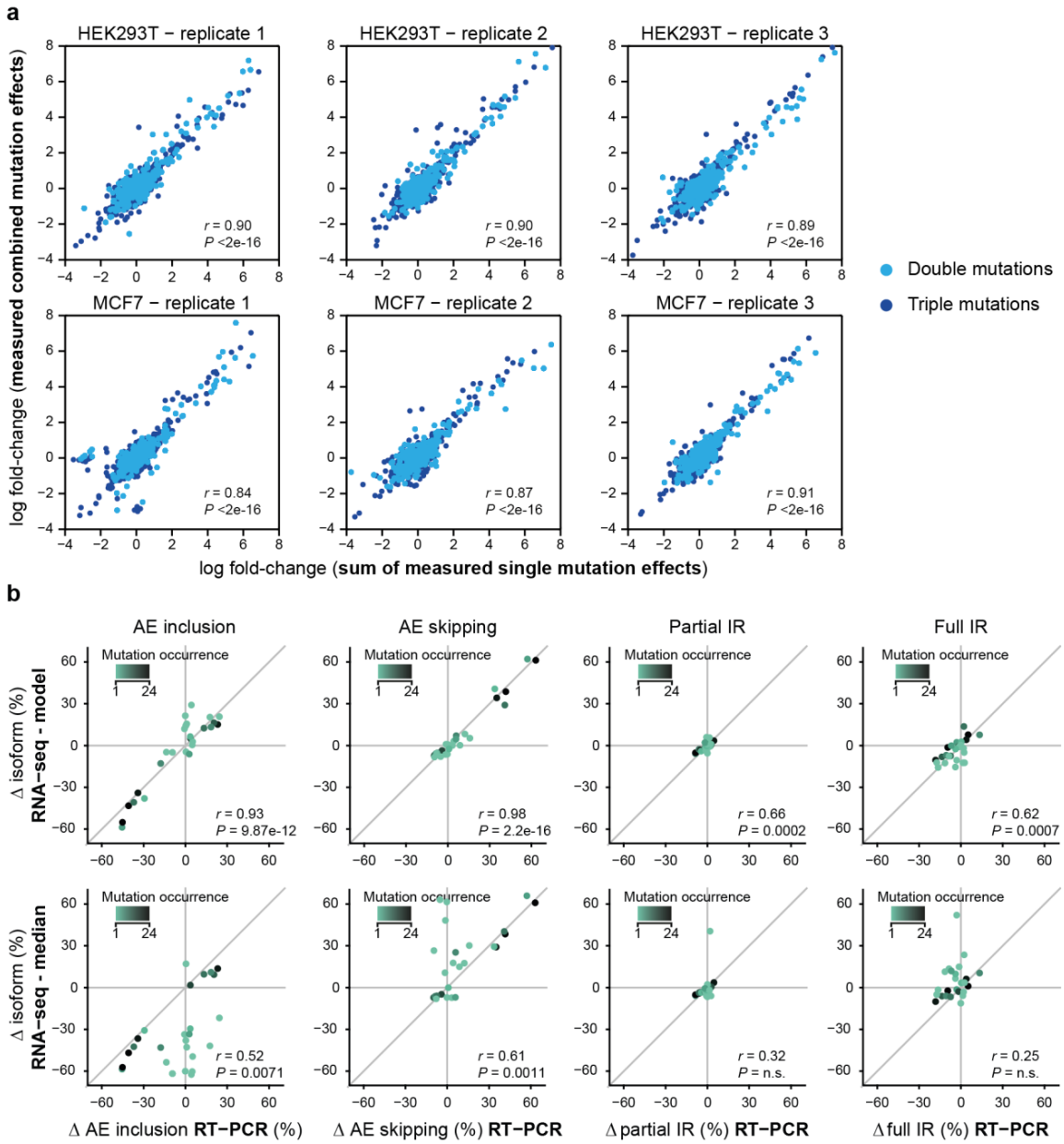

Supplementary Figure 4: Single mutation effects are additive and confirmed by semiquantitative RT-PCR. Related to Fig. 2d.

(a) Single mutation effects are additive. Scatterplots show that sum of directly measured single mutation effects (from single-mutation minigenes; according to linear regression assumption, **Fig. 2a**; x-axes) agrees well with corresponding experimental measurements (y-axes) of minigenes containing two or three of these mutations (double and triple mutations, respectively). Analyses are shown for three replicates in HEK293T (top) and MCF7 cells (bottom).

(b) Regression model outperforms a median-based estimation of single mutation effects. Effects of mutations that rarely occur in the library (colour-coded) correlate better with model-inferred than median-based estimates. Scatterplots compare model-inferred (top row) and median-based (bottom row) estimations of single mutation effects relative to wt (y-axes) to semiquantitative RT-PCR measurements (x-axes) of targeted minigenes harbouring single point mutations, insertions and deletions (**Supplementary Data 8**). Separate plots are shown for different splice isoforms. First IR and second IR were summed up as 'partial IR', since these isoforms cannot be discriminated in RT-PCR. Pearson correlation coefficient and associated *P*-value are given in each panel. See Methods for description of median-based estimation.

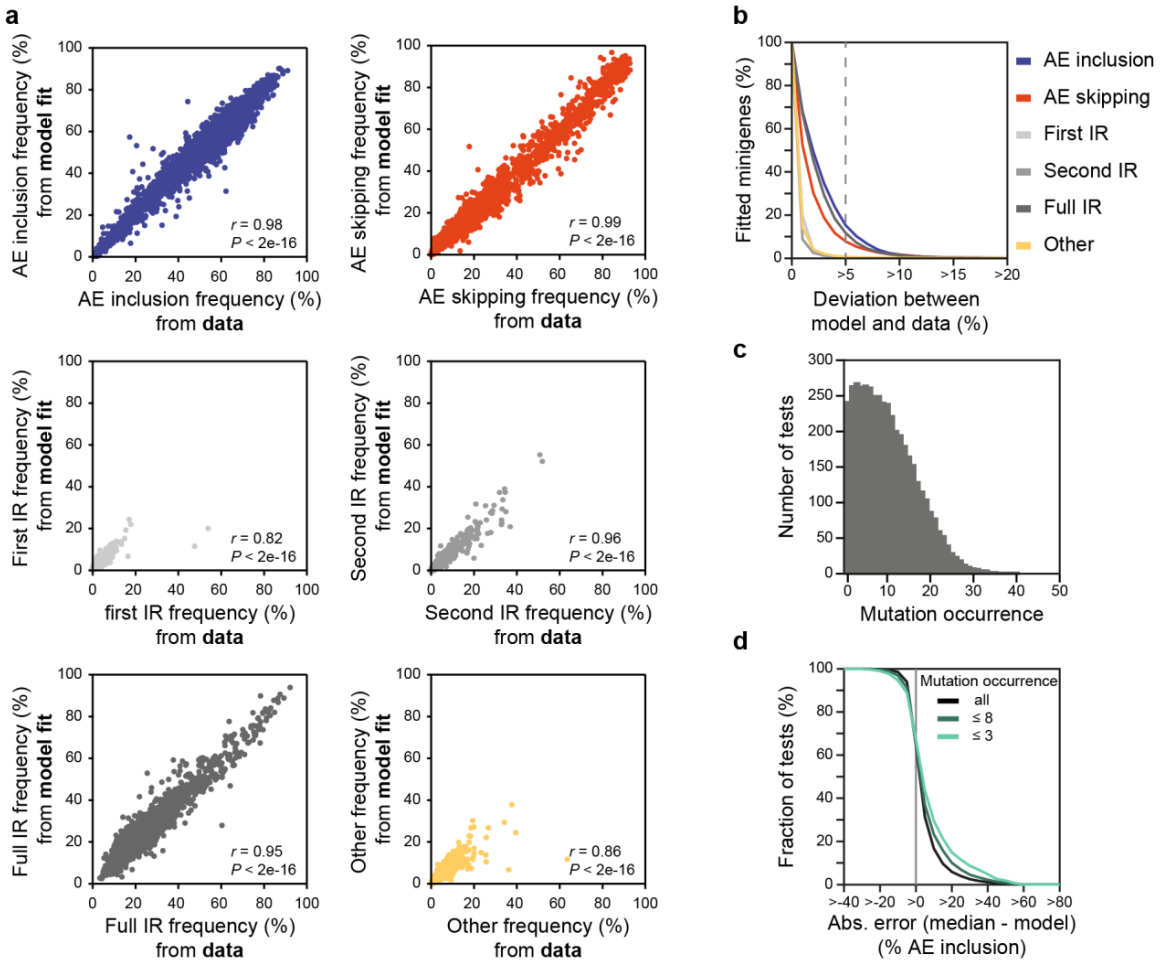

Supplementary Figure 5: The regression model increases the precision of isoform frequency estimations. Related to Fig. 2.

(a) Regression model describes experimentally measured isoform frequencies for each mutated minigene variant with high correlation (Pearson correlation coefficients r = 0.82-0.99, P-values < 2e-16). Scatterplots show frequencies of each of five canonical and non-canonical ('other') isoforms for combined mutations calculated from fitted model against measured data of one biological replicate (see **Supplementary Note 2**). Related to Fig. 2b.

(b) Majority of minigene variants are fitted within 5% deviation from measured value. For each isoform, fraction of fitted minigenes (y-axis) is shown for which model-derived isoform frequencies and measured data deviate more than a given %-value (x-axis). Related to Fig. 2b.

(c) Number of tests for different mutation occurrences that was used to calculate inference error of the model shown in Fig. 2c. Inference errors were estimated by separately benchmarking 561 mutation effects from single-mutation minigenes. To this end, minigenes containing the respective mutation were successively removed from the dataset, and subsequently model-inferred mutation effects were compared to isoform frequencies of single-mutation minigenes excluded from the analysis. Mutation occurrence shows number of different multi-mutation minigenes containing reference mutation used in one test. By successively reducing the dataset, we obtain the prediction accuracy for a particular mutation for different mutation occurrences. In some cases, estimation of mutational effects was not possible from a reduced dataset. These tests were left out, which explains the non-monotonical dependence of the number of tests on mutation occurrence. Related to Fig. 2c.

(d) Gain in accuracy for model-inferred isoform frequency estimations compared to median-based estimates. Difference of absolute errors in AE inclusion (%) between model and median-based calculation (x-axis) for a cumulative fraction of tests (y-axis) used in Fig. 2c. In 65% of tests, the model outperforms median-based estimation. Improvement of the model is more pronounced when considering only tests with low mutation occurrences (see legend). Related to Fig. 2c.

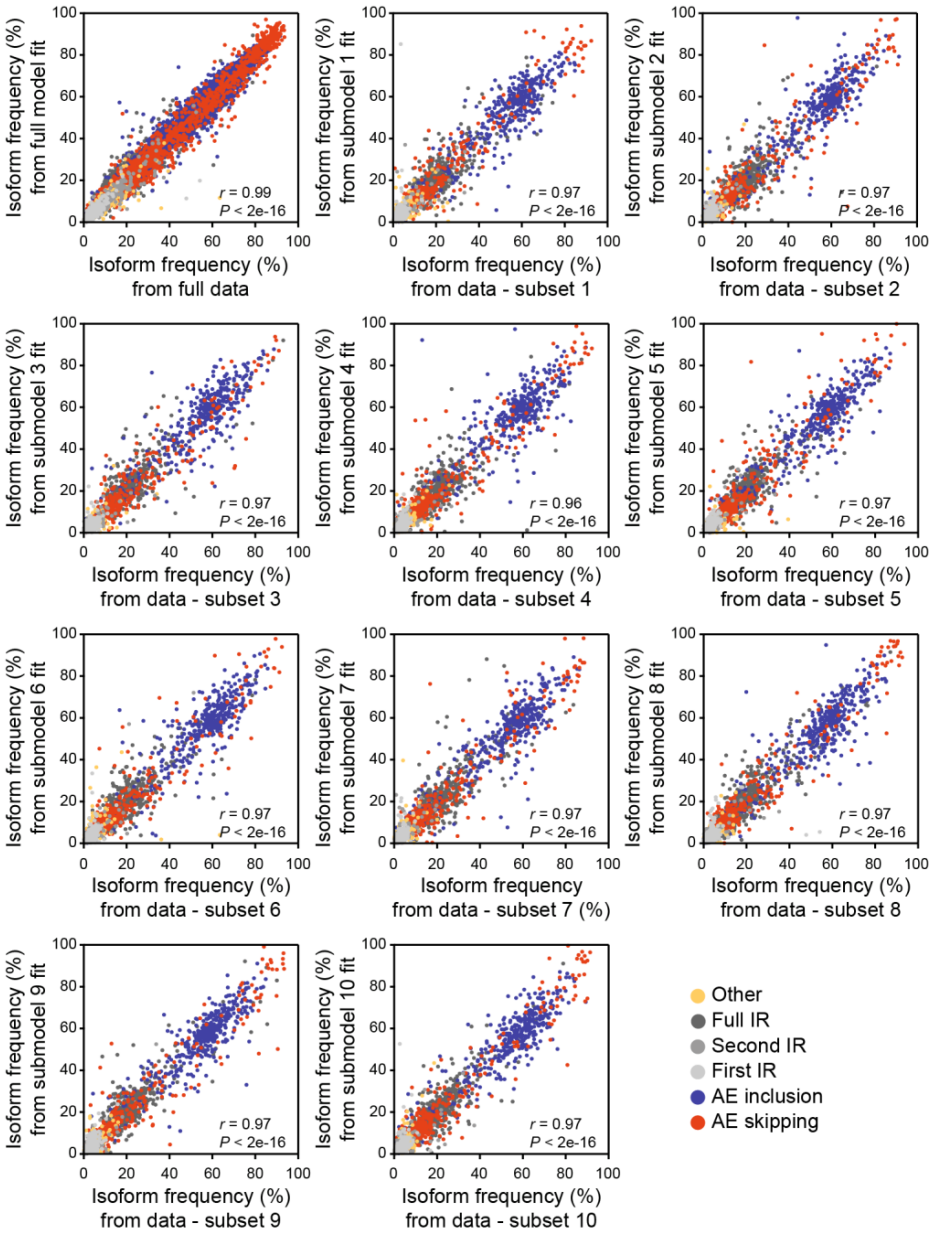

Supplementary Figure 6: Cross-validation underlines predictive power of the model for minigenes that were not used in training. Related to Fig. 2b.

The minigene library was randomly split into ten equal-sized subsets. During 10-fold cross-validation, regression models (one for each splice isoform) were fitted to all data excluding one subset. Scatterplots compare model-predicted splicing outcome for left-out subset to corresponding experimental data for all splice isoforms (see legend). In the first panel, full model fit is plotted against full dataset, followed by model prediction-data comparisons for ten different subsets. Pearson correlation coefficient and associated *P*-value are given in each panel.

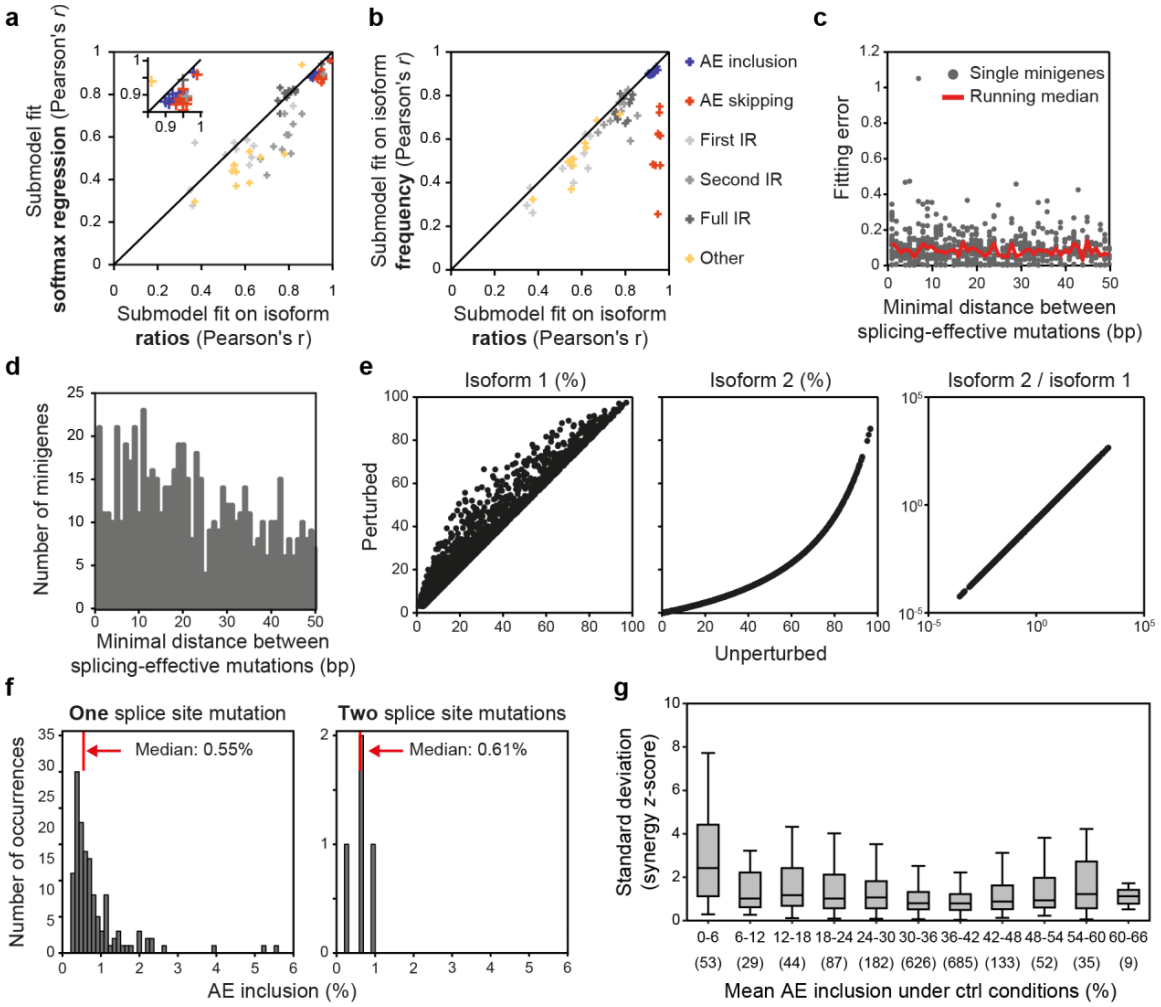

Supplementary Figure 7: Linear regression modelling based on splice isoform ratios accurately infers single mutation effects in HEK293T cells. Related to Fig. 5b.

(a,b) Correlation between model-inferred isoform frequencies and experimental data improves when using linear regression on isoform ratios compared to softmax regression **(a)** or constrained linear regression on isoform frequencies **(b)**. Comparison of Pearson correlation coefficients (*r*) from 10-fold cross-validation (see **Supplementary Note 2**). Isoforms are colour-coded as indicated in (b).

(c) Distance between mutations in the *RON* minigene does not influence the fitting error. Overall fitting error was computed by summing up the absolute deviation between fit and data for all isoforms. Only minigenes containing at least two mutations with significant effects on either isoform are plotted. The minimal distance between adjacent effective mutations contained in each minigene defines the x-axis.

(d) While 1,682 minigenes in our screen contained at least two splicing-effective mutations, only 84 of them occur within a distance of less than seven nucleotides. Histogram quantifies minigenes with a given minimal distance of splicing-effective mutations, corresponding to the number of data points for each value on the x-axis plotted in (c).

(e) Numeric simulation of competing splicing kinetic reactions reveals that perturbations of splicing rates have a linear effect on splice isoform ratios. Kinetic equations reflecting competing splicing reactions (Supplementary Equations 1 and 2 in **Supplementary Note 1**) were analysed *in silico*. The change of the steady-state after decreasing the production rate of one splicing isoform to 20% was simulated. The effect of this perturbation on all splicing isoforms is nonlinear and depends on the mutational context. In contrast, the perturbation has a linear effect on splice isoform ratios.

(f) The presence of two splice site mutations in a minigene does not further decrease AE inclusion compared to minigenes containing only one splice site mutation. Histograms of AE inclusion frequency in minigenes containing one or two splice site mutations.

(g) Computation of the synergy score is unstable for mutations abolishing AE inclusion. Boxplox shows the standard deviation of the synergy score for the AE skipping to AE inclusion ratio over the three replicates for mutations with mean control AE inclusion in different ranges. Bounds of each box represent quartiles, centre line denotes 50th percentile, and whiskers extend to most extreme data points. Mutations leading to control AE inclusion less than 6% show greatest uncertainty in the computation of the synergy *z*-score.

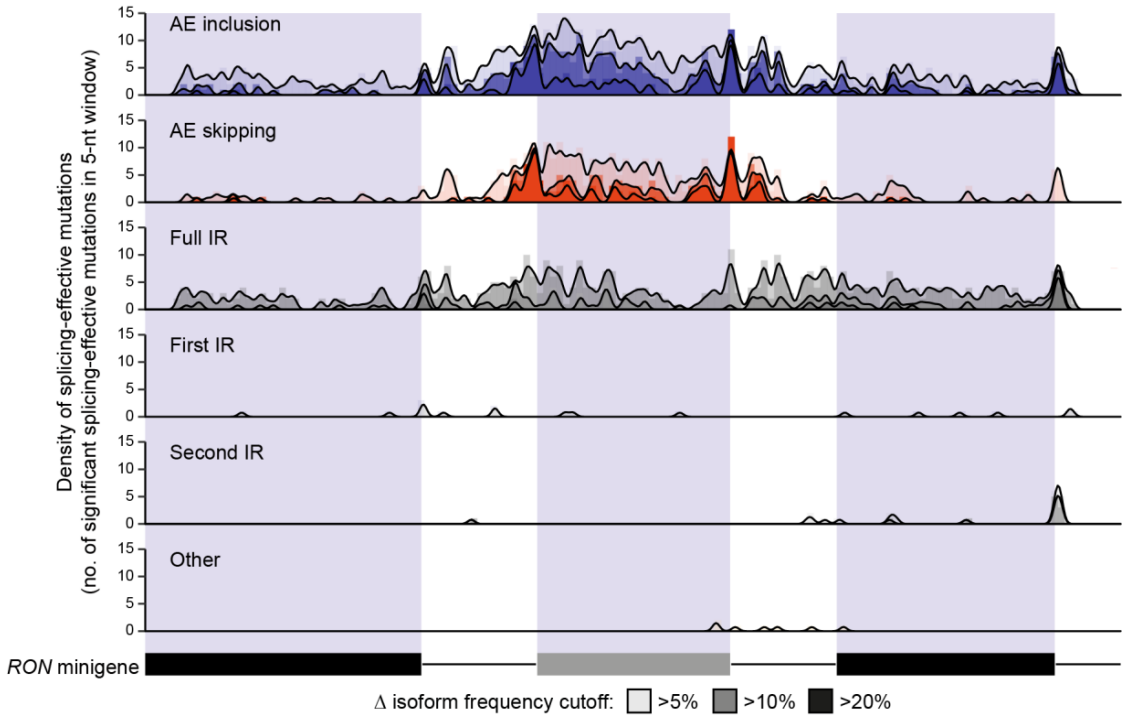

Supplementary Figure 8: Complete landscape of splicing-effective mutations in HEK293T cells. Related to Fig. 2e.

Bar diagrams for each isoform show the number of splicing-effective mutations in adjacent 5-nt windows across the *RON* minigene (FDR < 0.1%). Lines indicate the density of significant splicing-effective mutations in a 5-nt sliding window. Light to dark shading indicates cutoffs at >5%, >10%, and >20% change in isoform frequency, identifying a total of 778, 362 and 136 splicing-effective mutations, respectively. The alternative exon constitutes a regulatory hotspot for alternative exon (AE) inclusion and AE skipping. Mutations affecting full intron retention (IR) are dispersed across the alternative exon and the downstream constitutive exon.

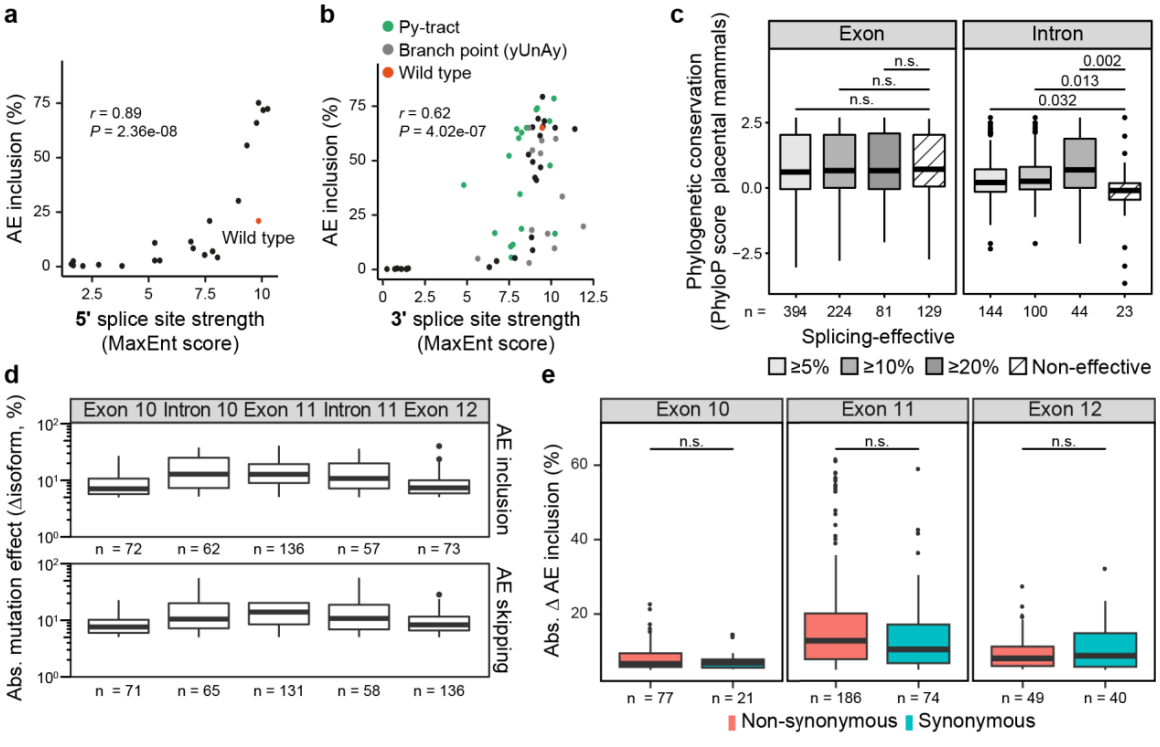

f

	Effective mutations	Non-effective mutations	Percentage of effective mutations
Non-synonymous	312	568	35%
Synonymous	135	272	33%

Supplementary Figure 9: Splice site strength, evolutionary conservation and coding potential of splicing-effective positions. Related to Fig. 2.

(a,b) Mutation effects at the 3' splice site **(a)** and 5' splice site **(b)** of *RON* exon 11 correlate with splice site strengths predicted by the MaxEntScan software. Scatterplots compare AE inclusion frequencies from HEK293T cells (y-axes) to the predicted splice site strength (MaxEnt score) for all mutations in positions considered by MaxEntScan (278-300 nt and 442-450 nt for 3' and 5' splice site, respectively). Red, green and grey dots indicate wt minigene and variants with mutations in polypyrimidine tract (Py-tract; 286-293 nt) and branch point motif (yUnAy, where y is pyrimidine and n is any base; 279-283 nt), respectively. *r*, Spearman correlation coefficient and corresponding *P*-value.

(c) Splicing-effective positions are significantly more conserved evolutionarily than permissive mutations within introns, but not exons. Boxplot shows distribution of conservation scores (PhyloP score across 46 placental mammals) for splicing-effective (light to dark shading indicating cutoffs at >5%, >10%, and >20% change in isoform frequency) and permissive positions in MCF7 cells in exons (left) and introns (right) of the *RON* minigene. Number of positions in each box indicated below. Centre line and bounds of each box denote 25th, 50th and 75th percentile, and whiskers extend to most extreme values within 1.5x interquartile range (IQR). *P*-values correspond to two-sided Mann-Whitney-Wilcoxon test. n.s., not significant.

(d) Splicing-effective mutations in *RON* exon 11 and the flanking introns are comparably strong. Boxplots summarise absolute changes in AE inclusion (top) or AE skipping (bottom) for significant splicing-effective mutations (>5%) in the different transcript regions (number given below). Box representation as in (c).

(e) Synonymous and non-synonymous mutations show similar effect sizes. Boxplots show absolute changes in AE inclusion in HEK293T cells for synonymous and non-synonymous mutations in exons 10-12. Number of positions in each box indicated below. Box representation as in (c). Significance was tested using two-sided Mann-Whitney-Wilcoxon test. n.s., not significant.

(f) Significant splicing-regulatory effects are observed with equal frequency among synonymous and non-synonymous mutations. Table summarises coincidence of significant splicing effects in HEK293T cells and synonymous/non-synonymous mutations across the three exons of the *RON* minigene.

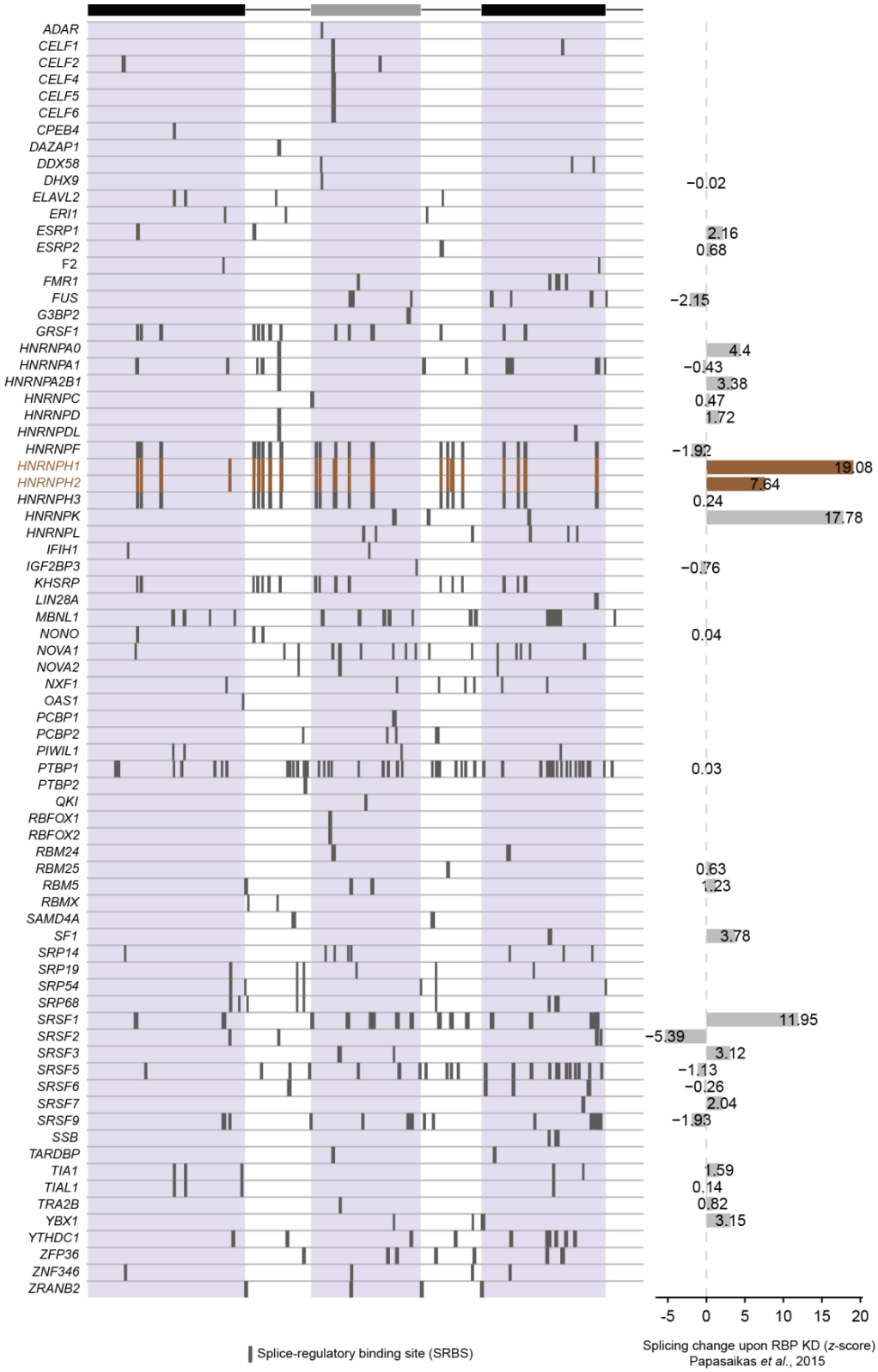

Supplementary Figure 10: Putative RBP regulators of *RON* exon 11 splicing and their predicted splice-regulatory binding sites. Related to Fig. 3e.

in silico binding site predictions for RNA-binding proteins (RBPs) identify splice-regulatory binding sites (SRBS; predicted binding sites that show substantial mutation effects, see Methods). Boxes indicate the location of SRBS for the 76 putative RBP regulators that were identified by ATtRACT. Predicted binding sites for HNRNPH1 and HNRNPH2 are highlighted in brown. Bar diagram (right) shows splicing effects (*z*-scores, values indicated at each bar) for 31 RBPs that are present in published data[2] on *RON* exon 11 splicing upon RBP knockdown (KD). Positive and negative *z*-scores correspond to increased and decreased *RON* exon 11 inclusion upon RBP KD, respectively.

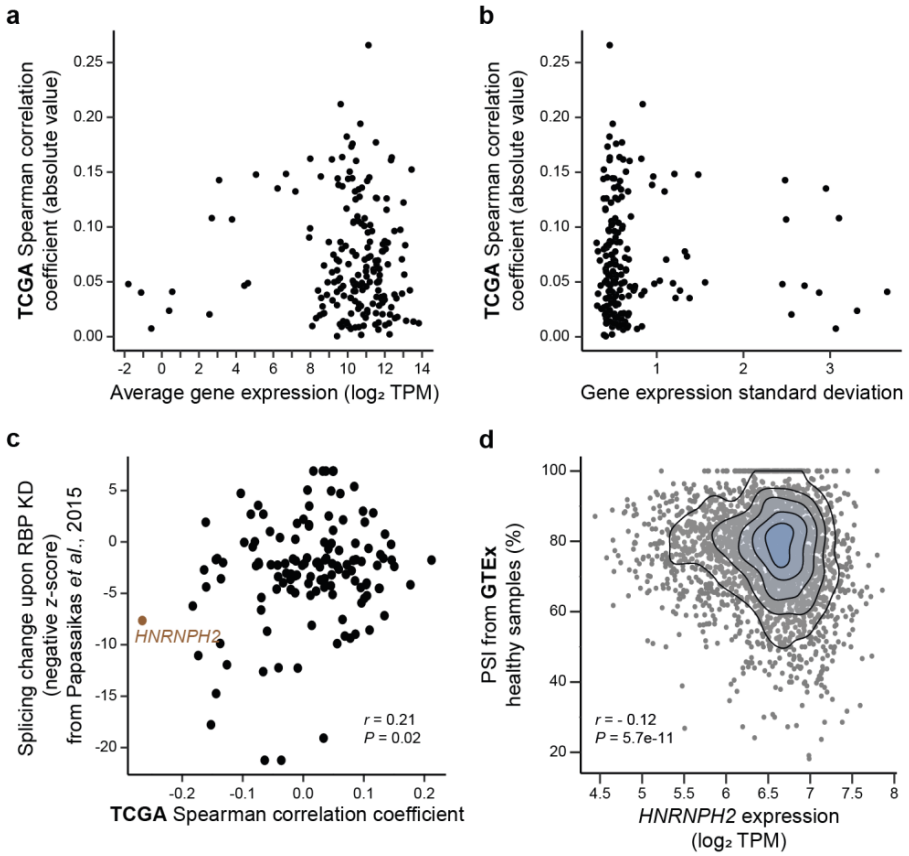

Supplementary Figure 11: Expression correlation of *HNRNPH2* and other RNA-binding proteins (RBPs) with *RON* exon 11 inclusion in TCGA and GTEx samples. Related to Fig. 3c,d,f.

(a,b) Absolute Spearman correlation coefficients of RBP expression (in transcripts per million, TPM) and *RON* exon 11 inclusion (in percent spliced-in, PSI) across TCGA samples do not depend on the average expression levels across samples **(a)** nor on the associated standard deviations **(b)**.

(c) Correlation between RBP expression and *RON* exon 11 inclusion in TCGA tumour samples partially recapitulates the observed effect of those RBPs in a previous knockdown (KD) screen[2]. Scatterplot compares Spearman correlation coefficients from TCGA samples with published *z*-scores (inverted sign) upon RBP KD. *HNRNPH2* is highlighted. *r*, Pearson correlation coefficient and corresponding *P*-value.

(d) *RON* exon 11 inclusion inversely correlates with *HNRNPH2* expression across 2,743 samples derived from 24 different healthy human tissues. Density scatterplot shows *HNRNPH2* expression (in TPM) and *RON* exon 11 inclusion (in PSI) across healthy samples from the Genotype-Tissue Expression (GTEx) project. *r*, Spearman correlation coefficient and corresponding *P*-value.

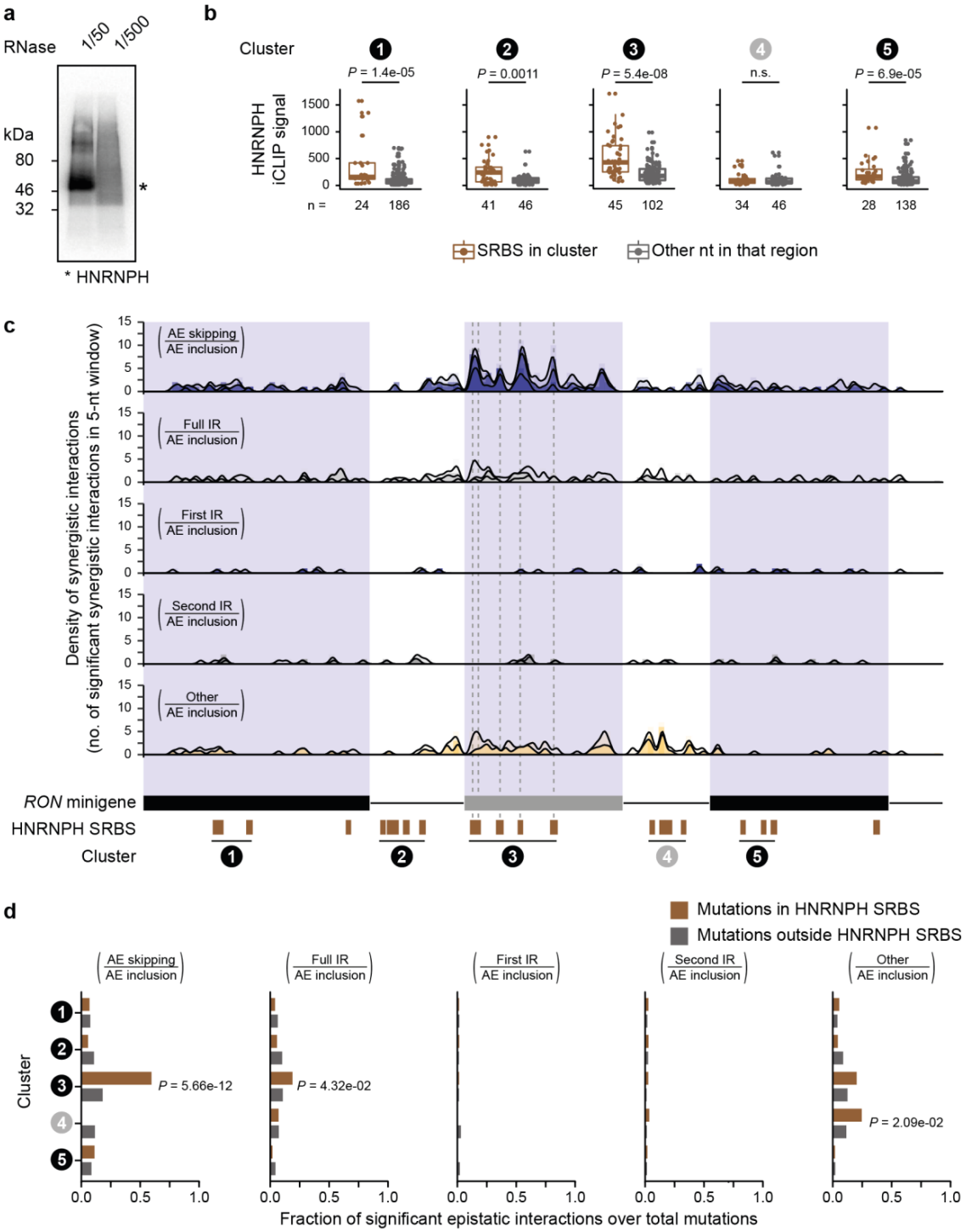

Supplementary Figure 12: HNRNPH iCLIP and synergistic interactions reveal functional HNRNPH binding sites. Related to Figs 4a and 5c.

(a) Autoradiograph shows crosslinked HNRNPH/RNA complexes that were treated with increasing RNase I dilutions prior to immunoprecipitation for optimisation of partial RNase digestion. Protein-RNA complexes run above expected molecular weight of HNRNPH (53 kDa; labelled by asterisk).

(b) HNRNPH crosslink events are significantly enriched in four out of five clusters of HNRNPH splice-regulatory binding sites (SRBS). Boxplots summarise HNRNPH iCLIP crosslink events on all nucleotides (nt) within SRBS ± 2 nt (brown) of each cluster (labelled by numbered circles) compared to all other positions within same exon/intron (grey). Number of positions in each box indicated below. Centre line and bounds of each box denote 25th, 50th and 75th percentile, and whiskers extend to most extreme values within 1.5x interquartile range (IQR). *P*-values correspond to two-sided Wilcoxon Rank-Sum test.

(c) Synergistic interactions between point mutations and *HNRNPH* KD are predominantly observed for AE inclusion, AE skipping, and 'other' isoforms. Bar diagrams for each splice isoform ratio show number of significant synergistic interactions (FDR < 0.1%) in adjacent 5-nt windows. Lines indicate the density in a 5-nt sliding window. Each panel

shows an overlay of increasing *z*-score cutoffs (|*z*|>2 >3, and >5), identifying a total of 354, 222 and 66 significant synergistic interactions, respectively (**Supplementary Table 2**). Splice sites ± 2 nt were excluded from this analysis. *RON* minigene structure and predicted HNRNPH SRBS clusters are given below.

(d) Synergistic interactions are significantly enriched within HNRNPH SRBS in cluster 3. Bar diagrams for each splice isoform ratio display the fraction of significant synergistic interactions over all mutations for SRBS within the five clusters (brown) compared to all other positions within same exon/intron (grey). Significant differences are shown with *P*-values correspond to one-sided Wilcoxon Rank-Sum test.

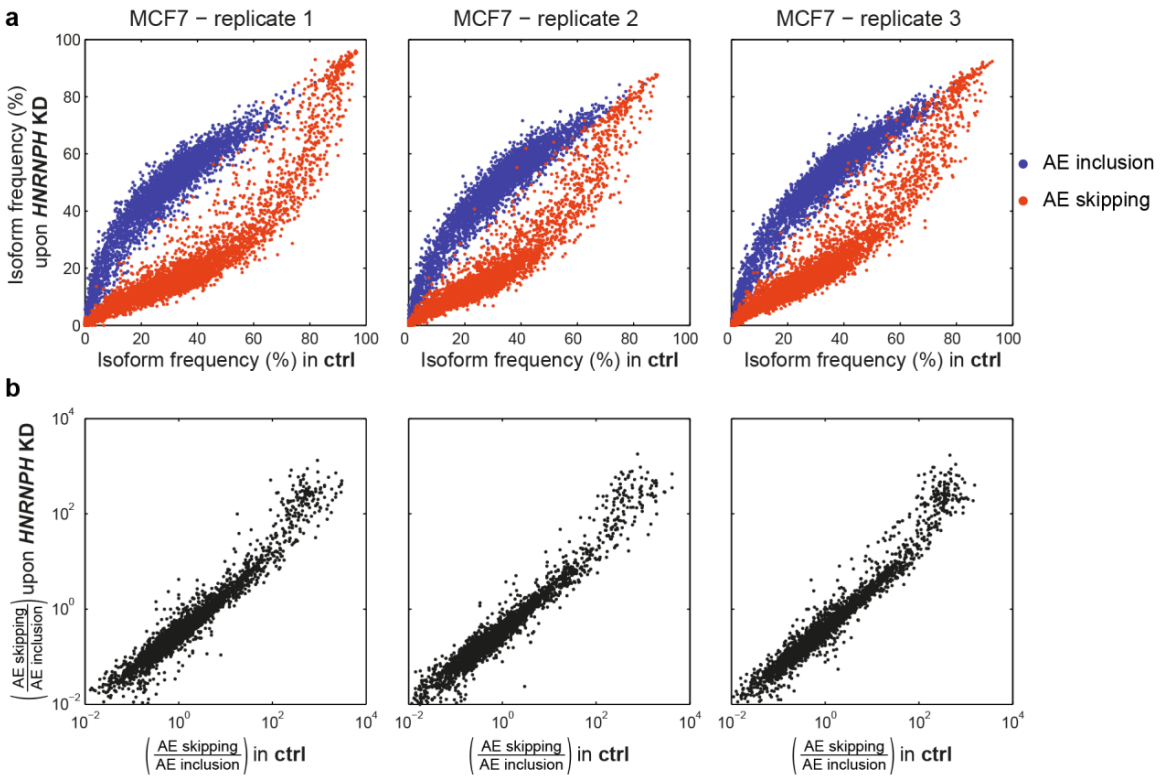

Supplementary Figure 13: *HNRNPH* KD shows non-linear effects on splice isoforms, while splice isoform ratios respond linearly.

(a) AE inclusion (blue) and AE skipping (red) isoform frequencies in MCF7 cells under control (ctrl) and *HNRNPH* KD conditions are shown for all individual minigene variants in three biological replicates. Depending on baseline frequency under control conditions, strength of KD-induced effect varies (top).

(b) Corresponding splice isoform ratios (AE skipping over AE inclusion) for individual minigene variants (black) are independent of baseline frequency and behave linearly.

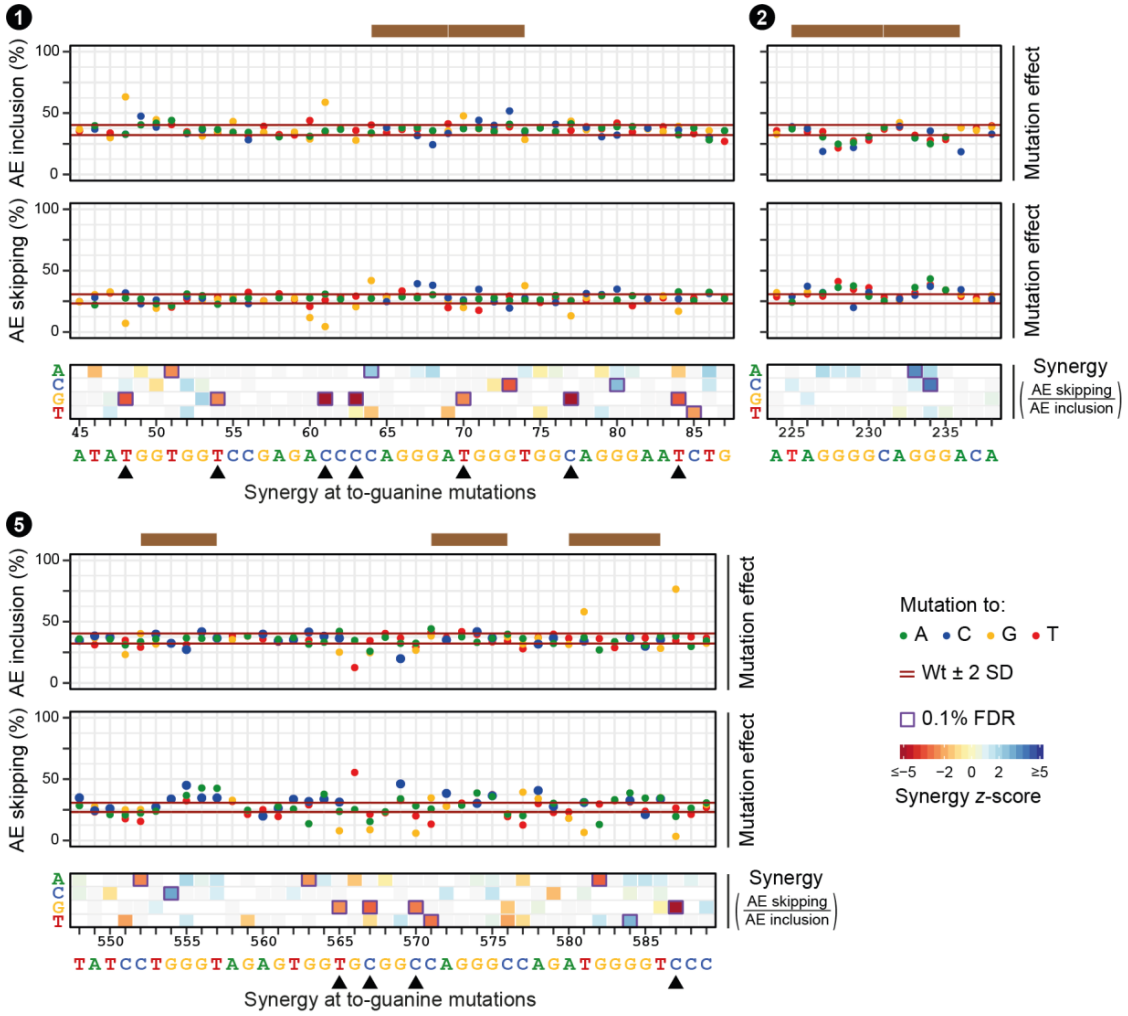

Supplementary Figure 14: Mutation effects and synergistic interactions between *HNRNPH* KD and single point mutations highlight mutations that reinforce HNRNPH binding. Related to Fig. 5d.

Within HNRNPH splice-regulatory binding sites (SRBS) of clusters 1 and 5 (indicated by numbered circles) in constitutive exons 10 and 12, respectively, mutations to guanines generally lead to increased AE inclusion, while AE skipping levels are reduced. Strong synergistic interactions of these mutations (highlighted by arrowheads) suggest that strengthening HNRNPH binding at these sites enhances its splicing-regulatory function. HNRNPH SRBS cluster 2 in first intron regulates AE skipping and AE inclusion in opposite direction compared to HNRNPH SRBS cluster 3 (**Fig. 5d**).

For each SRBS cluster, three plots are shown summarising single mutations effects on AE inclusion (top) and AE skipping (middle) as well as synergistic interactions of mutations with *HNRNPH* KD (based on splice isoform ratio of AE skipping over AE inclusion; bottom). Single mutation effects are displayed as dot plot, with y-axis showing the isoform frequency (mean of three biological replicates) resulting from each individual mutation in a given position along the y-axis. Each dot represents one mutation, with colours indicating inserted nucleotide (green, mutation to A; blue, to C; yellow, to G; red, to T). Red lines indicate median isoform frequency of wt minigenes ± 2 standard deviations (SD). HNRNPH SRBS (brown) are given above. Synergistic interactions are displayed as a heatmap of *z*-scores (mean of three biological replicates) as a quantitative measure of synergy between indicated mutation and *HNRNPH* KD. Each row represents one type of inserted nucleotide (indicated on the left). White and grey fields indicated mutations that were either not present or filtered out due to inconsistent signs (see Methods). Purple boxes highlight significant synergistic interactions (0.1% FDR).

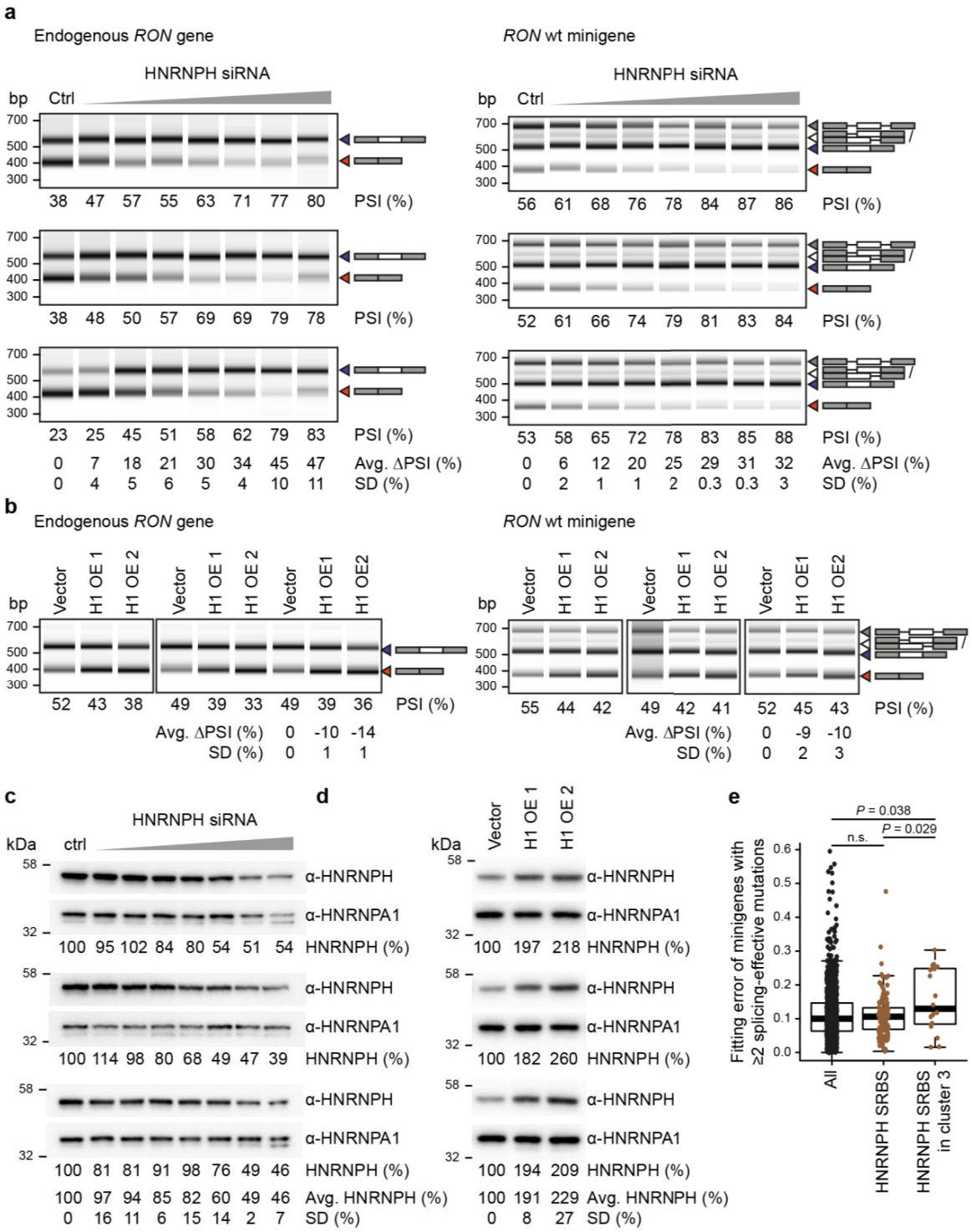

Supplementary Figure 15: *RON* exon 11 splicing is sensitive to reduced HNRNPH levels. Related to Fig. 6b.

(a) *RON* exon 11 inclusion for endogenous *RON* gene and wt *RON* minigene upon gradual reduction of HNRNPH using increasing concentrations of HNRNPH-specific siRNA. Semiquantitative RT-PCR results in MCF7 cells are visualised in a gel-like representation of capillary electrophoresis. Splice products are indicated on the right. Percent spliced-in (PSI) for each condition is given below. Average (Avg.) and standard deviation (SD) of splicing change (ΔPSI against non-targeting control siRNA, Ctrl) across the three replicates are given below. Whole gel images for these experiments are shown in Supplementary Fig. 16.

(b) *RON* exon 11 inclusion for the endogenous *RON* gene and the wt *RON* minigene upon gradual overexpression of *HNRNPH1* (H1 OE1/OE2) compared to a transfection with an empty vector control (Vector). Semiquantitative RT-PCR results of three biological replicates in MCF7 cells. Visualisation as in (a). Whole gel images for these experiments are shown in Supplementary Fig. 16.

(c) Western Blot analysis to quantify amount of HNRNPH upon gradual *HNRNPH* knockdown using increasing concentrations of HNRNPH-specific siRNA in three biological replicates. HNRNPA1 served as loading control. Relative HNRNPH abundance normalised against HNRNPA1 (in %) is given below. Average (Avg.) and standard deviation (SD) of HNRNPH abundance relative to non-targeting control siRNA (Ctrl) across the three replicates are given below. Whole gel images for these experiments are shown in Supplementary Fig. 16.

(d) Western Blot analysis to quantify amount of HNRNPH upon gradual *HNRNPH1* overexpression (H1 OE1/OE2) compared to empty vector transfection (Vector) in three biological replicates. Loading control and visualisation as in (c). Whole gel images for these experiments are shown in Supplementary Fig. 16.

(e) Minigenes with combination of splicing-effective mutations in HNRNPH SRBS cluster 3 show increased fitting errors, evidencing cooperative HNRNPH binding. Fitting error of minigenes with multiple splicing-effective mutations in HNRNPH SRBS cluster 3 is larger than for other minigenes containing splicing-effective mutations within other HNRNPH SRBS or elsewhere in the *RON* minigene. *P*-values correspond to one-sided Student's t-test. Whole gel images for these experiments are shown in Supplementary Fig. 16.

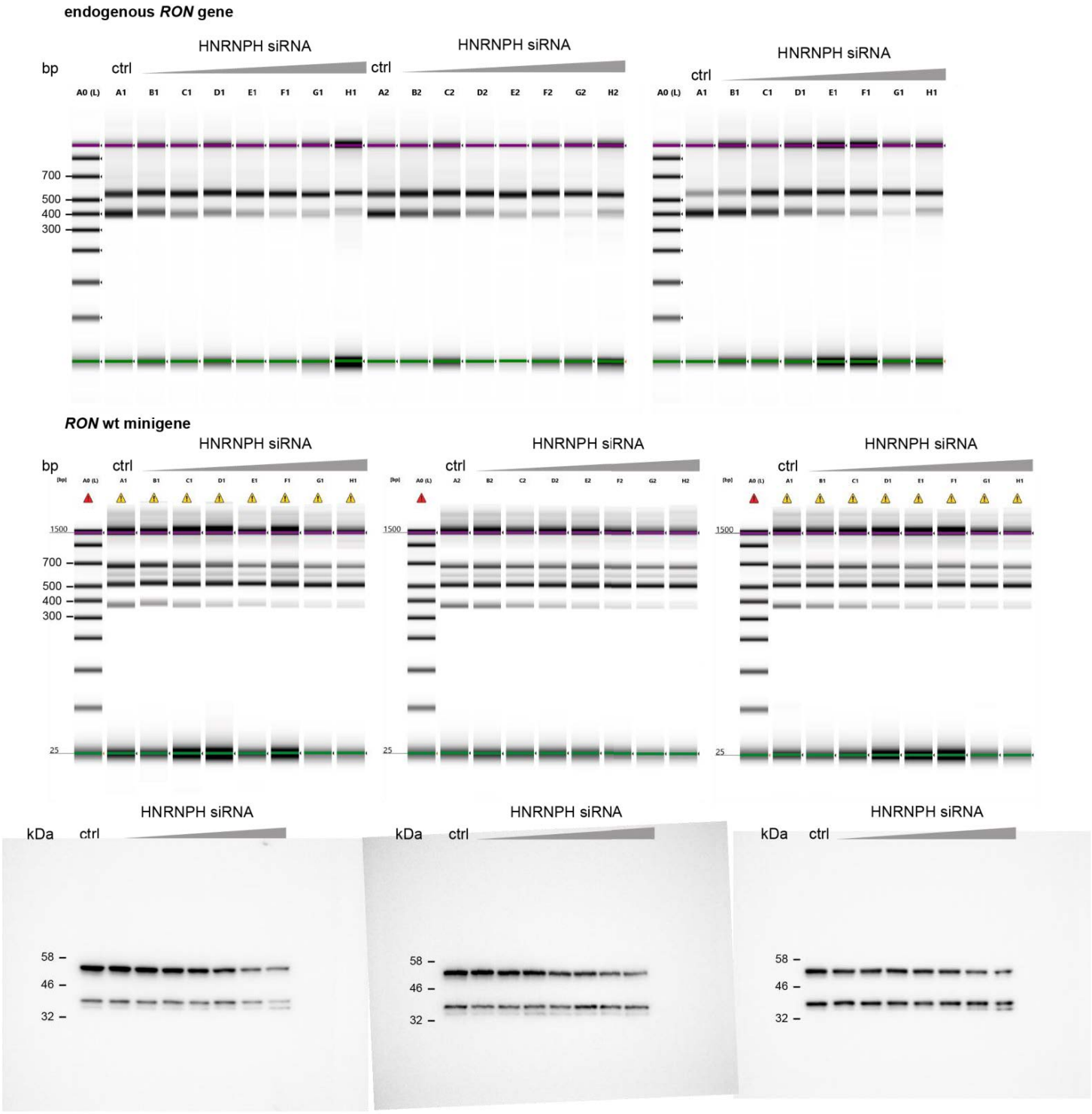

Supplementary Figure 16: Whole gel images for experiments shown in Supplementary Figure 15.

Semiquantitative RT-PCR analyses of *RON* exon 11 splicing upon gradual reduction of HNRNPH visualised in a gel-like representation of capillary electrophoresis (top) and corresponding Western blot analyses (bottom).

Supplementary References

1. Raue, A. *et al*. Structural and practical identifiability analysis of partially observed dynamical models by exploiting the profile likelihood. *Bioinformatics* **25**, 1923-1929 (2009).
2. Papasaikas, P., Tejedor, J. R., Vigevani, L. & Valcárcel, J. Functional splicing network reveals extensive regulatory potential of the core spliceosomal machinery. *Mol. Cell* **57**, 7-22 (2015).
3. Bonomi, S. *et al*. HnRNP A1 controls a splicing regulatory circuit promoting mesenchymal-to-epithelial transition. *Nucleic Acids Res.* **41**, 8665-8679 (2013).

Chapter 2

Direct long-read RNA sequencing identifies a subset of questionable exitrons likely arising from reverse transcription artifacts

Summary

Splicing errors have been frequently associated with disease, but also influence the response to therapy. Recent studies have reported that relatively short introns, arising from annotated exons (named "exitrons"), could be relevant in disease and, most importantly, a source for new epitopes. A recent example of such an exitron has been described in the CD19 gene. CD19 is the target for the CAR(Chimeric Antigen Receptor)T-19 therapy against B-cell acute lymphoblastic leukaemia (B-ALL). An exitron arising from exon 2 of *CD19* has recently been associated with the response to Blinatumomab, in CART-19 treatment. This exitron does not have canonical splice sites and it has been suggested to be a product of non-nuclear splicing by IRE1. Here, we demonstrate that *CD19* ex2Δpart is a product of the artificial polymerase slippage during reverse transcription (RT). We designed a dual-fluorescent reporter to assay the generation of this potential isoform and we could not find any proof that this isoform exists at the RNA level. Furthermore, we compared Nanopore (ONT) cDNA and direct RNA sequencing (dRNA) data of xenografts from patients with B-ALL and observed that the *CD19* ex2Δpart could only be detected in the protocols involving RT. We extended our analysis to create a bioinformatic pipeline that would allow us to identify similar "falsitrons" (false exitrons) on a global scale. Using publicly available datasets, we detected a total of 57 falsitrons. The majority of these falsitrons share characteristics with *CD19* ex2Δpart: e.g., the presence of direct repeats at the splice

sites which can explain the RT slippage event. In conclusion, we propose the use of ONT dRNA as a complementary approach to characterise new isoforms which could be mistakenly generated during protocols that require RT and amplification steps.

Zusammenfassung

Spleißfehler werden häufig mit Krankheiten in Verbindung gebracht, beeinflussen aber auch das Ansprechen auf eine Therapie. Neuere Studien haben berichtet, dass relativ kurze Introns, die aus annotierten Exons hervorgehen (sogenannte "Exitrons"), für Krankheiten relevant sein könnten und vor allem eine Quelle für neue Epitope darstellen. Ein aktuelles Beispiel für ein solches Exitron wurde im CD19-Gen beschrieben. CD19 ist das Ziel für die CAR(Chimeric Antigen Receptor)T-19 Therapie gegen akute lymphoblastische B-Zell-Leukämie (B-ALL). Ein Exitron, das sich aus Exon 2 von *CD19* ergibt, wurde kürzlich mit dem Ansprechen auf Blinatumomab bei der CART-19 Behandlung in Verbindung gebracht. Dieses Exitron hat keine kanonischen Spleißstellen und es wurde vermutet, dass es ein Produkt des nicht-nuklearen Spleißens durch IRE1 ist. Hier zeigen wir, dass der *CD19* ex2Δ-Teil ein Produkt des Abrutschens der künstlichen Polymerase während der reversen Transkription (RT) ist. Wir haben einen dualen Fluoreszenzreporter entwickelt, um die Erzeugung dieser potenziellen Isoform zu testen, und wir konnten keinen Beweis dafür finden, dass diese Isoform auf RNA-Ebene existiert. Darüber hinaus haben wir Nanopore (ONT) cDNA- und direkte RNA-Sequenzierungsdaten (dRNA) von Xenotransplantaten von Patienten mit B-ALL verglichen und festgestellt, dass der *CD19* ex2Δ-Teil nur in den Protokollen mit RT nachgewiesen werden konnte. Wir erweiterten unsere Analyse, um eine bioinformatische Pipeline zu erstellen, die es uns ermöglichen würde, ähnliche "Falsitrons" (falsche Exitrons) auf globaler Ebene zu identifizieren. Unter Verwendung öffentlich zugänglicher Datensätze konnten wir insgesamt 57 Falsitrone nachweisen. Die meisten dieser Falsitrons haben gemeinsame Merkmale mit *CD19* ex2Δpart: z.B. das Vorhandensein von direkten Wiederholungen an den Spleißstellen, die das RT-Slippage-Ereignis erklären können. Abschließend schlagen wir die Verwendung von ONT dRNA als ergänzenden Ansatz vor, um neue Isoformen zu charakterisieren, die bei Protokollen, die RT- und Amplifikationsschritte erfordern, fälschlicherweise erzeugt werden könnten.

Statement of contribution

This project is part of Laura Schulz and my main project. I have conceived, design and implemented the computational analysis to search the falsitrons, based on the initial discussions of the project. I also analysed complementary data (short-read sequencing and PacBio Iso-seq), included during the revisions. I generated Figure 1a,f, all panels in Figure 2, Supplementary Figure 2 and Supplementary Data 1 as well as the Supplementary Tables S1 and S2. I contributed to the manuscript with the methodology describing the computational pipeline. I read and edited the manuscript in all stages and participated in all project discussions.

Supervisor confirmation: _____

Schulz et al. Genome Biology (2021) 22:190
https://doi.org/10.1186/s13059-021-02411-1

Genome Biology

SHORT REPORT Open Access

Direct long-read RNA sequencing identifies a subset of questionable exitrons likely arising from reverse transcription artifacts

Laura Schulz[1†], Manuel Torres-Diz[2†], Mariela Cortés-López[1†], Katharina E. Hayer[3†], Mukta Asnani[2], Sarah K. Tasian[4], Yoseph Barash[5], Elena Sotillo[2,6], Kathi Zarnack[7], Julian König[1*] and Andrei Thomas-Tikhonenko[2,4,8*]

* Correspondence: j.koenig@imb-mainz.de; andreit@pennmedicine.upenn.edu
†Laura Schulz, Manuel Torres-Diz, Mariela Cortés-López and Katharina E. Hayer contributed equally to this work.
[1]Institute of Molecular Biology (IMB), Ackermannweg 4, 55128 Mainz, Germany
[2]Division of Cancer Pathobiology, Children's Hospital of Philadelphia, Philadelphia, PA 19104, USA
Full list of author information is available at the end of the article

Abstract

Resistance to CD19-directed immunotherapies in lymphoblastic leukemia has been attributed, among other factors, to several aberrant *CD19* pre-mRNA splicing events, including recently reported excision of a cryptic intron embedded within *CD19* exon 2. While "exitrons" are known to exist in hundreds of human transcripts, we discovered, using reporter assays and direct long-read RNA sequencing (dRNA-seq), that the *CD19* exitron is an artifact of reverse transcription. Extending our analysis to publicly available datasets, we identified dozens of questionable exitrons, dubbed "falsitrons," that appear only in cDNA-seq, but never in dRNA-seq. Our results highlight the importance of dRNA-seq for transcript isoform validation.

Keywords: Long-read sequencing, Oxford Nanopore Technologies, Alternative splicing, mRNA isoforms, Exitrons, Reverse transcription, CD19, Immunotherapy, Blinatumomab

Background

Aberrant splicing plays an important role in therapeutic resistance either by generating protein isoforms resistant to treatment or by eliminating target proteins entirely. A prime example of this phenomenon is B cell acute lymphoblastic leukemia (B-ALL) acquiring resistance to chimeric antigen receptor-armed autologous T cells (CART-19), which are engineered to target the CD19 surface antigen of B cells [1]. We previously demonstrated that skipping of exon 2 of *CD19* pre-mRNA generates a protein variant inherently resistant to killing by CART-19 and mis-localized in the endoplasmic reticulum [2, 3]. Subsequently, we and others have shown that retention of the *CD19* intron 2 containing a premature termination codon contributes to CART-19 resistance as well [4, 5]. Of note, several publications reported that apparent removal of a cryptic intron fully embedded within *CD19* exon 2 generates a novel isoform in healthy individuals and B-ALL patients (termed Δex2part) [2, 6–8]. One study further suggested that this event could mediate resistance to blinatumomab, a CD19-CD3-bispecific T

cell engager ([6]; commentary by [9]). The same publication hypothesized that excision of the embedded intron might be catalyzed by the IRE1 (ERN1) endoribonuclease, which is responsible for unconventional splicing of the *XBP1* transcript during the unfolded protein response [10].

Such "exitrons" are known to exist in hundreds of human transcripts and are thought to evolve from ancestral coding exons, often preserving the open reading frames [11]. Given the potential significance of the reported *CD19* exitron, we began to investigate its nature using long-read Oxford Nanopore Technologies (ONT) sequencing. Long-read applications allow sequencing of complete transcript isoforms and have re-shaped our understanding of the complexities of human transcriptomes [12–14]. Different ONT protocols are currently available. In cDNA-seq, reverse transcribed (and often PCR-amplified) cDNA molecules are sequenced, while in dRNA-seq, polyadenylated mRNA molecules themselves are passed through the pores and read [15]. Both protocols can capture full transcripts, including alternatively spliced isoforms. However, dRNA-seq typically yields fewer reads and thus is most commonly used for detecting RNA modifications, such as adenine methylation [16]. Our data presented here indicate that the use of this method also avoids mis-identification of questionable exitrons (dubbed "falsitrons"), including but not limited to the one in *CD19* exon 2.

Results and discussion

To investigate the processing of *CD19* exon 2, we treated the NALM-6 B-ALL cell line with thapsigargin, which induces unfolded protein response and IRE1 activity [10], and profiled select transcripts by RT-PCR. As anticipated, the levels of the spliced *XBP1* isoform were increased, but we did not detect changes in the reported *CD19* Δex2part product (Additional File 1: Fig. S1a). This called into question the role of IRE1 in exon 2 processing. We therefore decided to investigate aberrant splicing of *CD19* mRNA in B-ALL in more detail. To this end, we performed dRNA-seq and cDNA-seq on the same RNA sample from a therapy-resistant patient-derived xenograft [17] using long-read ONT sequencing. Both datasets documented the occurrence of several previously reported pathological *CD19* isoforms, including exon 2 skipping [2] and intron 2 retention [4]. Surprisingly, we failed to detect the Δex2part product in dRNA-seq, even though it was clearly observed in cDNA-seq (Fig. 1a). This suggested that it may be an artifact of the reverse transcription (RT)/PCR amplification-based protocol. Close examination of the *CD19* exon 2 sequence revealed that the putative exitron could be folding into a stable hairpin flanked by two 8-nt direct repeats (Fig. 1b), hinting at possible RT or PCR slippage at the base of the hairpin and ensuing product truncation.

To test this hypothesis, we engineered a dual-fluorescence GFP/RFP reporter (Fig. 1c) that would allow detection of *CD19* exitron excision by standard RT-PCR, and the corresponding protein product - via restoring the RFP open reading frame detectable by flow cytometry. Consistent with the *CD19* exitron excision being an RT-PCR artifact, we readily observed the corresponding RT-PCR product, but no RFP/GFP double-positive cells upon transfection into HEK293T cells (Fig. 1d, e). In addition, we introduced point mutations that were predicted to either increase the stability of the secondary structure (mut+; $\Delta\Delta G = -5.1$ kcal/mol) or disrupt one of the direct repeats (mut−; Fig. 1b). Consistent with our hairpin hypothesis, these reporter variants altered the levels of the Δex2part product in the RT-PCR-based assay. Namely, they were 82% higher in the case of mut+ or

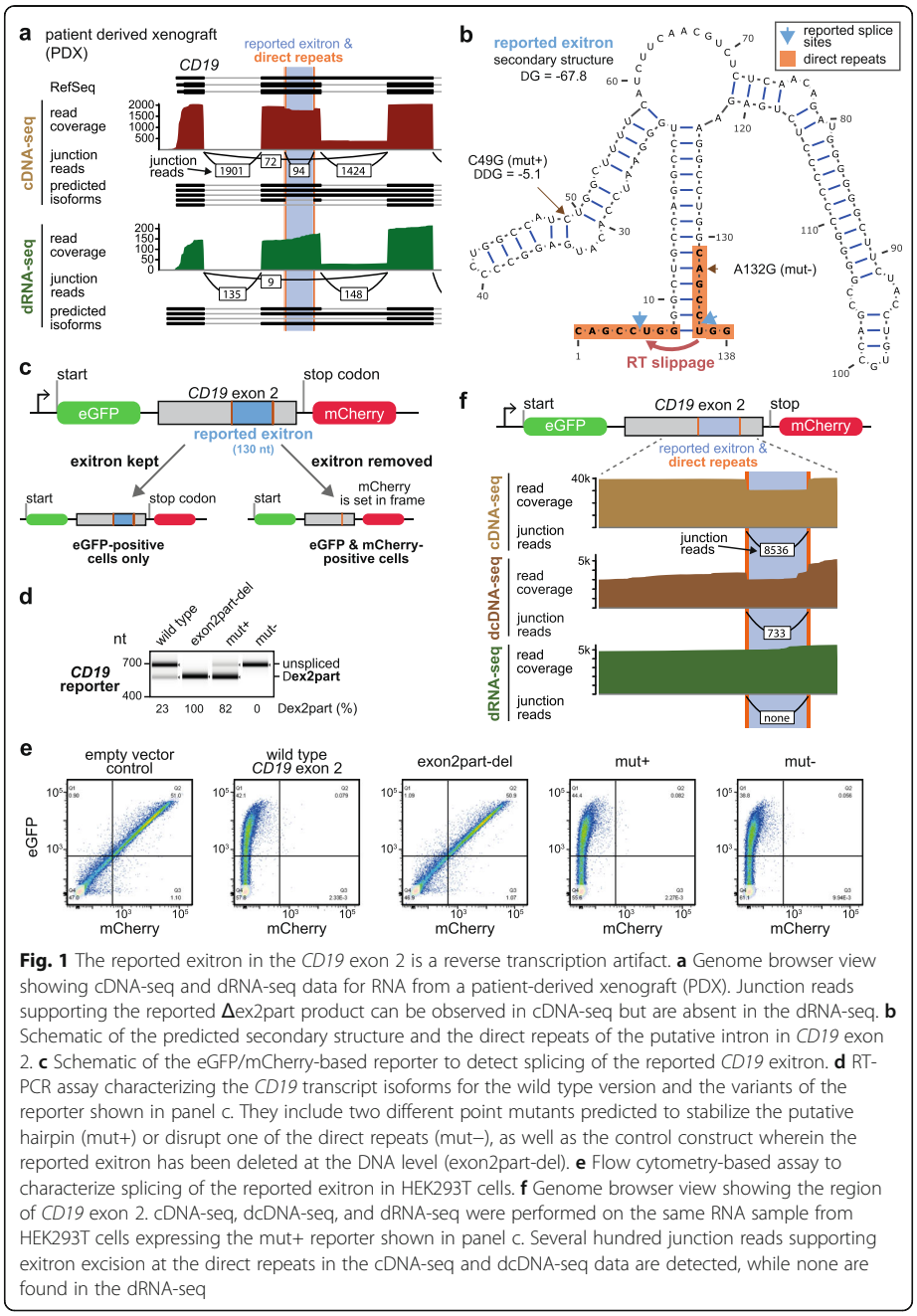

Fig. 1 The reported exitron in the *CD19* exon 2 is a reverse transcription artifact. **a** Genome browser view showing cDNA-seq and dRNA-seq data for RNA from a patient-derived xenograft (PDX). Junction reads supporting the reported **Δ**ex2part product can be observed in cDNA-seq but are absent in the dRNA-seq. **b** Schematic of the predicted secondary structure and the direct repeats of the putative intron in *CD19* exon 2. **c** Schematic of the eGFP/mCherry-based reporter to detect splicing of the reported *CD19* exitron. **d** RT-PCR assay characterizing the *CD19* transcript isoforms for the wild type version and the variants of the reporter shown in panel c. They include two different point mutants predicted to stabilize the putative hairpin (mut+) or disrupt one of the direct repeats (mut–), as well as the control construct wherein the reported exitron has been deleted at the DNA level (exon2part-del). **e** Flow cytometry-based assay to characterize splicing of the reported exitron in HEK293T cells. **f** Genome browser view showing the region of *CD19* exon 2. cDNA-seq, dcDNA-seq, and dRNA-seq were performed on the same RNA sample from HEK293T cells expressing the mut+ reporter shown in panel c. Several hundred junction reads supporting exitron excision at the direct repeats in the cDNA-seq and dcDNA-seq data are detected, while none are found in the dRNA-seq

completely abolished in the case of mut– (Fig. 1d). Again, neither of them, not even mut+, yielded GFP/RFP double-positive cells (Fig. 1e). As a positive control, we removed the reported exitron from the reporter at the DNA level (exon2part-del) and readily observed both truncated RT-PCR product (Fig. 1d, e; Additional File 1: Fig. S1b, c) and robust expression of RFP (Fig. 1e).

To differentiate between RT and PCR artifacts, we performed dRNA-seq, direct cDNA (dcDNA)-seq omitting PCR amplification, and regular PCR-aided cDNA-seq on the reporter-transfected cells. To rule out the sensitivity issue, we used the mut+

reporter variant, which yields the highest levels of the Δex2part product in RT-PCR (Fig. 1e). Strikingly, in the long-read ONT data, the Δex2part product accounted for > 25% of dcDNA-seq and almost 30% of cDNA-seq reads, but was undetectable using dRNA-seq (Fig. 1f). This direct comparison of sequencing protocols indicated that excision of the reported *CD19* exitron occurs not in live cells, but in the test tube during the RT step, possibly due to the two direct repeats brought together at the base of the predicted hairpin structure. A similar phenomenon has been previously observed in the human *LIP1* and *FOXL2* genes [18, 19].

Our results indicate that RT-based sequencing protocols can lead to the widespread mis-identification of exitrons. Indeed, the *CD19* exitron was recently reported to yield a new isoform in the long-read full-length cDNA-seq dataset obtained using the Rolling Circle Amplification to Concatemeric Consensus (R2C2) method serving to increase detection accuracy [7, 8]. To determine whether other transcripts are prone to such RT artifacts, we performed a targeted search in publicly available ONT sequencing datasets. Specifically, we screened for transcript isoforms that are present only in cDNA-seq but not in the matching dRNA-seq. This was achieved using several filtering steps, such as adjusting for read coverage and excluding the presence of canonical splice sites (Fig. 2a, Additional File 1: Fig. S2a, also see Methods). We first applied this comparison to cDNA-seq and dRNA-seq data for the B-lymphoblastoid cell line GM12878 from the Nanopore RNA Consortium [20]. We readily rediscovered the *CD19* exitron along with 19 other questionable exitrons, which we dubbed "falsitrons" (Fig. 2b, c, Additional File 1: Fig. S2b, Additional File 2: Data 1, Additional File 3: Table S1), supporting the common nature of such artifacts. We then extended our search to ONT sequencing data for five commonly used cell lines from the Singapore Nanopore Expression Project (SG-NEx) [21]: A549, HCT116, HepG2, K562, and MCF-7. In total, we discovered 100 candidate events corresponding to 57 unique falsitrons in 43 genes, for which "spliced" reads were present in the cDNA-seq (up to 70% of reads) but completely absent in the matched dRNA-seq (Fig. 2c, Additional File 2: Data 1, Additional File 3: Table S1). Many of these falsitrons were short (median length 353 nt; Fig. 2d), with the "spliced" regions flanked by direct repeats (35 out of 57; Fig. 2c, e). This discovery strengthens our hypothesis that falsitrons in many instances arise from RT slippage. These artifacts are not restricted to ONT data, but occur in other long-read sequencing protocols such as Iso-Seq (Isoform Sequencing, PacBio) as well [13]. We detected 33 out of 57 falsitrons in the reconstructed isoforms from publicly available Iso-Seq data for several human RNA samples (Alzheimer brain, lymphoblastoid cell line COLO829BL, melanoma cell line COLO829T and Human Universal Reference RNA—see the "Methods" section and Additional File 1: Fig. S2c).

Conceptually, such RT artifacts would not be restricted to long-read cDNA-seq data either and should also be found in conventional short-read RNA-seq protocols. To test this hypothesis, we screened the Cancer Genome Atlas (TCGA) database [22] and immediately found six of the falsitrons in several cancer types. Overall, the abundance of the corresponding isoforms was low (< 5%), but could rise up to > 90% for certain samples and tumor types (Fig. 2f). This is potentially important, because a recent paper reported more than 100,000 exitrons in the TCGA database and suggested that the corresponding isoforms are novel cancer drivers and neoepitopes [23]. To learn whether such analyses might be affected by RT artifacts, we overlaid the falsitrons from

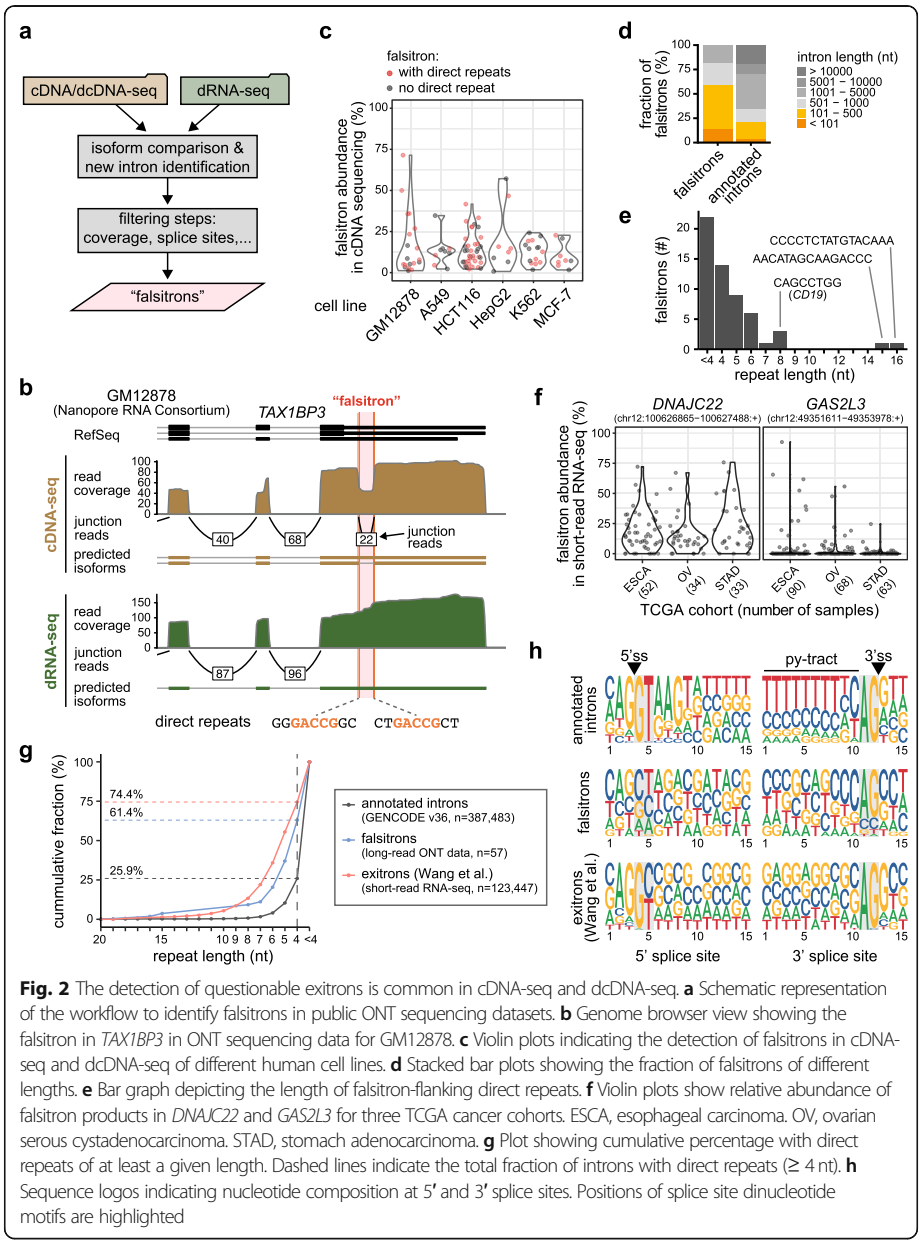

Fig. 2 The detection of questionable exitrons is common in cDNA-seq and dcDNA-seq. **a** Schematic representation of the workflow to identify falsitrons in public ONT sequencing datasets. **b** Genome browser view showing the falsitron in *TAX1BP3* in ONT sequencing data for GM12878. **c** Violin plots indicating the detection of falsitrons in cDNA-seq and dcDNA-seq of different human cell lines. **d** Stacked bar plots showing the fraction of falsitrons of different lengths. **e** Bar graph depicting the length of falsitron-flanking direct repeats. **f** Violin plots show relative abundance of falsitron products in *DNAJC22* and *GAS2L3* for three TCGA cancer cohorts. ESCA, esophageal carcinoma. OV, ovarian serous cystadenocarcinoma. STAD, stomach adenocarcinoma. **g** Plot showing cumulative percentage with direct repeats of at least a given length. Dashed lines indicate the total fraction of introns with direct repeats (≥ 4 nt). **h** Sequence logos indicating nucleotide composition at 5′ and 3′ splice sites. Positions of splice site dinucleotide motifs are highlighted

our ONT data comparison onto these reported exitrons. We found that five falsitrons, including the *CD19* one, overlapped with reported exitrons. To our surprise, we further detected direct repeats (≥ 4 nt) overlapping the putative splice sites in almost 75% of the reported exitrons (91,852 out of 123,337; median length 5 nt), i.e. even more than in our falsitron list (with the shorter median length of 4 nt; Fig. 2g). In contrast, only ~ 25% of all annotated introns harbored such direct repeats at their splice sites (median length < 4 nt). Moreover, even though exitrons had been selected for canonical splice site dinucleotides (GU/GC-AG), they lacked other characteristics of 5′ and 3′ splice sites such as U1 complementarity and the polypyrimidine tract (Fig. 2h). This finding indicates that a significant fraction of the reported exitrons could also be RT artifacts.

Although this observation awaits experimental validation, it suggests that caution is required when interpreting RNA-seq mapping data. We envision that as more dRNA-seq data become available, the unequivocal classification of cryptic introns as exitrons or falsitrons will be possible.

Conclusions

Here, we show that RT artifacts can lead to the detection of questionable exitrons ("falsitrons") and non-existing transcript isoforms. Such artifacts are not limited to one study and occur reproducibly in all protocols which rely on RT, including standard RT-PCR and short-read RNA-seq, but also in ONT-based sequencing of cDNA (PCR-amplified or not). For laboratories looking to validate specific exitrons, utilization of thermo-stable reverse transcriptases (as in TGIRT-Seq [24]) and Northern blotting can be used to avoid artifacts, especially when exitrons in question are reasonably long. Moreover, at least one computational tool (SQANTI) has been developed to flag suspicious introns by implementing a machine learning classifier based on a variety of transcript descriptors [25]. For example, in the publicly available Iso-Seq dataset (PacBio) from the lymphoblastoid cell line COLO829BL derived from a melanoma patient [26], SQANTI2 correctly filters out the *CD19* falsitron (Additional File 1: Fig. S2c). However, such flagging could come at the expense of filtering out real exitrons. Thus, in our opinion, dRNA-seq should be utilized beyond RNA modification detection as a reliable validation tool for high-throughput transcriptome analysis. While it requires significant amount of input RNA and typically yield fewer reads, it does not pick up falsitrons and allows for a more accurate cataloging of bona fide transcript isoforms. As our work illustrates, the accuracy is particularly important when putative isoforms have clinical correlates, such as resistance to life-saving immunotherapies.

Methods

Cell lines and patient-derived xenografts

HEK293T cells were obtained from DSMZ. They were cultured in DMEM (Life Technologies) with 10% fetal bovine serum (Life Technologies) and 1% L-glutamine (Life Technologies). NALM-6 cells were obtained from ATCC and cultured in RPMI medium with the same additives as for HEK293T cells. All cells were kept at 37 °C in a humidified incubator containing 5% CO_2. They were routinely tested for mycoplasma infection. Viably-cryopreserved cells from a patient-derived xenograft model of human B-ALL harboring a TCF3-HLF fusion (ALL1807) were established as previously described [17] and used for downstream sequencing studies.

Cloning

The backbone of the splicing reporter (including both fluorophores) was generously provided by Ramanujan S. Hegde (MRC Laboratory of Molecular Biology, Cambridge, UK) [27]. We introduced exon 2 and part of exon 3 of the human *CD19* gene between GFP and mCherry. To this end, we amplified the *CD19* exon 2 insert sequence from human genomic DNA (Promega) with the following primers:

5′-GATGACGATGACAAGGCCGGATCTGGAGATAACGCTGTGCTGCA-3′ and 5′-GCCAACTTTGAGCCCAGGTGAATCGGTCCGAAACATTCCACCGGAACAGC

TCCCCGCTGCCCTCCACATTGACT-3′. The backbone was amplified with the following primers 5′-GATTCACCTGGGCTCAAAGT-3′ and 5′-AGATCCGGCCTTGT CATCGT-3′. The amplification products were combined using Gibson assembly ready-made master mix from IMB Protein Production Core Facility. The generation of point mutations in the splicing reporter was achieved with the Q5 Site-Directed Mutagenesis Kit (New England Biolabs) according to the manufacturer's recommendations.

Dual-fluorescence splicing reporter assay via flow cytometry

Overexpression of the reporter plasmid was performed using Lipofectamine 2000 (Life Technologies) according to the manufacturer's recommendation. Samples were transfected with reporter plasmids 48 h prior to flow cytometric analysis. Cells were washed in DPBS and trypsinized. After centrifugation, cells were washed twice with Dulbecco's phosphate-buffered saline (DPBS) and resuspended in FACS buffer (DPBS, 1% BSA and 2 mM EDTA). Experiments were performed on the LSRFortessa SORP (BD Biosciences) and analyzed via the FlowJo (v10) software (FlowJo, LLC).

Thapsigargin assay

Thapsigargin (Biomol GmbH) was used after 24 h post-transfection at a concentration of 250 nM for 2, 6, and 24 h on NALM-6 cells. Afterwards, cells were harvested and washed twice in PBS. RNA was isolated with the RNeasy Plus Mini Kit (Qiagen).

Quantification of splicing isoforms with RT-PCR

Semiquantitative RT-PCR was used to quantify ratios of *CD19* and *XBP1* mRNA isoforms. To this end, reverse transcription was performed on 500 ng RNA with RevertAid Reverse Transcriptase (Thermo Fisher Scientific) according to the manufacturer's recommendations. Subsequently, 1 μl of the cDNA was used as template for the RT-PCR reaction with the OneTaq DNA Polymerase (New England Biolabs) (Cycler conditions: 94 °C for 30 s, 28 cycles [reporter PCR] or 34 cycles [endogenous *CD19*, *XBP1*] of [94 °C for 20 s, 53 °C [reporter assay] or 55 °C [*CD19* endogenous] or 54 °C [*XBP1*] for 30 s, 68 °C for 30 s] and final extension at 68 °C for 5 min). The primers 5′-CGCGATCACA TGGTCCTTAA-3′ and 5′-CATGTTATCCTCCTCGCCCT-3′ were used for the reporter assay, 5′-ACCTCCTCGCCTCCTCTTCTTC-3′ and 5′-CCGAAACATTCCAC CGGAACAGC-3′ for the endogenous PCR on *CD19* and 5′-CCTGGTTGCTGAA-GAGGAGG-3′ and 5′-CCATGGGGAGATGTTCTGGAG-3′ for *XBP1*. The TapeStation 2200 capillary gel electrophoresis instrument (Agilent) was used for quantification of the PCR products on D1000 tapes.

Nanopore sequencing

For the ONT sequencing of the PDX sample ALL1807 or HEK293T cells transfected with the mut+ reporter construct, total RNA was extracted using Trizol reagent following manufacturer's recommendation. The mRNA was isolated from 100 μg of total RNA using Dynabeads mRNA DIRECT Kit (Invitrogen). The mRNA samples were subjected to PCR-cDNA (SQK-PCS109, ONT), direct-cDNA (SQK-DCS109, ONT) and direct-RNA (SQK-RNA002, ONT) library preparation in parallel using the equipment and consumables according to each library protocol. Subsequently, each library was

loaded into a Spot-ON flow cell R9 Version (FLO-MIN106D, ONT) and sequenced on a MinION Mk1B device (ONT) for 48 h. The RNA from the sample ALL1807 was submitted to the Sequencing Technologies and Analysis Core at Cold Spring Harbor Laboratory for PCR-cDNA library preparation and sequencing on a PromethION device (ONT).

Nanopore sequence analysis

Base calling was performed using the ONT data processing toolkit guppy (version 3.4.5). guppy_basecaller was run with default settings providing the specific flow cell and library preparation pairs. The resulting reads were aligned to either the human reference genome (version hg38) or our custom *CD19* reporter (mut+) sequence using minimap2 (version 2.17-r941) [28], using the following flags "-k 12 -u b -x splice --secondary=no". For downstream transcriptome analysis, we used the ONT pipeline [github.com/nanoporetech/pipeline-nanopore-ref-isoforms], which implements preprocessing with pychopper (DNA only), mapping with minimap2 and transcriptome reconstruction with StringTie [29] in long-read mode. Finally, the annotation obtained from StringTie was compared back to the existing annotation using gffcompare [30]. This pipeline was modified to run StringTie without annotation to guide the reconstruction and we omitted the "--conservative" flag.

ONT data comparison to identify falsitrons

In order to identify additional falsitrons, we compared cDNA-seq and dRNA-seq data produced by the Nanopore RNA Consortium [20] and the Singapore Nanopore Expression Project (SG-NEx) [21]. The first dataset from the Nanopore RNA Consortium contains dRNA-seq and cDNA-seq data for the cell line GM12878. SG-NEx offers cDNA-seq, dcDNA-seq, and dRNA-seq for the five commonly used cell lines A549, HCT116, HepG2, K562 and MCF-7. For each dataset, we used StringTie for isoform reconstruction as described above. For read filtering, we used the default parameters specified in the pipeline: --minimum_mapping_quality 40, --poly_context 24, and --max_poly_run 8. We then contrasted the GFF transcript output files from StringTie using gffcompare which provides a summary of all the distinct isoforms between two GFF files. We searched for falsitrons that are supported by "spliced" reads only in cDNA-seq but not in dRNA-seq. To do this, we inspected the pairs of "non-equal" isoforms for junction-spanning reads that were present only in cDNA-seq and were fully contained within an exon (filter 1a, Additional File 1: Fig. S2a) or had start and end coordinates that were resided in two adjacent exons detected in the dRNA-seq (filter 1b, Additional File 1: Fig. S2a). Based on the characteristics of *CD19* Δexon2part, we applied additional filters, i.e. a minimum coverage of five reads of both cDNA-seq and dRNA-seq (as reported by StringTie), and the lack of canonical GU-AG splice sites. Using these search criteria, we identified 100 candidate events arising from 57 unique putative falsitrons. Of those, 35 contained direct repeats in the splice sites ranging from 3 to 16 nt, similar to the 8-nt repeats in *CD19* Δex2part. Read numbers, mapping statistics, and gffcompare results for the samples are reported in Additional File 4: Table S2. Genome browser views showing ONT cDNA-seq and dRNA-seq data from all putative falsitron

events are shown in Additional file 2: Data 1. The code for the falsitron search is available in Zenodo/Github under an open source MIT license [31, 32].

Direct repeat search

For each candidate event, we searched for the presence of the same *k*-mers with length from 4 to 20 nt in a 40-nt window around each splice site. The *k*-mers were required to overlap at least 1 nt of the 5′ and 3′ dinucleotide motifs. The same analysis was applied to all the exitrons detected in Wang et al. [23] as well as for all unique annotated introns in GENCODE gene annotation (v36, genome version hg38) [33].

Junction search in TCGA

We use the R/Bioconductor package snapcount [https://github.com/langmead-lab/snapcount] to query the 57 putative falsitrons from our ONT data comparison in short-read RNA-seq data from the Cancer Genome Atlas (TCGA) database. As most of the putative falsitrons end in repetitive regions, like in the case of *CD19* Δex2part, we allowed the splice sites to be shifted outwards by an offset of up to 1 repeat length of that given intron, as long as the resulting junction did not differ by more than ± 1 repeat length from the original junction length. Following these filters, we detected six of our putative falsitrons in TCGA. These reside in the following genes (genomic coordinates of falsitron in brackets): *PHAX* (chr5:126625543-126625746:+), *CCDC86* (chr11:60842626-60842700:+), *DNAJC22* (chr12:49351611-49353978:+), *GAS2L3* (chr12:100626865-100627488:+), *CDC27* (chr17:47118517-47118594:−), and *H1F0* (chr22:37807089-37807354:+).

Relative isoform abundance estimates

For the long-read ONT data, relative isoform abundance was calculated by dividing the number of split reads supporting the falsitron junction over the total number of reads overlapping the junction coordinates. Operations were performed using the R/Bioconductor package GenomicAlignments [34]. For the TCGA data, we calculated relative isoform abundances by dividing the spliced reads (quantified using snapcount) over the mean of reads overlapping the junction region. The latter were quantified with data from the ReCount database [35] via the R/Bioconductor packages megadepth and recount3 [36].

Nucleotide composition at splice sites

For the sequence logos at splice sites, we retrieved the sequence in a 15-nt window (3 nt in the exon + 12 nt in the intron) of the 3′ and 5′ splice sites of the different sets of introns: our putative falsitrons from the ONT comparison (n = 57), all unique exitrons reported by Wang et al. [23] (n = 123,337) and all unique introns in GENCODE gene annotation (v36, genome version hg38) (n = 387,483). We used the R package ggseqlogo [37] to plot the frequency of nucleotides in each set.

Analysis of Iso-Seq data

Isoform predictions for Iso-Seq data (PacBio Sequel) before and after SQANTI2 filtering (v2.7) were taken from https://github.com/PacificBiosciences/DevNet/wiki/Melanoma%2D%2DCancer-Cell-Line-Iso-Seq-Data (for the lymphoblastoid cell line

COLO829BL and melanoma COLO829T; PacBio Sequel), and https://downloads.pacbcloud.com/public/dataset/Alzheimer2019_IsoSeq/ (for total RNA from an Alzheimer's Disease brain sample; PacBio Sequel II). The Universal Human Reference (Agilent; PacBio Sequel II) did not contain the SQANTI2 correction in the initial 2019 release (https://downloads-ap.pacbcloud.com/public/dataset/UHR_IsoSeq/). Upon request, we obtained a 2021 version of the annotation, filtered with SQANTI3 (https://downloads.pacbcloud.com/public/dataset/UHRRisoseq2021/). In the filtered files only 4 falsitrons were detected, located in the following genes: *DNAJC22* (chr5:126625543-126625746:+), *GAS2L3* (chr12:49351611-49353978:+), *CDC27* (chr12:100626865-100627488:+), *PHAX* (chr17:47118517-47118594:–).

Supplementary Information

The online version contains supplementary material available at https://doi.org/10.1186/s13059-021-02411-1.

Additional file 1: Figure S1. Levels of the Δex2part product are not affected by thapsigargin treatment. a) RT-PCR experiments followed by capillary electrophoresis to quantify different *CD19* and *XBP1* isoforms. NALM-6 cells were treated with thapsigargin for indicated time intervals. b) RT-PCR experiments followed by capillary electrophoresis to quantify different *CD19* isoforms in HEK293T cells transfected with a mixture of mut- (A; does not produce Δex2partband) and exon2part-del (B; the reported intron is removed at the DNA level) reporter constructs. c) Flow cytometry-based assay performed on the same cells. **Figure S2.** The workflow to detect falsitrons captures the truncated *CD19* Δex2part product. a) Extended schematic representation of the workflow to identify questionable exitrons (dubbed "falsitrons"). b) Genome browser view depicting detection of the *CD19* falsitron (Δex2part) in ONT cDNA-seq, but not dRNA-seq data from the Nanopore RNA Consortium. c) Genome browser view shows that the *CD19* falsitron (Δex2part) is detected in PacBio Iso-Seq experiments but is filtered out when applying SQANTI2.

Additional file 2: Data 1. Putative falsitrons in the genomic context.

Additional file 3: Table S1. Putative falsitrons detected from Oxford Nanopore Technologies (ONT) sequencing data for the five commonly used cell lines A549, HCT116, HepG2, K562 and MCF-7, as well as the B-lymphoblastoid cell line GM12878.

Additional file 4: Table S2. Mapping and gffcompare statistics for Oxford Nanopore Technologies (ONT) sequencing datasets used in this study.

Additional file 5. Review history.

Acknowledgements

We thank all members of the Thomas-Tikhonenko, König, and Zarnack groups for many helpful discussions. We also gratefully acknowledge support of the IMB Bioinformatics and Flow Cytometry Core Facilities. The results published here are in part based upon data generated by the TCGA Research Network: https://www.cancer.gov/tcga.

Review history

The review history is available as additional file 5.

Peer review information

Barbara Cheifet was the primary editor of this article and managed its editorial process and peer review in collaboration with the rest of the editorial team.

Authors' contributions

LS generated the *CD19* reporter assay and performed RT-PCR and flow cytometry measurements. MTD and MA performed ONT sequencing on HEK293T cells. MCL conceived and implemented computational analysis strategies for falsitron identification in ONT sequencing data, TCGA search, Iso-Seq analysis, and exitron characterization. KEH performed ONT data analysis for PDX and HEK293T data. SKT has developed the ALL1807 PDX model. YB contributed to the analysis of short-read RNA-seq data. All authors contributed to the design of the study. KZ, JK, ES, and ATT wrote the manuscript with input from all coauthors. All authors read and approved the final manuscript.

Authors' information

Twitter handles: @koenig_lab (Julian König); @andrei_thomas_t (Andrei Thomas-Tikhonenko).

Funding

Research in the ATT laboratory was supported by grants from the NIH (U01 CA232563), St. Baldrick's-Stand Up to Cancer Pediatric Dream Team (SU2C-AACR-DT-27-17), the V Foundation for Cancer Research (T2018-014), and the Cookies for Kids' Cancer (CFKC) Foundation. ATT is Richard "Buz" Cooper Scholar of the Breakthrough Bike Challenge. SKT was supported by grants from NIH (U01 CA232486 and U01 CA243072), Department of Defense (CA180683P1), Philip A Sharp Award for Innovation in Collaboration, and Simutis family fund for childhood leukemia research. YB's work was supported by grants from the NIH (U01 CA232563, R01 LM013437, R01 GM128096). Research in the KZ

group and the JK laboratory was supported by grants from the German Research Foundation/Deutsche Forschungsgemeinschaft (ZA 881/2-1 and KO 4566/4-1, respectively).

Availability of data and materials

The long-read ONT sequencing data for the PDX sample ALL1807 (cDNA-seq and dRNA-seq) and the HEK293T cells transfected with the mut+ reporter construct (cDNA-seq, dcDNA-seq and RNA-seq) are avaible in NCBI Short Read Archive under accession numbers SRR14326969-14326973 [38]:
https://www.ncbi.nlm.nih.gov/sra/?term=SRR14326969
https://www.ncbi.nlm.nih.gov/sra/?term=SRR14326970
https://www.ncbi.nlm.nih.gov/sra/?term=SRR14326971
https://www.ncbi.nlm.nih.gov/sra/?term=SRR14326972
https://www.ncbi.nlm.nih.gov/sra/?term=SRR14326973
The computational code for the detection of falsitrons in ONT-Seq data is available in Zenodo/Github under an open source MIT license (https://doi.org/10.5281/zenodo.4906610) [31, 32].

Declarations

Ethics approval and consent to participate

Primary leukemia cells from the patient have been previously banked at the Children's Hospital of Philadelphia Center for Childhood Cancer biorepository with informed consent in accordance with the Declaration of Helsinki via IRB-approved research protocols.

Consent for publication

Not applicable

Competing interests

The authors declare that they have no competing interests.

Author details

[1]Institute of Molecular Biology (IMB), Ackermannweg 4, 55128 Mainz, Germany. [2]Division of Cancer Pathobiology, Children's Hospital of Philadelphia, Philadelphia, PA 19104, USA. [3]The Bioinformatics Group, Children's Hospital of Philadelphia, Philadelphia, PA 19104, USA. [4]Division of Oncology, Children's Hospital of Philadelphia, Philadelphia, PA 19104, USA. [5]Department of Genetics, Perelman School of Medicine at the University of Pennsylvania, Philadelphia, PA 19104, USA. [6]Present address: Stanford Cancer Institute, 265 Campus Dr., Stanford, CA 94305, USA. [7]Buchmann Institute for Molecular Life Sciences (BMLS) and Faculty of Biological Sciences, Goethe University Frankfurt, Max-von-Laue-Str. 15, 60438 Frankfurt, Germany. [8]Department of Pathology & Laboratory Medicine, Perelman School of Medicine at the University of Pennsylvania, Philadelphia, PA 19104, USA.

Received: 27 April 2021 Accepted: 16 June 2021
Published online: 28 June 2021

References

1. Maude SL, Laetsch TW, Buechner J, Rives S, Boyer M, Bittencourt H, et al. Tisagenlecleucel in children and young adults with B-cell lymphoblastic leukemia. N Engl J Med. 2018;378(5):439–48. https://doi.org/10.1056/NEJMoa1709866.
2. Sotillo E, Barrett DM, Black KL, Bagashev A, Oldridge D, Wu G, et al. Convergence of acquired mutations and alternative splicing of CD19 enables resistance to CART-19 immunotherapy. Cancer Discov. 2015;5(12):1282–95. https://doi.org/10.1158/2159-8290.CD-15-1020.
3. Bagashev A, Sotillo E, Tang C-HA, Black KL, Perazzelli J, Seeholzer SH, et al. CD19 alterations emerging after CD19-directed immunotherapy cause retention of the misfolded protein in the endoplasmic reticulum. Mol Cell Biol. 2018;38:e00383–18.
4. Asnani M, Hayer KE, Naqvi AS, Zheng S, Yang SY, Oldridge D, et al. Retention of CD19 intron 2 contributes to CART-19 resistance in leukemias with subclonal frameshift mutations in CD19. Leukemia. 2020;34(4):1202–7. https://doi.org/10.1038/s41375-019-0580-z.
5. Rabilloud T, Potier D, Pankaew S, Nozais M, Loosveld M, Payet-Bornet D. Single-cell profiling identifies pre-existing CD19-negative subclones in a B-ALL patient with CD19-negative relapse after CAR-T therapy. Nat Commun. 2021;12(1):865. https://doi.org/10.1038/s41467-021-21168-6.
6. Zhao Y, Aldoss I, Qu C, Crawford JC, Gu Z, Allen EK, et al. Tumor-intrinsic and -extrinsic determinants of response to blinatumomab in adults with B-ALL. Blood. 2021;137(4):471–84. https://doi.org/10.1182/blood.2020006287.
7. Volden R, Palmer T, Byrne A, Cole C, Schmitz RJ, Green RE, et al. Improving nanopore read accuracy with the R2C2 method enables the sequencing of highly multiplexed full-length single-cell cDNA. Proc Natl Acad Sci USA. 2018;115(39):9726–31. https://doi.org/10.1073/pnas.1806447115.
8. Cole C, Byrne A, Adams M, Volden R, Vollmers C. Complete characterization of the human immune cell transcriptome using accurate full-length cDNA sequencing. Genome Res. 2020;30(4):589–601. https://doi.org/10.1101/gr.257188.119.
9. Boissel N. ALL in escape room. Blood. 2021;137(4):432–4. https://doi.org/10.1182/blood.2020008850.
10. Maurel M, Chevet E, Tavernier J, Gerlo S. Getting RIDD of RNA: IRE1 in cell fate regulation. Trends Biochemical Sci. 2014;39(5):245–54. https://doi.org/10.1016/j.tibs.2014.02.008.
11. Marquez Y, Höpfler M, Ayatollahi Z, Barta A, Kalyna M. Unmasking alternative splicing inside protein-coding exons defines exitrons and their role in proteome plasticity. Genome Res. 2015;25(7):995–1007. https://doi.org/10.1101/gr.186585.114.

12. Tilgner H, Jahanbani F, Blauwkamp T, Moshrefi A, Jaeger E, Chen F, et al. Comprehensive transcriptome analysis using synthetic long-read sequencing reveals molecular co-association of distant splicing events. Nat Biotechnol. 2015;33(7):736–42. https://doi.org/10.1038/nbt.3242.
13. Sharon D, Tilgner H, Grubert F, Snyder M. A single-molecule long-read survey of the human transcriptome. Nat Biotechnol. 2013;31(11):1009–14. https://doi.org/10.1038/nbt.2705.
14. Byrne A, Beaudin AE, Olsen HE, Jain M, Cole C, Palmer T, et al. Nanopore long-read RNAseq reveals widespread transcriptional variation among the surface receptors of individual B cells. Nat Commun. 2017;8(1):16027. https://doi.org/10.1038/ncomms16027.
15. Hu T, Chitnis N, Monos D, Dinh A. Next-generation sequencing technologies: An overview. Human Immunol. 2021. https://doi.org/10.1016/j.humimm.2021.02.012.
16. Liu H, Begik O, Lucas MC, Ramirez JM, Mason CE, Wiener D, et al. Accurate detection of m6A RNA modifications in native RNA sequences. Nat Commun. 2019;10(1):4079. https://doi.org/10.1038/s41467-019-11713-9.
17. Hurtz C, Wertheim GB, Loftus JP, Blumenthal D, Lehman A, Li Y, et al. Oncogene-independent BCR-like signaling adaptation confers drug resistance in Ph-like ALL. J Clin Invest. 2020;130(7):3637–53. https://doi.org/10.1172/JCI134424.
18. Cocquet J, Chong A, Zhang G, Veitia RA. Reverse transcriptase template switching and false alternative transcripts. Genomics. 2006;88(1):127–31. https://doi.org/10.1016/j.ygeno.2005.12.013.
19. Zhang YJ, Pan HY, Gao SJ: Reverse transcription slippage over the mRNA secondary structure of the LIP1 gene. Biotechniques. 2001;31:1286.
20. Workman RE, Tang AD, Tang PS, Jain M, Tyson JR, Razaghi R, et al. Nanopore native RNA sequencing of a human poly(A) transcriptome. Nat Methods. 2019;16(12):1297–305. https://doi.org/10.1038/s41592-019-0617-2.
21. Chen Y, Davidson NM, Wan YK, Patel H, Yao F, Low HM, Hendra C, Watten L, Sim A, Sawyer C, et al: A systematic benchmark of Nanopore long read RNA sequencing for transcript level analysis in human cell lines. bioRxiv. 2021:2021.2004.2021.440736.
22. Sanchez-Vega F, Mina M, Armenia J, Chatila WK, Luna A, La KC, et al. Oncogenic signaling pathways in The Cancer Genome Atlas. Cell. 2018;173(2):321–37 e310. https://doi.org/10.1016/j.cell.2018.03.035.
23. Wang TY, Liu Q, Ren Y, Alam SK, Wang L, Zhu Z, et al. A pan-cancer transcriptome analysis of exitron splicing identifies novel cancer driver genes and neoepitopes. Mol Cell. 2021;81(10):2246–2260.e12. https://doi.org/10.1016/j.molcel.2021.03.028.
24. Qin Y, Yao J, Wu DC, Nottingham RM, Mohr S, Hunicke-Smith S, Lambowitz AM: High-throughput sequencing of human plasma RNA by using thermostable group II intron reverse transcriptases. RNA. 2015;22(1):111–28. https://doi.org/10.1261/rna.054809.115.
25. Tardaguila M, de la Fuente L, Marti C, Pereira C, Pardo-Palacios FJ, Del Risco H, et al. SQANTI: extensive characterization of long-read transcript sequences for quality control in full-length transcriptome identification and quantification. Genome Res. 2018;28(3):396–411. https://doi.org/10.1101/gr.222976.117.
26. Pleasance ED, Cheetham RK, Stephens PJ, McBride DJ, Humphray SJ, Greenman CD, et al. A comprehensive catalogue of somatic mutations from a human cancer genome. Nature. 2010;463(7278):191–6. https://doi.org/10.1038/nature08658.
27. Juszkiewicz S, Hegde RS: Initiation of quality control during poly(A) translation requires site-specific ribosome ubiquitination. Mol Cell. 2017; 65:743-750.e744.
28. Li H. Minimap2: pairwise alignment for nucleotide sequences. Bioinformatics. 2018;34(18):3094–100. https://doi.org/10.1093/bioinformatics/bty191.
29. Pertea M, Pertea GM, Antonescu CM, Chang TC, Mendell JT, Salzberg SL. StringTie enables improved reconstruction of a transcriptome from RNA-seq reads. Nat Biotechnol. 2015;33(3):290–5. https://doi.org/10.1038/nbt.3122.
30. Pertea G, Pertea M: GFF Utilities: GffRead and GffCompare. F1000Res 2020; 9.
31. Cortés-López M:IntronArtifacts. Github. 2021. https://github.com/mcortes-lopez/IntronArtifacts/tree/v1.0.1.
32. Cortés-López M:IntronArtifacts: exon2part. Zenodo. 2021. https://zenodo.org/record/4906611.
33. Frankish A, Diekhans M, Ferreira AM, Johnson R, Jungreis I, Loveland J, et al. GENCODE reference annotation for the human and mouse genomes. Nucleic Acids Res. 2019;47(D1):D766–d773. https://doi.org/10.1093/nar/gky955.
34. Lawrence M, Huber W, Pages H, Aboyoun P, Carlson M, Gentleman R, et al. Software for computing and annotating genomic ranges. PLoS Comput Biol. 2013;9(8):e1003118. https://doi.org/10.1371/journal.pcbi.1003118.
35. Frazee AC, Langmead B, Leek JT. ReCount: A multi-experiment resource of analysis-ready RNA-seq gene count datasets. BMC Bioinformatics. 2011;12(1):449. https://doi.org/10.1186/1471-2105-12-449.
36. Wilks C, Ahmed O, Baker DN, Zhang D, Collado-Torres L, Langmead B. Megadepth: efficient coverage quantification for BigWigs and BAMs. Bioinformatics. 2021. https://doi.org/10.1093/bioinformatics/btab152.
37. Wagih O. ggseqlogo: a versatile R package for drawing sequence logos. Bioinformatics. 2017;33(22):3645–7. https://doi.org/10.1093/bioinformatics/btx469.
38. Schulz L; Torres-Diz, M; Cortés-López, M; Hayer, KE; Asnani, M; Tasian, SK; Barash, Y; Sotillo, E; Zarnack, K; König, J; Thomas-Tikhonenko, A:Direct long-read RNA sequencing identifies a subset of questionable exitrons likely arising from reverse transcription artifacts. Datasets. Gene Expression Omnibus. https://www.ncbi.nlm.nih.gov/sra/?term=SRR14326969; https://www.ncbi.nlm.nih.gov/sra/?term=SRR14326970; https://www.ncbi.nlm.nih.gov/sra/?term=SRR14326971; https://www.ncbi.nlm.nih.gov/sra/?term=SRR14326972; https://www.ncbi.nlm.nih.gov/sra/?term=SRR14326973. (2021)

Publisher's Note

Direct long-read RNA sequencing identifies a subset of questionable exitrons likely arising from reverse transcription artifacts

Laura Schulz[1*], Manuel Torres-Diz[2*], Mariela Cortés-López[1*], Katharina E. Hayer[3*], Mukta Asnani[2], Sarah K. Tasian[4], Yoseph Barash[5], Elena Sotillo[2&], Kathi Zarnack[6], Julian König[1#], and Andrei Thomas-Tikhonenko[2,7 #]

[1] Institute of Molecular Biology (IMB), Ackermannweg 4, 55128 Mainz, Germany. [2] Division of Cancer Pathobiology, Children's Hospital of Philadelphia, Philadelphia, PA 19104, US. [3] The Bioinformatics Group, Children's Hospital of Philadelphia, Philadelphia, PA 19104, US. [4] Division of Oncology, Children's Hospital of Philadelphia, Philadelphia, PA 19104, US. [5] Department of Genetics, Perelman School of Medicine at the University of Pennsylvania, Philadelphia, PA 19104, US. [6] Buchmann Institute for Molecular Life Sciences (BMLS), Goethe University Frankfurt, Max-von-Laue-Str. 15, 60438 Frankfurt, Germany. [7] Department of Pathology & Laboratory Medicine, Perelman School of Medicine at the University of Pennsylvania, Philadelphia, PA 19104, US.

* These authors contributed equally.

[&] Present address: Stanford Cancer Institute, 265 Campus Dr., Stanford, CA 94305

[#] Corresponding authors: Julian König (j.koenig@imb-mainz.de) and Andrei Thomas-Tikhonenko (andreit@pennmedicine.upenn.edu)

SUPPLEMENTARY FIGURES

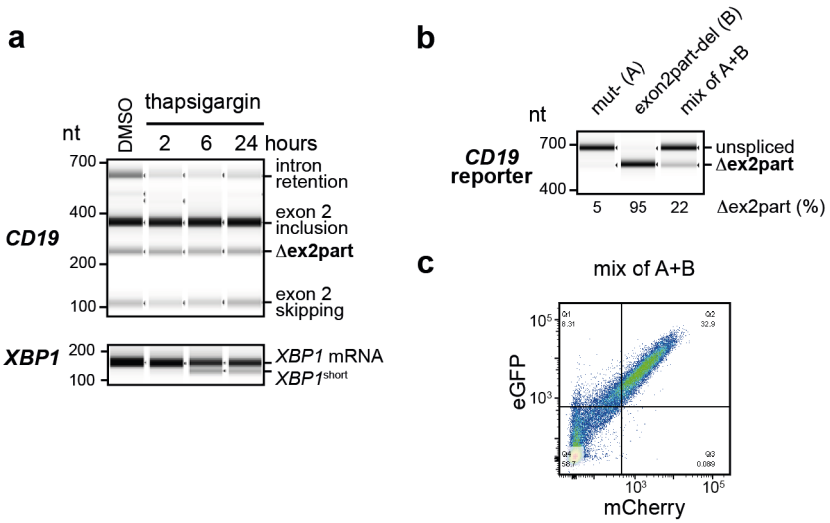

Figure S1. Levels of the Δex2part product are not affected by thapsigargin treatment. a) RT-PCR experiments followed by capillary electrophoresis to quantify different *CD19* and *XBP1* isoforms. NALM-6 cells were treated with thapsigargin for indicated time intervals. **b)** RT-PCR experiments followed by capillary electrophoresis to quantify different *CD19* isoforms in HEK293T cells transfected with a mixture of mut- (A; does not produce Δex2part band) and exon2part-del (B; the reported intron is removed at the DNA level) reporter constructs. **c)** Flow cytometry-based assay performed on the same cells.

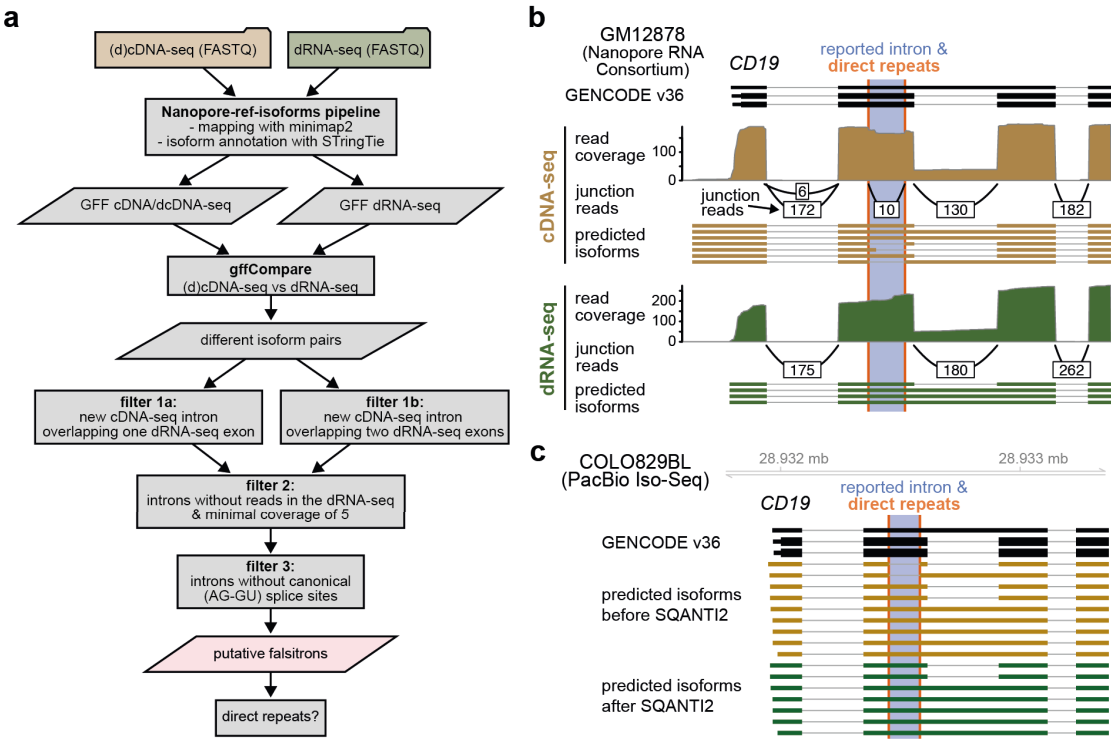

Figure S2. The workflow to detect falsitrons captures the truncated *CD19* Δex2part product. a) Extended schematic representation of the workflow to identify questionable exitrons (dubbed "falsitrons"). **b)** Genome browser view depicting detection of the *CD19* falsitron (Δex2part) in ONT cDNA-seq, but not dRNA-seq data from the Nanopore RNA Consortium. **c)** Genome browser view shows that the *CD19* falsitron (Δex2part) is detected in PacBio Iso-Seq experiments but is filtered out when applying SQANTI2.

Chapter 3

High-throughput mutagenesis identifies mutations and RNA binding proteins controlling *CD19* splicing and CART-19 therapy resistance

Summary

B-cell acute lymphoblastic leukaemia (B-ALL) is the most common type of cancer in children. Several therapies have been developed for this disease, CAR(Chimeric antigen receptor)T-19 is considered one of the most successful. For this therapy, modified T-cells express a CAR that recognizes the CD19 epitope on the surface of cancerous B cells, inducing their elimination. However, it has been estimated that up to ∼15% of patients experience a relapse after treatment. In almost half of the cases the relapse could be linked to the loss of the CD19 receptor from the surface, often due to errors in splicing of exon 2 in the *CD19* gene. Bearing in mind that alterations in splicing can be detrimental, we aimed to dissect the splicing regulatory network controlling the alternative splicing of *CD19* exon 2. We developed a massively parallel reporter assay using more than 10,000 wild-type and mutated minigenes containing the first three exons of *CD19*. By measuring the RNA products of each minigene we identified point mutations that influence the splicing of CD19. Some of these mutations lead to the generation of cryptic isoforms, many of which will not produce a functional CD19 receptor. Along with these cryptic isoforms, we also detected mutations resulting in the retention of *CD19* intron 2 , which has been linked to relapse in CART-19 patients. Given that the control of splicing is highly

dependent on *trans*-regulators like RNA binding proteins, we also complemented our results with data from other B-ALL cohorts and state-of-the-art prediction tools to characterise potential RBP regulators. We identified 6 RBPs with strong effects on CD19 splicing, PTBP1 being one of the strongest regulators of the intron 2 retention isoform. In summary, this approach allowed us to clarify the mechanisms of splicing regulation in *CD19* and in future may, contribute to predicting the success of a therapy before treatment.

Zusammenfassung

Spleißfehler werden häufig mit Krankheiten in Verbindung gebracht, beeinflussen aber auch das Ansprechen auf eine Therapie. Neuere Studien haben berichtet, dass relativ kurze Introns, die aus annotierten Exons hervorgehen (sogenannte “Exitrons”), für Krankheiten relevant sein könnten und vor allem eine Quelle für neue Epitope darstellen. Ein aktuelles Beispiel für ein solches Exitron wurde im CD19-Gen beschrieben. CD19 ist das Target für die CAR(Chimeric Antigen Receptor)T-19 Therapie gegen akute lymphoblastische B-Zell-Leukämie (B-ALL). Ein Exitron, das sich aus Exon 2 von *CD19* ergibt, wurde kürzlich mit dem Ansprechen auf Blinatumomab bei der CART-19 Behandlung in Verbindung gebracht. Dieses Exitron hat keine kanonischen Spleißstellen und es wurde vermutet, dass es ein Produkt des nicht-nuklearen Spleißens durch IRE1 ist. Hier zeigen wir, dass der *CD19* ex2Δ-Teil ein Produkt des Abrutschens der künstlichen Polymerase während der reversen Transkription (RT) ist. Wir haben einen dualen Fluoreszenzreporter entwickelt, um die Erzeugung dieser potenziellen Isoform zu testen, und wir konnten keinen Beweis dafür finden, dass diese Isoform auf RNA-Ebene existiert. Darüber hinaus haben wir Nanopore (ONT) cDNA- und direkte RNA-Sequenzierungsdaten (dRNA) von Xenotransplantaten von Patienten mit B-ALL verglichen und festgestellt, dass der *CD19* ex2Δ-Teil nur in den Protokollen mit RT nachgewiesen werden konnte. Wir erweiterten unsere Analyse, um eine bioinformatische Pipeline zu erstellen, die es uns ermöglichen würde, ähnliche “Falsitrons” (falsche Exitrons) auf globaler Ebene zu identifizieren. Unter Verwendung öffentlich zugänglicher Datensätze konnten wir insgesamt 57 Falsitrone nachweisen. Die meisten dieser Falsitrons haben gemeinsame Merkmale mit *CD19* ex2Δpart: z.B. das Vorhandensein von direkten Wiederholungen an den Spleißstellen, die das RT-Slippage-Ereignis erklären können. Abschließend schlagen wir die Verwendung von ONT dRNA als ergänzenden Ansatz vor, um neue Isoformen zu charakterisieren, die bei Protokollen, die RT- und Amplifikationsschritte erfordern, fälschlicherweise erzeugt werden könnten.

Statement of contribution

This work is part of Laura Schulz and my main project. We designed the library, Laura performed the experiments, and I performed most of the bioinformatical analysis including the DNA mutational barcode demultiplexing and variant calling, quantification of mutation effects, data acquisition and reanalysis of published patient data, RBP predictions, SpliceAI and MaxEnt analysis, comparisons with the prevalence scores and other downstream analysis specified in the manuscript. I prepared most of the figures and wrote the corresponding methods. I also reviewed and contributed to the main text and supplementary material. I organised and participated in the discussion meetings and contributed to the interpretation of the results.

Supervisor confirmation: _____

High-throughput mutagenesis identifies mutations and RNA-binding proteins controlling *CD19* splicing and CART-19 therapy resistance

Mariela Cortés-López[1#], Laura Schulz[1#], Mihaela Enculescu[1#], Claudia Paret[2], Bea Spiekermann[1], Anke Busch[1], Anna Orekhova[1], Fridolin Kielisch[1], Mathieu Quesnel-Vallières[3], Manuel Torres-Diz[4], Jörg Faber[2], Yoseph Barash[3], Andrei Thomas-Tikhonenko[4,5], Kathi Zarnack[6*], Stefan Legewie[1,7*], and Julian König[1*]

Affiliations:
[1] Institute of Molecular Biology (IMB), Ackermannweg 4, 55128 Mainz, Germany
[2] Department of Pediatric Hematology/Oncology, Center for Pediatric and Adolescent Medicine, University Medical Center of the Johannes Gutenberg University Mainz, 55131 Mainz, Germany & University Cancer Center (UCT), University Medical Center of the Johannes Gutenberg University Mainz, 55131 Mainz & German Cancer Consortium (DKTK), site Frankfurt/Mainz, Germany, German Cancer Research Center (DKFZ), 69120 Heidelberg, Germany
[3] Department of Genetics, Perelman School of Medicine at the University of Pennsylvania, Philadelphia, PA 19104, US and Department of Biochemistry and Biophysics, Perelman School of Medicine at the University of Pennsylvania, Philadelphia, PA 19104, US
[4] Division of Cancer Pathobiology, Children's Hospital of Philadelphia, Philadelphia, PA 19104, US
[5] Department of Pathology & Laboratory Medicine, Perelman School of Medicine at the University of Pennsylvania, Philadelphia, PA 19104, US
[6] Buchmann Institute for Molecular Life Sciences (BMLS) and Faculty Biological Sciences, Goethe University Frankfurt, Max-von-Laue-Str. 15, 60438 Frankfurt, Germany
[7] Department of Systems Biology and Stuttgart Research Center for Systems Biology (SRCSB), University of Stuttgart, Stuttgart, Germany

# These authors contributed equally.
* Corresponding authors: Kathi Zarnack (kathi.zarnack@bmls.de), Stefan Legewie (legewie@iig.uni-stuttgart.de), Julian König (j.koenig@imb-mainz.de)

Keywords: *CD19*, B-ALL, CART-19 therapy, relapse, massively parallel reporter assay, *cis*-regulatory mutations, *trans*-acting regulators, cryptic splice sites, modelling, PTBP1

Abstract

During CART-19 immunotherapy for B-cell acute lymphoblastic leukaemia (B-ALL), many patients relapse due to loss of the cognate CD19 epitope. Since epitope loss can be caused by aberrant *CD19* exon 2 processing, we herein investigate the regulatory code that controls *CD19* splicing. We combine high-throughput mutagenesis with mathematical modelling to quantitatively disentangle the effects of all mutations in the region comprising *CD19* exons 1-3. Thereupon, we identify ~200 single point mutations that alter *CD19* splicing and thus could predispose B-ALL patients to CART-19 resistance. Furthermore, we report almost 100 previously unknown splice isoforms that emerge from cryptic splice sites and likely encode non-functional CD19 proteins. We further identify *cis*-regulatory elements and *trans*-acting RNA-binding proteins that control *CD19* splicing (e.g., PTBP1 and SF3B4) and validate that loss of these factors leads to enhanced *CD19* mis-splicing. Our dataset represents a comprehensive resource for potential prognostic factors predicting success of CART-19 therapy.

Highlights

- Mutations in relapsed CART-19 patients lead to *CD19* mis-splicing
- High-throughput mutagenesis uncovers ~200 single point mutations with a potential role in CART-19 therapy resistance
- Many mutations generate non-functional CD19 proteins by activating cryptic splice sites
- RNA-binding proteins such as PTBP1 are key to the expression of properly spliced, CART-19 immunotherapy-sensitive isoforms

Introduction

B-cell acute lymphoblastic leukaemia (B-ALL) is a hematologic malignancy which causes a significant number of childhood and adult cancer deaths. In CART-19 immunotherapy, chimeric antigen receptor-armed autologous T-cells (CARTs) are engineered to target the surface antigen CD19 on B-cells by linking the single-chain variable fragment (scFv) of an anti-CD19 antibody to the intracellular signalling domain of the T-cell receptor [1]. Upon CD19 recognition, the chimeric antigen receptors activate the cytotoxic T-cells to attack the tumour cells. CART-19 therapy was recently approved for the treatment of paediatric B-ALL in the US and Europe. Unfortunately, up to 50% of children relapse under CART-19 therapy, and response rates are even worse in adults [2,3]. Several studies reported that in 40-60% of cases the cancerous B-cells get invisible to the CARTs due to loss of detectable CD19 epitope (CD19-negative) [4-7]. This recurrently involves alternative splicing of the *CD19* pre-mRNA [8-10].

Splicing comprises the excision of introns and the joining of exons by the spliceosome to generate mature mRNAs. During alternative splicing, certain exons can be either included or excluded ("skipped"), thus leading to different transcript isoforms. The splicing outcome at each exon is controlled by a large set of *cis*-regulatory elements in the RNA sequence which are recognised by *trans*-acting RNA-binding proteins (RBPs) that guide the spliceosome activity. It is increasingly recognised that widespread alterations in splicing are a molecular hallmark of cancer and often contribute to therapeutic resistance (reviewed in [11]). For instance, intron retention, i.e., the failure to remove certain introns, often disrupts the open reading frame with premature termination codons (PTCs) and thereby compromises the expression of the encoded proteins. Consistent with the widespread splicing changes, cancer-causing driver mutations frequently occur in splice-regulatory *cis*-elements, and many splicing factors have oncogenic properties, being commonly mutated or dysregulated in cancer [11-13].

Multiple alternative splicing events in *CD19* mRNA have been described to interfere with CART-19 therapy [8,10,14-17]. Most prominently, skipping of exon 2 results in a truncated CD19 protein which is no longer presented on the cell surface and hence fails to trigger CART-19-mediated killing [8,14]. In addition, it was reported that relapsed patients showed retention of intron 2 which introduces a PTC, thereby disrupting CD19 expression [10]. Similarly, simultaneous skipping of exons 5 and 6 introduces a PTC [8]. The splicing alterations can be caused by mutations within the *CD19* gene or by changes in the expression of *trans*-acting RBPs. For instance, it has been suggested that the known splicing regulator SRSF3 binds to *cis*-regulatory elements within *CD19* exon 2 to promote its inclusion [8]. Of note, alternative *CD19* isoforms showing exon 2 skipping were observed to pre-exist in patients prior to CART-19 therapy [15,16], suggesting that *CD19* splicing patterns may harbour prognostic information and could be modulated to re-establish sensitivity to CART-19 mediated killing. However, Orlando and co-workers suggested that alternative splicing changes in B-ALL patients are present in diagnostic samples at low frequency and may not contribute meaningfully to CD19 epitope loss [4]. We therefore set out to investigate *CD19* alternative splicing and its molecular determinants in B-ALL in more detail.

High-throughput mutagenesis screens combined with next-generation sequencing provide comprehensive insights into the regulatory code of splicing [18-21]. The interpretation of such data is challenging, as the mutation effects often depend on other mutations and are typically most pronounced at intermediate exon inclusion levels [18,19,22]. We and others have shown

by mathematical modelling that kinetic models account for the context-dependence of mutation effects on splice isoforms [18,19]. By these models, systems-level insights can be gained into complex *cis*-regulatory landscapes, effects of *trans*-acting RBPs and principles of splicing regulation [18,19,23].

In this manuscript, we combine B-ALL patient data with high-throughput mutagenesis, mathematical modelling and RBP knockdowns to comprehensively characterise *cis*-regulatory mutations and *trans*-acting RBPs controlling *CD19* exon 2 splicing. Unlike previous mutagenesis screens, we determine all intronic and exonic mutation effects in a 1.2 kb region and quantify the abundance of 100 alternative isoforms, including intron 2 retention and alternative 3'/5' splice site usage. Many of these isoforms encode for a non-functional CD19 protein and are therefore likely to impair CART-19 therapy. By *in silico* analyses and RBP knockdowns, we identify *trans*-regulators of *CD19* splicing that promote the production of the therapy-relevant isoforms. Taken together, our dataset is a comprehensive resource for prognostic markers of CART-19 therapy resistance and for a systems-level understanding of the splicing code.

Results

CART-19 patients show increased *CD19* intron 2 retention after relapse

To resolve the contribution of *CD19* splicing in CART-19 therapy, we re-analysed RNA-seq data from Orlando and co-workers [4], in which B-ALL cells of 17 patients were sequenced at initial screening and after relapse. In contrast to the original study, we expanded the analyses to intron retention surrounding *CD19* exon 2. We found that the average frequency of retention of intron 2 across patients significantly increases from 63% before therapy to 82% after relapse (*P* value = 0.022, Wilcoxon signed-rank test; **Figure 1A, B**). The trend towards higher intron 2 retention is preserved in 7 out of 10 individual patients that were sequenced both before therapy and after relapse (**Figure 1B**). Since the resulting isoform does not encode the CD19 epitope, this suggests that increased intron 2 retention contributes to CART-19 therapy relapse as reported in a recent study [10].

Somatic mutations in relapsed patients cause splicing alterations

The majority of relapsed patients in the Orlando study (12 out of 17) [4] harbour somatic mutations within the *CD19* gene, including frameshift insertions, deletions and single nucleotide missense variants. We selected nine mutations in exons 2 or 3 from eight patients for further analysis (**Table S1**). To test for effects on splicing, we constructed a minigene reporter that harbours *CD19* exon 1-3 including the two intervening introns 1 and 2 (**Figure 1C**). We confirmed that the minigene gives rise to the same transcript isoforms as the endogenous gene in the human B-ALL cell line NALM-6 (**Figure 1D, E**). When introducing the patient mutations into our minigene reporter, we found that six out of nine tested mutations lead to the production of alternative *CD19* isoforms linked to CART-19 therapy resistance (**Figure 1F, G**): The mutation from patient #2 induces exon 2 skipping, while mutations from patients #4 and #14.2 cause intron 2 retention. In addition, three mutations enhance the production of an additional isoform that uses an alternative 3' splice site in exon 2 (termed alt-exon2; mutations from patients #5, #14.1 and #15). The alternative splice junction in alt-exon2 introduces a frameshift causing a PTC and will hence abolish the production of a targetable CD19 epitope. We note that as reported by Orlando and co-workers [4], most of the tested mutations also introduce frameshifts, making it difficult to discriminate between PTC-induced and splicing-mediated defects. For instance, the alternative 3' splice site of alt-exon2, which is prevalent in patient #5, in fact compensates for the frameshift that is introduced by the concomitant deletion, i.e., restores the open reading frame (**Figure S1A**). Thus, taking the splicing information into account changes the interpretation of what CD19 protein variants are expressed in a given patient. More broadly speaking, these results suggest that *CD19* mutations in CART-19 relapse patients frequently trigger splicing changes that potentially influence therapeutic outcomes.

High-throughput screening of *CD19* exons 1-3 alternative splicing

To systematically study the effects of point mutations on *CD19* exons 1-3 splicing, we adopted our previously developed massively parallel splicing reporter assay [18] (**Figure 2A**). To this end, we randomly introduced point mutations as well as short insertions and deletions into the *CD19* minigene reporter by error-prone PCR. This yielded a pool of 10,295 minigene variants, each with a different set of mutations and tagged with a unique 15-nt barcode sequence. As an internal control, 194 wild type (WT) minigenes with distinct barcodes were added. Mutations in all minigene variants were mapped using targeted long-read DNA sequencing (DNA-seq, PacBio SMRT-seq, **Figure S1B, C**) and validated for 30 minigene clones via Sanger

sequencing. The DNA-seq data shows that the minigene variants contain on average 9.7 mutations (**Figure S1D**). This allows for a comprehensive characterisation of the mutation landscape, as each position is on average mutated in 80 different minigene variants and 90% of the mutations are present in at least four distinct minigene variants (**Figure S1E, F**). To measure splicing outcomes, the minigene pool was transfected into NALM-6 cells and the resulting transcripts were quantified by targeted RNA sequencing (RNA-seq) using 350 nt + 250 nt paired-end reads (Illumina MiSeq, **Figure S1B, S2A**). We detected around 100 different splice isoforms (see below) which were unambiguously identified by paired-end sequencing. Two replicate experiments showed high correlation in the measured isoform frequencies (R between 0.91 and 0.98 for the different isoforms, **Figure S2B**). Based on the common barcode sequence, information from DNA and RNA sequencing could be combined, linking mutations at the DNA level to frequencies of RNA splice isoforms for a total of 10,295 minigenes in two replicate experiments (**Table S2**).

Therapy-relevant isoforms accumulate in response to numerous point mutations

To our surprise, the screen revealed a high complexity of *CD19* exon 1-3 splicing, with a total of 101 alternative isoforms occurring with a frequency of ≥5% of all transcripts in at least two minigene variants (**Table S3**). Out of these, the five major isoforms exceed 1% in WT minigenes, whereas the others, termed cryptic isoforms, only accumulate in mutated minigene variants (**Figure 2B**). In WT, the by far most abundant major isoform is exon 2 inclusion (termed “inclusion”, followed by exon 2 skipping (termed “skipping”) and intron 2 retention (termed “intron2-retention”). Two additional major isoforms in WT originate from alternative 3’ splice site usage within exon 2 (alt-exon2) and 3 (alt-exon3) (**Figure 2B, C**). Notably, alt-exon2 is the same isoform as observed upon patient mutations above. As expected, the measured frequencies for the major isoforms show little variance for the 194 unmutated WT minigenes (standard deviation < 6%, **Figure 2C**). In contrast, many mutated minigene variants show strong changes relative to WT, suggesting a large impact of specific mutations on splicing outcomes (**Figure 2C**). For instance, all minigenes with a mutation in the 3’ splice site of exon 2 lose the inclusion isoform, accompanied by strong alterations in the remaining major isoforms. Taken together, these observations support the accuracy of our screening results.

All major isoforms, except exon 2 inclusion, encode for a truncated CD19 receptor lacking a functional CART-19 epitope and could thus contribute to therapy resistance. Our unbiased screening approach extends the list of potentially therapy-relevant *CD19* mutations, since 1,721 out of 9,127 mutated minigenes show exon 2 skipping, intron 2 retention and/or alt-exon2 isoform frequencies of >25% (**Figure 2C**). However, since the minigene variants carry on average 9.7 point mutations, the observed splicing changes represent the combined effects of several mutations. To extract the impact of individual mutations, we adapted our previous mathematical modelling framework [18] and implemented a multinomial logistic regression approach. Here, the splicing change in each minigene variant is described as the sum of the underlying point mutation effects (**Figure 3A**, see Methods). These single mutation effects are unknown and are determined by simultaneously fitting the model to all minigene measurements. Thereby, we were able to infer the individual effects of 4,255 point mutations on the five major isoforms (**Figure 3A, S3A**). We validated the reliability of this model in describing combined mutations using a 10-fold cross-validation approach, in which we left out 10% of all minigene variants from fitting and were able to accurately predict them after model fitting (Pearson correlation coefficients 0.65-0.95; **Figure 3B, S3B**). Furthermore, the model performed well in predicting single mutation effects, as soon as a mutation occurred in three

or more minigenes in the dataset (**Figure S4C**), which applied to 90% of all mutations (**Figure S1F**).

Out of 4,255 quantified single mutation effects, we find 193 splicing-effective mutations that significantly alter the frequency of at least one isoform in the two replicates beyond the 2.5 and 97.5% quantiles of the WT minigene distribution (**Figure 3C, Table S4, Data S1**). 33 of these splicing-effective mutations overlap with single nucleotide variants (SNVs) that were previously reported in the human population from whole-genome or exome sequencing data (**Table S5**). The strongest mutation effects accumulate around the four main splice sites and throughout exon 2 and correspond to the core *cis*-regulatory elements, such as splice-site dinucleotides, branchpoint and polypyrimidine tract, as well as auxiliary elements (**Figure 3C, D**). Inspecting in more detail the 83 mutations that specifically impact on *CD19* exon 2 skipping, we find them to cluster within and around exon 2. In particular, 21% of all positions within exon 2 (55 out of 267 nt) harbour at least one splicing-effective mutation, suggesting that *CD19* exon 2 is densely packed with *cis*-regulatory elements controlling its inclusion. In addition, we observe smaller clusters of mutations within the introns and flanking constitutive exons which likely represent more distal *cis*-regulatory elements (**Figure 3C**). Similarly, we explored the 54 splicing-effective mutations that impact on intron 2 retention. As expected, strongest effects are observed at the splice sites of intron 2. In addition, we find clusters of mutations in intron 2 and exon 3 that might reflect important *cis*-regulatory elements. The effect of all mutations on the five major isoforms can be explored in **Data S1**.

In conclusion, our combined screening and modelling approach quantitatively describes alternative splicing of *CD19* exons 1-3 by predicting the effects of all individual point mutations and combinations thereof. Our screen thereby represents a comprehensive resource for the identification of mutations with clinical relevance in CART-19 therapy resistance.

Cryptic isoforms destroy the *CD19* ORF and are associated with recurrent mutations

Besides the five major isoforms, the *CD19* exons 1-3 can give rise to 96 cryptic isoforms which are rare (<1%) in WT, but accumulate upon certain mutations (**Figure 2B, Table S3**). The cryptic isoforms involve a total of 71 cryptic splice sites (**Figure 4A**). Of note, 33 of these cryptic isoforms make up more than 50% of total transcripts and are therefore dominant in certain minigene variants (**Figure 2B, C**). To assess whether these cryptic isoforms impact on CD19 epitope presentation, we analysed their coding potential and found that the vast majority of cryptic *CD19* isoforms (78 out of 96) show a frameshift and/or carry a PTC (**Figure 4B**). This will either lead to the production of truncated CD19 peptides that likely do not allow for presentation on the cell surface [14] or will induce nonsense-mediated mRNA decay of the cryptic isoforms and will hence reduce *CD19* transcript and protein levels.

To derive a mechanistic understanding of cryptic isoform biogenesis, we analysed the underlying point mutations. To this end, we calculated a prevalence score which quantifies the degree of association between an isoform and a point mutation. This was done based on the measured isoform frequencies in the minigene library by multiplying: (i) the frequency of a mutation being present if the isoform level is high (>5%), and (ii) the frequency of the isoform level being high given that the mutation is present. A prevalence score of 1 indicates perfect correspondence between mutation and isoform, whereas a prevalence score of 0 is observed if they are unrelated. This score-based analysis showed that 36 cryptic isoforms are specifically associated with 31 specific point mutations (38 mutation-isoform pairs with prevalence score > 0.25, **Figure S4A, Table S3**). The remaining 60 cryptic isoforms do not show a specific association, implying that they can either be generated by multiple redundant

mutations, or that our screen lacks sufficient coverage to support a reliable association. To directly test the predicted associations, we introduced five mutations with a specific association to a cryptic isoform in our minigene reporter (C535G, chr16:28932405, prevalence score = 0.18; C806A, chr16:28932676, 0.68; A827T, chr16:28932697, 0.93; C864G, chr16:28932875, 1; G1005A, chr16:28932734, 0.89). Semi-quantitative RT-PCR confirmed that all five tested mutations lead to the appearance of the associated cryptic isoform (**Figure 4C, D**).

Altogether, our analysis provides a list of 31 mutations that are likely to trigger cryptic isoform formation. Importantly, the resulting cryptic isoforms show a maximum usage of up to 91% (**Table S3**), which is likely to drastically interfere with normal *CD19* splicing, protein production and subsequent epitope presentation. The associated mutations may thus provide predictive biomarkers for CART-19 therapy response in the future.

The cryptic isoforms are caused by mutations that disrupt or create splice sites

Due to their potential clinical relevance, we wanted to learn more about how the mutations activate the cryptic isoforms. We found that the majority of mutations with a prevalence score > 0.25 are either in close proximity or directly overlap with the associated cryptic splice site (78.9% with distance < 5 nt; **Figure 4E**). Further inspection showed that the underlying mutations either destroy the original splice site (7.9%) or generate a new cryptic splice site (57.9%). Hence, the cryptic isoforms do originate from the generation or destruction of core *cis*-regulatory elements rather than affecting auxiliary elements.

Currently, major efforts are ongoing to implement artificial intelligence (AI) tools to predict the effect of clinical variants on the splicing outcome. We therefore tested whether the state-of-the-art neural network [24], which predicts changes in the splicing patterns induced by single point mutations, captures the gain and loss of splice sites in *CD19*. To this end, we applied SpliceAI using all possible single point mutations in the *CD19* minigene as an input. Similar to the results from our mutagenesis screen (**Figure 4A**), SpliceAI predicts cryptic splice site activation by mutations throughout the minigene, with an increased density around the 3' splice site of exon 3 (**Figure S4B**). All SpliceAI-predicted mutations are close to the affected cryptic splice sites (**Figure S4C**). Hence, SpliceAI successfully reflects the global landscape of mutation-induced cryptic splice site activation in the *CD19* minigene.

With respect to the accuracy of the individual predictions, we found that 10 out of 38 mutations with strong SpliceAI predictions (SpliceAI score > 0.5) indeed lead to the accumulation of splice isoforms with the corresponding cryptic splice sites in the experimental data (prevalence score > 0.25, **Figure 4F**). In the remaining 28 cases, either weak overall cryptic splice site activation occurred in the data (9 cases) or a different cryptic splice site was activated than predicted by SpliceAI (19 cases; **Figure S4B**). In quantitative terms, the likelihood of a cryptic splice site activation according to the SpliceAI prediction ("SpliceAI score") is correlated to the magnitude of the prevalence score linking the mutation to the corresponding cryptic isoform in our screen (**Figure 4F**). Overall, the comparison supports that SpliceAI can guide the interpretation of mutation effects in clinical samples, though direct experimental validation is necessary. As such, our data can be used to benchmark new tools for splicing prediction.

The cryptic isoforms arise from numerous 3' and 5' cryptic splice sites that distribute over the entire minigene and accumulate at exon 3 (**Figure 4A**). In line with a high penetrance, 26 cryptic splice sites reach more than 50% usage upon certain mutations, particularly around the start of exon 3. We hypothesised that cryptic splice site activation occurs in exon 3 because

its canonical splice site can be outcompeted by neighbouring cryptic sites. To test this, we scored the strength of local consensus sequences using MaxEntScan [25], and indeed found that the 3' splice site of exon 3 is weak compared to all other canonical splice sites of *CD19* exons 1-3 (**Figure 4G, S4D, E**). In line with our hypothesis, mutations around the 3' splice site of exon 3 frequently create stronger splice sites than elsewhere in the minigene that exceed the strength of the canonical 3' splice site of exon 3 (**Figure 4G**). This suggests that weak splice sites are particularly vulnerable for the activation of competing cryptic splice sites and should be of particular interest when assessing the impact of clinical variants on splicing outcomes.

An extensive network of RBP regulators might drive *CD19* mis-splicing

Besides *CD19* mutations, CART-19 therapy resistance may also stem from altered expression of *trans*-acting RBPs which bind to the *CD19* pre-mRNA to control alternative splicing. To identify putative RBP regulators, we explored publicly available databases containing experimentally determined RBP binding motifs (ATtRACT [26], oRNAment [27]). Furthermore, we employed DeepRiPe [28], a neural network-based algorithm trained on PAR-CLIP and ENCODE eCLIP datasets that predicts changes of RBP binding upon mutation. In combination, these tools predict a total of 198 RBPs to bind within *CD19* exons 1-3 (ATtRACT: 62 RBPs; oRNAment: 70 RBPs) or to change binding upon mutation (DeepRiPe: 128 RBPs; **Figure 5A-C, S5A**).

To link the putative RBP regulators to the observed splicing changes, we overlaid the predicted binding sites (or predicted mutations for DeepRiPe) with splicing-effective mutations from our screen. Overall, we find that 79% and 60% of ATtRACT and oRNAment binding sites, respectively, overlap with a splicing-effective mutation (affecting any of the five major isoforms). Furthermore, 105 (5%) of the mutations predicted to change RBP binding by DeepRiPe overlap with splicing-effective mutations, suggesting that modulating RBP binding at these sites may have a functional impact on *CD19* splicing (**Figure 5A, S5A**). By merging these sets, we obtained a list of 119 RBPs that may regulate splicing by binding to *CD19* exons 1-3 (**Table S6**). Most of these are expressed in cancerous B-cells from B-ALL patients from [29] (80 with mean FPKM [fragments per kilobase of transcript per million mapped reads] > 10; **Figure S5B**) and could thus interfere with CART-19 therapy. Among these RBPs are SRSF3, a previously reported regulator of *CD19* splicing [8], but also new candidates such as PTBP1. Altogether, the *in silico* predictions suggest the presence of an extensive RBP network controlling *CD19* splicing that may impact on the CART-19 therapy success.

Depletion of PTBP1 and several other RBPs results in non-functional *CD19* isoforms

Based on our experimental data, *in silico* predictions, expression, literature information and manual curation, we shortlisted 11 RBP candidates for further analysis, including *SRSF3* as a positive control. To test their impact on endogenous *CD19* splicing, we generated NALM-6 cell lines stably expressing shRNAs against the shortlisted RBPs (depletion to <40% transcripts; **Figure S6A**). As previously described [8], knockdown of *SRSF3* leads to increased exon 2 skipping in the endogenous *CD19* transcripts, confirming that this SR protein is required for exon 2 inclusion (**Figure 5E, F**). Importantly, we find that knockdown of six additional RBPs (PTBP1, PCBP2, SF3B4, HNRNPK, MBNL1 and HNRNPM*)* has significant effects on *CD19* alternative splicing (**Figure 5E, F, S6B, C**). The knockdown of these factors reduces *CD19* exon 2 inclusion, while promoting intron 2 retention and/or exon 2 skipping, thus shifting the cells towards expression of relapse-associated *CD19* isoforms. This implies that reduced levels of these factors can impair targetable CD19 epitope expression.

PTBP1 stands out among the putative regulators as it shows the strongest effects on intron 2 retention, which emerged as the most prominent *CD19* mis-splicing isoform in our re-analysis of B-ALL patient data (**Figure 1B**). PTBP1 recognises clusters of UC-rich motifs [30,31]. Remarkably, ATtRACT predicts almost 100 such PTBP1 binding motifs across the studied *CD19* region, including 25 that overlap with splicing-effective mutations (**Figure 5D, Table S6**). Moreover, DeepRiPe predicts 78 mutations in 63 positions that change PTBP1 binding, out of which 10 are splicing-effective in our screen. The high number of predicted binding sites suggests a partial redundancy, indicating that PTBP1 regulation might be difficult to disrupt with individual point mutations as introduced in our screen. To experimentally test if PTBP1 binds to the predicted sites, we performed PTBP1 iCLIP2 experiments in NALM-6 cells. In line with a role in intron 2 retention, we find extensive PTBP1 binding particularly in intron 2, where it spreads over an extended cluster of predicted binding sites (**Figure 5G**). The broad binding at splicing-effective positions and beyond supports that PTBP1 is a direct and central regulator of *CD19* alternative splicing, with most prominent effects on intron 2 retention.

Given these results, we reasoned that accumulation of the *CD19* intron 2 retention isoform in B-ALL patients due to RBP dysregulation or *CD19* sequence mutations could serve as a predictive biomarker for a poor response to CART-10 therapy. To support this hypothesis, we extended our analysis of patient RNA-seq data (**Figure 1B**) to the complete panel of 220 B-ALL patients from the Therapeutically Applicable Research To Generate Effective Treatments (TARGET) program. Although these patients had not been treated with CART-19 yet, intron 2 retention appeared as the predominant isoform in almost all of them (**Figure 5H, I, S6D**). This supports previous findings [10,15] that unproductive *CD19* splicing disrupts CD19 epitope presentation B-ALL patients already prior to CART-19 therapy exposure. Therefore, the splicing-effective mutations and RBP regulators identified in this work may harbour prognostic information for CART-19 therapy success.

Discussion

Massively parallel reporter assays such as our high-throughput mutagenesis screen provide comprehensive insights into the regulatory code of splicing, as they characterise the complete set of *cis*-acting sequence mutations and reveal the binding sites of *trans*-acting RNA-binding proteins (e.g., [18-20,32-34]). The interpretation of these datasets is challenging due to nonlinear interactions of individual mutation effects. For instance, competition effects in splicing reduce the impact of individual mutations at low and high isoform frequencies, i.e., depending on the mutational background [18,19]. In addition, other factors such as RBP expression patterns and cell type/tissue identity determine the effects of sequence mutations. Using kinetic modelling, we and others derived regression models taking competition in splicing into account, thereby showing that the effects of complex mutation combinations can be quantitatively described as the sum of individual mutation effects [18,19]. Thus, mutations seem to control splicing additively rather than synergistically, and this principle also holds for *CD19* splicing.

In our *CD19* mutagenesis dataset, we comprehensively characterised the full set of splice isoforms generated in response to thousands of sequence mutations. In particular, we find that cryptic splice site activation and thus alternative 3' and 5' splice site usage are common modes of alternative splicing. Intriguingly, such events do not require extensive sequence remodelling, but can often be triggered by single point mutations, as indicated by strong associations between putative cryptic isoforms and certain nucleotide substitutions. This suggests, in accordance with previous reports [35], that neighbouring splice sites frequently compete for spliceosome assembly, especially if the canonical splice site is comparably weak. While this finding shows the enormous isoform complexity that can arise already from such a simple exon configuration, it raises the question of how protein function can be robustly maintained, since most cryptic *CD19* splicing isoforms likely encode non-functional proteins.

Unlike previous mutagenesis screens, which mainly focused on exonic sequence mutations, the present *CD19* dataset characterises the complete set of intronic and exonic mutations in a 1,200 nt sequence stretch. The complete characterisation of *CD19* exons 1-3 required the use of long-read sequencing technology. Given that introns in human protein-coding genes on average span ~8.1 kb (GENCODE v31), the long-read sequencing methodology described in this work opens the approach for broad applications. For *CD19*, we find that strong mutation effects are mainly centred around canonical and cryptic splice sites, whereas mutation effects seem to be dispersed for highly regulated exons such as *MSTR1* exon 11 [18]. This suggests that (near-)constitutive exons like *CD19* exon 2 may exhibit stronger and redundant splicing enhancers and that their inclusion is therefore less sensitive to individual point mutations [19]. More generally, constitutive exons may require more specific perturbations and as we show here, do not respond with only exon skipping, but tend to employ alternative splice site usage and intron retention, both of which are clinically relevant in the case of *CD19* splicing and CART-19 therapy resistance.

Our retrospective analyses of clinical B-ALL samples implicate unproductive *CD19* splice isoforms in the development of CART-19 therapy resistance. Using minigene assays, we directly show that *CD19* mutations that are observed in relapsed patients lead to exon 2 skipping, intron 2 retention or an additional isoform that uses an alternative 3' splice site in exon 2. Furthermore, based on our mutational scan, we report ~200 additional point mutations significantly affecting these and other therapy-relevant isoforms. Taken together, our results strongly suggest that *CD19* mutations contribute to CART-19 therapy resistance by inducing

splicing changes and likely do so by changing RBP binding sites in the *CD19* pre-mRNA. The detection of such mutations in longitudinal samples may provide predictive biomarkers for therapy response in the future.

At the same time, alterations in the expression of *trans*-acting RBPs can induce aberrant *CD19* splicing, explaining the presence of CD19-negative relapses in samples with a low allelic frequency of mutations or without mutations in the *CD19* locus. Mutations in splicing factors such as SRSF2, SF3B1 and U2AF1 are common in myelodysplastic syndrome/acute myelogenous leukaemia [36] and chronic lymphocytic leukaemia [37], and are associated with aberrant splicing. In B-ALL, mutations in splicing factors are not common, but previous work suggests that several splicing factors are deregulated [38]. In the context of *CD19*, we confirm that SRSF3 deregulation induces exon 2 skipping [8] and identify several other RBPs that promote CD19 protein isoforms invisible to the immunotherapeutic agent, including PTBP1, PCBP2, SF3B4, HNRNPK, MBNL1 and HNRNPM. Several of the newly identified regulators have been found as deregulated in other cancer types and are discussed as potential targets for anti-cancer therapy [39-41]. Moreover, an upregulation of PTBP1 has been implicated in the acquired resistance of pancreatic ductal carcinoma cells to the chemotherapeutic drug gemcitabine [42]. In the context of lymphocytes, PTBP1 is upregulated in B cells and required for early B cell selection [43]. It was reported, however, that treatment of leukemic cells with the targeted therapy drug imatinib, which inactivates the BCR-ABL kinase encoded by the translocated Philadelphia (Ph) chromosome, lowers PTBP1 levels [44]. In the light of our finding that *PTBP1* knockdown increases *CD19* intron 2 retention and thereby most likely reduces CD19 epitope presentation, previous treatments with imatinib may have negative impacts on subsequent responses to the CART-19 therapy in a subset of Ph+ B-ALL patients. In addition, a recent study showed that the repeat RNA *PNCTR* sequesters substantial amounts of nuclear PTBP1 in various cancers [45]. Thus, besides the regulation of protein expression, other factors like cellular availability may further impact on PTBP1 function in B-ALL cells under CART-19 therapy.

Currently, we cannot predict which patients with a CD19-positive B-ALL have a high risk of developing a CD19-negative relapsed disease. The pre-existence of isoforms skipping exon 2 or exons 5-6 has been previously discussed as a possible biomarker [15,16]. Our results indicate the necessity to extend the analysis to more isoforms and possibly to include the expression of splicing factors in screening approaches to identify patients at risk to relapse under CART-19 therapy. Notably, the same biomarkers might also be relevant for other malignancies arising from B-cell lineage, such as large B-cell lymphoma. Here, sequential loss of CD19 following CART-19 therapy has been described as a mechanism for relapse following immunotherapy [46], accounting for 29% of relapses in recent clinical studies [47]. Our data show that *CD19* splicing is highly complex, with already ~100 alternative isoforms concerning just exons 1-3. Of them, about 80% encode for a CD19 receptor lacking a functional CART-19 epitope and are thus expected to contribute to therapy resistance. The specific detection of alternative splicing might serve as a reliable biomarker and may provide a novel approach to monitor disease progression as already suggested in other tumour entities [48].

The contribution of aberrant splicing to CART-19 resistance may further be relevant for future combination therapies. Small-molecule splicing modulators are currently in clinical trials for myeloid neoplasms and splice site-switching antisense oligonucleotides are in development for different targets (reviewed in [11]). Our mutagenesis dataset provides a strong basis for designing and systematically evaluating splice-switching oligonucleotides for the modulation

of *CD19* splicing. The combined application of these splicing modulators with immunotherapy may represent a way to limit the generation of resistance to CART therapies.

Methods

Cell lines

NALM-6 cells were obtained from ATCC and cultured in RPMI medium (Life Technologies) with 10% foetal bovine serum (Life Technologies) and 1% l-glutamine (Life Technologies). HEK293T cells were obtained from DSMZ and grown with the same additives as for NALM-6. All cells were kept at 37 °C in a humidified incubator containing 5% CO_2. They were routinely tested for mycoplasma infection.

Cloning

The *CD19* minigene was amplified from human genomic DNA (Promega) with the primers 5'-catAAGCTTgaccaccgccttcctctctg-3' and 5'-catGAATTCNNNNNNNNNNNNNNNGGATCCttcccggcatctccccagtc-3'. pcDNA3.1 was used as the vector backbone for the *CD19* minigene plasmid. Both the backbone as well as the minigene amplicons were digested with the restriction enzymes *EcoR*I and *Hind*III (New England Biolabs). The backbone was extracted from a 1% agarose gel using QIAquick Gel Extraction Kit (Qiagen) and the minigene insert was cleaned up using QIAquick PCR Purification Kit (Qiagen). Ligation was conducted overnight at 16 °C with T4 DNA Ligase (New England Biolabs). All minigene mutations were introduced via Q5 Site-Directed Mutagenesis Kit (New England Biolabs). The nine mutations from eight patients in Orlando et al. [4] are listed in **Table S1**. All kits were used according to the manufacturers' recommendations.

Mutagenesis of minigene and library construction

For the random mutagenesis of the *CD19* minigene, GeneMorph II Random Mutagenesis Kit (Agilent) was used according to manufacturer's recommendations using 500 ng *CD19* minigene for 30 cycles at 56 °C with the amplification primers 5'-catAAGCTTgaccaccgccttcctctctg-3' and 5'-catGAATTCNNNNNNNNNNNNNNNGGATCCttcccggcatctccccagtc-3'. PCR products were purified using QIAquick Gel Extraction Kit (Qiagen), digested with *EcoR*I and *Hind*III (New England Biolabs) and then ligated into the backbone. To raise the baseline level of exon 2 inclusion in the *CD19* minigene to a similar level as in the endogenous *CD19* gene, position 748 (nucleotide 6 of intron 2) was exchanged from G to T.

Transfection of minigene

Cells were twice washed in Dulbecco's phosphate buffered saline (DPBS, Gibco Thermo Fisher Scientific) and then collected in R buffer with a density of 2 x 10^7 cells/ml. For electroporation, we used 5 µg plasmid DNA (with a concentration of at least 1 µg/µl) to 2 x 10^6 cells in R buffer for a 100 µl NEON electroporation pipette tip (Thermo Fisher Scientific) at 1600 V for 30 ms and 1 pulse. Cells were harvested 24 h later.

Quantification of splicing isoforms using semi-quantitative RT-PCR

Semi-quantitative RT-PCR was used to quantify ratios of *CD19* mRNA isoform variants. To this end, reverse transcription was performed on 500 ng RNA with RevertAid Reverse Transcriptase (Thermo Fisher Scientific) according to the manufacturer's recommendations. Subsequently, 1 µl of the cDNA was used as template for the RT-PCR reaction with OneTaq DNA Polymerase (New England Biolabs). PCRs were run at the following conditions: 94 °C for 30 s, 28 cycles (minigene) or 34 cycles (endogenous *CD19*) of [94 °C for 20 s, 55 °C for 30 s, 68 °C for 30 s] and final extension at 68 °C for 5 min.

The primers 5'-ACCTCCTCGCCTCCTCTTCTTC-3' and 5'-GCAACTAGAAGGCACAGTCG-3' were used for the *CD19* minigene, and 5'-ACCTCCTCGCCTCCTCTTCTTC-3' and 5'-CCGAAACATTCCACCGGAACAGC-3' for the endogenous *CD19* gene. The TapeStation 2200 capillary gel electrophoresis instrument (Agilent) was used for quantification of the PCR products on D1000 tapes.

Generation of stable and inducible shRNA knockdown cell lines

Production and preparation of lentivirus

Oligonucleotides with shRNA inserts against eleven RBPs (**Table S7**) were ordered as Ultramer DNA Oligos from Integrated DNA Technologies (Leuven, Belgium). All sequences were based on [49]. Oligonucleotides containing shRNA inserts were PCR-amplified with primers 5'-TCTCGAATTCTAGCCCCTTGAAGTCCGAGGCAGTAGGC-3' and 5'-TGAACTCGAGAAGGTATATTGCTGTTGACAGTGAGCG-3' and purified with QIAquick PCR Purification Kit (Qiagen). shRNA inserts and miRE18_LT3GEPIR_Ren714 backbone (inducible via Tet-On system) were cut with *EcoR*I and *Xho*I (New England Biolabs). Backbone was purified from agarose gel with QIAquick Gel Extraction Kit (Qiagen). The fragments were then ligated with T4 DNA Ligase (New England Biolabs) at 16 °C overnight.

Constructs were transduced into NALM-6 via HEK293T-produced lentiviruses. To this end, 10 cm dishes of HEK293T were transfected using 30 µl Lipofectamine 2000 (Thermo Fisher Scientific) with three plasmids: 4 µg shRNA-producing constructs + 2 µg psPAX2 (lentiviral packaging) + 1 µg pMD2.G (lentiviral envelope) at 72 h prior to transduction. On the first day after transfection, the medium was changed. Work with cells used for lentiviral production was conducted in the S2 laboratory.

Transduction of NALM-6 cells

Lentiviral production was confirmed with Lenti-X GoStix (Takara) and lentiviruses were concentrated with Lenti-X Concentrator (Takara) according to the manufacturer's recommendations. For transduction, 1 x 10^6 NALM-6 cells in 500 µl of medium were added to the concentrated virus. 5 µg/ml polybrene (Sigma-Aldrich) was added. The cells were centrifuged at 800 g and 32 °C for 30 min. Cells were then transferred into 6-well plates and cultivated in normal growth medium without antibiotics. Selection was started after 48 h with 0.5 µg/ml puromycin (Thermo Fisher Scientific). Antibiotic medium was exchanged every 2 to 3 days. As soon as cells were not dying under selection anymore and the population was stable, induction experiments were started. After transduction, cells remained in the S2 laboratory for at least 6 weeks. Then, Lenti-X GoStix was used to check for any remaining lentivirus.

Induction of stable shRNA-expressing NALM-6 cells

Controlled by the Tet-responsive *TRE3G* promoter, the expression of shRNA was induced by addition of doxycycline (Thermo Fisher Scientific). To this end, 2 x 10^6 NALM-6 cells were seeded into a 6-well plate in 2 ml medium containing 0.5 µg/ml puromycin and induced with 0.5 µg/ml doxycycline, diluted in RPMI 1640 medium (Thermo Fisher Scientific). Induction was conducted at 37 °C and 5% CO_2 and cells were harvested after 48 h. During induction, the shRNA expression system is coupled to the production of eGFP, which was examined by fluorescence microscopy before harvesting.

Quantitative real-time PCR (qPCR)

RNA was extracted from the induced harvested cells using the RNeasy Plus Mini Kit (Qiagen). This RNA was used for qPCR to validate the RBP knockdown as well as for semi-quantitative RT-PCR experiments to check the splicing pattern of endogenous *CD19*. The qPCR was conducted using the Luminaris HiGreen qPCR Master Mix, low ROX (Thermo Fisher Scientific) according to the manufacturer's recommendations. Oligonucleotide sequences of all qPCR primers are given in **Table S8**.

Targeted DNA sequencing

DNA-seq of the minigene library was performed on the PacBio SMRT sequencing platform at MPI-CBG Dresden. For this purpose, the minigene plasmid library was digested with *EcoR*I and *Hind*III (New England Biolabs) and run on an agarose gel. The desired band at the size of 1,301 nt was cut out and purified using QIAquick Gel Extraction Kit (Qiagen). For the run on the PacBio SMRT cell, a standard library preparation was performed.

Targeted RNA sequencing

NALM-6 cells were electroporated with the mutated minigene library (see above). 24 h later cells were harvested and RNA was isolated via the RNeasy Mini Kit (Qiagen). 20 µg isolated RNA was poly-A-selected using Dynabeads Oligo $(dT)_{25}$ beads (Invitrogen) according to the manufacturer's recommendations. Reverse transcription was performed on 500 ng poly-A-selected RNA with RevertAid Reverse Transcriptase (Thermo Fisher Scientific) according to the manufacturer's recommendations. To prevent chimeric amplicons, the RNA-seq libraries were amplified via emulsion PCR [50] using the Phusion DNA Polymerase (New England Biolabs). The following primers containing Illumina adapters were used in the PCR: 5'-CAAGCAGAAGACGGCATACGAGATCGGTCTCGGCATTCCTGCTGAACCGCTCTTCCGATCTNNNNNNNNNNGGAACCTCTAGTGGTGAAGG-3' (fwd) 5'-AATGATACGGCGACCACCGAGATCTACACTCTTTCCCTACACGACGCTCTTCCGATCTNNNNNNNNNCCGCCAGTGTGATGGATATC-3' (rev) under following conditions: 98 °C for 30 s, 25 cycles of [98 °C for 10 s, 63 °C for 20 s, 72 °C for 1 min] and final extension at 72 °C for 5 min. Amplicons were purified using Agencourt AMPure XP beads (Backman Coulter). Purified products were analysed on the TapeStation 2200 capillary gel electrophoresis instrument (Agilent) and quantified using the Qubit assay (Thermo Fisher Scientific). RNA-seq was carried out on the Illumina MiSeq platform using paired-end reads of 350 nt + 250 nt length and a 10% PhiX spike-in to increase sequence complexity.

Re-analysis of RNA-seq data from Orlando et al.

We re-analysed RNA-seq data of B-ALL patients at screening and after CART-19 therapy relapse from Orlando et al. [4] to quantify intron 2 retention in *CD19*. Since raw data were not available, we obtained BAM files for the different patients deposited in the Short Read Archive (SRA) under the accession SRP141691. For 10 patients, matched data were available at screening and relapse. The data contained the aligned reads mapped to several genes from the immune system including *CD19*. Using custom scripts, we extracted the sequence of the reads, reformatted them and generated fastq files. We then mapped the fastq files to our minigene sequence using STAR (v2.6.1) [51]. We used the re-mapped reads to quantify the levels of intron 2 retention in the different samples using the R/Bioconductor package ASpli [52].

DNA-seq barcode demultiplexing

We obtained the circular consensus sequences (CCS), stored as fastq files. Two rounds of sequencing yielded a total of 337,215 CCS. We kept only reads with a length of 150-1,150 nt. We adapted the demultiplexing procedure described in [18]. In this case, we searched for the 15-nt barcode in the last 50 nt of the read. If the barcode was not found, we searched in the last 50 nt of the reverse complementary strand. We only allowed the recovery of barcodes ranging from 14 to 16 nt, which would account for barcodes containing one nucleotide inserted or deleted. Before proceeding with the variant calling, we determined a cutoff to decide the minimal number of CCS to call variants on. Here, we kept only barcodes supported by at least 4 CCS. In total, we recovered 68.5% of all the demultiplexed barcodes which corresponded to 10,558 different minigenes, closely resembling the ~10,000 minigene clones that were used to generate the library.

DNA-seq mapping and variant calling

We use BLASR [53] with the standard parameters to map the de-multiplexed minigene sequences to the minigene reference. We performed variant calling in the aligned BAM files using the GATK [54] HaplotypeCaller (v4.0.10) with the parameters *--kmer-size 10 --kmer-size 15 --kmer-size 25 --allow-non-unique-kmers-in-ref*. We used different k-mer sizes to improve the detection of problematic regions. Mixed barcodes, i.e., barcodes containing two classes of mutations, were removed based on the "penetrance score", reported as allele frequency (AF) in the GATK vcf output files, such that barcodes with more than 25% variants of low penetrance (AF < 0.8) were discarded. Using this strategy, we were able to recover 100,135 mutations of high quality coming from 10,295 distinct minigenes plus an additional 194 unmutated WT minigenes with distinct barcodes. 57.4% of the mutations appeared in at least ten different minigenes.

RNA-seq barcode demultiplexing

RNA-seq libraries were sequenced on Illumina MiSeq as 350 nt + 250 nt paired-end reads, yielding approximately 23 million reads. We controlled their quality using FastQC (v0.11.5, https://www.bioinformatics.babraham.ac.uk/projects/fastqc/) and removed bad quality ends of reads using Trimmomatic [55] (v0.36, parameters: SLIDINGWINDOW:6:10 MINLEN:0). After trimming, we filtered for read pairs with a minimal length of 305 nt (read1) and 157 nt (read2) and, as done in Braun et al. [18], we used matchLRPatterns() and trimLRPatterns() from the R/Bioconductor package Biostrings to extract the 15 nt barcode in read1 between the two flanking restriction sites (Lpattern = TGCAGAATTC, Rpattern = GGATCC) allowing one mismatch. All read pairs with barcode length between 14 and 16 nt were kept for further processing. Barcode sequences were added to the read names in the fastq file and 5' ends of reads were trimming (read1: everything until the second anchor sequence GGATCC, read2: the first 12 nt). After identifying and trimming the barcode and other regions, we used Cutadapt [56] (v1.6, parameters: --adapter=TAGAGGTTCC --overlap=3 --error-rate=0.1 --no-indels --minimum-length=244 --pair-filter=both) to remove remaining primer sequences from read1. Lastly, the barcode information attached to the read names was used to demultiplex all read pairs into individual fastq files for each minigene.

Isoform quantification from RNA-seq data

Only barcodes/minigenes also detected in the DNA-seq library were kept for further analysis. All minigenes with insertions or deletions of 10 or more base pairs were removed from further analysis. For better mapping results, we shortened read1 to at most 260 nt. Read pairs of each minigene were mapped to the respective minigene (including all mutations, but excluding

insertions and deletions) using STAR [51] (v2.6.1b). An annotation of three isoforms (exon 2 inclusion and skipping, as well as the artefact PCR product Δex2part which lacks an internal fragment of exon 2 due to a reverse transcription artefact [57]) was provided to STAR during mapping and an --sjdbOverhang of 259 was set. When running STAR, all SAM attributes were written, up to ten mismatches were allowed, soft-clipping was prohibited on both ends of the reads and only uniquely mapping reads were kept for further analysis. BAM files were sorted and indexed using SAMtools [58] (v1.5).

Properly and consistently mapped pairs were used for isoform reconstruction using a custom Perl script. Read pairs were considered properly mapped if they mapped with the right orientation on opposite strands. Read pairs mapped consistently if they either did not overlap or in case of an overlap, agreed in their detected splice junctions. Besides, only read pairs for which both mates exceeded the constitutive exon boundaries by at least 10 nt were used for isoform reconstruction. All other pairs were removed since they did not provide any isoform information. Only minigenes covered by at least 100 read pairs usable for isoform reconstruction were kept for further analysis. For each read pair, the CIGAR strings of the two mates were used to reconstruct their splicing isoform. Regarding the artefact product Δex2part, we combined the eight possible mappings of the missing internal fragment of exon 2 which are possible due the associated 8-nt repeat sequence [57]. Only isoforms, which were supported by >=1% of the read pairs and at least two read pairs in at least one minigene, were kept for further analysis.

The analysis described above was done separately for two replicates. All isoforms occurring with a frequency of at least 5% in two or more minigene variants in either of the two replicates were kept as individual isoforms. All other detected isoforms were summarised into a category “discarded”. Isoforms with Δex2part, i.e., excluding the internal intron in exon 2, were combined with their “real” counterparts without Δex2part by merging isoforms that only differed in the exclusion of the internal fragment of exon 2. In total, this leads to a set of 101 individual isoforms.

Estimation of single mutation effects and splicing-effective mutations

Since the majority of the minigenes in the dataset exhibit more than one mutation, with a mean of 9.6 mutations per minigene, the splicing-effective mutations cannot be read out directly from the data. We used multinomial logistic regression to infer the effects of single mutations from combined measurements. The regression is based on hypothetical minigenes containing only one mutation, and on the assumption that mutation effects (log fold-changes compared to WT) add up into combined ones at the levels splice isoform ratios [18].

For regression, we focused on the five major isoforms that are already present in the WT minigene (see main text). Therefore, minigenes exhibiting more than 5% cryptic isoforms were removed from the dataset, and for the remaining minigenes the cryptic isoforms were merged into a lumped splicing category which we termed “other”. Thus, six categorical splicing outputs (inclusion, skipping, intron2-retention, alt-exon2, alt-exon3, other) were considered in the regression model, and the probability of each these outputs to be observed was assumed to equal the measured isoform frequencies. The regression was formulated as a softmax regression problem using the LogisticRegression command from the Python package scikit-learn [59].

Given the large number of mutations per minigene in the dataset, the regression was prone to overfitting (i.e., mutations with weak effects on splicing were assigned non-zero coefficients to

fit random fluctuations in the data; not shown). To avoid this problem, we employed L1 penalisation. The strength of the penalty was optimised by tenfold cross-validation, and the resulting inverse regularisation strength was C=10 for both replicates.

The goodness of the model in describing the measured combined mutation effects (minigenes) was tested by assessing the correlation between model and data in training and test datasets (**Figure S3A**). Tenfold cross-validation at the final penalisation strength showed that the method performs very well in estimating the minigene isoform frequencies of the test dataset (**Figure S3B**). In the cross-validation, the Pearson correlation coefficients between softmax predictions of combined mutation effects and measurements lie for the single isoforms between 0.68-0.95 for the first replicate and between 0.71-0.93 for the second replicate (**Figure 3B**).

The accuracy of the model-predicted single mutation effects in the softmax regression was assessed by leaving out 56 directly measured single mutation minigenes (i.e., minigenes bearing only one mutation) from the training data. Since most of these 56 mutations are not splicing-effective, we focused our analysis on the seven mutations that change the inclusion isoform level beyond two standard deviations of the WT minigene distribution: For each of the seven mutations, we performed multiple softmax fits in which the training data: (i) contained all minigenes not harbouring the mutation of interest, (ii) excluded its single mutation minigenes, and (iii) comprised varying numbers of combined mutation minigenes containing the mutation. For each mutation occurrence between 1 and 10, we used up to 7 different, randomly chosen combinations of multiple mutated minigenes including the mutation of interest. For each of these models, we generated predictions for the single mutation effect. The prediction accuracy was assessed by calculating the difference between model and direct single mutation measurements for a certain mutation occurrence. The standard deviation of the difference between model and data was used as a measure for the model error. We find that a mutation occurrence of 3 leads to an error level equal to two WT standard deviations (calculated based on inclusion levels of all WT minigenes in the first replicate). For higher mutation occurrences, the prediction accuracy does not improve further (**Figure S3C**).

The final modelling step was to identify splicing-effective mutations. For this purpose, we adopted an approach analogous to empirical *P* values, i.e., we compared predicted single mutation effects to empirical isoform frequency distributions in the WT. Isoform frequencies were measured for 195 and 194 WT minigenes in the two replicates. For each isoform and replicate, we chose the 2.5% and 97.5% quantiles of the respective empirical WT frequency distribution as cutoffs (corresponding to a two-sided 5% cutoff). A mutation was considered to have an effect on a splice isoform if, for both replicates, the frequencies predicted by the model were beyond the respective cutoffs and if the effects were in the same direction.

Splice site characterisation

Splice site usage for a given position represents the frequency of the isoforms using a given splice site in a particular minigene divided by the sum of all isoform frequencies for the same minigene. For **Figure 4A**, we used the maximum usage of a particular splice site across all minigenes. The strength of putative splice sites along the minigene was calculated using MaxEnt scores [25] in sliding windows of 9 nt or 23 nt to evaluate the corresponding sequences as potential 5' or 3' splice sites, respectively. The procedure was repeated for all individual point mutations to assess their potential to create cryptic splice sites. For the calculations we used the Python implementation of MaxEnt (maxentpy, v0.0.1, https://github.com/kepbod/maxentpy). We filtered the output by keeping only windows that

contained a GU or AG dinucleotide in the positions 4-5 (5' splice site) or 19-20 (3' splice site), respectively.

We compared the effects of single point mutations in our library to predictions by the state-of-the-art deep learning algorithm SpliceAI [24]. We ran SpliceAI (v1.3.1) with the default parameters plus masking (-M1), using GENCODE [60] (v31) annotation for the human genome version hg38 as a reference. Given that SpliceAI results are reported in terms of a probability of gain or loss of a particular splice site, we assigned the gained splice sites in our cryptic isoforms by comparison to the canonical exon 2 inclusion isoform, such that if a new splice site appears in the cryptic isoform, it is considered as "gained" with respect to the "lost" WT splice site. All splice sites in a cryptic isoform were given the same prevalence score, i.e., the prevalence score of the mutation-isoform pair. To compare the SpliceAI scores for a given splice site gain with our prevalence score (**Figure 4F**), we considered the mutations that (i) share the same gain-loss pair of positions in both assays, and (ii) are predicted by SpliceAI to gain of a new splice site (i.e., a cryptic site where score_gain > score_loss) upon a given mutation.

RBP binding site predictions

For the prediction of RBP binding motifs, we used the web versions of the oRNAment (http://rnabiology.ircm.qc.ca/oRNAment) [27] and ATtRACT (https://attract.cnic.es/) [26] databases to query the minigene sequence for presence of RBP motifs (**Figure S5A**). From the obtained predictions, we collapsed overlapping binding sites from the same tool and RBP.

We used DeepRiPe [28] to predict the potential impact of single point mutations on RBP binding. To this end, we downloaded the trained models for PAR-CLIP and ENCODE eCLIP data on 159 RBPs available in the Github repository (https://github.com/ohlerlab/DeepRiPe). We scored each mutation (annotated with regards to the hg38 reference genome) across the individual RBP models and preserved every mutation for which the model score changed by at least 0.25 compared to the WT sequence. The scoring functions are based on the iPython notebooks provided by DeepRiPe: https://colab.research.google.com/drive/18yeqRE7KmOjfbUaLAfJ6rMBjAulYo-Uc?usp=sharing

For the definition of significant RBP binding sites, we used the following strategy. For binding sites predicted by oRNAment and ATtRACT, we first checked their overlap separately for each isoform. If a binding site overlapped in at least one position with a splicing-effective mutation with respect to this particular isoform, we defined this binding site as an isoform-specific significant binding site. All binding sites that were significant for at least one isoform were collapsed into the complete list of significant binding sites, yielding a total of 315 significant binding sites for 74 RBPs. In the case of DeepRiPe, a mutation with a delta score > 0.25 for a given RBP model was required to overlap with a splicing-effective mutation for a particular isoform (our screen) to be considered an isoform-specific significant RBP-changing mutation. In a similar manner, all isoform-specific mutations for any isoform were collapsed into a complete list of significant RBP-changing mutations, yielding a total of 222 significant mutations that affected the binding of 58 RBPs.

iCLIP data processing

iCLIP libraries were sequenced on an Illumina NextSeq 500 sequencing machine as 92 nt single-end reads including a 6 nt sample barcode as well as 5+4 nt unique molecular identifiers (UMIs). Basic quality controls were done with FastQC (v0.11.8)

(https://www.bioinformatics.babraham.ac.uk/projects/fastqc/) and reads were filtered based on sequencing qualities (Phred score) in the barcode region using the FASTX-Toolkit (v0.0.14) (http://hannonlab.cshl.edu/fastx toolkit/) and seqtk (v1.3) (https://github.com/lh3/seqtk/). Reads were de-multiplexed based on the experimental barcode, which is found on positions 6 to 11 of the reads, using Flexbar [61] (v3.4.0). Afterwards, barcode regions and adapter sequences were trimmed from read ends using Flexbar. Here, a minimal overlap of 1 nt of read and adapter was required, UMIs were added to the read names and reads shorter than 15 nt were removed from further analysis. Downstream analysis was done as described in Chapters 3.4 and 4.1 of Busch et al. [62]. Genome assembly and annotation of GENCODE [60] v31 were used during mapping.

Patient data analysis

RNA-seq data of 222 B-ALL patients from the Therapeutically Applicable Research To Generate Effective Treatments (TARGET) program (https://ocg.cancer.gov/programs/target) were processed from fastq files. Sequencing adapters were trimmed with TrimGalore [63] (v0.6.6), aligned to the hg38 human genome assembly with STAR [51] (v2.5.2a), and sorted and indexed with SAMtools [58] (v1.11). Splice junctions were quantified individually for each sample using MAJIQ [64] (v2.2) and ENSEMBL reference transcriptome GRCh38.94 [65]. Only splice junctions with a usage level (percent selected index, PSI) of at least 5% in any given TARGET B-ALL samples were quantified.

Data availability

All the sequencing data is available as a SuperSeries collection in the Gene Expression Omnibus (GEO) under the accession number GSE182894. The collection consists of the PacBio DNA-seq libraries (GSE182891), the Illumina RNA-seq libraries (GSE182892) and the PTBP1 iCLIP2 libraries in NALM-6 cells (GSE182893).

Scripts used to process the files are accessible under the GitHub repository located at: https://github.com/mcortes-lopez/CD19_splicing_mutagenesis.

The results published here are in whole or part based upon data generated by the Therapeutically Applicable Research to Generate Effective Treatments (https://ocg.cancer.gov/programs/target) initiative, phs000218. The data used for this analysis are available at https://portal.gdc.cancer.gov/projects.

Competing interests

A.T.-T. has an interest in intellectual property “Discovery of CD19 Spliced Isoforms Resistant to CART-19”. This interest does not meet the definition of a reviewable interest under Children’s Hospital of Philadelphia’s (CHOP’s) conflict of interest policy and is therefore not a financial conflict of interest. Furthermore, this intellectual property has not been licensed or otherwise commercialised to date. However, should this technology be commercialised in the future, A.T.-T. would be entitled to a share of royalties earned by CHOP per its patent policy.

The other authors have no competing interests.

Acknowledgements

The authors would like to thank the members of the participating labs for support and discussion. We gratefully acknowledge the Institute of Molecular Biology Core Facilities for their support, especially the Genomics Core Facility and the use of its NextSeq 500 (funded by the Deutsche Forschungsgemeinschaft [DFG, German Research Foundation] INST 247/870-1 FUGG) and the Bioinformatics Core Facilities. We gratefully acknowledge the PacBio SMRT sequencing platform at MPI-CBG Dresden.

Author contributions

M.C.-L. performed most bioinformatics analyses. L.S. performed the *CD19* minigene experiments as well as the massively parallel *CD19* splicing reporter assay. L.S. and B.S performed shRNA-mediated RBP knockdown experiments and corresponding splicing assays. M.E. and S.L. designed the mathematical modelling and prevalence score approach, and M.E. performed the analyses. F.K. contributed to quantification of mutation effects. A.O., M.C.-L., L.S. and J.K. performed PTB iCLIP experiments. A.B. performed iCLIP and RNA-seq data processing as well as splice isoform quantification. M.Q.-V. and M.T.D., performed TARGET ALL data analysis under supervision of Y.B. and A.T.-T.. Study was designed by M.C.-L., L.S., M.E., K.Z., S.L. and J.K. with help from C.P., J.F. and all co-authors. K.Z., S.L. and J.K. supervised most of the bioinformatics analyses, mathematical modelling, and experimental work, respectively. M.C.-L, L.S., M.E., C.P., K.Z., S.L., and J.K. wrote the manuscript with help and comments from all co-authors.

Funding

This work was funded by the Naturwissenschaftlich-Medizinische Forschungszentrum (NMFZ) to J.F., J.K. and C.P. and the Deutsche Forschungsgemeinschaft (DFG) to K.Z., J.K. and S.L. (ZA 881/2-3 to K.Z., KO 4566/4-3 to J.K., and LE 3473/2-3 to S.L.). K.Z. was also supported

by the Deutsche Forschungsgemeinschaft (SFB902 B13). This work was supported by the grant from the National Institutes of Health (U01 CA232563 to A.T.-T. and Y.B.), St. Baldrick's-Stand Up to Cancer (SU2C-AACR-DT-27-17 to A.T.-T.) and the V Foundation for Cancer Research (T2018-014 to A.T.-T.).

References

1. Maude SL, Frey N, Shaw PA, Aplenc R, Barrett DM, Bunin NJ, Chew A, Gonzalez VE, Zheng Z, Lacey SF, Mahnke YD, Melenhorst JJ, Rheingold SR, Shen A, Teachey DT, Levine BL, June CH, Porter DL & Grupp SA. Chimeric antigen receptor T cells for sustained remissions in leukemia. *N Engl J Med* **371**, 1507-1517 (2014).
2. Wudhikarn K, Flynn JR, Riviere I, Gonen M, Wang X, Senechal B, Curran KJ, Roshal M, Maslak PG, Geyer MB, Halton EF, Diamonte C, Davila ML, Sadelain M, Brentjens RJ & Park JH. Interventions and outcomes of adult patients with B-ALL progressing after CD19 chimeric antigen receptor T-cell therapy. *Blood* **138**, 531-543 (2021).
3. Roberts KG. Genetics and prognosis of ALL in children vs adults. *Hematology Am Soc Hematol Educ Program* **2018**, 137-145 (2018).
4. Orlando EJ, Han X, Tribouley C, Wood PA, Leary RJ, Riester M, Levine JE, Qayed M, Grupp SA, Boyer M, De Moerloose B, Nemecek ER, Bittencourt H, Hiramatsu H, Buechner J, Davies SM, Verneris MR, Nguyen K, Brogdon JL, Bitter H, Morrissey M, Pierog P, Pantano S, Engelman JA & Winckler W. Genetic mechanisms of target antigen loss in CAR19 therapy of acute lymphoblastic leukemia. *Nat Med* **24**, 1504-1506 (2018).
5. Park JH, Riviere I, Gonen M, Wang X, Senechal B, Curran KJ, Sauter C, Wang Y, Santomasso B, Mead E, Roshal M, Maslak P, Davila M, Brentjens RJ & Sadelain M. Long-Term Follow-up of CD19 CAR Therapy in Acute Lymphoblastic Leukemia. *N Engl J Med* **378**, 449-459 (2018).
6. Gardner RA, Finney O, Annesley C, Brakke H, Summers C, Leger K, Bleakley M, Brown C, Mgebroff S, Kelly-Spratt KS, Hoglund V, Lindgren C, Oron AP, Li D, Riddell SR, Park JR & Jensen MC. Intent-to-treat leukemia remission by CD19 CAR T cells of defined formulation and dose in children and young adults. *Blood* **129**, 3322-3331 (2017).
7. Maude SL, Laetsch TW, Buechner J, Rives S, Boyer M, Bittencourt H, Bader P, Verneris MR, Stefanski HE, Myers GD, Qayed M, De Moerloose B, Hiramatsu H, Schlis K, Davis KL, Martin PL, Nemecek ER, Yanik GA, Peters C, Baruchel A, Boissel N, Mechinaud F, Balduzzi A, Krueger J, June CH, Levine BL, Wood P, Taran T, Leung M, Mueller KT, Zhang Y, Sen K, Lebwohl D, Pulsipher MA & Grupp SA. Tisagenlecleucel in Children and Young Adults with B-Cell Lymphoblastic Leukemia. *N Engl J Med* **378**, 439-448 (2018).
8. Sotillo E, Barrett DM, Black KL, Bagashev A, Oldridge D, Wu G, Sussman R, Lanauze C, Ruella M, Gazzara MR, Martinez NM, Harrington CT, Chung EY, Perazzelli J, Hofmann TJ, Maude SL, Raman P, Barrera A, Gill S, Lacey SF, Melenhorst JJ, Allman D, Jacoby E, Fry T, Mackall C, Barash Y, Lynch KW, Maris JM, Grupp SA & Thomas-Tikhonenko A. Convergence of Acquired Mutations and Alternative Splicing of CD19 Enables Resistance to CART-19 Immunotherapy. *Cancer Discov* **5**, 1282-1295 (2015).
9. Shah NN & Fry TJ. Mechanisms of resistance to CAR T cell therapy. *Nat Rev Clin Oncol* **16**, 372-385 (2019).
10. Asnani M, Hayer KE, Naqvi AS, Zheng S, Yang SY, Oldridge D, Ibrahim F, Maragkakis M, Gazzara MR, Black KL, Bagashev A, Taylor D, Mourelatos Z, Grupp SA, Barrett D, Maris JM, Sotillo E, Barash Y & Thomas-Tikhonenko A. Retention of CD19 intron 2 contributes to CART-19 resistance in leukemias with subclonal frameshift mutations in CD19. *Leukemia* **34**, 1202-1207 (2020).
11. Bonnal SC, López-Oreja I & Valcárcel J. Roles and mechanisms of alternative splicing in cancer - implications for care. *Nat Rev Clin Oncol* **17**, 457-474 (2020).
12. Dvinge H, Kim E, Abdel-Wahab O & Bradley RK. RNA splicing factors as oncoproteins and tumour suppressors. *Nat Rev Cancer* **16**, 413-430 (2016).
13. El Marabti E & Abdel-Wahab O. Therapeutic Modulation of RNA Splicing in Malignant and Non-Malignant Disease. *Trends Mol Med* **27**, 643-659 (2021).

14. Bagashev A, Sotillo E, Tang CH, Black KL, Perazzelli J, Seeholzer SH, Argon Y, Barrett DM, Grupp SA, Hu CC & Thomas-Tikhonenko A. CD19 Alterations Emerging after CD19-Directed Immunotherapy Cause Retention of the Misfolded Protein in the Endoplasmic Reticulum. *Mol Cell Biol* **38** (2018).
15. Fischer J, Paret C, El Malki K, Alt F, Wingerter A, Neu MA, Kron B, Russo A, Lehmann N, Roth L, Fehr EM, Attig S, Hohberger A, Kindler T & Faber J. CD19 Isoforms Enabling Resistance to CART-19 Immunotherapy Are Expressed in B-ALL Patients at Initial Diagnosis. *J Immunother* **40**, 187-195 (2017).
16. Rabilloud T, Potier D, Pankaew S, Nozais M, Loosveld M & Payet-Bornet D. Single-cell profiling identifies pre-existing CD19-negative subclones in a B-ALL patient with CD19-negative relapse after CAR-T therapy. *Nat Commun* **12**, 865 (2021).
17. Zhao Y, Aldoss I, Qu C, Crawford JC, Gu Z, Allen EK, Zamora AE, Alexander TB, Wang J, Goto H, Imamura T, Akahane K, Marcucci G, Stein AS, Bhatia R, Thomas PG, Forman SJ, Mullighan CG & Roberts KG. Tumor-intrinsic and -extrinsic determinants of response to blinatumomab in adults with B-ALL. *Blood* **137**, 471-484 (2021).
18. Braun S, Enculescu M, Setty ST, Cortés-López M, de Almeida BP, Sutandy FXR, Schulz L, Busch A, Seiler M, Ebersberger S, Barbosa-Morais NL, Legewie S, König J & Zarnack K. Decoding a cancer-relevant splicing decision in the *RON* proto-oncogene using high-throughput mutagenesis. *Nat Commun* **9**, 3315 (2018).
19. Baeza-Centurion P, Minana B, Schmiedel JM, Valcárcel J & Lehner B. Combinatorial Genetics Reveals a Scaling Law for the Effects of Mutations on Splicing. *Cell* **176**, 549-563 e523 (2019).
20. Baeza-Centurion P, Minana B, Valcárcel J & Lehner B. Mutations primarily alter the inclusion of alternatively spliced exons. *Elife* **9** (2020).
21. Ke S, Anquetil V, Zamalloa JR, Maity A, Yang A, Arias MA, Kalachikov S, Russo JJ, Ju J & Chasin LA. Saturation mutagenesis reveals manifold determinants of exon definition. *Genome Res* **28**, 11-24 (2018).
22. Glidden DT, Buerer JL, Saueressig CF & Fairbrother WG. Hotspot exons are common targets of splicing perturbations. *Nat Commun* **12**, 2756 (2021).
23. Enculescu M, Braun S, Thonta Setty S, Busch A, Zarnack K, König J & Legewie S. Exon Definition Facilitates Reliable Control of Alternative Splicing in the *RON* Proto-Oncogene. *Biophys J* **118**, 2027-2041 (2020).
24. Jaganathan K, Kyriazopoulou Panagiotopoulou S, McRae JF, Darbandi SF, Knowles D, Li YI, Kosmicki JA, Arbelaez J, Cui W, Schwartz GB, Chow ED, Kanterakis E, Gao H, Kia A, Batzoglou S, Sanders SJ & Farh KK. Predicting Splicing from Primary Sequence with Deep Learning. *Cell* **176**, 535-548 e524 (2019).
25. Yeo G & Burge CB. Maximum entropy modeling of short sequence motifs with applications to RNA splicing signals. *J Comput Biol* **11**, 377-394 (2004).
26. Giudice G, Sanchez-Cabo F, Torroja C & Lara-Pezzi E. ATtRACT-a database of RNA-binding proteins and associated motifs. *Database (Oxford)* **2016** (2016).
27. Benoit Bouvrette LP, Bovaird S, Blanchette M & Lecuyer E. oRNAment: a database of putative RNA binding protein target sites in the transcriptomes of model species. *Nucleic Acids Res* **48**, D166-D173 (2020).
28. Ghanbari M & Ohler U. Deep neural networks for interpreting RNA-binding protein target preferences. *Genome Res* **30**, 214-226 (2020).
29. Gu Z, Churchman ML, Roberts KG, Moore I, Zhou X, Nakitandwe J, Hagiwara K, Pelletier S, Gingras S, Berns H, Payne-Turner D, Hill A, Iacobucci I, Shi L, Pounds S, Cheng C, Pei D, Qu C, Newman S, Devidas M, Dai Y, Reshmi SC, Gastier-Foster J, Raetz EA, Borowitz MJ, Wood BL, Carroll WL, Zweidler-McKay PA, Rabin KR, Mattano LA, Maloney KW, Rambaldi A, Spinelli O, Radich JP, Minden MD, Rowe JM, Luger S, Litzow MR,

Tallman MS, Racevskis J, Zhang Y, Bhatia R, Kohlschmidt J, Mrozek K, Bloomfield CD, Stock W, Kornblau S, Kantarjian HM, Konopleva M, Evans WE, Jeha S, Pui CH, Yang J, Paietta E, Downing JR, Relling MV, Zhang J, Loh ML, Hunger SP & Mullighan CG. PAX5-driven subtypes of B-progenitor acute lymphoblastic leukemia. *Nat Genet* **51**, 296-307 (2019).

30. Spellman R & Smith CW. Novel modes of splicing repression by PTB. *Trends Biochem Sci* **31**, 73-76 (2006).
31. Haberman N, Huppertz I, Attig J, König J, Wang Z, Hauer C, Hentze MW, Kulozik AE, Le Hir H, Curk T, Sibley CR, Zarnack K & Ule J. Insights into the design and interpretation of iCLIP experiments. *Genome Biol* **18**, 7 (2017).
32. Mikl M, Hamburg A, Pilpel Y & Segal E. Dissecting splicing decisions and cell-to-cell variability with designed sequence libraries. *Nat Commun* **10**, 4572 (2019).
33. Cheng J, Nguyen TYD, Cygan KJ, Celik MH, Fairbrother WG, Avsec Z & Gagneur J. MMSplice: modular modeling improves the predictions of genetic variant effects on splicing. *Genome Biol* **20**, 48 (2019).
34. Mount SM, Avsec Z, Carmel L, Casadio R, Celik MH, Chen K, Cheng J, Cohen NE, Fairbrother WG, Fenesh T, Gagneur J, Gotea V, Holzer T, Lin CF, Martelli PL, Naito T, Nguyen TYD, Savojardo C, Unger R, Wang R, Yang Y & Zhao H. Assessing predictions of the impact of variants on splicing in CAGI5. *Hum Mutat* **40**, 1215-1224 (2019).
35. Yu Y, Maroney PA, Denker JA, Zhang XH, Dybkov O, Luhrmann R, Jankowsky E, Chasin LA & Nilsen TW. Dynamic regulation of alternative splicing by silencers that modulate 5' splice site competition. *Cell* **135**, 1224-1236 (2008).
36. Yoshida K, Sanada M, Shiraishi Y, Nowak D, Nagata Y, Yamamoto R, Sato Y, Sato-Otsubo A, Kon A, Nagasaki M, Chalkidis G, Suzuki Y, Shiosaka M, Kawahata R, Yamaguchi T, Otsu M, Obara N, Sakata-Yanagimoto M, Ishiyama K, Mori H, Nolte F, Hofmann WK, Miyawaki S, Sugano S, Haferlach C, Koeffler HP, Shih LY, Haferlach T, Chiba S, Nakauchi H, Miyano S & Ogawa S. Frequent pathway mutations of splicing machinery in myelodysplasia. *Nature* **478**, 64-69 (2011).
37. Quesada V, Conde L, Villamor N, Ordonez GR, Jares P, Bassaganyas L, Ramsay AJ, Bea S, Pinyol M, Martinez-Trillos A, Lopez-Guerra M, Colomer D, Navarro A, Baumann T, Aymerich M, Rozman M, Delgado J, Gine E, Hernandez JM, Gonzalez-Diaz M, Puente DA, Velasco G, Freije JM, Tubio JM, Royo R, Gelpi JL, Orozco M, Pisano DG, Zamora J, Vazquez M, Valencia A, Himmelbauer H, Bayes M, Heath S, Gut M, Gut I, Estivill X, Lopez-Guillermo A, Puente XS, Campo E & Lopez-Otin C. Exome sequencing identifies recurrent mutations of the splicing factor SF3B1 gene in chronic lymphocytic leukemia. *Nat Genet* **44**, 47-52 (2011).
38. Black KL, Naqvi AS, Asnani M, Hayer KE, Yang SY, Gillespie E, Bagashev A, Pillai V, Tasian SK, Gazzara MR, Carroll M, Taylor D, Lynch KW, Barash Y & Thomas-Tikhonenko A. Aberrant splicing in B-cell acute lymphoblastic leukemia. *Nucleic Acids Res* **46**, 11357-11369 (2018).
39. Desterro J, Bak-Gordon P & Carmo-Fonseca M. Targeting mRNA processing as an anticancer strategy. *Nat Rev Drug Discov* **19**, 112-129 (2020).
40. Xu Y, Gao XD, Lee JH, Huang H, Tan H, Ahn J, Reinke LM, Peter ME, Feng Y, Gius D, Siziopikou KP, Peng J, Xiao X & Cheng C. Cell type-restricted activity of hnRNPM promotes breast cancer metastasis via regulating alternative splicing. *Genes Dev* **28**, 1191-1203 (2014).
41. Itskovich SS, Gurunathan A, Clark J, Burwinkel M, Wunderlich M, Berger MR, Kulkarni A, Chetal K, Venkatasubramanian M, Salomonis N, Kumar AR & Lee LH. MBNL1 regulates essential alternative RNA splicing patterns in MLL-rearranged leukemia. *Nat Commun* **11**, 2369 (2020).

42. Calabretta S, Bielli P, Passacantilli I, Pilozzi E, Fendrich V, Capurso G, Fave GD & Sette C. Modulation of PKM alternative splicing by PTBP1 promotes gemcitabine resistance in pancreatic cancer cells. *Oncogene* **35**, 2031-2039 (2016).
43. Monzón-Casanova E, Matheson LS, Tabbada K, Zarnack K, Smith CW & Turner M. Polypyrimidine tract-binding proteins are essential for B cell development. *Elife* **9** (2020).
44. Shinohara H, Kumazaki M, Minami Y, Ito Y, Sugito N, Kuranaga Y, Taniguchi K, Yamada N, Otsuki Y, Naoe T & Akao Y. Perturbation of energy metabolism by fatty-acid derivative AIC-47 and imatinib in BCR-ABL-harboring leukemic cells. *Cancer Lett* **371**, 1-11 (2016).
45. Yap K, Mukhina S, Zhang G, Tan JSC, Ong HS & Makeyev EV. A Short Tandem Repeat-Enriched RNA Assembles a Nuclear Compartment to Control Alternative Splicing and Promote Cell Survival. *Mol Cell* **72**, 525-540 e513 (2018).
46. Shalabi H, Kraft IL, Wang HW, Yuan CM, Yates B, Delbrook C, Zimbelman JD, Giller R, Stetler-Stevenson M, Jaffe ES, Lee DW, Shern JF, Fry TJ & Shah NN. Sequential loss of tumor surface antigens following chimeric antigen receptor T-cell therapies in diffuse large B-cell lymphoma. *Haematologica* **103**, e215-e218 (2018).
47. Spiegel JY, Patel S, Muffly L, Hossain NM, Oak J, Baird JH, Frank MJ, Shiraz P, Sahaf B, Craig J, Iglesias M, Younes S, Natkunam Y, Ozawa MG, Yang E, Tamaresis J, Chinnasamy H, Ehlinger Z, Reynolds W, Lynn R, Rotiroti MC, Gkitsas N, Arai S, Johnston L, Lowsky R, Majzner RG, Meyer E, Negrin RS, Rezvani AR, Sidana S, Shizuru J, Weng WK, Mullins C, Jacob A, Kirsch I, Bazzano M, Zhou J, Mackay S, Bornheimer SJ, Schultz L, Ramakrishna S, Davis KL, Kong KA, Shah NN, Qin H, Fry T, Feldman S, Mackall CL & Miklos DB. CAR T cells with dual targeting of CD19 and CD22 in adult patients with recurrent or refractory B cell malignancies: a phase 1 trial. *Nat Med* (2021).
48. Venables JP, Klinck R, Bramard A, Inkel L, Dufresne-Martin G, Koh C, Gervais-Bird J, Lapointe E, Froehlich U, Durand M, Gendron D, Brosseau JP, Thibault P, Lucier JF, Tremblay K, Prinos P, Wellinger RJ, Chabot B, Rancourt C & Elela SA. Identification of alternative splicing markers for breast cancer. *Cancer Res* **68**, 9525-9531 (2008).
49. Fellmann C, Zuber J, McJunkin K, Chang K, Malone CD, Dickins RA, Xu Q, Hengartner MO, Elledge SJ, Hannon GJ & Lowe SW. Functional identification of optimized RNAi triggers using a massively parallel sensor assay. *Mol Cell* **41**, 733-746 (2011).
50. Williams R, Peisajovich SG, Miller OJ, Magdassi S, Tawfik DS & Griffiths AD. Amplification of complex gene libraries by emulsion PCR. *Nat Methods* **3**, 545-550 (2006).
51. Dobin A, Davis CA, Schlesinger F, Drenkow J, Zaleski C, Jha S, Batut P, Chaisson M & Gingeras TR. STAR: ultrafast universal RNA-seq aligner. *Bioinformatics* **29**, 15-21 (2013).
52. Estefania M, Andres R, Javier I, Marcelo Y & Ariel C. ASpli: Integrative analysis of splicing landscapes through RNA-Seq assays. *Bioinformatics* (2021).
53. Chaisson MJ & Tesler G. Mapping single molecule sequencing reads using basic local alignment with successive refinement (BLASR): application and theory. *BMC Bioinformatics* **13**, 238 (2012).
54. McKenna A, Hanna M, Banks E, Sivachenko A, Cibulskis K, Kernytsky A, Garimella K, Altshuler D, Gabriel S, Daly M & DePristo MA. The Genome Analysis Toolkit: a MapReduce framework for analyzing next-generation DNA sequencing data. *Genome Res* **20**, 1297-1303 (2010).
55. Bolger AM, Lohse M & Usadel B. Trimmomatic: a flexible trimmer for Illumina sequence data. *Bioinformatics* **30**, 2114-2120 (2014).
56. Martin M. Cutadapt removes adapter sequences from high-throughput sequencing reads. *EMBnet.journal* **17**, 10-12 (2011).
57. Schulz L, Torres-Diz M, Cortés-López M, Hayer KE, Asnani M, Tasian SK, Barash Y, Sotillo E, Zarnack K, König J & Thomas-Tikhonenko A. Direct long-read RNA sequencing

identifies a subset of questionable exitrons likely arising from reverse transcription artifacts. *Genome Biol* **22**, 190 (2021).

58. Li H, Handsaker B, Wysoker A, Fennell T, Ruan J, Homer N, Marth G, Abecasis G, Durbin R & Genome Project Data Processing S. The Sequence Alignment/Map format and SAMtools. *Bioinformatics* **25**, 2078-2079 (2009).
59. Pedregosa F, Varoquaux G, Gramfort A, Michel V, Thirion B, Grisel O, Blondel M, Prettenhofer P, Weiss R, Dubourg V, Vanderplas J, Passos A, Cournapeau D, Brucher M, Perrot M & Duchesnay E. scikit-learn: Machine learning in Python. *Journal of Machine Learning Research* **12**, 2825-2830 (2011).
60. Frankish A, Diekhans M, Ferreira AM, Johnson R, Jungreis I, Loveland J, Mudge JM, Sisu C, Wright J, Armstrong J, Barnes I, Berry A, Bignell A, Carbonell Sala S, Chrast J, Cunningham F, Di Domenico T, Donaldson S, Fiddes IT, Garcia Giron C, Gonzalez JM, Grego T, Hardy M, Hourlier T, Hunt T, Izuogu OG, Lagarde J, Martin FJ, Martinez L, Mohanan S, Muir P, Navarro FCP, Parker A, Pei B, Pozo F, Ruffier M, Schmitt BM, Stapleton E, Suner MM, Sycheva I, Uszczynska-Ratajczak B, Xu J, Yates A, Zerbino D, Zhang Y, Aken B, Choudhary JS, Gerstein M, Guigo R, Hubbard TJP, Kellis M, Paten B, Reymond A, Tress ML & Flicek P. GENCODE reference annotation for the human and mouse genomes. *Nucleic Acids Res* **47**, D766-D773 (2019).
61. Roehr JT, Dieterich C & Reinert K. Flexbar 3.0 - SIMD and multicore parallelization. *Bioinformatics* **33**, 2941-2942 (2017).
62. Busch A, Brüggemann M, Ebersberger S & Zarnack K. iCLIP data analysis: A complete pipeline from sequencing reads to RBP binding sites. *Methods* **178**, 49-62 (2020).
63. Krueger F. TrimGalore. *GitHub repository* (2021).
64. Vaquero-Garcia J, Barrera A, Gazzara MR, González-Vallinas J, Lahens NF, Hogenesch JB, Lynch KW & Barash Y. A new view of transcriptome complexity and regulation through the lens of local splicing variations. *Elife* **5**, e11752 (2016).
65. Howe KL, Achuthan P, Allen J, Allen J, Alvarez-Jarreta J, Amode MR, Armean IM, Azov AG, Bennett R, Bhai J, Billis K, Boddu S, Charkhchi M, Cummins C, Da Rin Fioretto L, Davidson C, Dodiya K, El Houdaigui B, Fatima R, Gall A, Garcia Giron C, Grego T, Guijarro-Clarke C, Haggerty L, Hemrom A, Hourlier T, Izuogu OG, Juettemann T, Kaikala V, Kay M, Lavidas I, Le T, Lemos D, Gonzalez Martinez J, Marugan JC, Maurel T, McMahon AC, Mohanan S, Moore B, Muffato M, Oheh DN, Paraschas D, Parker A, Parton A, Prosovetskaia I, Sakthivel MP, Salam AIA, Schmitt BM, Schuilenburg H, Sheppard D, Steed E, Szpak M, Szuba M, Taylor K, Thormann A, Threadgold G, Walts B, Winterbottom A, Chakiachvili M, Chaubal A, De Silva N, Flint B, Frankish A, Hunt SE, GR II, Langridge N, Loveland JE, Martin FJ, Mudge JM, Morales J, Perry E, Ruffier M, Tate J, Thybert D, Trevanion SJ, Cunningham F, Yates AD, Zerbino DR & Flicek P. Ensembl 2021. *Nucleic Acids Res* **49**, D884-D891 (2021).
66. Barretina J, Caponigro G, Stransky N, Venkatesan K, Margolin AA, Kim S, Wilson CJ, Lehar J, Kryukov GV, Sonkin D, Reddy A, Liu M, Murray L, Berger MF, Monahan JE, Morais P, Meltzer J, Korejwa A, Jane-Valbuena J, Mapa FA, Thibault J, Bric-Furlong E, Raman P, Shipway A, Engels IH, Cheng J, Yu GK, Yu J, Aspesi P, Jr., de Silva M, Jagtap K, Jones MD, Wang L, Hatton C, Palescandolo E, Gupta S, Mahan S, Sougnez C, Onofrio RC, Liefeld T, MacConaill L, Winckler W, Reich M, Li N, Mesirov JP, Gabriel SB, Getz G, Ardlie K, Chan V, Myer VE, Weber BL, Porter J, Warmuth M, Finan P, Harris JL, Meyerson M, Golub TR, Morrissey MP, Sellers WR, Schlegel R & Garraway LA. The Cancer Cell Line Encyclopedia enables predictive modelling of anticancer drug sensitivity. *Nature* **483**, 603-607 (2012).

Figures

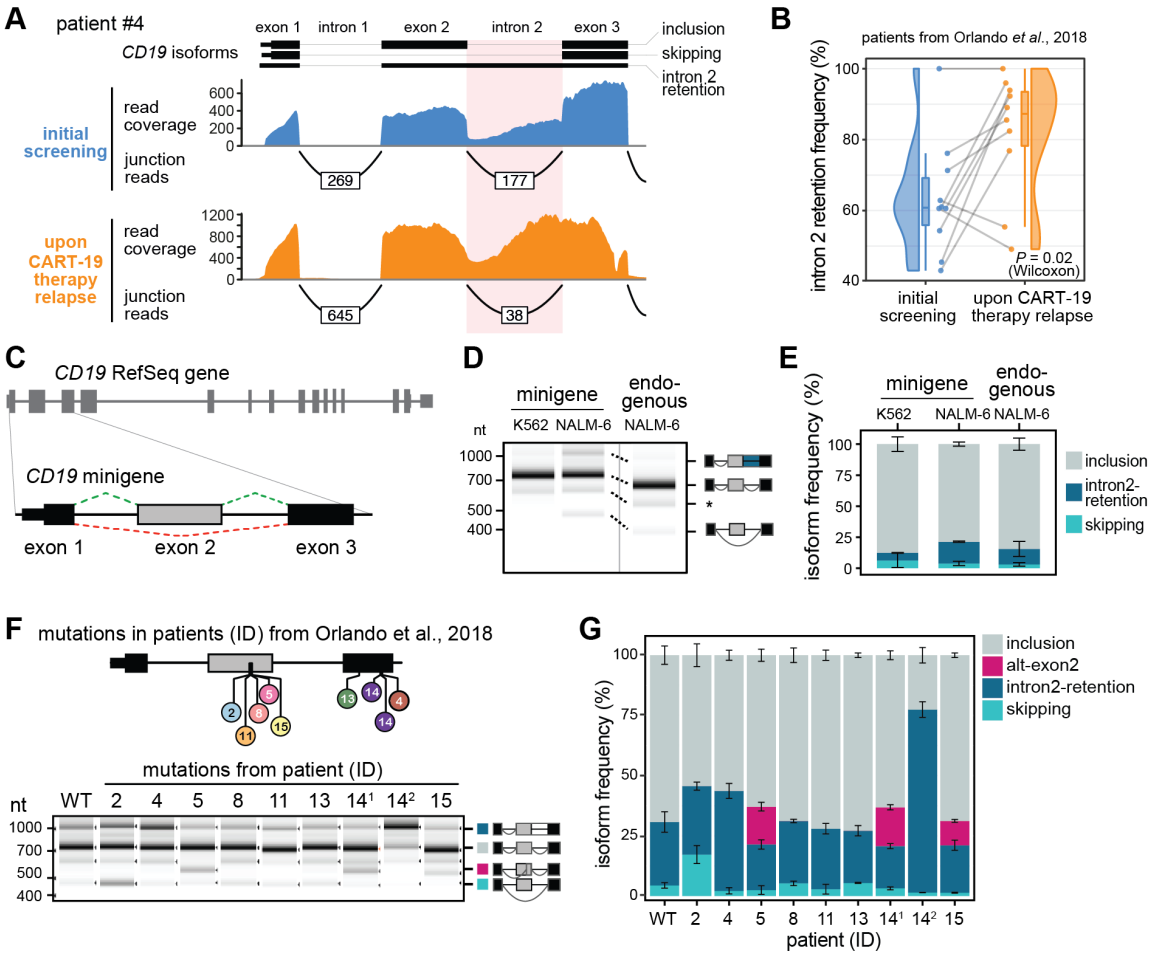

Figure 1. Mutations from B-ALL patients cause *CD19* mis-splicing.
(A) Patient #4 shows increased *CD19* intron 2 retention after CART-19 therapy relapse, evidenced by reduced junction-spanning reads and increased intron coverage. Re-analysed RNA-seq data from Orlando et al. [4]. Selected isoforms (GENCODE) are shown above.
(B) Intron 2 retention increases in B-ALL patients after CART-19 therapy relapse. Intron 2 retention frequency (as % of all isoforms) is shown for 10 patients with matched RNA-seq data at screening and after relapse. *P* value = 0.02, paired Wilcoxon signed-rank test.
(C) The *CD19* minigene spans exons 1-3 and the intervening introns from the *CD19* gene.
(D, E) The minigene generates the same isoforms as the endogenous *CD19* gene in NALM-6 cells. Gel-like representation (D) and quantification (E) of semi-quantitative RT-PCR showing detected isoforms intron2-retention (blue), inclusion (grey) and skipping (turquoise) for the WT minigene in NALM-6 and K562 cells as control. Isoforms of *CD19* gene in NALM-6 cells are shown for comparison. Asterisk indicates a previously reported RT-PCR artefact [57] (see methods). Error bars indicate standard deviation of mean (s.d.m.), n = 3 replicates.
(F, G) Patient mutations cause splicing changes in the *CD19* minigene. Top: Location of the tested mutations. Numbers refer to patient IDs as reported in Orlando et al. [4]. 14.1 and 14.2 correspond to distinct mutations from patient #14. Gel-like representation (F) and quantification (G) of semi-quantitative RT-PCR as in (D) and (E). Additional isoform alt-exon2 (purple) includes a truncated version of exon 2. Error bars indicate s.d.m., n = 3 replicates.

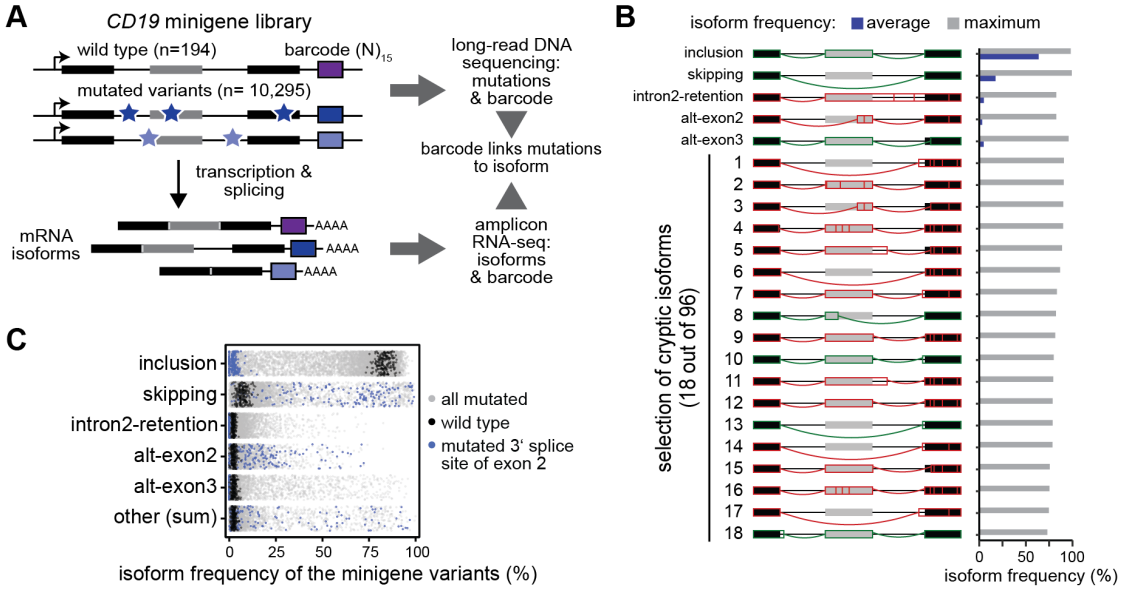

Figure 2. High-throughput mutagenesis identifies splicing-effective mutations and cryptic isoforms in the *CD19* minigene.

(A) High-throughput detection of splicing-effective mutations and cryptic isoforms. Mutagenic PCR creates mutated minigene variants (top) that upon transfection into NALM-6 cells give rise to alternatively spliced transcripts (bottom). Mutations (stars) and corresponding splicing products are characterised by DNA and RNA sequencing, respectively, and linked by a unique 15-nt barcode sequence in each minigene (coloured boxes). Black and grey boxes depict constitutive and alternative exons, respectively.

(B) A large number of *CD19* splice isoforms arise in the minigene library. *CD19* splice isoforms with highest maximal isoform frequency across all 9,321 minigene variants. Schematic representation (left) of 5 major and 18 cryptic isoforms depicts exons 1-3 (boxes) and introns (horizontal lines) with splice junctions for each isoform (arches). Colour indicates coding potential (green, coding; red, non-coding). Bar graph (right) shows average and maximal isoform frequency across all minigenes. Cryptic isoforms are sorted by maximal isoform frequency (**Table S3**).

(C) Inclusion isoform dominates in WT minigenes, whereas mutated variants show broad spread in all major isoforms. Frequencies of five major isoforms in replicate 1 for all wild type (black; n = 195) and mutated (grey; n = 9,476) minigenes in the library. Minigene variants harbouring a mutation in the 3' splice site of exon 2 (n = 174) are highlighted in blue. "Other" refers to the sum of 96 cryptic isoforms.

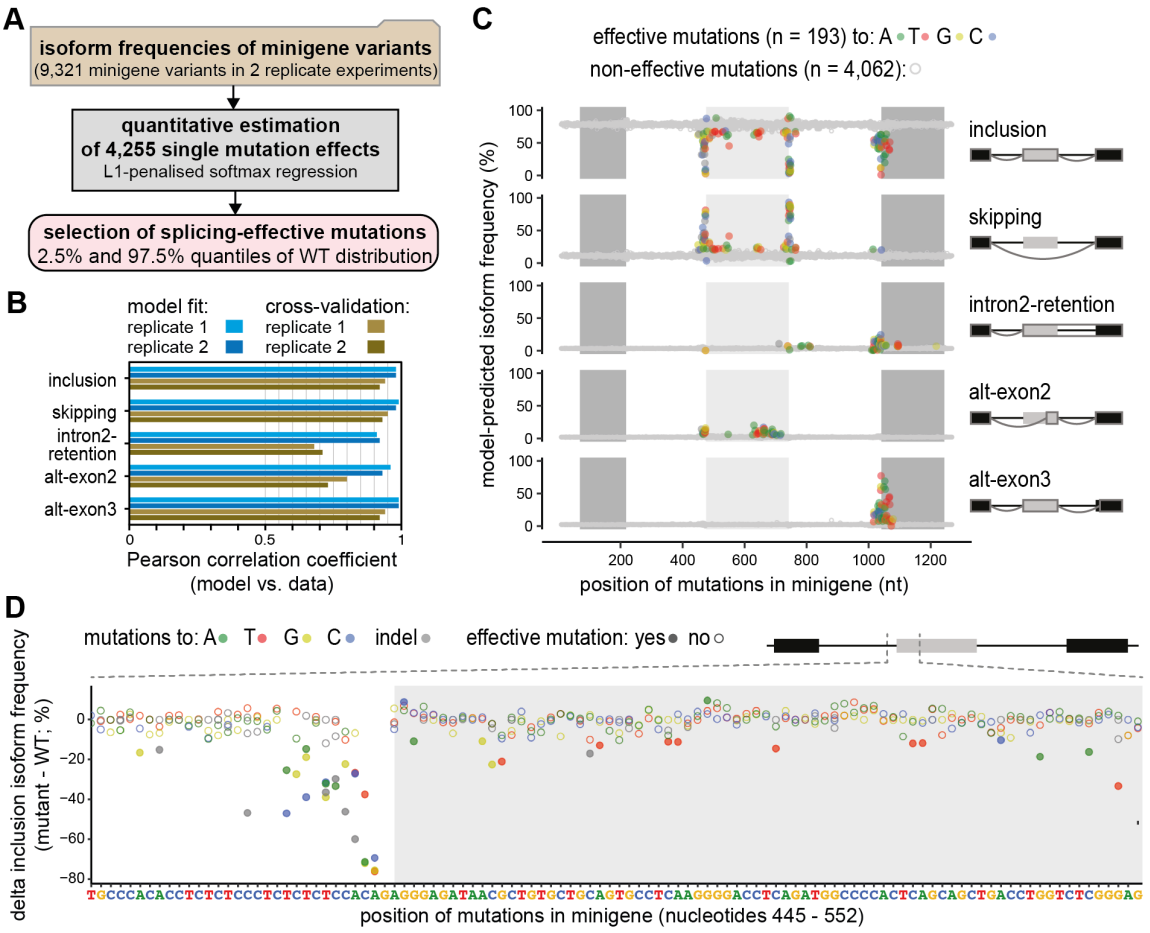

Figure 3. Quantitative modelling predicts single mutation effects on splice isoforms.
(A) Multinomial logistic regression workflow for the quantification and selection of single mutation effects. Based on the experimentally measured frequencies of five major isoforms in 9,321 minigene variants (top box), a softmax regression model was formulated to estimate 4,255 single mutation effects from the data (middle box) using L1 penalisation to prevent overfitting. Splicing-effective mutations were selected for each isoform based on the respective empirical WT frequency distribution using the 2.5% and 97.5% quantiles as cutoff.
(B) Splicing-effective mutations accumulate in distinct regions around exons 2 and 3. Landscape of model-predicted single mutation effects on five major isoforms (indicated on the right). Predicted isoform frequencies are plotted as a function of the position of a mutation. Colours indicate the nucleotide substitution of splicing-effective point mutations (see legend), whereas non-effective mutations are grey.
(C) The model performs well in fitting and 10-fold cross-validation. Bars show Pearson correlation coefficients between model and data for two replicates and each of the five isoforms across all combined mutation minigenes considered in model training and validation, respectively. See **Figure S3A, B** for corresponding scatter plots.
(D) Zoom-in shows the model-predicted delta inclusion isoform frequency (frequency for a point mutation - frequency in WT) for nucleotides 445-552 of the minigene. The type of nucleotide substitution is shown for all mutations, with splicing-effective mutations highlighted as filled circles.

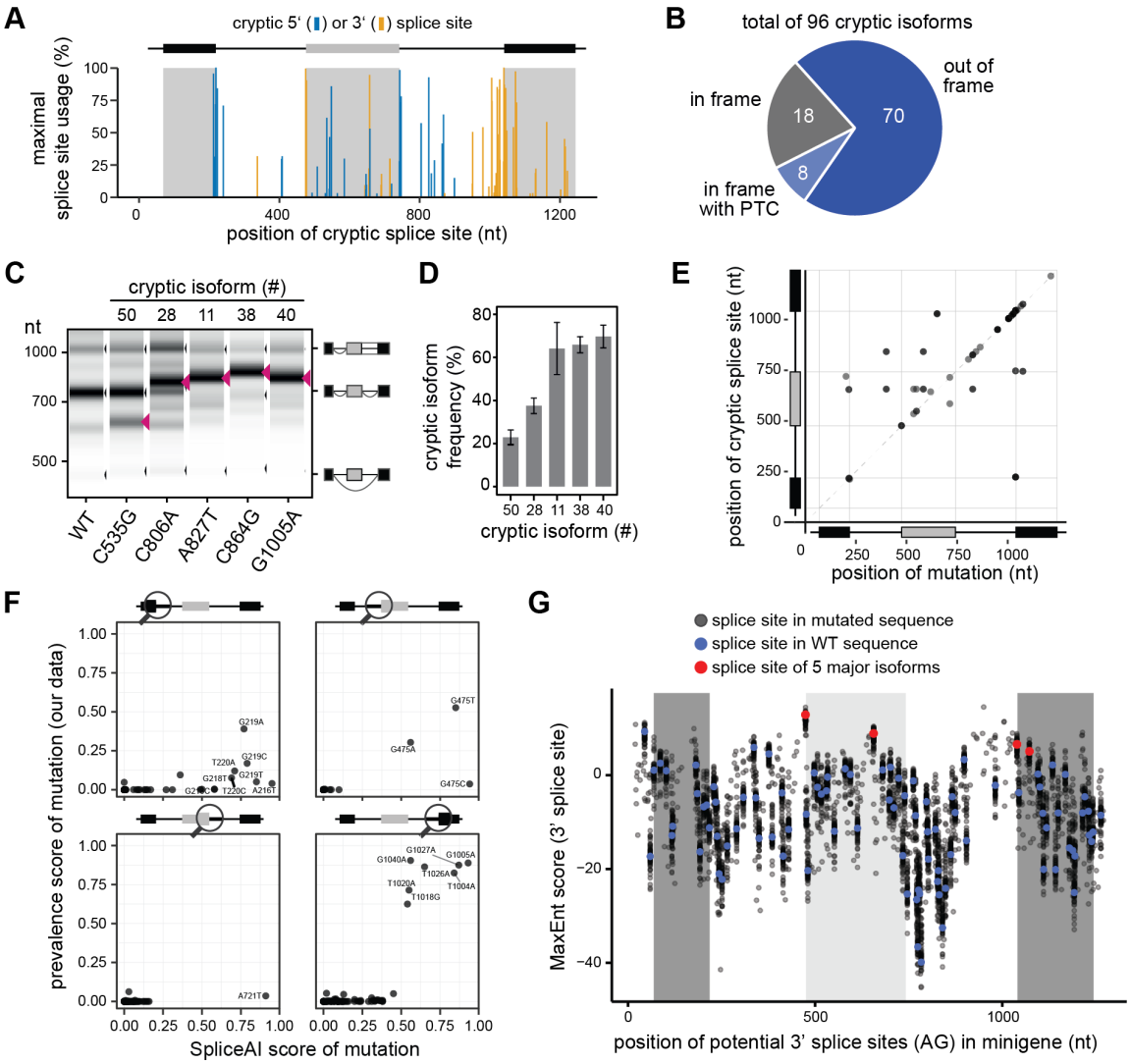

Figure 4. *CD19* mutations frequently activate cryptic splice sites.

(A) Alternative splicing of *CD19* minigene variants involves 71 cryptic splice sites. Splice site usage was calculated for each minigene variant by dividing the sum of junction reads involving a particular splice site by the total number of reads. The maximum usage across all minigenes is plotted against the corresponding position to the cryptic splice sites.

(B) Cryptic isoforms code for non-functional CD19 proteins. Out of 96 cryptic isoforms, 8 run into a premature termination codon (PTC) and 70 are out-of-frame, thus potentially encoding non-functional CD19 protein variants. The remaining 18 remain in frame, but are shortened or extended relative to the reference inclusion isoform.

(C, D) Experimental validation of five point mutations that are associated with distinct cryptic isoforms. Targeted point mutations were introduced into the *CD19* minigene, and splicing outcomes were determined by semi-quantitative RT-PCR. Predicted cryptic isoforms are indicated by red arrowheads. Gel-like representation (C), with major isoforms indicated on the right, and quantification (D). Error bars indicate s.d.m., n = 3 replicates.

(E) Mutations leading to cryptic isoforms are often located within or near cryptic splice sites. For 31 cryptic isoforms that are highly associated with a mutation (prevalence score > 0.25;

y-axis), the position of this mutation (x-axis) was related to the position of the used cryptic splice site (y-axis).
(F) SpliceAI correctly predicts single mutations leading to the generation of cryptic isoforms. SpliceAI was used to predict changes in splice junctions based on pre-mRNA sequence for all possible *CD19* minigene single mutants. SpliceAI scores of 0 and 1 reflect 0% or 100% probability to gain a cryptic splice site in response to a mutation, respectively (see Methods). Scatter plots compare the SpliceAI score against the prevalence score from our data, which quantifies the association of a mutation with a cryptic isoform, for 254 mutation-splice site pairs that match in their positions with SpliceAI. Separate panels are shown for each region around a canonical splice site (circle in schematic minigene representation).
(G) Exon 3 harbours a weak 3' splice site and is preceded by a high number of potentially competing cryptic 3’ splice sites, which often reach similar strength upon mutation. Dotplot shows splice site strengths (MaxEnt score) for putative 3’ splice sites (AG dinucleotides) in the *CD19* minigenes. MaxEnt score was calculated in a 23-nt sliding window for the WT sequence (red and blue dots) and hypothetical mutant minigenes, in which all possible single point mutations were introduced (grey dots). The 3’ splice sites used in the five major isoforms are highlighted in red.

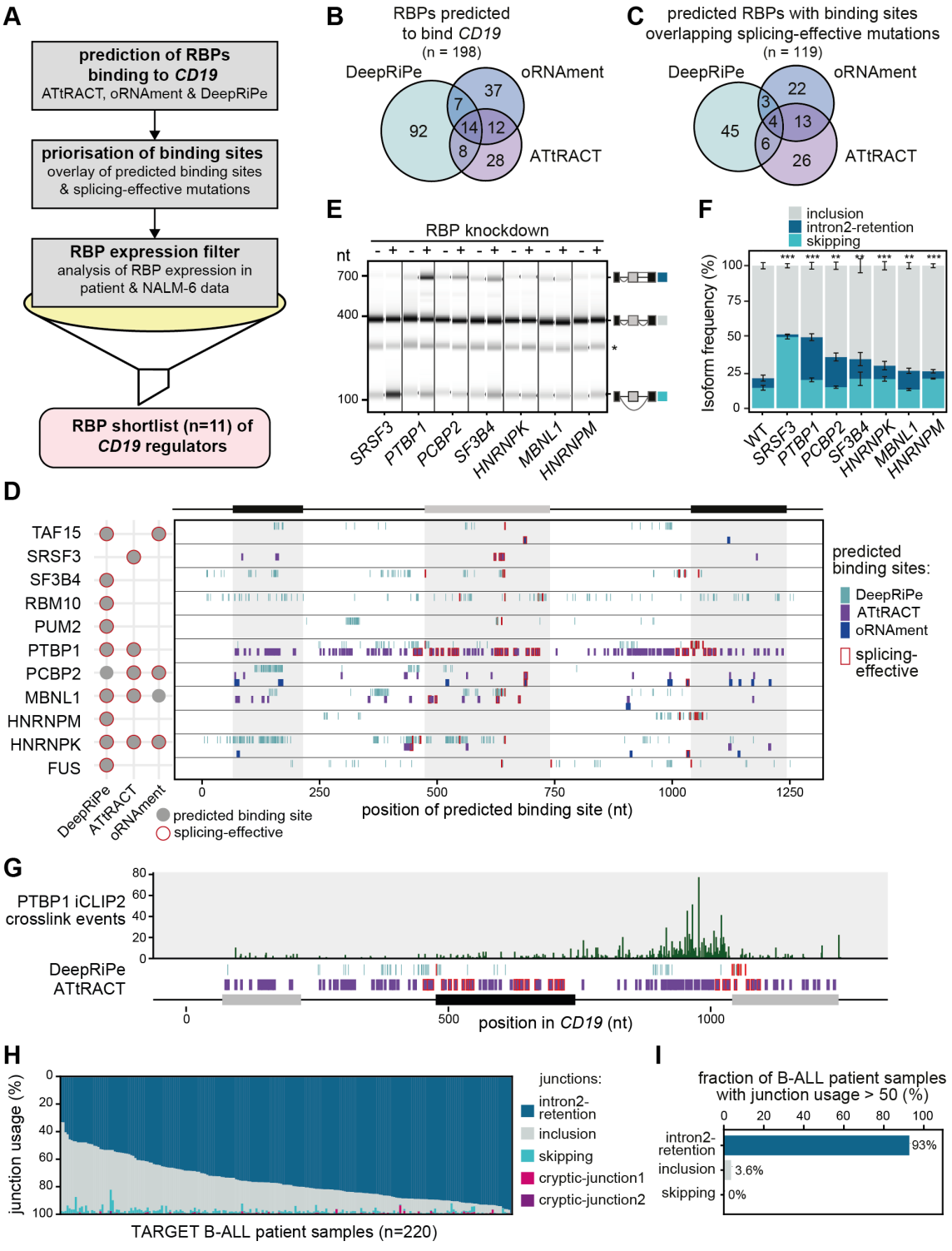

Figure 5. *In silico* predictions identify RBP regulators of *CD19* alternative splicing.
(A) Pipeline for the identification of potential RBP regulators of *CD19* splicing. Starting with *in silico* predictions, we obtained 198 candidate RBPs with predicted binding motifs (ATtRACT/oRNAment) or predicted differential binding upon mutation (DeepRiPe). These were prioritised by overlapping with the splicing-effective mutations from our screen.

Additionally, based on publicly available RNA-seq data, we required a minimum mean expression in RNA-seq data from B-ALL patients [29] and NALM-6 cells [66]. Together with literature information, we shortlisted 11 candidate RBPs for knockdown (KD) experiments, including SRSF3 as a positive control.

(B, C) *In silico* analyses predict dozens of RBPs binding to *CD19*. Venn diagrams show overlap of RBPs in initial predictions (B) and after overlay with splicing-effective mutations (C).

(D) The 11 candidate RBPs are predicted to bind throughout the *CD19* minigene region. For each RBP, the binding sites predicted by ATtRACT and oRNAment and disrupting mutations predicted by DeepRiPe, are indicated (see legend). Sites overlapping with splicing-effective mutations are framed in red. The schematic summary (left) shows that all 11 candidate RBPs have at least one predicted site that overlaps with a splicing-effective mutation. A full list of predicted binding sites (ATtRACT/oRNAment) and differential binding mutations (DeepRiPe) is provided in **Table S6**.

(E, F) Seven RBP KDs significantly change *CD19* splicing. Gel-like representation (E) and quantification (F) of semi-quantitative RT-PCR showing detected isoforms exon 2 inclusion (grey), intron 2 retention (blue) and skipping (turquoise) from the endogenous *CD19* gene in KD and control NALM-6 cells. Asterisk indicates a previously reported RT-PCR artefact [57] (see methods). Error bars indicate s.d.m., n = 3 replicates. ** *P* value < 0.01, *** *P* value < 0.001, Student's *t*-test. Measurements for all 11 KD experiments are shown in **Figure S6B, C**.

(G) PTBP1 shows extensive binding to *CD19* intron 2. Bar diagram shows the number of PTBP1 iCLIP crosslink events from NALM-6 cells on each nucleotide in endogenous *CD19* exons 1-3. Predicted PTBP1 binding motifs (ATtRACT) and mutations predicted to alter PTBP1 binding (DeepRiPe) are shown below (see legend in panel D). Nucleotide positions are given relative to minigene sequence.

(H, I) Intron 2 retention is the predominant isoform in B-ALL patients. **(H)** Stacked barchart shows the relative usage (percent selected index, PSI) of all junctions originating from exon 3 (**Figure S6D**) in 220 B-ALL patients (TARGET program). **(I)** Barchart quantifies the fraction of patients in which a given junction rises to PSI > 50%.

High-throughput mutagenesis identifies mutations and RNA-binding proteins controlling *CD19* splicing and CART-19 therapy resistance

Mariela Cortés-López[1#], Laura Schulz[1#], Mihaela Enculescu[1#], Claudia Paret[2], Bea Spiekermann[1], Anke Busch[1], Anna Orekhova[1], Fridolin Kielisch[1], Mathieu Quesnel-Vallières[3], Manuel Torres-Diz[4], Jörg Faber[2], Yoseph Barash[3], Andrei Thomas-Tikhonenko[4,5], Kathi Zarnack[6*], Stefan Legewie[1,7*], and Julian König[1*]

[1] Institute of Molecular Biology (IMB), Ackermannweg 4, 55128 Mainz, Germany. [2] Department of Pediatric Hematology/Oncology, Center for Pediatric and Adolescent Medicine, University Medical Center of the Johannes Gutenberg University Mainz, 55131 Mainz, Germany & University Cancer Center (UCT), University Medical Center of the Johannes Gutenberg University Mainz, 55131 Mainz & German Cancer Consortium (DKTK), site Frankfurt/Mainz, Germany, German Cancer Research Center (DKFZ), 69120 Heidelberg, Germany. [3] Department of Genetics, Perelman School of Medicine at the University of Pennsylvania, Philadelphia, PA 19104, US and Department of Biochemistry and Biophysics, Perelman School of Medicine at the University of Pennsylvania, Philadelphia, PA 19104, US. [4] Division of Cancer Pathobiology, Children's Hospital of Philadelphia, Philadelphia, PA 19104, US. [5] Department of Pathology & Laboratory Medicine, Perelman School of Medicine at the University of Pennsylvania, Philadelphia, PA 19104, US. [6] Buchmann Institute for Molecular Life Sciences (BMLS) and Faculty Biological Sciences, Goethe University Frankfurt, Max-von-Laue-Str. 15, 60438 Frankfurt, Germany. [7] Department of Systems Biology and Stuttgart Research Center for Systems Biology (SRCSB), University of Stuttgart, Stuttgart, Germany.

# These authors contributed equally.
* Corresponding authors: Kathi Zarnack (kathi.zarnack@bmls.de), Stefan Legewie (legewie@iig.uni-stuttgart.de), Julian König (j.koenig@imb-mainz.de)

SUPPLEMENTARY MATERIAL

Table of content:

Supplementary Figures

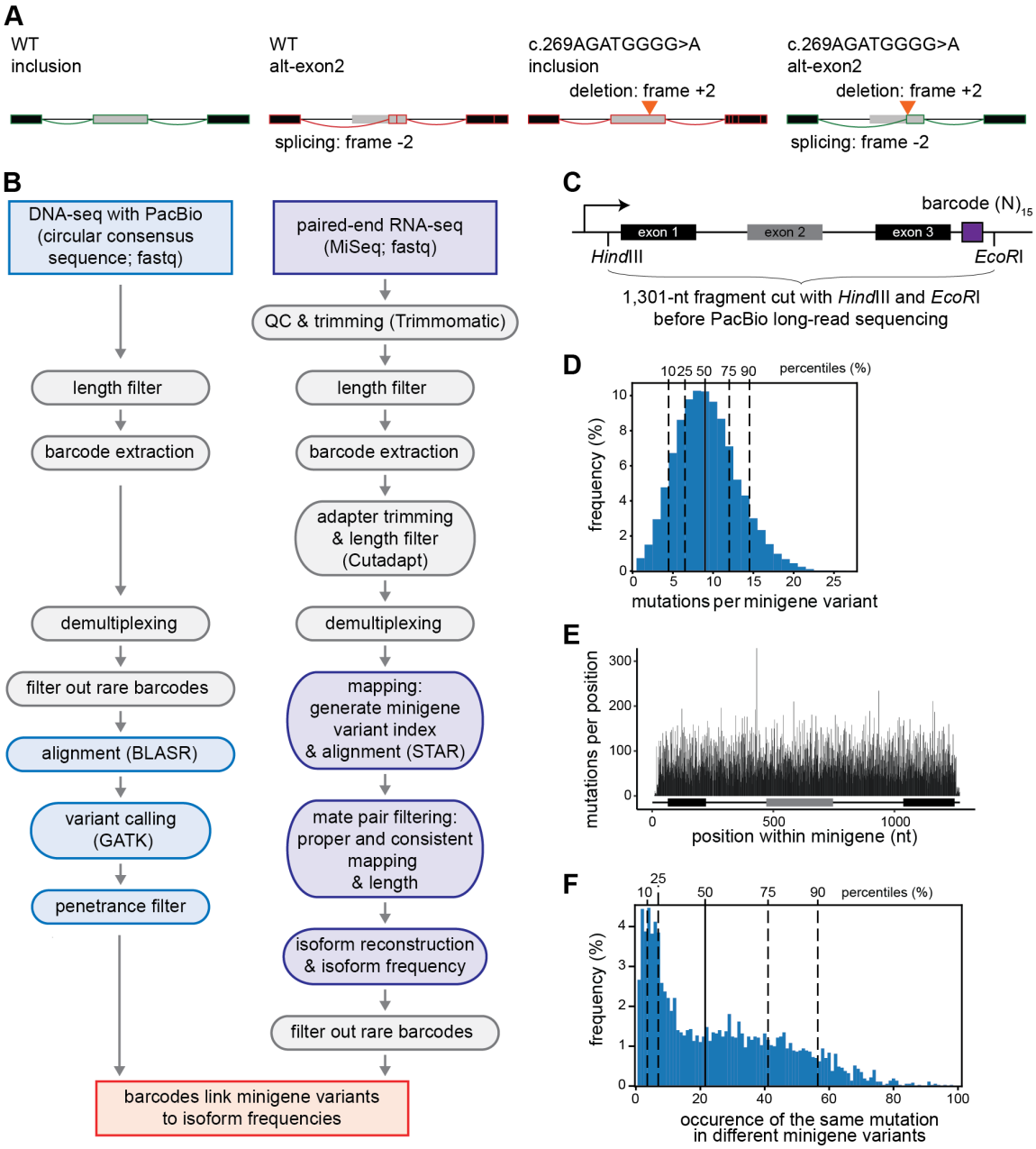

Figure S1. Long-read sequencing identifies the introduced mutations. (A) The deletion c.269AGATGGGG>A from patient #5 in Orlando et al. [1] introduces a frameshift (+2) that is compensated by the activation of an out-of-frame cryptic splice site (-2). Shown are the major isoforms inclusion and alt-exon2 and their coding potential in the absence (left) or presence (right) of the deletion (orange arrowhead). Schematic representation of depicts exons 1-3 (boxes) and introns (horizontal lines) with splice junctions for each isoform (arches). Colour indicates coding potential (green, coding; red, non-coding). **(B)** Analysis pipeline for the targeted DNA-seq and RNA-seq data. Left: Long-read DNA-seq data (PacBio, Pacific Bioscience) in the form of circular consensus sequences (CSS) were filtered by length (1,150-1,500 nt). 15-nt barcodes were extracted and demultiplexed, keeping only minigenes supported by at least 4 CSS. Alignment to the minigene reference was performed with BLASR [2] and variants were called using GATK HaplotypeCaller [3]. Mutations in the minigene were

filtered by the “penetrance score” (allele frequency, AF), discarding all the barcodes with more than 25% variants of low penetrance (AF < 0.8). Right: Short-read RNA-seq data (Illumina) were trimmed based on quality using Trimmomatic [4] and filtered by length (305 nt for read 1, 157 nt for read 2), and adapters were trimmed using Cutadapt [5] and 15-nt barcodes were extracted and demultiplexed, keeping only minigenes supported by at least 100 read pairs. Alignment to the specific mutated version of the minigene was performed using STAR [6]. Isoform reconstruction and isoform frequency estimation was done using custom scripts (see Methods). Only minigenes with 100 or more read pairs usable for isoform reconstruction were kept. **(C)** Structure of the *CD19* minigene fragment for long-read sequencing (PacBio) to identify introduced mutations. The minigene covers exons 1-3 with the intervening introns, followed by a 15-nt barcode. The fragment for PacBio sequencing is defined by the restriction sites for *Hind*III upstream of exon 1 and *EcoR*I downstream of the barcode sequence. **(D)** 91.6% of the minigene variants carry five or more mutations. Histogram shows number of mutations per minigene for 10,295 mutated minigene variants. **(E)** 4,255 distinct mutations are spread along the *CD19* minigene, with an average of 21 mutations per position. Barplot shows the sum of mutations per position in the minigene. **(F)** 81.9% of the mutations occur in at least three minigenes, which is sufficient for a reliable estimation of single mutation effects (**Figure S3C**). Histogram shows the frequencies of the same mutations in different minigene variants.

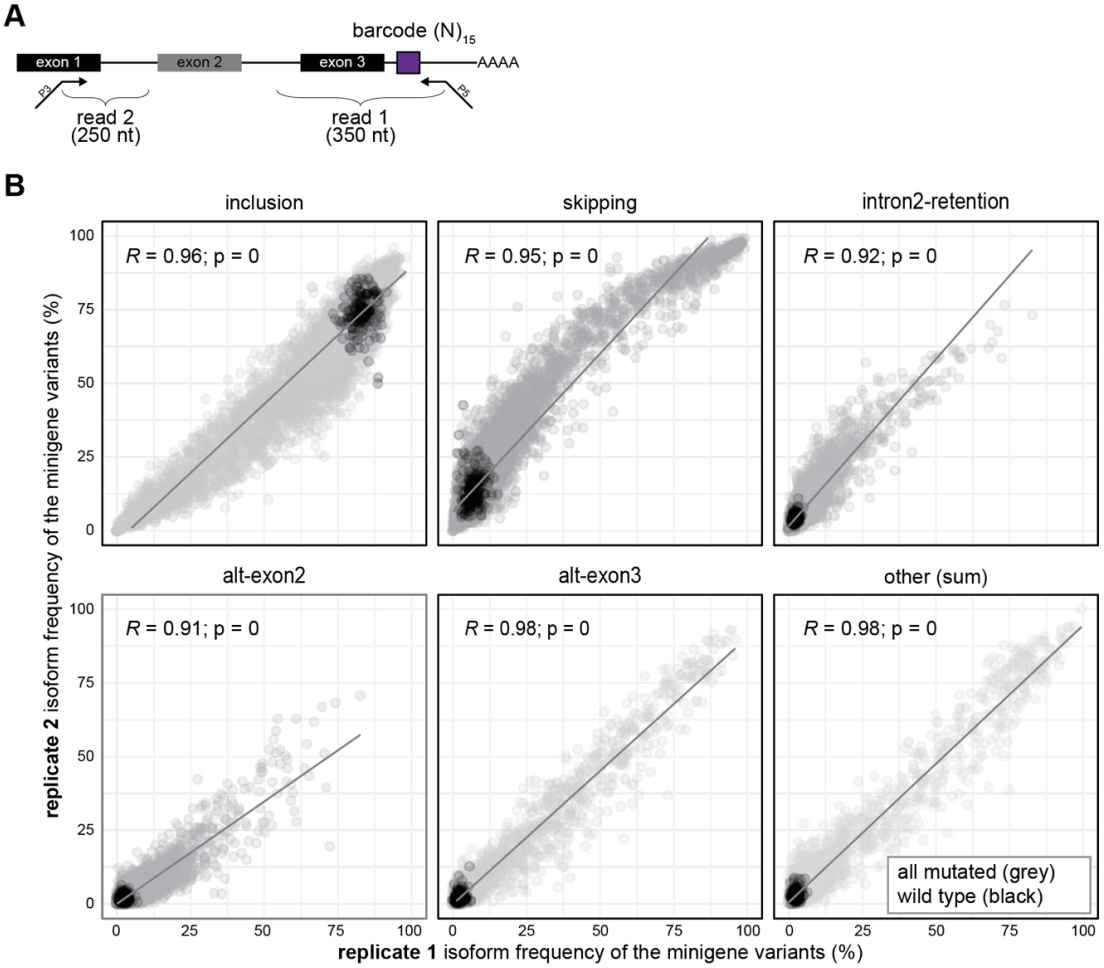

Figure S2. Isoform measurements from targeted RNA-seq results are consistent between replicates. (A) Description of the short-read RNA-seq strategy (Illumina) to capture the splicing products in the *CD19* minigene. Read 2 (250 nt) extends beyond exon 1, i.e. covering the exon 1/exon 2 junction, while read 1 (350 nt) includes the 15-nt barcode and extends beyond exon 3. **(B)** The isoform measurements correlate well between replicates. Scatterplots compare isoform frequencies for five major isoforms as well as the sum of 96 cryptic isoforms between replicate 1 and 2. Each dot represents a particular minigene captured in both replicates. WT and mutated minigenes appear in black and grey, respectively. Pearson correlation coefficients (*R*) and associated *P* values are given.

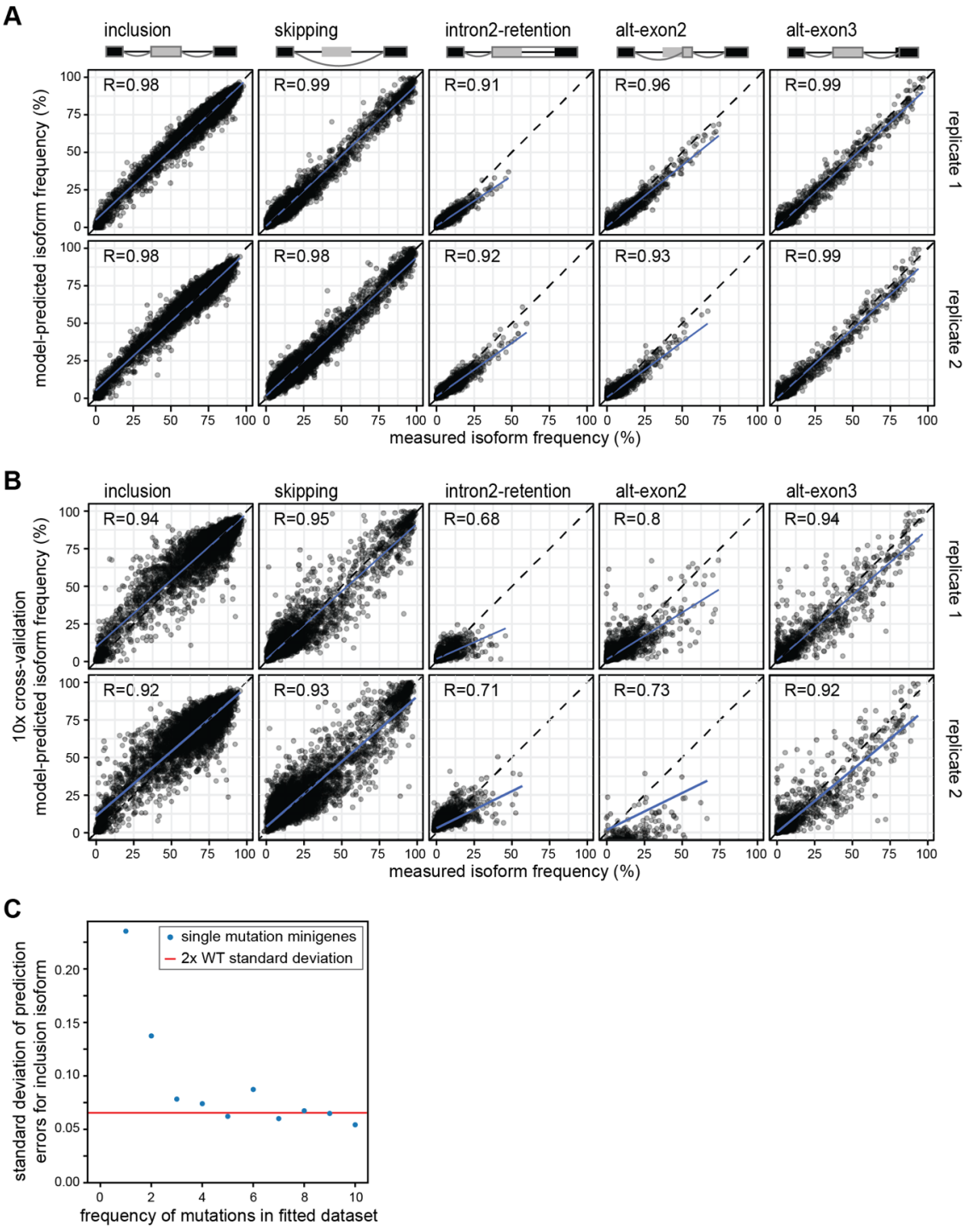

Figure S3. The softmax regression model performs well for training and test data. (A) Regression model fits measured combined mutation effects (i.e., minigene measurements) with high accuracy. Scatterplots show frequencies of the five major isoforms in the measurements (x-axis) against the model fit (y-axis) for two biological replicates and 9,321 minigene variants used in model training. Pearson correlation coefficients (*R*) are shown for each scatter plot. **(B)** Cross-validation confirms the predictive power of the model for minigenes not used in training. The minigene library was randomly split into ten equally sized subsets. During 10-fold cross-validation, the softmax regression model was fitted to all data excluding one subset. Scatterplots compare model-predicted splicing outcome for left-out

subsets to corresponding experimental data for all major splice isoforms and are an overlay of the results of all cross-validation runs. Representation as in (A). **(C)** The model correctly infers single mutation effects. Seven single-mutation minigenes in which inclusion is significantly changed were left-out separately from softmax regression fitting and their effects were predicted based on the fit to the remaining minigene data. This procedure was repeated while additionally excluding random permutations of other minigenes containing the mutation. The standard deviation of the prediction error (y-axis) is plotted against the number of minigenes used in model training (x-axis). The inference power of the model reaches two standard deviations of the WT minigenes (horizontal line) if more than two minigenes containing the mutation are considered in model training. See Methods for details.

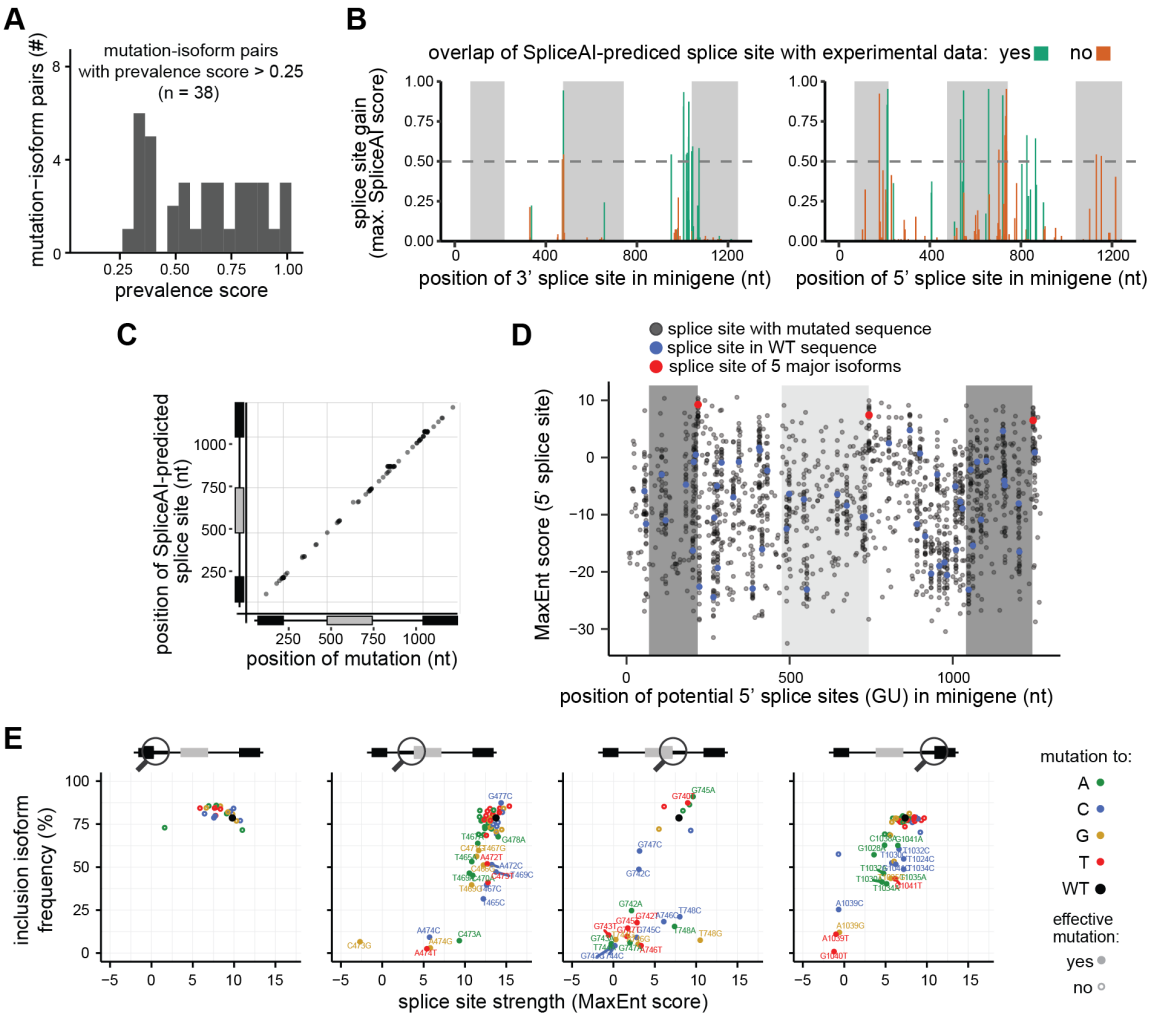

Figure S4. Multiple mutations give rise to distinct cryptic isoforms. (A) Multiple mutations are associated with a specific cryptic isoform. Histogram shows distribution of prevalence scores for 38 mutation-isoform pairs in which a specific mutation is associated with a distinct cryptic isoform (prevalence score > 0.25). A prevalence score of 1 indicates perfect correspondence between mutation and isoform. **(B)** SpliceAI [7] predictions for gained cryptic splice sites overlap with experimental data. Barplot shows the maximum SpliceAI score ("acceptor gain") for all the mutations that increase the probability of a given cryptic splice site to be used (38 mutations with Splice AI score [gain] > 0.5, including 15 and 23 gained 3' [left] and 5' splice sites [right]). Dotted horizontal line represents the recommended minimum threshold for a SpliceAI prediction (SpliceAI score > 0.2) [7]. Predicted gained splice sites that also appear in our experimental data are shown in green. **(C)** The mutation effects predicted by SpliceAI exclusively occur in close range, such that all SpliceAI-predicted effective mutations reside on average within 6 nt from the cryptic splice site generated. Scatterplot shows location of the gained cryptic splice sites with respect to the mutations. Only the splice site with the highest score for each mutation is considered. **(D)** The 5' splice sites of the main isoforms (red) are stronger than most other 5' splice sites in the *CD19* minigene sequence. Dotplot shows splice site strengths (MaxEnt score) [8] for putative 5' splice sites in WT (blue) and mutated (grey) minigenes in a 9-nt sliding window containing a GU dinucleotide at positions 4-5. 5' splice sites used in the five major isoforms are shown in red. **(E)** Mutation effects at 3' and 5' splice sites of *CD19* exons 2 and 3 are consistent with predicted splice site strengths. Mutations are coloured according to the changed nucleotides. Scores for WT sequence are coloured in black. Splicing-effective mutations (according to our results) are shown as filled circles and labelled, while non-effective mutations are shown as open circles.

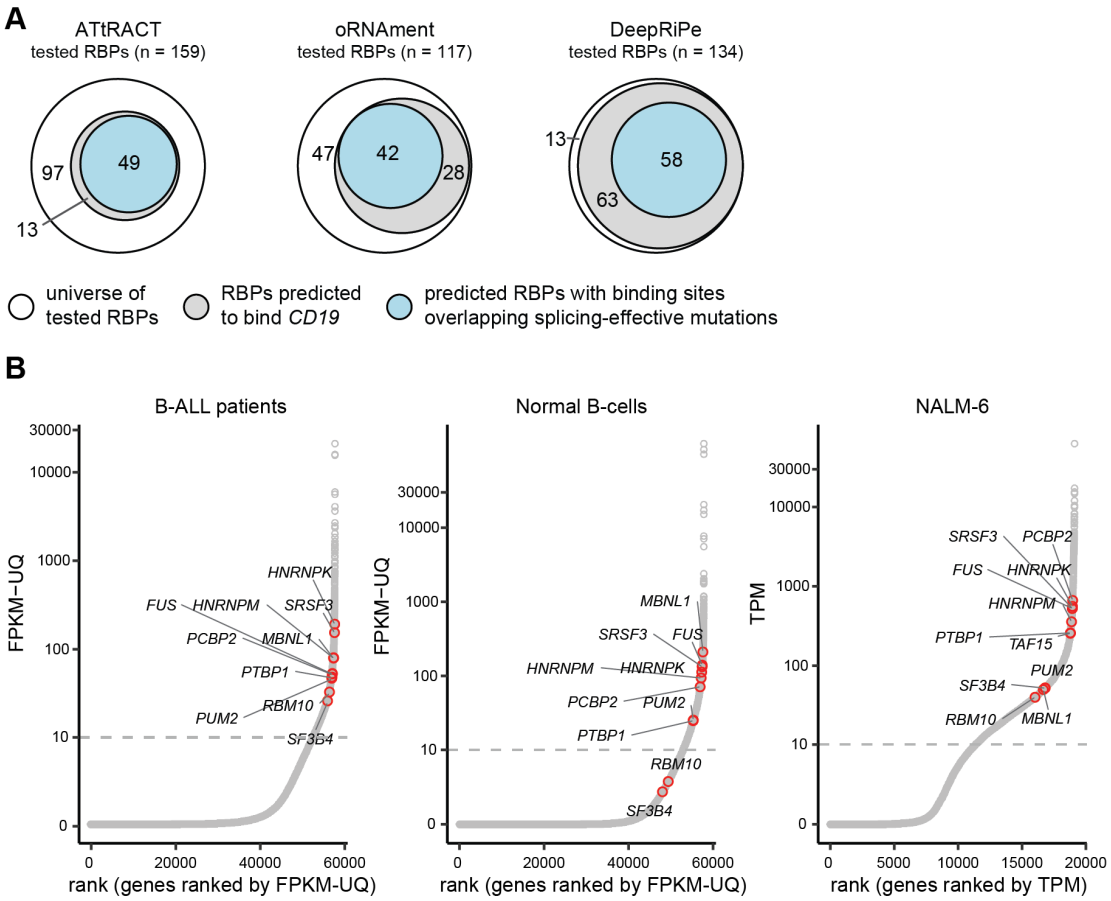

Figure S5. *In silico* RBP binding site predictions suggest dozens of candidate regulators of *CD19* alternative splicing. (A) *In silico* predictions of RBP binding sites were performed with ATtRACT [9] and oRNAment [10] as well as of point mutations affecting RBP binding using DeepRiPe [11]. For each prediction tool, the total number of available RBPs (white circles) is split up into those that are predicted to bind *CD19* (grey circles) and whose predicted binding sites overlap with splicing-effective mutations from our data (blue circles). Numbers refer to exclusive RBPs in each area. **(B)** Predicted RBPs were filtered based on their expression observed in B-ALL patients reported in [12]. Plot shows ranked expression values for all detected genes in samples from B-ALL patients, normal B-cells [13] and NALM-6 cells [14]. Highlighted in red are the RBP candidate genes (n = 11) tested in knockdown experiments. TPM, transcripts per million. FPKM-UQ, fragments per kilobase of transcript per million mapped reads upper quartile, a modified RNA-seq normalisation method (https://docs.gdc.cancer.gov/Encyclopedia/pages/HTSeq-FPKM-UQ/).

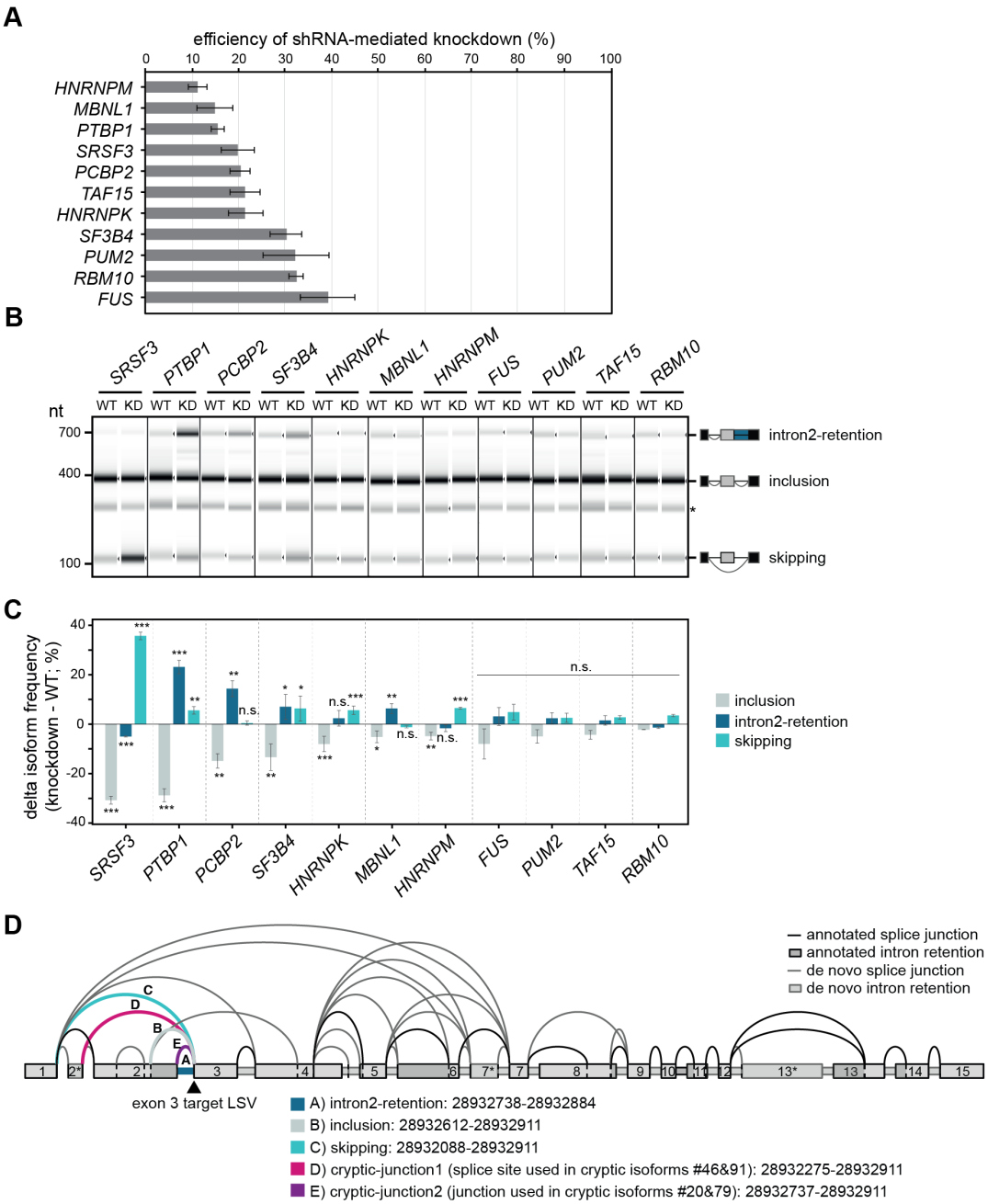

Figure S6. Knockdown experiments show significant effects on endogenous *CD19* splicing for seven candidate RBPs. (A) All tested RBPs are efficiently depleted upon shRNA knockdown (KD). Barplot shows mean qPCR measurements of remaining transcripts (relative to WT) for 11 candidate RBPs. Error bars indicate standard deviation of the mean (s.d.m.), n = 3 replicates. **(B, C)** Seven RBP knockdowns significantly affect *CD19* alternative splicing. Semiquantitative RT-PCR was performed to detect isoforms generated from exons 1-3 of the endogenous *CD19* gene. Gel-like representation (B), with major isoforms indicated on the right, and quantification (C), as difference in isoform frequency compared to WT, are shown. Error bars indicate s.d.m., n = 3 replicates. * *P* value < 0.05, ** *P* value < 0.01, *** *P* value < 0.01, n.s., not significant, Student's *t*-test. **(D)** *CD19* shows extensive mis-splicing in B-ALL patients. Splice junctions were quantified with MAJIQ [15] for 222 B-ALL patients from the Therapeutically Applicable Research To Generate Effective Treatments (TARGET) program (https://ocg.cancer.gov/programs/target). Splicegraph shows all splice junctions with a usage

level (percent selected index, PSI) of at least 5% in any patient. Junctions and target exon of the local splicing variation (LSV) shown in **Figure 5H, I** are highlighted.

Supplementary Data

Data S1. Single mutation effects on the major isoforms from the *CD19* minigene in NALM-6 cells. For each isoform, the y-axis shows the isoform frequency (mean of two biological replicates) resulting from each individual mutation in a given position along the y-axis. Each dot represents one mutation, with colours indicating the inserted nucleotide (green, mutation to A; blue, to C; yellow, to G; red, to T). Splicing-effective mutations are shown as filled circles and non-effective mutations as open circles. Dashed lines indicate the median isoform frequency of the WT minigenes (black) ± 2 standard deviations (grey). The shown isoforms are *CD19* exon 2 inclusion, skipping, intron2-retention, alt-exon2 and alt-exon3 as well as the sum of 96 cryptic isoforms ("other").

Supplementary Tables

Table S1. Mutations from relapsed B-ALL patients reported in Orlando et al. that were tested in the *CD19* minigene splicing reporter. Patient IDs are given as reported in Orlando et al. [1]. Note that for patient #14, two separate minigene variants were tested (#14.1 and #14.2), and that #14.2 is a combination of two adjacent mutations reported in patient #14, namely c.509A>AGTGG and c.510GCCTC>GTGGGGGAG.

patient ID	mutation	genomic coordinate (hg38)	position in minigene	reference allele (REF)	alternative allele (ALT)
#2	c.259G>GGGGGC	chr16:28932516	646	G	GGGGGC
#4	c.517TGTCTCCCACCG>T	chr16:28933072	1202	TGTCTCCCACCG	T
#5	c.269AGATGGGG>A	chr16:28932526	656	AGATGGGG	A
#8	c.265CA>C	chr16:28932522	652	CA	C
#11	c.264TCAACAGATGGGGGGCTTCTACCTGTGC>T	chr16:28932521	651	TCAACAGATGGGGGGCTTCTACCTGTGC	T
#13	c.421T>TC	chr16:28932976	1106	T	TC
#14.1	c.297GGGGC>G	chr16:28932554	684	GGGGC	G
#14.2	c.510AGCCTC>AGTGGGGGAG	chr16:28933065	1195	AGCCTC	AGTGGGGGAG
#15	c.271ATGGGGGGCTTCTACCTGTGCCAGCCGGGGCCC>AAGACGT	chr16:28932528	658	ATGGGGGGCTTCTACCTGTGCCAGCCGGGGCCC	AAGACGT

Table S2. Quantification of splicing isoforms for all minigene variants in the library. For each minigene variant, the 15-nt barcode sequence is shown together with the contained mutations, with multiple mutations separated by commas. The total number of reads per minigene variant and their distribution among the 101 isoforms are given for RNA-seq replicates 1 and 2 from NALM-6 cells. Isoform notation (219 475) indicates a splice junction that removed the region from nucleotides 219 to 475. The five major isoforms are *CD19* exon 2 inclusion (219 475)(743 1040), skipping (219 1040), intron2-retention (219 475), alt-exon2 (219 657)(743 1040) and alt-exon3 (219 475)(743 1073). In total, we detected splicing isoforms for 9,671 minigene variants in replicate 1 and for 9,372 minigene variants in replicate 2, including 9,321 minigene variants that were present in both replicates.

< provided as Excel file >

Table S3. List of detected isoforms from the *CD19* minigene. A total of 101 isoforms reached a relative frequency of at least 5% in at least one minigene variant, including the five major isoforms inclusion, skipping, intron2-retention, alt-exon2 and alt-exon3 (>5% in WT) as well as 96 cryptic isoforms. For each isoform, the assigned name or number is shown together with the isoform specification. Isoform notation (219 475) indicates a splice junction that removed the region from nucleotides 219 to 475. With respect to the predicted impact on the encoded CD19 protein, the number of premature stop codons (PTCs), the frame (in-frame or out-of-frame) and the resulting coding potential (coding or non-coding) are reported. With respect to an isoform's relative abundance, the average isoform frequency in the library and the maximal isoform frequency in an individual minigene are given. For the 38 cryptic isoforms that are associated with a specific mutation (prevalence score > 0.25), the respective mutations are provided together with their prevalence score and genomic coordinate (hg38). Notation G475T indicates that G in position 475 was mutated to T.

< provided as Excel file >

Table S4. Single mutation effects predicted by the mathematical model. Worksheet "Mutation effects" provides the model estimates of splice isoform frequencies (in %) and average delta frequency (compared to WT) in replicates (rep) 1 and 2 in response to individual mutations (single nucleotide variants, SNV; insertions or deletions, INDEL) in NALM-6 cells. Notation G475T indicates that G in position 475 was mutated to T. Individual entries are given for each affected isoform. Isoform notation (219 475) indicates a splice junction that removed the region from nucleotides 219 to 475. The five major isoforms are *CD19* exon 2 inclusion (219 475)(743 1040), skipping (219 1040), intron2-retention (219 475), alt-exon2 (219 657)(743 1040) and alt-exon3 (219 475)(743 1073). Worksheet "WT statistics" provides the mean, standard deviation (sd) and median of measured splice isoform frequencies (in %) for the five major isoforms as well as the sum of 96 cryptic isoforms ("other"). Isoform frequencies were measured for 195 and 194 WT minigenes in the two replicates.

< provided as Excel file >

Table S5. Overlapping single nucleotide variants (SNVs) and cancer-related mutations. Worksheet "Annotated variants" contains the SNVs (from ENSEMBL [16] v104, gnomAD [17] v3.1 and ClinVar [18] accessed 09/2021) and cancer-related variants (obtained from COSMIC [19] v94) that overlap with splicing-effective mutations and mutations with a prevalence score > 0.25 in our screen. Notation A950G indicates that A in position 950 was mutated to G. For variants present in the database dbSNP [20], the respective ID is also included. REF and ALT refer to the reference and alternative allele.

< provided as Excel file >

Table S6. Predicted RBP binding sites in the region of the *CD19* minigene. Worksheet "Binding sites" reports *in silico* predictions by ATtRACT [9] and oRNAment [10], providing the source tool, start and end and width (relative to the *CD19* minigene), predicted RNA-binding protein (RBP) and whether the binding site overlaps with splicing-effective mutations from our screen (see Methods). Worksheet "DeepRiPe mutations" reports all mutations predicted by DeepRiPe [11] to change RBP binding (i.e., with a delta score > 0.25), including RBP, mutation, DeepRiPe score and set as well as whether the mutation overlaps with a splicing-effective mutation from our screen and if so, for which isoform. Set refers to the DeepRiPe model that was trained for a given RBP using PAR-CLIP or ENCODE eCLIP data from HepG2 or K562 cells (see [11] for details).

< provided as Excel file >

Table S7. Oligonucleotides used to clone the different shRNA sequence carrying vectors in this study. Oligonucleotides were purchased from Integrated DNA Technologies.

shRNA_FUS	TGCTGTTGACAGTGAGCGCACAGGATAATTCAGACAACAATAG TGAAGCCACAGATGTATTGTTGTCTGAATTATCCTGTTTGCCTA CTGCCTCGGA
shRNA_HNRNPK	TGCTGTTGACAGTGAGCGACGAGTTGAGGCTGTTGATTCATAG TGAAGCCACAGATGTATGAATCAACAGCCTCAACTCGCTGCCT ACTGCCTCGGA
shRNA_HNRNPM	TGCTGTTGACAGTGAGCGAAGCAGACATTCTTGAAGATAATAGT GAAGCCACAGATGTATTATCTTCAAGAATGTCTGCTCTGCCTAC TGCCTCGGA
shRNA_MBNL1	TGCTGTTGACAGTGAGCGCCAGCACAATGATTGACACCAATAG TGAAGCCACAGATGTATTGGTGTCAATCATTGTGCTGTTGCCTA CTGCCTCGGA
shRNA_PCBP2	TGCTGTTGACAGTGAGCGCTCCATCATTGAGTGTGTCAAATAGT GAAGCCACAGATGTATTTGACACACTCAATGATGGATTGCCTAC TGCCTCGGA
shRNA_PTBP1	TGCTGTTGACAGTGAGCGCTAGCAAGATGATACAATGGTATAG TGAAGCCACAGATGTATACCATTGTATCATCTTGCTATTGCCTA CTGCCTCGGA
shRNA_PUM2	TGCTGTTGACAGTGAGCGCAACATAGTTGTTGACTGTTAATAGT GAAGCCACAGATGTATTAACAGTCAACAACTATGTTATGCCTAC TGCCTCGGA
shRNA_RBM10	TGCTGTTGACAGTGAGCGCCGGCAAGACCATCAATGTTGATAG TGAAGCCACAGATGTATCAACATTGATGGTCTTGCCGTTGCCTA CTGCCTCGGA
shRNA_SF3B4	TGCTGTTGACAGTGAGCGCTGCCTTCAAGAAGGACTCCAATAG TGAAGCCACAGATGTATTGGAGTCCTTCTTGAAGGCATTGCCTA CTGCCTCGGA
shRNA_SRSF3	TGCTGTTGACAGTGAGCGCTAAGATGTTTTAGCTGTTCAATAGT GAAGCCACAGATGTATTGAACAGCTAAAACATCTTAATGCCTAC TGCCTCGGA
shRNA_TAF15	TGCTGTTGACAGTGAGCGATCAGGCTATGATCAACATCAATAGT GAAGCCACAGATGTATTGATGTTGATCATAGCCTGACTGCCTAC TGCCTCGGA

Table S8. qPCR oligonucleotide pairs used in this study. Oligonucleotides were purchased from Sigma-Aldrich.

	Forward primer	Reverse primer
qPCR_FUS	AAGGCCTGGGTGAGAATGTT	GGCTGTCCCGTTTTCTTGTT
qPCR_HNRNPK	GCGAGTTGAGGCTGTTGATT	TCAGTGGAATGAGGACAGCA
qPCR_HNRNPM	GTCAAGGGGATGTGCTGTTG	TCCGCTCAGACTATGCTTGT
qPCR_MBNL1	CGGTTTGCTCATCCTGCTGA	TTTGCACTTTTCCCGAGAGC
qPCR_PCBP2	CCAGCTCTCCGGTCATCTTT	CTGGTGCAGCTTGGTCAAAT
qPCR_PTBP1	CGAGATGAACACGGAGGAGG	CTGGATGTAGATGGGCTGGC
qPCR_PUM2	TCAGCGTCCTCTTACTCCCA	CCAGTAGCAAGACCCTGACC
qPCR_RBM10	TGTTCCCGACGTCTCTACCT	TCTCCCCATCCCAGTACAGG
qPCR_SF3B4	GAACGACTTCTGGCAGCTCA	CACAGGATTGGGAGCAGAGG
qPCR_SRSF3	CCCGGCTTTGCTTTTGTTGA	TTCCACTCTTACACGGCAGC
qPCR_TAF15	GGTCACAGGGAGGAGGTAGA	CAGCATCTGTTCTGGGTCCA

Supplementary References

1. Orlando EJ, Han X, Tribouley C, Wood PA, Leary RJ, Riester M, Levine JE, Qayed M, Grupp SA, Boyer M, De Moerloose B, Nemecek ER, Bittencourt H, Hiramatsu H, Buechner J, Davies SM, Verneris MR, Nguyen K, Brogdon JL, Bitter H, Morrissey M, Pierog P, Pantano S, Engelman JA & Winckler W. Genetic mechanisms of target antigen loss in CAR19 therapy of acute lymphoblastic leukemia. *Nat Med* **24**, 1504-1506 (2018).
2. Chaisson MJ & Tesler G. Mapping single molecule sequencing reads using basic local alignment with successive refinement (BLASR): application and theory. *BMC Bioinformatics* **13**, 238 (2012).
3. McKenna A, Hanna M, Banks E, Sivachenko A, Cibulskis K, Kernytsky A, Garimella K, Altshuler D, Gabriel S, Daly M & DePristo MA. The Genome Analysis Toolkit: a MapReduce framework for analyzing next-generation DNA sequencing data. *Genome Res* **20**, 1297-1303 (2010).
4. Bolger AM, Lohse M & Usadel B. Trimmomatic: a flexible trimmer for Illumina sequence data. *Bioinformatics* **30**, 2114-2120 (2014).
5. Martin M. Cutadapt removes adapter sequences from high-throughput sequencing reads. *EMBnet.journal* **17**, 10-12 (2011).
6. Dobin A, Davis CA, Schlesinger F, Drenkow J, Zaleski C, Jha S, Batut P, Chaisson M & Gingeras TR. STAR: ultrafast universal RNA-seq aligner. *Bioinformatics* **29**, 15-21 (2013).
7. Jaganathan K, Kyriazopoulou Panagiotopoulou S, McRae JF, Darbandi SF, Knowles D, Li YI, Kosmicki JA, Arbelaez J, Cui W, Schwartz GB, Chow ED, Kanterakis E, Gao H, Kia A, Batzoglou S, Sanders SJ & Farh KK. Predicting Splicing from Primary Sequence with Deep Learning. *Cell* **176**, 535-548 e524 (2019).
8. Yeo G & Burge CB. Maximum entropy modeling of short sequence motifs with applications to RNA splicing signals. *J Comput Biol* **11**, 377-394 (2004).
9. Giudice G, Sanchez-Cabo F, Torroja C & Lara-Pezzi E. ATtRACT-a database of RNA-binding proteins and associated motifs. *Database (Oxford)* **2016** (2016).
10. Benoit Bouvrette LP, Bovaird S, Blanchette M & Lecuyer E. oRNAment: a database of putative RNA binding protein target sites in the transcriptomes of model species. *Nucleic Acids Res* **48**, D166-D173 (2020).
11. Ghanbari M & Ohler U. Deep neural networks for interpreting RNA-binding protein target preferences. *Genome Res* **30**, 214-226 (2020).
12. Gu Z, Churchman ML, Roberts KG, Moore I, Zhou X, Nakitandwe J, Hagiwara K, Pelletier S, Gingras S, Berns H, Payne-Turner D, Hill A, Iacobucci I, Shi L, Pounds S, Cheng C, Pei D, Qu C, Newman S, Devidas M, Dai Y, Reshmi SC, Gastier-Foster J, Raetz EA, Borowitz MJ, Wood BL, Carroll WL, Zweidler-McKay PA, Rabin KR, Mattano LA, Maloney KW, Rambaldi A, Spinelli O, Radich JP, Minden MD, Rowe JM, Luger S, Litzow MR, Tallman MS, Racevskis J, Zhang Y, Bhatia R, Kohlschmidt J, Mrozek K, Bloomfield CD, Stock W, Kornblau S, Kantarjian HM, Konopleva M, Evans WE, Jeha S, Pui CH, Yang J, Paietta E, Downing JR, Relling MV, Zhang J, Loh ML, Hunger SP & Mullighan CG. PAX5-driven subtypes of B-progenitor acute lymphoblastic leukemia. *Nat Genet* **51**, 296-307 (2019).
13. Alexander TB, Gu Z, Iacobucci I, Dickerson K, Choi JK, Xu B, Payne-Turner D, Yoshihara H, Loh ML, Horan J, Buldini B, Basso G, Elitzur S, de Haas V, Zwaan CM, Yeoh A, Reinhardt D, Tomizawa D, Kiyokawa N, Lammens T, De Moerloose B, Catchpoole D, Hori H, Moorman A, Moore AS, Hrusak O, Meshinchi S, Orgel E, Devidas M, Borowitz M, Wood B, Heerema NA, Carrol A, Yang YL, Smith MA, Davidsen TM, Hermida LC, Gesuwan P, Marra MA, Ma Y, Mungall AJ, Moore RA, Jones SJM,

Valentine M, Janke LJ, Rubnitz JE, Pui CH, Ding L, Liu Y, Zhang J, Nichols KE, Downing JR, Cao X, Shi L, Pounds S, Newman S, Pei D, Guidry Auvil JM, Gerhard DS, Hunger SP, Inaba H & Mullighan CG. The genetic basis and cell of origin of mixed phenotype acute leukaemia. *Nature* **562**, 373-379 (2018).

14. Barretina J, Caponigro G, Stransky N, Venkatesan K, Margolin AA, Kim S, Wilson CJ, Lehar J, Kryukov GV, Sonkin D, Reddy A, Liu M, Murray L, Berger MF, Monahan JE, Morais P, Meltzer J, Korejwa A, Jane-Valbuena J, Mapa FA, Thibault J, Bric-Furlong E, Raman P, Shipway A, Engels IH, Cheng J, Yu GK, Yu J, Aspesi P, Jr., de Silva M, Jagtap K, Jones MD, Wang L, Hatton C, Palescandolo E, Gupta S, Mahan S, Sougnez C, Onofrio RC, Liefeld T, MacConaill L, Winckler W, Reich M, Li N, Mesirov JP, Gabriel SB, Getz G, Ardlie K, Chan V, Myer VE, Weber BL, Porter J, Warmuth M, Finan P, Harris JL, Meyerson M, Golub TR, Morrissey MP, Sellers WR, Schlegel R & Garraway LA. The Cancer Cell Line Encyclopedia enables predictive modelling of anticancer drug sensitivity. *Nature* **483**, 603-607 (2012).
15. Vaquero-Garcia J, Barrera A, Gazzara MR, González-Vallinas J, Lahens NF, Hogenesch JB, Lynch KW & Barash Y. A new view of transcriptome complexity and regulation through the lens of local splicing variations. *Elife* **5**, e11752 (2016).
16. Howe KL, Achuthan P, Allen J, Allen J, Alvarez-Jarreta J, Amode MR, Armean IM, Azov AG, Bennett R, Bhai J, Billis K, Boddu S, Charkhchi M, Cummins C, Da Rin Fioretto L, Davidson C, Dodiya K, El Houdaigui B, Fatima R, Gall A, Garcia Giron C, Grego T, Guijarro-Clarke C, Haggerty L, Hemrom A, Hourlier T, Izuogu OG, Juettemann T, Kaikala V, Kay M, Lavidas I, Le T, Lemos D, Gonzalez Martinez J, Marugan JC, Maurel T, McMahon AC, Mohanan S, Moore B, Muffato M, Oheh DN, Paraschas D, Parker A, Parton A, Prosovetskaia I, Sakthivel MP, Salam AIA, Schmitt BM, Schuilenburg H, Sheppard D, Steed E, Szpak M, Szuba M, Taylor K, Thormann A, Threadgold G, Walts B, Winterbottom A, Chakiachvili M, Chaubal A, De Silva N, Flint B, Frankish A, Hunt SE, GR II, Langridge N, Loveland JE, Martin FJ, Mudge JM, Morales J, Perry E, Ruffier M, Tate J, Thybert D, Trevanion SJ, Cunningham F, Yates AD, Zerbino DR & Flicek P. Ensembl 2021. *Nucleic Acids Res* **49**, D884-D891 (2021).
17. Karczewski KJ, Francioli LC, Tiao G, Cummings BB, Alfoldi J, Wang Q, Collins RL, Laricchia KM, Ganna A, Birnbaum DP, Gauthier LD, Brand H, Solomonson M, Watts NA, Rhodes D, Singer-Berk M, England EM, Seaby EG, Kosmicki JA, Walters RK, Tashman K, Farjoun Y, Banks E, Poterba T, Wang A, Seed C, Whiffin N, Chong JX, Samocha KE, Pierce-Hoffman E, Zappala Z, O'Donnell-Luria AH, Minikel EV, Weisburd B, Lek M, Ware JS, Vittal C, Armean IM, Bergelson L, Cibulskis K, Connolly KM, Covarrubias M, Donnelly S, Ferriera S, Gabriel S, Gentry J, Gupta N, Jeandet T, Kaplan D, Llanwarne C, Munshi R, Novod S, Petrillo N, Roazen D, Ruano-Rubio V, Saltzman A, Schleicher M, Soto J, Tibbetts K, Tolonen C, Wade G, Talkowski ME, Genome Aggregation Database C, Neale BM, Daly MJ & MacArthur DG. The mutational constraint spectrum quantified from variation in 141,456 humans. *Nature* **581**, 434-443 (2020).
18. Landrum MJ, Chitipiralla S, Brown GR, Chen C, Gu B, Hart J, Hoffman D, Jang W, Kaur K, Liu C, Lyoshin V, Maddipatla Z, Maiti R, Mitchell J, O'Leary N, Riley GR, Shi W, Zhou G, Schneider V, Maglott D, Holmes JB & Kattman BL. ClinVar: improvements to accessing data. *Nucleic Acids Res* **48**, D835-D844 (2020).
19. Tate JG, Bamford S, Jubb HC, Sondka Z, Beare DM, Bindal N, Boutselakis H, Cole CG, Creatore C, Dawson E, Fish P, Harsha B, Hathaway C, Jupe SC, Kok CY, Noble K, Ponting L, Ramshaw CC, Rye CE, Speedy HE, Stefancsik R, Thompson SL, Wang S, Ward S, Campbell PJ & Forbes SA. COSMIC: the Catalogue Of Somatic Mutations In Cancer. *Nucleic Acids Res* **47**, D941-D947 (2019).
20. Sherry ST, Ward M & Sirotkin K. dbSNP-database for single nucleotide polymorphisms and other classes of minor genetic variation. *Genome Res* **9**, 677-679 (1999).

Chapter 4

Discussion and outlook

In this work, I investigated alternative splicing regulatory networks and their mechanisms in cancer-relevant events. In out group, we developed high-throughput mutagenesis assays that examined the impact of mutations on splicing outcomes. Our work has been based on pioneer approaches that developed methods to look at individual splicing events and assessed how perturbations in the *cis*- and *trans*-elements could influence the composition of mRNAs. We focused on two alternative splicing events where we explored all possible single mutation effects, intronic and exonic, in the complete region where they take place. This allowed us to look at the effects beyond the canonical signals of splicing.

In Chapter 1 we developed our screen and applied it to the exon 11 of the proto-oncogene *RON*, important in solid tumours. We dissected the regulatory network and identified HNRNPH as the main regulator. This approach allowed us to expand our assay to study longer regions to look at a cell-specific gene and therapeutic target, *CD19*. In Chapter 3, we uncovered splicing regulation beyond inclusion/skipping of exon 2 and at the same time, we identified multiple isoforms of unknown significance. One of these isoforms was the object of study of Chapter 2, where we debunked the existence of the described isoform and proposed an approach to verify isoform annotations. Together, these three publications give an overview of several aspects of splicing regulation that I discuss hereinafter.

A need for cell-specific event descriptions

Splicing changes are highly dependent on the cellular context. The levels of RBP regulators and other signalling interactions in individual cell types can influence the transcripts that a tissue and individual cells express. Most of the splicing mutagenesis assays to date have been performed in a handful of cell lines like

HEK293, HeLa or K562 exclusively (See Table (1)). An initial approach to dissect how the cellular background can affect splicing is to use the same library across several cell lines and compare the effects. This was the method that we followed in our work on *RON* exon 11: we obtained data from two distinct cell lines, HEK293 and MCF7. Even though the mutation effects showed a high agreement, the initial exon inclusion effects were different between both cell lines, highlighting the variable cellular states between these cancer cell lines.

For *RON* exon 11, testing different cell lines was not a considerable complication, as the expression of the *RON* gene is rather ubiquitous, showing increased expression in a handful of tissues (Uhlen et al. 2017). Nonetheless, cell-type-specific genes can also be alternatively spliced, making it difficult to predict the effects of variant alterations learned from more common events. An example that we studied in our work is *CD19* exon 2. *CD19* expression is rather restricted to B cells, which is why using the classic cell lines is not ideal. We used a B-ALL derived cell line, NALM-6, which was more challenging to transfect but helped us detect the gene and alternative splicing isoforms that could only arise in such a specific cellular context.

Big collaborative sequencing projects like 1000 Genomes or UK BioBank have uncovered genetic mutations for which we do not understand their effects. Furthermore, with genome wide association studies (GWAS), we have learned how specific SNPs can define observed phenotypes. Most of the studies have focused on mutations that modulate expression (expression quantitative loci or eQTLs). However, other regulatory layers, like splicing, also have a strong impact on the phenotypes. Recent analyses have shown that splicing quantitative loci (sQTLs) are mostly shared across tissues, but interestingly, hundreds of them can be very tissue-specific, particularly in the brain but also testis, skeletal muscle, or liver (Garrido-Martín et al. 2021). Both observations have implications that can be approached from the perspective of our observations in *RON* and *CD19*. On one hand, the shared mutation effects could be modelled in commonly used cell lines and their effects can be generalized. Nonetheless, controlled systems where we can analyse the individual effects of tissue-specific mutations, like in the case of our CD19 minigene, are also valuable to disentangle the complex effects.

Currently, several splicing prediction tools have a very accurate performance on predicting new splicing signals or the levels of splicing changes, and some of them have been trained using massive parallel assay, like Vex-seq or SPANR (See Table (2)). While some tools could benefit from included tissue-specific data, it has not been explored yet the kind of experimental data that could be more useful to improve the predictions. MTSplice, for instance, introduced GTEx information, but, although their results were superior in brain samples, in testis the predictions performed better using the non-tissue specific version (Cheng et

al. 2021). Perhaps benchmarking these algorithms with the design of cell-specific massive parallel splicing assays has the potential to increase the predictability of such algorithms.

Measuring the mutation impact beyond exons

As discussed extensively in Baeza-Centurion et al. (2019) and Baeza-Centurion et al. (2020), one of the determinants on the impacts of mutations in splicing is the initial level of inclusion in an exon. In our screens, *RON* and *CD19* showed different base levels of inclusion: *RON* exon 11 is mostly around 60%, which could be considered as a medium level, whereas *CD19* exon 2 is closer to 80%, which makes it rather constant. Their predictions hold in our studies: in the case of *RON*, we observe multiple positions that, upon mutation, perturb exon 11 inclusion. For *CD19* however, the strongest effects only come from mutations affecting the canonical splicing signals.

One point of debate in the splicing community is the true impact of intronic mutations. These mutations are usually difficult to capture, as in humans, the average intron is around 6.4 kb (Dey and Mattick 2021), which makes it difficult to insert into a minigene system. In the case of cassette exons, evidence points to near intronic mutations, closer to the splice sites, to be more relevant on affecting splicing inclusion of the exon in question. Coincidently, those near intronic mutations overlap splicing signals like the polypyrimidine track or the branch point. On the other hand, deep intronic mutations, located far from the splice sites, are more challenging to study but their effect would probably be reflected in other splicing alterations beyond cassette exon inclusion changes. Some effects in the transcriptome of these mutations are mostly transcriptional (inactivating non-coding RNAs or transcriptional regulatory motifs), but also most of the reports concerning splicing point to the activation of cryptic splicing sites and subsequent integration of pseudo exons (as reviewed by Vaz-Drago et al. (2017)). Thus, one of the advantages of our mutagenesis assays, described in Chapters 1 and 3, is the quantification of effects beyond exon skipping/inclusion. In *CD19*, for instance, we were able to identify positions that influence the formation of new isoforms, activating multiple cryptic splicing sites. This observation suggests that the effect of mutations in splicing should be expanded beyond measurements of exon inclusion levels, and rather also consider aberrant splicing isoform formation that arises after the activation of cryptic splice sites.

The impact of aberrant isoforms

Part of the regulation of the aberrant isoforms involves their degradation of unproductive transcripts via nonsense-mediated decay (NMD). The efficient degradation of some untranslatable isoforms frequently prevents the detection of intermediate products that are generated during mRNA processing. In the minigene systems, however, given that not all the elements of a transcript are present, it is possible to detect intermediate fragments of the aberrant isoforms produced. This helps to improve the interpretation of mutation effects, as in the case of *CD19* exon 2. There, we observe that upon specific mutations, numerous isoforms were generated. Interestingly, most of these isoforms (>80) would potentially disrupt protein production by favouring the production of NMD-prone isoforms. This reflects the necessity to consider the missing effects of mutations in transcript production.

Degradation is not the only destination of aberrant transcripts. In fact, in many cancers, NMD pathways are altered (Hu et al. 2017) or contain mutations that help the mRNAs to avoid NMD (Litchfield et al. 2020). Consequently, some isoforms escape from degradation. One of the recurrent topics in recent years has been the possibility of alternatively spliced transcripts being translated and producing neo-antigens: peptides that generate an immune reaction. Detection and prediction of neo-antigens are currently challenging (van Endert 2021), however, their therapeutic potential could have a great impact. In our mutagenesis assays, the transcript products detected with RNA-seq do not proceed to translation, allowing the detection and quantification of isoform transcripts containing NMD signals. It would be interesting to test whether mutation-induced isoforms can reveal immunogenicity in patients.

Although the idea of activating immune reactions through perturbations at the level of splicing has a strong therapeutic implication, it is important to be cautious with the new isoform detection and interpretation. In our work, we described the case of the isoform ex2Δpart which was suggested to be a potential marker for B-ALL blinatumomab treatment (Zhao et al. 2021). We have shown that the isoform is an artefact of reverse transcription. One could argue that if the isoform is not detected in the dRNA-seq it might be due to the prediction of the new isoform being a target of NMD. In that sense, the deep sequencing performed in the fluorescent reporter should be able to identify it, as it lacks the elements to be recognised by the NMD machinery. On top of this, we were also able to observe aberrant isoforms containing the ex2Δpart junction in our *CD19* mutagenesis, where we can quantify isoforms that otherwise would be degraded.

Aberrant isoform detection

The improvement of third-generation sequencing technologies has shed light on the darkness of the transcriptome. As we showed in Chapter 2, for ONT, the comparison of RT vs non-RT protocols can be useful to investigate protocol-specific artefacts. Some might argue that the comparison is not always fair, particularly in the direction of sequencing depth. As previously outlined, dRNA ONT still requires a high input level and the output tends to be minor than cDNA ONT, however, benchmarking studies have shown that the estimation of transcript abundance is consistent between protocols (Chen et al. 2021). Thus, isoform estimations can become more reliable in the long term.

In addition to the low coverage of some isoforms in long-read technologies, one issue that we also observed in ex2Δpart was the 5´end bias: the coverage of the transcripts tends to decrease closer to the start of the transcript due to ONT starting the sequencing from the polyadenylated 3´end. Algorithmic solutions encourage quantifying first the transcript abundance to then reduce the bias during the isoform reconstruction (Amarasinghe et al. 2020). Additionally, experimental approaches such as TERA-seq, which uses a 5´adapter in its version 5TERA (Ibrahim et al. 2021), seem to partially overcome the limitation of capturing the isoforms from end to end in dRNA-seq. Improvements in the protocol and signal detection could perhaps lead to a reduction of input material requirements in the future.

Isoforms as therapeutic markers

One of the open questions, after the initial observations that motivated Chapter 2, was to understand what caused the increased ex2Δpart signal in blinatumomab non-responder patients from Zhao et al. (2021). Bringing together the data from Chapter 3, it is possible that other isoforms are responsible for the apparent increase ratio of the fake isoform. Given that (Zhao et al. 2021), quantify ex2Δpart over the total levels of the spliced junction from *CD19* exon 2 to exon 3, changes in this junction will alter the quantification. Therefore, and in agreement with our observations from patient data, intron 2 retention, for which levels are complementary to the measured exon 2-3 junction, could be the actual isoform that is increased in relapsed patients.

Even though, the intron 2 retention isoform seems to be abundant in relapsed patients, interestingly, it can also be detected at high levels (>60%) before therapy. The impact of this isoform on resistance to therapy is not completely clear. For instance, Asnani et al. (2019) detected the increased retention in the Orlando et al. (2018) data and coupling the isoform quantification with ribosome association analysis they concluded that the production of intron 2 retention limits

CD19 protein expression (Asnani et al. 2019). In general, it is difficult to estimate the total number of B-ALL clones that produce a certain isoform. A recent study characterised single cells derived from a patient and detected the intron 2 retention isoform in CD19$^-$ B-ALL cells, before CAR-T treatment, however, the clones represented only 0.03% of all cells (Rabilloud et al. 2021).

There is also a knowledge gap in the selection of aberrant isoforms in cancer. Many cancer studies have looked at the evolutionary trajectory of mutations affecting genes that act as drivers of the disease (Gerstung et al. 2020; Kent and Green 2017). However, little is known about non-genetic mechanisms like the selection of certain isoforms in cancer, especially when a therapy constrain is added. As has been described in the case of *CD19*, it is not clear whether relevant isoforms are present before therapy and then selected or if it is rather that, upon the pressure of therapy, resistant clones emerge, which then change their isoform expression. As discussed in Frankiw et al. (2019), using isoforms therapeutically will be most effective in the cases where the alternative spliced isoform behaves as a diver of tumorogenesis, otherwise, more resistant clones will emerge. In the case of *CD19*, some studies claim that isoforms might not be the major mechanism of resistance, as reported in Plaks et al. (2021) in B cell lymphoma patients. Nevertheless, it is necessary to decipher the scale of their contribution in the different stages of the disease.

RBP control of splicing

In Chapters 1 and 3 we investigated which are the RBP regulators that bind the regions around the events of interest and more specifically, how their binding is affected by mutations in a particular cellular context. On a first level, our mutagenesis assays provide us with a census of positions that, upon mutation, can cause a strong disruption of splicing and are not necessarily core splicing signals. It has been suggested that such *cis*- regulatory elements are abundant in alternative exons (Baeza-Centurion et al. 2020) but also, that their conservation is highly dependent on their interactors and potentially, the impact that such mutations could have on the protein level (Glidden et al. 2021).

Disentangling the networks through computational predictions

In *RON* exon 11, coincidently with the observations in alternatively spliced events, we could see a high proportion of mutations that perturbed the inclusion levels of the exon. We used predictive tools, based on a diverse set of experiments, to infer the potential RBPs with binding sites that overlapped positions that had an effect in splicing. Based on previous work by Papasaikas et al. (2015)

we were able to decrease the list of potential regulators by considering the global changes in PSI of exon 11. On the other hand, given that for CD19 exon 2 there was no previous assessment of splicing effects. We employed distinct tools to discriminate across potential binders, leaving open the possibility that other RBPs not contained in the predictions, might have a stronger regulatory role than the ones which we described in Chapter 3.

In general, RBP binding predictions have a long way to go. Although it is estimated that there are more than 2000 RBPs, only a few hundreds have been assayed on a large scale to determine their binding preferences (Van Nostrand et al. 2020). The specificity of binding has been usually attributed to the combination of domains that an RBP has, but only a handful of domains have a strict linear binding motif, whereas the rest are more dependent on weak, dynamic or multimeric interactions (Corley et al. 2020). In Chapter 3 we also explore the new approaches for dissecting binding preferences based on deep neural networks (DNN). Such algorithms, like DeepRiPe (Ghanbari and Ohler 2020) or GrapProt2(Uhl et al. 2019), have become very popular in recent years, and in the case of RBP data, they are usually trained in experimental binding data on the form of cross-linking and immunoprecipitation (CLIP). One of the improvements over motif prediction tools is that these models have also tried to predict binding changes induced by single nucleotides. In our experience with DeepRiPe, given that the algorithm does not receive information regarding RBP abundance, it predicted binding scores along the *CD19* minigene for the majority of the RBPs trained. We also observed that many of the binding-altering mutations predicted by the algorithm do not always match with the sites that we detected as effective. This observation could indicate that the interactions of the network that go beyond linear relationships but also could reflect the quality of the data used to train the models. Improvements in the generated data sets used to train these algorithms could be helpful, but also implies a high experimental demand. Alternatively, novel de-noising algorithms, such as the ones implemented for single cell approaches (Lal et al. 2021) and other areas (Fischer-Hwang et al. 2019; Nounou et al. 2012) could help to clean up the input data and improve their performance.

Structure in RBP binding

An aspect that we explore in Chapter 1 is the RBP binding dynamics: we measured the effect of mutations in a context where the RBP levels were decreased. We learned that HNRNPH, the main regulator of *RON* exon 11, has multiple binding clusters that appear to work cooperatively, promoting the binding of more HNRNPH proteins and introducing a switch-like effect on the inclusion of *RON*

exon 11. One of the possible explanations for the effective switch-like regulation of HNRNPH is that perhaps some of the motifs where it binds are affected by a secondary structure. As mentioned in the paper, HNRNPH tends to bind to G-runs, which are often associated with the formation of G quadruplex structures (G4). In fact, following the publication of our results, another article showed that HNRNPH1 can modulate the splicing of a fusion oncogene by interaction with exonic G4 sequences, but the exact mechanism that the structure plays in regulation remained clear (Neckles et al. 2019). Added to this, with the reports of HNRNPH regulation through G4 interactions at the transcriptional (Xu et al. 2019) and translational level (Herviou et al. 2020), in the future, it will be required to assess whether the G4 regulatory action of HNRNPH is more specific to splicing or rather a generally used mechanism that impacts in other layers of regulation.

While the observations of our mutagenesis have shown that, at least in our assayed minigenes, the effects of mutations in splicing are mostly linear, we can also see how the structure could explain the deviations to the rule. As previously mentioned, in the case of HNRNPH, changes in the RNA structure might be related to the synergistic effects of certain mutations. The implication of RNA structures in splicing has been observed in several events and more recently, structure-specific exonic motifs with implications on splicing regulation in cancer have been described (Fish et al. 2021). It is unclear how frequent structures act as *cis*-regulators of splicing or whether more structures have features of ESEs or ISEs on regulating splicing. One alternative could be to use high-throughput minigene assays in combination with other techniques, like SHAPE (Selective 2'-Hydroxyl Acylation analysed by Primer Extension) (Wilkinson et al. 2006) or new single-molecule derivatives like PORE-cupine (Aw et al. 2020), which allows measuring individual structures on top of transcript outcomes. Mapping precisely the isoforms that are specific to structures could not only enhance the understanding of *cis*-regulatory mechanisms but also provide a better insight into the isoform preference of binding of many RBPs.

Regardless of the importance of RNA structure for regulation, as we have observed in Chapter 2, structures can also lead to technical artefacts which can limit our interpretation of the results. In our work, we bioinformatically predicted a strong secondary structure that generates the falsitron in ex2Δpart. Such structure was characterised by repetitive sequences located in the splice sites. Interestingly, similar repetitive structures were abundant in the detected falsitrons and cancer-exitrons described in (Wang et al. 2021; Wang and Yang 2021) and thus, it would be important to investigate if there is a common denominator in terms of the secondary structures produced by the interaction of these repetitive sequences. Potentially, training algorithms using high-quality structural data could

help to predict areas that contain very stable structures that could lead to RT artefacts such as falsitrons. On that line, our description of falsitrons could guide the identification of more artefacts in new paired dRNA/cDNA-seq sets.

Global understanding of splicing regulatory networks

At its core, splicing specificity relies on the activity of RBP regulators, but more precisely, how these regulators play a role in the individual splicing networks. Ideally, knowing the components of the network, their interactions, and its context could lead to the creation of a model that will allow us to make predictions that could potentially extend to other networks. In the case of splicing, we have a basic understanding of the interactions and rules for some components, but there are many others that we have not uncovered. In our work, for instance, we not only characterised the effects that alterations in the sequence could have in our system, but we also tried to uncover the components that could explain the observed transcript isoforms and their levels. For example, in the case of *RON* exon 11, even when we focused mainly on HNRNPH, we also looked at how its regulatory role would fit in an interconnected disease context by employing RNA-seq data from The Cancer Genome Atlas (TCGA). We analysed how expression and splicing levels correlate in patients with different cancer types. From this analysis, HNRNP H2 turned out to be the one of the RBPs with the highest correlation levels between splicing and expression. While this approach can be helpful and is often used when dealing with clinical data, it is prone to be affected by confounding factors in the data (Slaff et al. 2021; Zhang et al. 2020). Even using different metrics to measure splicing or expression can drive distinct conclusions (Dankó et al. 2021). Thus, using correlations between splicing and expression to infer regulations need to be carefully benchmarked and perhaps strict statistical validations would need to be adapted to produce reliable results.

Another challenge in the interpretation of splicing regulatory networks can be the intrinsic regulation that the distinct RBPs excerpt over each other. For instance, in Chapter 3 we describe the regulation of *CD19* intron 2 retention and skipping, demonstrating that together with SRSF3, other proteins such as PTBP1, HNRNPM, PCBP2, and SF3B4 can also influence the levels of the distinct isoforms. Interestingly, PTBP1, together with PTBP2 has been described as a regulator of SRSF3 levels by controlling the inclusion of its unproductive (poison) exon 4, which at the same time is autoregulated in cancer cells (Guo et al. 2015). These types of mechanisms, involving the generation of unproductive transcripts, are common across *trans*-acting factors. However, even when most of the splicing

factors tend to have some increased tendency to regulate other splicing factors, analysis of their regulatory networks has not managed to distinguish clear groups of master regulators like in the case of transcriptional factors (Desai et al. 2020). Therefore, and in agreement with other observations in B cell development networks (Zandhuis et al. 2021) it is possible that other splicing factors contribute directly to the regulatory network of *CD19*. Further research including perturbation screens using technologies like CRISPRi (Larson et al. 2013) coupled with splicing reporters could improve the characterisation of the B-ALL specific network.

Future challenges and opportunities for splicing mutagenesis assays

Our work has demonstrated that there are many elements and mechanisms in splicing that are still to be uncovered and understood. Additionally, we have also shown that massive parallel splicing assays can provide of detailed resources for the community. Already a couple of studies have shown the applicability of our mutagenesis data to understand the generalities of alternatively spliced cassette exons (Baeza-Centurion et al. 2020) as well as the competition between splicing sites in the exon definition model (Enculescu et al. 2020). The data required to train such types of models benefits high-quality data in a controlled system where other regulatory layers, like the transcriptional, have a decreased intervention. Thus, for some problems, a good design of massive parallel reporter assays (MPRAs) combined with integrative computational models could help to answer relevant biological questions.

We have shown that it is possible to extend the mutagenesis systems beyond 1 kb. In the future, with the increased accessibility of long-read technologies at the RNA level, these minigene assays could potentially be implemented in longer regions. Recent developments have shown that is possible to barcode RNA reads for native RNA sequence (Smith et al. 2020). This implementation, in the context of high-throughput minigene assays, could allow the recovery of information regarding RNA modifications, which have been associated multiple times with splicing during the last decade(Martinez et al. 2020; Mendel et al. 2021; Ishigami et al. 2021).

Finally, as we have described, this type of analysis could become relevant in the clinic. As we described for *CD19*, splicing-impacting variants could be helpful to stratify patients during the treatment. On the other hand, as show with *RON*, monitoring the *trans*-acting factors expression levels can be a predictive measurement of survival. Beyond screenings, therapy development can also benefit

from a deeper understanding of splicing. Perhaps the most famous example of how the information of splicing regulation can be used is the development of the antisense-oligonucleotide (ASO) therapy Nusinersen (Mercuri et al. 2018). This therapy targets the *SMN2* gene to promote the inclusion of a single exon. Our splicing catalogues describe areas sensitive to mutations or relevant for binding sites that could potentially be effectively targeted by ASO therapies. We provide or data-rich resources that hopefully in the future can be applied and refined to gain a better understanding of the splicing code in the context of disease.

Abbreviations

ALL Acute lymphoblastic leukaemia

ASO Antisense oligonucleotide

B-ALL B-cell Acute lymphoblastic leukaemia

BCR B cell reptor

CAR Chimeric Antigen Receptor

CCS Circular Consensus Sequence

cDNA-seq cDNA sequencing

CRISPR Clustered regularly interspaced palindromic repeats

CTD Carboxyl-terminal domain

DNA Desoxyribonucleic acid

DNN Deep Neural Networks

dNTP Deoxyribonucleoside triphosphates

dRNA-seq Direct RNA sequencing

dsRNA Double stranded RNA

eQTL Expression quantitative loci

ESE Exonic splicing enhancer

ESS Exonic splicing silencer

G4 G quadruplex

GWAS Genome wide association studies

HiFi read High-fidelity read

hnRNP heterogeneous nuclear ribonucleoprotein

IDR Intrinsically disordered regions

ISE Intronic splicing enhancer

ISE Intronic splicing silencer

kb Kilobase

KRAB Krüppel-associated box

MED Maximum Entropy Distribution

mRNA messenger RNA

NGS Next Generation Sequencing

NMD Nonsense-mediated decay

nt nucleotide

ONT Oxford Nanopore Technologies

PacBio Pacific Biosciences

PSI Percent splice-in

PWM Positional weight matrix

qRRMs quasi RNA recognition motifs

RBP RNA binding protein

RNA Ribonucleid acid

rRNA Ribosomal RNA

RT-PCR Reverse-Transcription Polymerase chain reaction

RT-qPCR Reverse-Transcription quantitative polymerase chain reaction

SHAPE Selective 2'-Hydroxyl Acylation analysed by Primer Extension

SMRT-seq Single-molecule, real-time sequencing

SNP Single nucleotide polymorphism

snRNA small nuclear RNA

ss splice site

TCGA The Cancer Genome Atlas

tRNA Transfer RNA

References

Adamson SI, Zhan L, Graveley BR. 2018. Vex-seq: high-throughput identification of the impact of genetic variation on pre-mRNA splicing efficiency. *Genome Biology* **19**. http://dx.doi.org/10.1186/s13059-018-1437-x.

Adamson S, Zhan L, Graveley B. 2021. Functional characterization of splicing regulatory elements. http://dx.doi.org/10.1101/2021.05.14.444228.

Amarasinghe SL, Su S, Dong X, Zappia L, Ritchie ME, Gouil Q. 2020. Opportunities and challenges in long-read sequencing data analysis. *Genome Biology* **21**. http://dx.doi.org/10.1186/s13059-020-1935-5.

Asnani M, Hayer KE, Naqvi AS, Zheng S, Yang SY, Oldridge D, Ibrahim F, Maragkakis M, Gazzara MR, Black KL, et al. 2019. Retention of CD19 intron 2 contributes to CART-19 resistance in leukemias with subclonal frameshift mutations in CD19. *Leukemia* **34**: 1202–1207. http://dx.doi.org/10.1038/s41375-019-0580-z.

Attig J, Agostini F, Gooding C, Chakrabarti AM, Singh A, Haberman N, Zagalak JA, Emmett W, Smith CWJ, Luscombe NM, et al. 2018. Heteromeric RNP Assembly at LINEs Controls Lineage-Specific RNA Processing. *Cell* **174**: 1067–1081.e17. http://dx.doi.org/10.1016/j.cell.2018.07.001.

Aw JGA, Lim SW, Wang JX, Lambert FRP, Tan WT, Shen Y, Zhang Y, Kaewsapsak P, Li C, Ng SB, et al. 2020. Determination of isoform-specific RNA structure with nanopore long reads. *Nature Biotechnology* **39**: 336–346. http://dx.doi.org/10.1038/s41587-020-0712-z.

Baeza-Centurion P, Miñana B, Schmiedel JM, Valcárcel J, Lehner B. 2019. Combinatorial Genetics Reveals a Scaling Law for the Effects of Mutations on Splicing. *Cell* **176**: 549–563.e23. http://dx.doi.org/10.1016/j.cell.2018.12.010.

Baeza-Centurion P, Miñana B, Valcárcel J, Lehner B. 2020. Mutations primarily alter the inclusion of alternatively spliced exons. *eLife* **9**. http://dx.doi.org/10.7554/eLife.59959.

Barash Y, Calarco JA, Gao W, Pan Q, Wang X, Shai O, Blencowe BJ, Frey BJ. 2010. Deciphering the splicing code. *Nature* **465**: 53–59. http://dx.doi.org/10.1038/nature09000.

Berget SM, Moore C, Sharp PA. 1977. Spliced segments at the 5' terminus of adenovirus 2 late mRNA. *Proceedings of the National Academy of Sciences* **74**: 3171–3175. http://dx.doi.org/10.1073/pnas.74.8.3171.

Bowling EA, Wang JH, Gong F, Wu W, Neill NJ, Kim IS, Tyagi S, Orellana M, Kurley SJ, Dominguez-Vidaña R, et al. 2021. Spliceosome-targeted therapies trigger an antiviral immune response in triple-negative breast cancer. *Cell* **184**: 384–403.e21. http://dx.doi.org/10.1016/j.cell.2020.12.031.

Braun S, Enculescu M, Setty ST, Cortés-López M, de Almeida BP, Sutandy FX0167emR, Schulz L, Busch A, Seiler M, Ebersberger S, et al. 2018. Decoding a cancer-relevant splicing decision in the RON proto-oncogene using high-throughput mutagenesis. *Nature Communications* **9**. http://dx.doi.org/10.1038/s41467-018-05748-7.

Brinkerhoff H, Kang ASW, Liu J, Aksimentiev A, Dekker C. 2021. Infinite re-reading of single proteins at single-amino-acid resolution using nanopore sequencing. http://dx.doi.org/10.1101/2021.07.13.452225.

Busch A, Hertel KJ. 2011. Evolution of SR protein and hnRNP splicing regulatory factors. *Wiley Interdisciplinary Reviews: RNA* **3**: 1–12. http://dx.doi.org/10.1002/wrna.100.

Chen Y, Davidson NM, Wan YK, Patel H, Yao F, Low HM, Hendra C, Watten L, Sim A, Sawyer C, et al. 2021. A systematic benchmark of nanopore long read RNA sequencing for transcript level analysis in human cell lines. http://dx.doi.org/10.1101/2021.04.21.440736.

Cheng J, Çelik MH, Kundaje A, Gagneur J. 2021. MTSplice predicts effects of genetic variants on tissue-specific splicing. *Genome Biology* **22**. http://dx.doi.org/10.1186/s13059-021-02273-7.

Cheng J, Nguyen TYD, Cygan KJ, Çelik MH, Fairbrother WG, Avsec žiga, Gagneur J. 2019. MMSplice: modular modeling improves the predictions of genetic variant effects on splicing. *Genome Biology* **20**. http://dx.doi.org/10.1186/s13059-019-1653-z.

Cheung R, Insigne KD, Yao D, Burghard CP, Wang J, Hsiao Y-HE, Jones EM, Goodman DB, Xiao X, Kosuri S. 2019. A Multiplexed Assay for Exon Recognition Reveals that an Unappreciated Fraction of Rare Genetic Variants Cause Large-Effect Splicing Disruptions. *Molecular Cell* **73**: 183–194.e8. http://dx.doi.org/10.1016/j.molcel.2018.10.037.

Chou M-Y, Rooke N, Turck CW, Black DL. 1999. hnRNP H Is a Component of a Splicing Enhancer Complex That Activates a c- src Alternative Exon in Neuronal Cells. *Molecular and Cellular Biology* **19**: 69–77. http://dx.doi.org/10.1128/MCB.19.1.69.

Chow LT, Gelinas RE, Broker TR, Roberts RJ. 1977. An amazing sequence arrangement at the 5' ends of adenovirus 2 messenger RNA. *Cell* **12**: 1–8. http://dx.doi.org/10.1016/0092-8674(77)90180-5.

Cobb M. 2017. 60 years ago, Francis Crick changed the logic of biology. *PLOS Biology* **15**: e2003243. http://dx.doi.org/10.1371/journal.pbio.2003243.

Collesi C, Santoro MM, Gaudino G, Comoglio PM. 1996. A splicing variant of the RON transcript induces constitutive tyrosine kinase activity and an invasive phenotype. *Molecular and Cellular Biology* **16**: 5518–5526. http://dx.doi.org/10.1128/MCB.16.10.5518.

Cooper TA. 2005. Use of minigene systems to dissect alternative splicing elements. *Methods* **37**: 331–340. http://dx.doi.org/10.1016/j.ymeth.2005.07.015.

Corley M, Burns MC, Yeo GW. 2020. How RNA-Binding Proteins Interact with RNA: Molecules and Mechanisms. *Molecular Cell* **78**: 9–29. http://dx.doi.org/10.1016/j.molcel.2020.03.011.

Cortés-López M, Schulz L, Enculescu M, Paret C, Spiekermann B, Busch A, Orekhova A, Kielisch F, Quesnel-Vallières M, Torres-Diz M, et al. 2021. High-throughput mutagenesis identifies mutations and RNA binding proteins controlling CD19 splicing and CART-19 therapy resistance. http://dx.doi.org/10.1101/2021.10.08.463671.

Cosby RL, Judd J, Zhang R, Zhong A, Garry N, Pritham EJ, Feschotte C. 2021. Recurrent evolution of vertebrate transcription factors by transposase capture. *Science* **371**. http://dx.doi.org/10.1126/science.abc6405.

Dainis A, Tseng E, Clark TA, Hon T, Wheeler M, Ashley E. 2019. Targeted Long-Read RNA Sequencing Demonstrates Transcriptional Diversity Driven by Splice-Site Variation in MYBPC3. *Circulation: Genomic and Precision Medicine* **12**. http://dx.doi.org/10.1161/CIRCGEN.119.002464.

Dankó B, Szikora P, Pór T, Szeifert A, Sebestyén E. 2021. SplicingFactorysplicing diversity analysis for transcriptome data ed. P. Robinson. *Bioinformatics*. http://dx.doi.org/10.1093/bioinformatics/btab648.

David CJ, Manley JL. 2010. Alternative pre-mRNA splicing regulation in cancer: pathways and programs unhinged. *Genes & Development* **24**: 2343–2364. http://dx.doi.org/10.1101/gad.1973010.

De Conti L, Baralle M, Buratti E. 2012. Exon and intron definition in pre-mRNA splicing. *Wiley Interdisciplinary Reviews: RNA* **4**: 49–60. http://dx.doi.org/10.1002/wrna.1140.

Deamer D, Akeson M, Branton D. 2016. Three decades of nanopore sequencing. *Nature Biotechnology* **34**: 518–524. http://dx.doi.org/10.1038/nbt.3423.

Del Gatto-Konczak F, Olive M, Gesnel M-C, Breathnach R. 1999. hnRNP A1 Recruited to an Exon In Vivo Can Function as an Exon Splicing Silencer. *Molecular and Cellular Biology* **19**: 251–260. http://dx.doi.org/10.1128/MCB.19.1.251.

Desai A, Hu Z, French CE, Lloyd JPB, Brenner SE. 2020. Networks of splice factor regulation by unproductive splicing coupled with nonsense mediated mRNA decay. http://dx.doi.org/10.1101/2020.05.20.107375.

Deveson IW, Brunck ME, Blackburn J, Tseng E, Hon T, Clark TA, Clark MB, Crawford J, Dinger ME, Nielsen LK, et al. 2018. Universal Alternative Splicing of Noncoding Exons. *Cell Systems* **6**: 245–255.e5. http://dx.doi.org/10.1016/j.cels.2017.12.005.

Dey P, Mattick JS. 2021. High frequency of intron retention and clustered H3K4me3-marked nucleosomes in short first introns of human long noncoding RNAs. *Epigenetics & Chromatin* **14**. http://dx.doi.org/10.1186/s13072-021-00419-2.

Dominguez C. 2006. NMR structure of the three quasi RNA recognition motifs (qRRMs) of human hnRNP F and interaction studies with Bcl-x G-tract RNA: a novel mode of RNA recognition. *Nucleic Acids Research* **34**: 3634–3645. http://dx.doi.org/10.1093/nar/gkl488.

Dvinge H, Kim E, Abdel-Wahab O, Bradley RK. 2016. RNA splicing factors as oncoproteins and tumour suppressors. *Nature Reviews Cancer* **16**: 413–430. http://dx.doi.org/10.1038/nrc.2016.51.

Eid J, Fehr A, Gray J, Luong K, Lyle J, Otto G, Peluso P, Rank D, Baybayan P, Bettman B, et al. 2009. Real-Time DNA Sequencing from Single Polymerase Molecules. *Science* **323**: 133–138. http://dx.doi.org/10.1126/science.1162986.

El Marabti E, Abdel-Wahab O. 2021. Therapeutic Modulation of RNA Splicing in Malignant and Non-Malignant Disease. *Trends in Molecular Medicine* **27**: 643–659. http://dx.doi.org/10.1016/j.molmed.2021.04.005.

Enculescu M, Braun S, Thonta Setty S, Busch A, Zarnack K, König J, Legewie S. 2020. Exon Definition Facilitates Reliable Control of Alternative Splicing in the RON Proto-Oncogene. *Biophysical Journal* **118**: 2027–2041. http://dx.doi.org/10.1016/j.bpj.2020.02.022.

Eng L, Coutinho G, Nahas S, Yeo G, Tanouye R, Babaei M, Dörk T, Burge C, Gatti RA. 2003. Nonclassical splicing mutations in the coding and noncoding regions of the ATM Gene: Maximum entropy estimates of splice junction strengths. *Human Mutation* **23**: 67–76. http://dx.doi.org/10.1002/humu.10295.

Erkelenz S, Mueller WF, Evans MS, Busch A, Schoneweis K, Hertel KJ, Schaal H. 2012. Position-dependent splicing activation and repression by SR and hnRNP proteins rely on common mechanisms. *RNA* **19**: 96–102. http://dx.doi.org/10.1261/rna.037044.112.

Eskens FALM, Ramos FJ, Burger H, O'Brien JP, Piera A, de Jonge MJA, Mizui Y, Wiemer EAC, Carreras MJ, Baselga J, et al. 2013. Phase I Pharmacokinetic and Pharmacodynamic Study of the First-in-Class Spliceosome Inhibitor E7107 in Patients with Advanced Solid Tumors. *Clinical Cancer Research* **19**: 6296–6304. http://dx.doi.org/10.1158/1078-0432.CCR-13-0485.

Fischer J, Paret C, El Malki K, Alt F, Wingerter A, Neu MA, Kron B, Russo A, Lehmann N, Roth L, et al. 2017. CD19 Isoforms Enabling Resistance to CART-19 Immunotherapy Are Expressed in B-ALL Patients at Initial Diagnosis. *Journal of Immunotherapy* **40**: 187–195. http://dx.doi.org/10.1097/CJI.0000000000000169.

Fischer-Hwang I, Ochoa I, Weissman T, Hernaez M. 2019. Denoising of Aligned Genomic Data. *Scientific Reports* **9**. http://dx.doi.org/10.1038/s41598-019-51418-z.

Fisette J-F, Montagna DR, Mihailescu M-R, Wolfe MS. 2012. A G-Rich element forms a G-quadruplex and regulates BACE1 mRNA alternative splicing. *Journal of Neurochemistry* **121**: 763–773. http://dx.doi.org/10.1111/j.1471-4159.2012.07680.x.

Fish L, Khoroshkin M, Navickas A, Garcia K, Culbertson B, Hänisch B, Zhang S, Nguyen HCB, Soto LM, Dermit M, et al. 2021. A prometastatic splicing program regulated by SNRPA1 interactions with structured RNA elements. *Science* **372**: eabc7531. http://dx.doi.org/10.1126/science.abc7531.

Frankiw L, Baltimore D, Li G. 2019. Alternative mRNA splicing in cancer immunotherapy. *Nature Reviews Immunology* **19**: 675–687. http://dx.doi.org/10.1038/s41577-019-0195-7.

Gardner R, Wu D, Cherian S, Fang M, Hanafi L-A, Finney O, Smithers H, Jensen MC, Riddell SR, Maloney DG, et al. 2016. Acquisition of a CD19-negative myeloid phenotype allows immune escape of MLL-rearranged B-ALL from CD19 CAR-T-cell therapy. *Blood* **127**: 2406–2410. http://dx.doi.org/10.1182/blood-2015-08-665547.

Garneau D, Revil T, Fisette J-F, Chabot B. 2005. Heterogeneous Nuclear Ribonucleoprotein F/H Proteins Modulate the Alternative Splicing of the Apoptotic Mediator Bcl-x. *Journal of Biological Chemistry* **280**: 22641–22650. http://dx.doi.org/10.1074/jbc.M501070200.

Garrido-Martín D, Borsari B, Calvo M, Reverter F, Guigó R. 2021. Identification and analysis of splicing quantitative trait loci across multiple tissues in the

human genome. *Nature Communications* **12**. http://dx.doi.org/10.1038/s41467-020-20578-2.

Gerstung M, Jolly C, Leshchiner I, Dentro SC, Gonzalez S, Rosebrock D, Mitchell TJ, Rubanova Y, Anur P, Yu K, et al. 2020. The evolutionary history of 2,658 cancers. *Nature* **578**: 122–128. http://dx.doi.org/10.1038/s41586-019-1907-7.

Geuens T, Bouhy D, Timmerman V. 2016. The hnRNP family: insights into their role in health and disease. *Human Genetics* **135**: 851–867. http://dx.doi.org/10.1007/s00439-016-1683-5.

Ghanbari M, Ohler U. 2020. Deep neural networks for interpreting RNA-binding protein target preferences. *Genome Research* **30**: 214–226. http://dx.doi.org/10.1101/gr.247494.118.

Ghigna C, Giordano S, Shen H, Benvenuto F, Castiglioni F, Comoglio PM, Green MR, Riva S, Biamonti G. 2005. Cell Motility Is Controlled by SF2/ASF through Alternative Splicing of the Ron Protooncogene. *Molecular Cell* **20**: 881–890. http://dx.doi.org/10.1016/j.molcel.2005.10.026.

Glidden DT, Buerer JL, Saueressig CF, Fairbrother WG. 2021. Hotspot exons are common targets of splicing perturbations. *Nature Communications* **12**. http://dx.doi.org/10.1038/s41467-021-22780-2.

Golan-Gerstl R, Cohen M, Shilo A, Suh S-S, Bakàcs A, Coppola L, Karni R. 2011a. Splicing Factor hnRNP A2/B1 Regulates Tumor Suppressor Gene Splicing and Is an Oncogenic Driver in Glioblastoma. *Cancer Research* **71**: 4464–4472. http://dx.doi.org/10.1158/0008-5472.CAN-10-4410.

Golan-Gerstl R, Cohen M, Shilo A, Suh S-S, Bakàcs A, Coppola L, Karni R. 2011b. Splicing Factor hnRNP A2/B1 Regulates Tumor Suppressor Gene Splicing and Is an Oncogenic Driver in Glioblastoma. *Cancer Research* **71**: 4464–4472. http://dx.doi.org/10.1158/0008-5472.CAN-10-4410.

Gonzalez-Garay ML. 2015. Introduction to isoform sequencing using pacific biosciences technology (iso-seq). pp. 141–160, Springer Netherlands http://dx.doi.org/10.1007/978-94-017-7450-5_6.

Grabow D, Spix C, Blettner M, Kaatsch P. 2011. Strategy for Long-Term Surveillance at the German Childhood Cancer Registry - an Update. *Klinische Pädiatrie* **223**: 159–164. http://dx.doi.org/10.1055/s-0031-1275352.

Grupp SA, Kalos M, Barrett D, Aplenc R, Porter DL, Rheingold SR, Teachey DT, Chew A, Hauck B, Wright JF, et al. 2013. Chimeric Antigen ReceptorModified T Cells for Acute Lymphoid Leukemia. *New England Journal of Medicine* **368**: 1509–1518. http://dx.doi.org/10.1056/NEJMoa1215134.

Gueroussov S, Weatheritt RJ, O'Hanlon D, Lin Z-Y, Narula A, Gingras A-C, Blencowe BJ. 2017. Regulatory Expansion in Mammals of Multivalent

hnRNP Assemblies that Globally Control Alternative Splicing. *Cell* **170**: 324–339.e23. http://dx.doi.org/10.1016/j.cell.2017.06.037.

Guo J, Jia J, Jia R. 2015. PTBP1 and PTBP2 impaired autoregulation of SRSF3 in cancer cells. *Scientific Reports* **5**. http://dx.doi.org/10.1038/srep14548.

Han H, Braunschweig U, Gonatopoulos-Pournatzis T, Weatheritt RJ, Hirsch CL, Ha KCH, Radovani E, Nabeel-Shah S, Sterne-Weiler T, Wang J, et al. 2017. Multilayered Control of Alternative Splicing Regulatory Networks by Transcription Factors. *Molecular Cell* **65**: 539–553.e7. http://dx.doi.org/10.1016/j.molcel.2017.01.011.

Han S, Tang Y, Smith R. 2010. Functional diversity of the hnRNPs: past, present and perspectives. *Biochemical Journal* **430**: 379–392. http://dx.doi.org/10.1042/BJ20100396.

Harvey SE, Cheng C. 2016. Methods for characterization of alternative RNA splicing. pp. 229–241, Springer New York http://dx.doi.org/10.1007/978-1-4939-3378-5_18.

Hegele A, Kamburov A, Grossmann A, Sourlis C, Wowro S, Weimann M, Will Cindy L, Pena V, Lührmann R, Stelzl U. 2012. Dynamic Protein-Protein Interaction Wiring of the Human Spliceosome. *Molecular Cell* **45**: 567–580. http://dx.doi.org/10.1016/j.molcel.2011.12.034.

Herviou P, Le Bras M, Dumas L, Hieblot C, Gilhodes J, Cioci G, Hugnot J-P, Ameadan A, Guillonneau F, Dassi E, et al. 2020. hnRNP H/F drive RNA G-quadruplex-mediated translation linked to genomic instability and therapy resistance in glioblastoma. *Nature Communications* **11**. http://dx.doi.org/10.1038/s41467-020-16168-x.

Honoré B, Baandrup U, Vorum H. 2004. Heterogeneous nuclear ribonucleoproteins F and H/H' show differential expression in normal and selected cancer tissues. *Experimental Cell Research* **294**: 199–209. http://dx.doi.org/10.1016/j.yexcr.2003.11.011.

Howorka S, Siwy ZS. 2020. Reading amino acids in a nanopore. *Nature Biotechnology* **38**: 159–160. http://dx.doi.org/10.1038/s41587-019-0401-y.

Hu Z, Yau C, Ahmed AA. 2017. A pan-cancer genome-wide analysis reveals tumour dependencies by induction of nonsense-mediated decay. *Nature Communications* **8**. http://dx.doi.org/10.1038/ncomms15943.

Huang F, Liao E, Li C, Yen C, Yu S. 2020. Pathogenesis of pediatric b?cell acute lymphoblastic leukemia: Molecular pathways and disease treatments (review). *Oncology Letters* **20**: 448–454. http://dx.doi.org/10.3892/ol.2020.11583.

Ibrahim F, Oppelt J, Maragkakis M, Mourelatos Z. 2021. TERA-Seq: true end-to-end sequencing of native RNA molecules for transcriptome characterization.

Nucleic Acids Research. http://dx.doi.org/10.1093/nar/gkab713.

Ilagan JO, Ramakrishnan A, Hayes B, Murphy ME, Zebari AS, Bradley P, Bradley RK. 2014. U2AF1mutations alter splice site recognition in hematological malignancies. *Genome Research* **25**: 14–26. http://dx.doi.org/10.1101/gr.181016.114.

Ishigami Y, Ohira T, Isokawa Y, Suzuki Y, Suzuki T. 2021. A single m6A modification in U6 snRNA diversifies exon sequence at the 5' splice site. *Nature Communications* **12**. http://dx.doi.org/10.1038/s41467-021-23457-6.

Jaganathan K, Kyriazopoulou Panagiotopoulou S, McRae JF, Darbandi SF, Knowles D, Li YI, Kosmicki JA, Arbelaez J, Cui W, Schwartz GB, et al. 2019. Predicting Splicing from Primary Sequence with Deep Learning. *Cell* **176**: 535–548.e24. http://dx.doi.org/10.1016/j.cell.2018.12.015.

Jha A, Gazzara MR, Barash Y. 2017. Integrative deep models for alternative splicing. *Bioinformatics* **33**: i274–i282. http://dx.doi.org/10.1093/bioinformatics/btx268.

Jian X, Boerwinkle E, Liu X. 2013. In silico tools for splicing defect prediction: a survey from the viewpoint of end users. *Genetics in Medicine* **16**: 497–503. http://dx.doi.org/10.1038/gim.2013.176.

Joseph B, Lai EC. 2021. The Exon Junction Complex and intron removal prevent re-splicing of mRNA ed. T. Bowman. *PLOS Genetics* **17**: e1009563. http://dx.doi.org/10.1371/journal.pgen.1009563.

Jourdain AA, Begg BE, Mick E, Shah H, Calvo SE, Skinner OS, Sharma R, Blue SM, Yeo GW, Burge CB, et al. 2021. Loss of LUC7L2 and U1 snRNP subunits shifts energy metabolism from glycolysis to OXPHOS. *Molecular Cell* **81**: 1905–1919.e12. http://dx.doi.org/10.1016/j.molcel.2021.02.033.

Julien P, Miñana B, Baeza-Centurion P, Valcárcel J, Lehner B. 2016. The complete local genotypephenotype landscape for the alternative splicing of a human exon. *Nature Communications* **7**. http://dx.doi.org/10.1038/ncomms11558.

Karni R, de Stanchina E, Lowe SW, Sinha R, Mu D, Krainer AR. 2007. The gene encoding the splicing factor SF2/ASF is a proto-oncogene. *Nature Structural & Molecular Biology* **14**: 185–193. http://dx.doi.org/10.1038/nsmb1209.

Karst SM, Ziels RM, Kirkegaard RH, Sørensen EA, McDonald D, Zhu Q, Knight R, Albertsen M. 2021. High-accuracy long-read amplicon sequences using unique molecular identifiers with Nanopore or PacBio sequencing. *Nature Methods* **18**: 165–169. http://dx.doi.org/10.1038/s41592-020-01041-y.

Katz Y, Wang ET, Airoldi EM, Burge CB. 2010. Analysis and design of RNA sequencing experiments for identifying isoform regulation. *Nature Methods* **7**: 1009–1015. http://dx.doi.org/10.1038/nmeth.1528.

Ke S, Anquetil V, Zamalloa JR, Maity A, Yang A, Arias MA, Kalachikov S, Russo JJ, Ju J, Chasin LA. 2017. Saturation mutagenesis reveals manifold determinants of exon definition. *Genome Research* **28**: 11–24. http://dx.doi.org/10.1101/gr.219683.116.

Ke S, Shang S, Kalachikov SM, Morozova I, Yu L, Russo JJ, Ju J, Chasin LA. 2011. Quantitative evaluation of all hexamers as exonic splicing elements. *Genome Research* **21**: 1360–1374. http://dx.doi.org/10.1101/gr.119628.110.

Kent DG, Green AR. 2017. Order Matters: The Order of Somatic Mutations Influences Cancer Evolution. *Cold Spring Harbor Perspectives in Medicine* **7**: a027060. http://dx.doi.org/10.1101/cshperspect.a027060.

Koh CM, Bezzi M, Low DHP, Ang WX, Teo SX, Gay FPH, Al-Haddawi M, Tan SY, Osato M, Sabò A, et al. 2015. MYC regulates the core pre-mRNA splicing machinery as an essential step in lymphomagenesis. *Nature* **523**: 96–100. http://dx.doi.org/10.1038/nature14351.

Krishnaswamy S, Bukhari I, Mohammed AK, Amer OE, Tripathi G, Alokail MS, Al-Daghri NM. 2018. Identification of the splice variants of Recepteur d'Origine nantais (RON) in lung cancer cell lines. *Gene* **679**: 335–340. http://dx.doi.org/10.1016/j.gene.2018.09.027.

Lal A, Chiang ZD, Yakovenko N, Duarte FM, Israeli J, Buenrostro JD. 2021. Deep learning-based enhancement of epigenomics data with AtacWorks. *Nature Communications* **12**. http://dx.doi.org/10.1038/s41467-021-21765-5.

Larson MH, Gilbert LA, Wang X, Lim WA, Weissman JS, Qi LS. 2013. CRISPR interference (CRISPRi) for sequence-specific control of gene expression. *Nature Protocols* **8**: 2180–2196. http://dx.doi.org/10.1038/nprot.2013.132.

Lee SC-W, Abdel-Wahab O. 2016. Therapeutic targeting of splicing in cancer. *Nature Medicine* **22**: 976–986. http://dx.doi.org/10.1038/nm.4165.

LeFave CV, Squatrito M, Vorlova S, Rocco GL, Brennan CW, Holland EC, Pan Y-X, Cartegni L. 2011. Splicing factor hnRNPH drives an oncogenic splicing switch in gliomas. *The EMBO Journal* **30**: 4084–4097. http://dx.doi.org/10.1038/emboj.2011.259.

Li X, Chen W. 2019. Mechanisms of failure of chimeric antigen receptor T-cell therapy. *Current Opinion in Hematology* **26**: 427–433. http://dx.doi.org/10.1097/MOH.0000000000000548.

Li X, Liu S, Zhang L, Issaian A, Hill RC, Espinosa S, Shi S, Cui Y, Kappel K, Das R, et al. 2019. A unified mechanism for intron and exon definition and back-splicing. *Nature* **573**: 375–380. http://dx.doi.org/10.1038/s41586-019-1523-6.

Li YI, Knowles DA, Humphrey J, Barbeira AN, Dickinson SP, Im HK, Pritchard JK. 2017. Annotation-free quantification of RNA splicing using LeafCutter. *Nature*

Genetics **50**: 151–158. http://dx.doi.org/10.1038/s41588-017-0004-9.

Liao SE, Regev O. 2020. Splicing at the phase-separated nuclear speckle interface: a model. *Nucleic Acids Research* **49**: 636–645. http://dx.doi.org/10.1093/nar/gkaa1209.

Litchfield K, Reading JL, Lim EL, Xu H, Liu P, Al-Bakir M, Wong YNS, Rowan A, Funt SA, Merghoub T, et al. 2020. Escape from nonsense-mediated decay associates with anti-tumor immunogenicity. *Nature Communications* **11**. http://dx.doi.org/10.1038/s41467-020-17526-5.

Liu H, Begik O, Lucas MC, Ramirez JM, Mason CE, Wiener D, Schwartz S, Mattick JS, Smith MA, Novoa EM. 2019. Accurate detection of m6A RNA modifications in native RNA sequences. *Nature Communications* **10**. http://dx.doi.org/10.1038/s41467-019-11713-9.

Lord J, Baralle D. 2021. Splicing in the diagnosis of rare disease: Advances and challenges. *Frontiers in Genetics* **12**. http://dx.doi.org/10.3389/fgene.2021.689892.

Martinez NM, Su A, Nussbacher JK, Burns MC, Schaening C, Sathe S, Yeo GW, Gilbert WV. 2020. Pseudouridine synthases modify human pre-mRNA co-transcriptionally and affect splicing. http://dx.doi.org/10.1101/2020.08.29.273565.

Mayer S, Hirschfeld M, Jaeger M, Pies S, Iborra S, Erbes T, Stickeler E. 2015. RON alternative splicing regulation in primary ovarian cancer. *Oncology Reports* **34**: 423–430. http://dx.doi.org/10.3892/or.2015.3995.

Mehmood A, Laiho A, Venäläinen MS, McGlinchey AJ, Wang N, Elo LL. 2019. Systematic evaluation of differential splicing tools for RNA-seq studies. *Briefings in Bioinformatics* **21**: 2052–2065. http://dx.doi.org/10.1093/bib/bbz126.

Mendel M, Delaney K, Pandey RR, Chen K-M, Wenda JM, Vågbø CB, Steiner FA, Homolka D, Pillai RS. 2021. Splice site m6A methylation prevents binding of U2AF35 to inhibit RNA splicing. *Cell* **184**: 3125–3142.e25. http://dx.doi.org/10.1016/j.cell.2021.03.062.

Mercuri E, Darras BT, Chiriboga CA, Day JW, Campbell C, Connolly AM, Iannaccone ST, Kirschner J, Kuntz NL, Saito K, et al. 2018. Nusinersen versus Sham Control in Later-Onset Spinal Muscular Atrophy. *New England Journal of Medicine* **378**: 625–635. http://dx.doi.org/10.1056/NEJMoa1710504.

Meyer K, Koester T, Staiger D. 2015. Pre-mRNA Splicing in Plants: In Vivo Functions of RNA-Binding Proteins Implicated in the Splicing Process. *Biomolecules* **5**: 1717–1740. http://dx.doi.org/10.3390/biom5031717.

Mikl M, Hamburg A, Pilpel Y, Segal E. 2019. Dissecting splicing decisions and cell-to-cell variability with designed sequence libraries. *Nature Communications* **10**. http://dx.doi.org/10.1038/s41467-019-12642-3.

NCI. 2016. Risk-Directed Therapy in Treating Younger Patients with Newly Diagnosed Acute Lymphoblastic Leukemia.

Neckles C, Boer RE, Aboreden N, Cross AM, Walker RL, Kim B-H, Kim S, Schneekloth, Jr JS, Caplen NJ. 2019. HNRNPH1-dependent splicing of a fusion oncogene reveals a targetable RNA G-quadruplex interaction. *RNA* **25**: 1731–1750. http://dx.doi.org/10.1261/rna.072454.119.

Newman A. 1998. RNA splicing. *Current Biology* **8**: R903–R905. http://dx.doi.org/10.1016/S0960-9822(98)00005-0.

Nie Y, Lu W, Chen D, Tu H, Guo Z, Zhou X, Li M, Tu S, Li Y. 2020. Mechanisms underlying CD19-positive ALL relapse after anti-CD19 CAR T cell therapy and associated strategies. *Biomarker Research* **8**. http://dx.doi.org/10.1186/s40364-020-00197-1.

Nojima T, Rebelo K, Gomes T, Grosso AR, Proudfoot NJ, Carmo-Fonseca M. 2018. RNA Polymerase II Phosphorylated on CTD Serine 5 Interacts with the Spliceosome during Co-transcriptional Splicing. *Molecular Cell* **72**: 369–379.e4. http://dx.doi.org/10.1016/j.molcel.2018.09.004.

Nounou MN, Nounou HN, Meskin N, Datta A, Dougherty ER. 2012. Multiscale denoising of biological data: A comparative analysis. *IEEE/ACM Transactions on Computational Biology and Bioinformatics* **9**: 1539–1545. http://dx.doi.org/10.1109/TCBB.2012.67.

Okunola HL, Krainer AR. 2009. Cooperative-Binding and Splicing-Repressive Properties of hnRNP A1. *Molecular and Cellular Biology* **29**: 5620–5631. http://dx.doi.org/10.1128/MCB.01678-08.

ONT. 2019. RNA and gene expression analysis using direct RNA and cDNA sequencing.

Orlando EJ, Han X, Tribouley C, Wood PA, Leary RJ, Riester M, Levine JE, Qayed M, Grupp SA, Boyer M, et al. 2018. Genetic mechanisms of target antigen loss in CAR19 therapy of acute lymphoblastic leukemia. *Nature Medicine* **24**: 1504–1506. http://dx.doi.org/10.1038/s41591-018-0146-z.

Pan Q, Shai O, Lee LJ, Frey BJ, Blencowe BJ. 2008. Deep surveying of alternative splicing complexity in the human transcriptome by high-throughput sequencing. *Nature Genetics* **40**: 1413–1415. http://dx.doi.org/10.1038/ng.259.

Papaemmanuil E, Cazzola M, Boultwood J, Malcovati L, Vyas P, Bowen D, Pellagatti A, Wainscoat JS, Hellstrom-Lindberg E, Gambacorti-Passerini C, et al. 2011. SomaticSF3B1Mutation in Myelodysplasia with Ring Sideroblasts. *New England Journal of Medicine* **365**: 1384–1395. http://dx.doi.org/10.1056/NEJMoa1103283.

Papasaikas P, Tejedor J Ramón, Vigevani L, Valcárcel J. 2015. Functional Splicing Network Reveals Extensive Regulatory Potential of the Core Spliceosomal Ma-

chinery. *Molecular Cell* **57**: 7–22. http://dx.doi.org/10.1016/j.molcel.2014.10.030.

Park E, Pan Z, Zhang Z, Lin L, Xing Y. 2018. The Expanding Landscape of Alternative Splicing Variation in Human Populations. *The American Journal of Human Genetics* **102**: 11–26. http://dx.doi.org/10.1016/j.ajhg.2017.11.002.

Pehlivan KC, Duncan BB, Lee DW. 2018. CAR-T Cell Therapy for Acute Lymphoblastic Leukemia: Transforming the Treatment of Relapsed and Refractory Disease. *Current Hematologic Malignancy Reports* **13**: 396–406. http://dx.doi.org/10.1007/s11899-018-0470-x.

Phillips JW, Pan Y, Tsai BL, Xie Z, Demirdjian L, Xiao W, Yang HT, Zhang Y, Lin CH, Cheng D, et al. 2020. Pathway-guided analysis identifies Myc-dependent alternative pre-mRNA splicing in aggressive prostate cancers. *Proceedings of the National Academy of Sciences* **117**: 5269–5279. http://dx.doi.org/10.1073/pnas.1915975117.

Plaks V, Rossi JM, Chou J, Wang L, Poddar S, Han G, Wang Z, Kuang S-Q, Chu F, Davis RE, et al. 2021. CD19 target evasion as a mechanism of relapse in large B-cell lymphoma treated with axicabtagene ciloleucel. *Blood* **138**: 1081–1085. http://dx.doi.org/10.1182/blood.2021010930.

Pratanwanich PN, Yao F, Chen Y, Koh CWQ, Wan YK, Hendra C, Poon P, Goh YT, Yap PML, Chooi JY, et al. 2021. Identification of differential RNA modifications from nanopore direct RNA sequencing with xPore. *Nature Biotechnology*. http://dx.doi.org/10.1038/s41587-021-00949-w.

Protter DSW, Rao BS, Van Treeck B, Lin Y, Mizoue L, Rosen MK, Parker R. 2018. Intrinsically Disordered Regions Can Contribute Promiscuous Interactions to RNP Granule Assembly. *Cell Reports* **22**: 1401–1412. http://dx.doi.org/10.1016/j.celrep.2018.01.036.

Rabilloud T, Potier D, Pankaew S, Nozais M, Loosveld M, Payet-Bornet D. 2021. Single-cell profiling identifies pre-existing CD19-negative subclones in a B-ALL patient with CD19-negative relapse after CAR-T therapy. *Nature Communications* **12**. http://dx.doi.org/10.1038/s41467-021-21168-6.

Rahimi K, Venø MT, Dupont DM, Kjems J. 2021. Nanopore sequencing of brain-derived full-length circRNAs reveals circRNA-specific exon usage, intron retention and microexons. *Nature Communications* **12**. http://dx.doi.org/10.1038/s41467-021-24975-z.

Richardson DN, Rogers MF, Labadorf A, Ben-Hur A, Guo H, Paterson AH, Reddy ASN. 2011. Comparative Analysis of Serine/Arginine-Rich Proteins across 27 Eukaryotes: Insights into Sub-Family Classification and Extent of Alternative Splicing ed. S.-H. Shiu. *PLoS ONE* **6**: e24542. http://dx.doi.org/10.1371/journal.pone.0024542.

Roberts KG. 2018. Genetics and prognosis of ALL in children vs adults. *Hematology* **2018**: 137–145. http://dx.doi.org/10.1182/asheducation-2018.1.137.

Rosenberg AB, Patwardhan RP, Shendure J, Seelig G. 2015. Learning the Sequence Determinants of Alternative Splicing from Millions of Random Sequences. *Cell* **163**: 698–711. http://dx.doi.org/10.1016/j.cell.2015.09.054.

Ruiz-Velasco M, Kumar M, Lai MC, Bhat P, Solis-Pinson AB, Reyes A, Kleinsorg S, Noh K-M, Gibson TJ, Zaugg JB. 2017. CTCF-Mediated Chromatin Loops between Promoter and Gene Body Regulate Alternative Splicing across Individuals. *Cell Systems* **5**: 628–637.e6. http://dx.doi.org/10.1016/j.cels.2017.10.018.

Saez B, Walter MJ, Graubert TA. 2017. Splicing factor gene mutations in hematologic malignancies. *Blood* **129**: 1260–1269. http://dx.doi.org/10.1182/blood-2016-10-692400.

Schafer S, Miao K, Benson CC, Heinig M, Cook SA, Hubner N. 2015. Alternative Splicing Signatures in RNA-seq Data: Percent Spliced in (PSI). *Current Protocols in Human Genetics* **87**. http://dx.doi.org/10.1002/0471142905.hg1116s87.

Schroeder HW, Imboden JB, Torres RM. 2019. Antigen receptor genes, gene products, and coreceptors. pp. 55–77.e1, Elsevier http://dx.doi.org/10.1016/B978-0-7020-6896-6.00004-1.

Shao W, Kim H-S, Cao Y, Xu Y-Z, Query CC. 2012. A U1-U2 snRNP Interaction Network during Intron Definition. *Molecular and Cellular Biology* **32**: 470–478. http://dx.doi.org/10.1128/MCB.06234-11.

Shen H, Green MR. 2006. RS domains contact splicing signals and promote splicing by a common mechanism in yeast through humans. *Genes & Development* **20**: 1755–1765. http://dx.doi.org/10.1101/gad.1422106.

Shen S, Park JW, Lu Z, Lin L, Henry MD, Wu YN, Zhou Q, Xing Y. 2014. rMATS: Robust and flexible detection of differential alternative splicing from replicate RNA-Seq data. *Proceedings of the National Academy of Sciences* **111**: E5593–E5601. http://dx.doi.org/10.1073/pnas.1419161111.

Sheynkman GM, Tuttle KS, Laval F, Tseng E, Underwood JG, Yu L, Dong D, Smith ML, Sebra R, Willems L, et al. 2020. ORF Capture-Seq as a versatile method for targeted identification of full-length isoforms. *Nature Communications* **11**. http://dx.doi.org/10.1038/s41467-020-16174-z.

Sibley CR, Blazquez L, Ule J. 2016. Lessons from non-canonical splicing. *Nature Reviews Genetics* **17**: 407–421. http://dx.doi.org/10.1038/nrg.2016.46.

Slaff B, Radens CM, Jewell P, Jha A, Lahens NF, Grant GR, Thomas-Tikhonenko A, Lynch KW, Barash Y. 2021. MOCCASIN: a method for correcting for known and unknown confounders in RNA splicing analysis. *Nature Communications* **12**. http://dx.doi.org/10.1038/s41467-021-23608-9.

Smith MA, Ersavas T, Ferguson JM, Liu H, Lucas MC, Begik O, Bojarski L, Barton K, Novoa EM. 2020. Molecular barcoding of native RNAs using nanopore sequencing and deep learning. *Genome Research* **30**: 1345–1353. http://dx.doi.org/10.1101/gr.260836.120.

Soemedi R, Cygan KJ, Rhine CL, Wang J, Bulacan C, Yang J, Bayrak-Toydemir P, McDonald J, Fairbrother WG. 2017. Pathogenic variants that alter protein code often disrupt splicing. *Nature Genetics* **49**: 848–855. http://dx.doi.org/10.1038/ng.3837.

Sotillo E, Barrett DM, Black KL, Bagashev A, Oldridge D, Wu G, Sussman R, Lanauze C, Ruella M, Gazzara MR, et al. 2015. Convergence of Acquired Mutations and Alternative Splicing of CD19 Enables Resistance to CART-19 Immunotherapy. *Cancer Discovery* **5**: 1282–1295. http://dx.doi.org/10.1158/2159-8290.CD-15-1020.

Souček P, Réblová K, Kramárek M, Radová L, Grymová T, Hujová P, Kováčová T, Lexa M, Grodecká L, Freiberger T. 2019. High-throughput analysis revealed mutations' diverging effects on SMN1 exon 7 splicing. *RNA Biology* **16**: 1364–1376. http://dx.doi.org/10.1080/15476286.2019.1630796.

St. Jude Hospital. 2021. Risk-directed childhood leukemia treatment takes a step forward.

Stevens M, Oltean S. 2019. Modulation of the apoptosis gene bcl-x function through alternative splicing. *Frontiers in Genetics* **10**. http://dx.doi.org/10.3389/fgene.2019.00804.

Syed NH, Kalyna M, Marquez Y, Barta A, Brown JWS. 2012. Alternative splicing in plants coming of age. *Trends in Plant Science* **17**: 616–623. http://dx.doi.org/10.1016/j.tplants.2012.06.001.

Tajnik M, Vigilante A, Braun S, Hänel H, Luscombe NM, Ule J, Zarnack K, König J. 2015. IntergenicAluexonisation facilitates the evolution of tissue-specific transcript ends. *Nucleic Acids Research* gkv956. http://dx.doi.org/10.1093/nar/gkv956.

Tang Q, Rodriguez-Santiago S, Wang J, Pu J, Yuste A, Gupta V, Moldón A, Xu Y-Z, Query CC. 2016. SF3B1/Hsh155 HEAT motif mutations affect interaction with the spliceosomal ATPase Prp5, resulting in altered branch site selectivity in pre-mRNA splicing. *Genes & Development* **30**: 2710–2723. http://dx.doi.org/10.1101/gad.291872.116.

Thomas N, Poodari V, Jain M, Olsen H, Akeson M, Abu-Shumays R. 2021. Direct nanopore sequencing of individual full length tRNA strands. http://dx.doi.org/10.1101/2021.04.26.441285.

Trincado JL, Entizne JC, Hysenaj G, Singh B, Skalic M, Elliott DJ, Eyras E. 2018. SUPPA2: fast, accurate, and uncertainty-aware differential splicing analysis across multiple conditions. *Genome Biology* **19**. http://dx.doi.org/10.1186/s13059-018-1417-1.

Uhl M, Tran VD, Heyl F, Backofen R. 2019. GraphProt2: A graph neural network-based method for predicting binding sites of RNA-binding proteins. http://dx.doi.org/10.1101/850024.

Uhlen M, Zhang C, Lee S, Sjöstedt E, Fagerberg L, Bidkhori G, Benfeitas R, Arif M, Liu Z, Edfors F, et al. 2017. A pathology atlas of the human cancer transcriptome. *Science* **357**: eaan2507. http://dx.doi.org/10.1126/science.aan2507.

Uren PJ, Bahrami-Samani E, de Araujo PR, Vogel C, Qiao M, Burns SC, Smith AD, Penalva LOF. 2016. High-throughput analyses of hnRNP H1 dissects its multi-functional aspect. *RNA Biology* **13**: 400–411. http://dx.doi.org/10.1080/15476286.2015.1138030.

Van Dusen CM, Yee L, McNally LM, McNally MT. 2010. A Glycine-Rich Domain of hnRNP H/F Promotes Nucleocytoplasmic Shuttling and Nuclear Import through an Interaction with Transportin 1. *Molecular and Cellular Biology* **30**: 2552–2562. http://dx.doi.org/10.1128/MCB.00230-09.

van Endert P. 2021. Beware the algorithm. *eLife* **10**. http://dx.doi.org/10.7554/eLife.69657.

Van Nostrand EL, Freese P, Pratt GA, Wang X, Wei X, Xiao R, Blue SM, Chen J-Y, Cody NAL, Dominguez D, et al. 2020. A large-scale binding and functional map of human RNA-binding proteins. *Nature* **583**: 711–719. http://dx.doi.org/10.1038/s41586-020-2077-3.

Vaquero-Garcia J, Barrera A, Gazzara MR, González-Vallinas J, Lahens NF, Hogenesch JB, Lynch KW, Barash Y. 2016. A new view of transcriptome complexity and regulation through the lens of local splicing variations. *eLife* **5**. http://dx.doi.org/10.7554/eLife.11752.

Vaz-Drago R, Custódio N, Carmo-Fonseca M. 2017. Deep intronic mutations and human disease. *Human Genetics* **136**: 1093–1111. http://dx.doi.org/10.1007/s00439-017-1809-4.

Waanders E, Gu Z, Dobson SM, Antić Ž, Crawford JC, Ma X, Edmonson MN, Payne-Turner D, van de Vorst M, Jongmans MCJ, et al. 2020. Mutational Landscape and Patterns of Clonal Evolution in Relapsed Pediatric Acute Lymphoblastic Leukemia. *Blood Cancer Discovery* **1**: 96–111. http://dx.doi.

org/10.1158/0008-5472.BCD-19-0041.

Wan Y, Anastasakis DG, Rodriguez J, Palangat M, Gudla P, Zaki G, Tandon M, Pegoraro G, Chow CC, Hafner M, et al. 2021. Dynamic imaging of nascent RNA reveals general principles of transcription dynamics and stochastic splice site selection. *Cell* **184**: 2878–2895.e20. http://dx.doi.org/10.1016/j.cell.2021.04.012.

Wang K, Wei G, Liu D. 2012. CD19: a biomarker for B cell development, lymphoma diagnosis and therapy. *Experimental Hematology & Oncology* **1**. http://dx.doi.org/10.1186/2162-3619-1-36.

Wang L, Brooks Angela N, Fan J, Wan Y, Gambe R, Li S, Hergert S, Yin S, Freeman Samuel S, Levin Joshua Z, et al. 2016. Transcriptomic Characterization of SF3B1 Mutation Reveals Its Pleiotropic Effects in Chronic Lymphocytic Leukemia. *Cancer Cell* **30**: 750–763. http://dx.doi.org/10.1016/j.ccell.2016.10.005.

Wang Q, Rio DC. 2018. JUM is a computational method for comprehensive annotation-free analysis of alternative pre-mRNA splicing patterns. *Proceedings of the National Academy of Sciences* **115**: E8181–E8190. http://dx.doi.org/10.1073/pnas.1806018115.

Wang T-Y, Liu Q, Ren Y, Alam SkK, Wang L, Zhu Z, Hoeppner LH, Dehm SM, Cao Q, Yang R. 2021. A pan-cancer transcriptome analysis of exitron splicing identifies novel cancer driver genes and neoepitopes. *Molecular Cell* **81**: 2246–2260.e12. http://dx.doi.org/10.1016/j.molcel.2021.03.028.

Wang T-Y, Yang R. 2021. Integrated protocol for exitron and exitron-derived neoantigen identification using human RNA-seq data with ScanExitron and ScanNeo. *STAR Protocols* **2**: 100788. http://dx.doi.org/10.1016/j.xpro.2021.100788.

Wang Z, Burge CB. 2008. Splicing regulation: From a parts list of regulatory elements to an integrated splicing code. *RNA* **14**: 802–813. http://dx.doi.org/10.1261/rna.876308.

Webb TR, Joyner AS, Potter PM. 2013. The development and application of small molecule modulators of SF3b as therapeutic agents for cancer. *Drug Discovery Today* **18**: 43–49. http://dx.doi.org/10.1016/j.drudis.2012.07.013.

Weiland J, Pal D, Case M, Irving J, Ponthan F, Koschmieder S, Heidenreich O, von Stackelberg A, Eckert C, Vormoor J, et al. 2016. BCP-ALL blasts are not dependent on CD19 expression for leukaemic maintenance. *Leukemia* **30**: 1920–1923. http://dx.doi.org/10.1038/leu.2016.64.

Wenger AM, Peluso P, Rowell WJ, Chang P-C, Hall RJ, Concepcion GT, Ebler J, Fungtammasan A, Kolesnikov A, Olson ND, et al. 2019. Accurate circular consensus long-read sequencing improves variant detection and assembly of

a human genome. *Nature Biotechnology* **37**: 1155–1162. http://dx.doi.org/10.1038/s41587-019-0217-9.

Wilkinson KA, Merino EJ, Weeks KM. 2006. Selective 2'-hydroxyl acylation analyzed by primer extension (SHAPE): quantitative RNA structure analysis at single nucleotide resolution. *Nature Protocols* **1**: 1610–1616. http://dx.doi.org/10.1038/nprot.2006.249.

Wojtowicz WM, Flanagan JJ, Millard SS, Zipursky SL, Clemens JC. 2004. Alternative Splicing of Drosophila Dscam Generates Axon Guidance Receptors that Exhibit Isoform-Specific Homophilic Binding. *Cell* **118**: 619–633. http://dx.doi.org/10.1016/j.cell.2004.08.021.

Wong MS, Kinney JB, Krainer AR. 2018. Quantitative Activity Profile and Context Dependence of All Human 5' Splice Sites. *Molecular Cell* **71**: 1012–1026.e3. http://dx.doi.org/10.1016/j.molcel.2018.07.033.

Wu JY, Maniatis T. 1993. Specific interactions between proteins implicated in splice site selection and regulated alternative splicing. *Cell* **75**: 1061–1070. http://dx.doi.org/10.1016/0092-8674(93)90316-I.

Xiao X, Wang Z, Jang M, Nutiu R, Wang ET, Burge CB. 2009. Splice site strength-dependent activity and genetic buffering by poly-G runs. *Nature Structural & Molecular Biology* **16**: 1094–1100. http://dx.doi.org/10.1038/nsmb.1661.

Xiong HY, Alipanahi B, Lee LJ, Bretschneider H, Merico D, Yuen RKC, Hua Y, Gueroussov S, Najafabadi HS, Hughes TR, et al. 2014. The human splicing code reveals new insights into the genetic determinants of disease. *Science* **347**: 1254806–1254806. http://dx.doi.org/10.1126/science.1254806.

Xu C, Xie N, Su Y, Sun Z, Liang Y, Zhang N, Liu D, Jia S, Xing X, Han L, et al. 2019. HnRNP F/H associate with hTERC and telomerase holoenzyme to modulate telomerase function and promote cell proliferation. *Cell Death & Differentiation* **27**: 1998–2013. http://dx.doi.org/10.1038/s41418-019-0483-6.

Yao H-P, Zhou Y-Q, Zhang R, Wang M-H. 2013. MSPRON signalling in cancer: pathogenesis and therapeutic potential. *Nature Reviews Cancer* **13**: 466–481. http://dx.doi.org/10.1038/nrc3545.

Yeo G, Burge CB. 2004. Maximum Entropy Modeling of Short Sequence Motifs with Applications to RNA Splicing Signals. *Journal of Computational Biology* **11**: 377–394. http://dx.doi.org/10.1089/1066527041410418.

Zamora AE, Crawford JC, Allen EK, Guo XJ, Bakke J, Carter RA, Abdelsamed HA, Moustaki A, Li Y, Chang T-C, et al. 2019. Pediatric patients with acute lymphoblastic leukemia generate abundant and functional neoantigen-specific CD8+T cell responses. *Science Translational Medicine* **11**: eaat8549. http://dx.doi.org/10.1126/scitranslmed.aat8549.

Zandhuis ND, Nicolet BP, Wolkers MC. 2021. Mapping RNA-binding proteins in human b cells and t cells upon differentiation. http://dx.doi.org/10.1101/2021.06.10.447413.

Zarnack K, König J, Tajnik M, Martincorena I, Eustermann S, Stévant I, Reyes A, Anders S, Luscombe NM, Ule J. 2013. Direct Competition between hnRNP C and U2AF65 Protects the Transcriptome from the Exonization of Alu Elements. *Cell* **152**: 453–466. http://dx.doi.org/10.1016/j.cell.2012.12.023.

Zhang Y, Parmigiani G, Johnson WE. 2020. ComBat-seq: batch effect adjustment for RNA-seq count data. *NAR Genomics and Bioinformatics* **2**. http://dx.doi.org/10.1093/nargab/lqaa078.

Zhao Y, Aldoss I, Qu C, Crawford JC, Gu Z, Allen EK, Zamora AE, Alexander TB, Wang J, Goto H, et al. 2021. Tumor-intrinsic and -extrinsic determinants of response to blinatumomab in adults with B-ALL. *Blood* **137**: 471–484. http://dx.doi.org/10.1182/blood.2020006287.

MARIELA CORTÉS LÓPEZ

NATIONALITY

Mexican

EDUCATION

current – 2017 | **Ph.D., Biology**
Institute of Molecular Biology, Mainz, Germany

- Working on dissecting alternative splicing networks using high throughtput mutagenesis approaches.
- Development of saturation mutagenesis experiments and data analysis for disease-relevant splicing events: *RON* exon 11, *CD19* exon 2 and *Alu* exonisation in *BRCA2*.

2016 – 2012 | **BSc., Genomics**
Licenciatura en Ciencias Genómicas
Universidad Nacional Autónoma de México, Cuernavaca, Mexico

- Thesis: "CircRNA accumulation in the aging mouse brain"

RESEARCH EXPERIENCE

2017 – 2016 | **Research Assistant**
University of Nevada, Reno

- Scientific technician position, collaborating in RNA related bioinformatics projects.

2016 – 2015 | **Undergraduate Researcher**
University of Nevada, Reno

- Internship and bachelor thesis project.
- Developing a computational pipeline to analyze RNA-Seq data in order to identify circRNA transcripts.
- Collaboration in several projects inside the group but also with other groups from UNR (Dr. Alexander van der Linden group) and external (Dr. Brian Johnson from UC Davis and Dr. Joe Chakkalakal from Rochester University).

CONTACT

m.corteslopez@imb-mainz.de
alt_spliced
mcortes-lopez
Personal website
Google Scholar
ORCID

Last updated on 2021-10-10.

2015 | 2013

Undergraduate Researcher

Centro de Ciencias Genómicas, Cuernavaca, Mexico

- Project: "Bacteria with a phospholipid methyltransferase activity can synthesize their own choline and glycine betaine"
- Training in molecular biology and lipidomics techniques.

2014 | 2014

Summer Undergraduate Researcher

MIT EAPS, Cambridge, MA, USA

- Participation in MISTI-Mexico Workshop (June 26th, 2014).
- Training in basic analysis of MS data.

PUBLICATIONS

2021

Direct long-read RNA sequencing identifies a subset of questionable exitrons likely arising from reverse transcription artifacts

Genome Biology

- Schulz, Laura*, Manuel Torres-Diz*, **Mariela Cortés-López***, Katharina E. Hayer* , Mukta Asnani, Sarah K. Tasian, Yoseph Barash, Elena Sotillo, Kathi Zarnack, Julian König#, Andrei Thomas-Tikhonenko#
- https://doi.org/10.1186/s13059-021-02411-1[1]

2021

High-throughput mutagenesis identifies mutations and RNA binding proteins controlling *CD19* splicing and CART-19 therapy resistance

Preprint (BioRxiV)

- **Cortés-López, Mariela***, Laura Schulz*, Mihaela Enculescu*, Claudia Paret, Bea Spiekermann, Anke Busch, Anna Orekhova, Fridolin Kielisch, Mathieu Quesnel-Vallières, Manuel Torres-Diz, Jörg Faber, Yoseph Barash, Andrei Thomas-Tikhonenko, Kathi Zarnack#., Stefan Legewie#., Julian König#.
- https://www.biorxiv.org/content/10.1101/2021.10.08.463671v1[2]

2018

Decoding a cancer-relevant splicing decision in the RON proto-oncogene using high-throughput mutagenesis

Nature Communications

- Braun, Simon*, Mihaela Enculescu*, Samarth T. Setty*, **Mariela Cortés-López**, Bernardo P. de Almeida, FX Reymond Sutandy, Laura Schulz, Anke Busch, Markus Seiler, Stefanie Ebersberger, Nuno L Barbosa-Morais, Stefan Legewie#, Julian König#, Kathi Zarnack#
- https://doi.org/10.1038/s41467-018-05748-7[3]

2018

Global accumulation of circRNAs during aging in Caenorhabditis elegans

BMC Genomics

- **Cortés-López, Mariela***, Matthew R. Gruner, Daphne A. Cooper, Hannah N. Gruner, Alexandru-Ioan Voda, Alexander M. van der Linden#, and Pedro Miura#.
- https://doi.org/10.1186/s12864-017-4386-y[4]

∗ indicates equal contribution

# indicates corresponding author

2017

Loss of adult skeletal muscle stem cells drives age-related neuromuscular junction degeneration

eLife

- Liu, Wenxuan, Alanna Klose, Sophie Forman, Nicole D. Paris, Lan Wei-Lapierre, **Mariela Cortés-López**, Aidi Tan, Morgan Flaherty, Pedro Miura, Robert T. Dirksen, and Joe V. Chakkalakal[#].
- https://doi.org/10.7554/eLife.26464.001[5]

2017

Genome-wide circRNA profiling from RNA-seq data

Humana Press

- Cooper, Daphne A.*, **Mariela Cortés-López**, and Pedro Miura[#].
- https://doi.org/10.1007/978-1-4939-7562-4_3[6]

2016

CircRNA accumulation in the aging mouse brain

Scientific Reports

- Gruner, Hannah*, **Mariela Cortés-López***, Daphne A. Cooper, Matthew Bauer, and Pedro Miura[#].
- https://10.1038/srep38907[7]

2016

Focus: epigenetics: emerging functions of circular RNAs

Yale Journal of Biology and Medicine

- **Cortés-López, Mariela***, and Pedro Miura[#].
- https://www.ncbi.nlm.nih.gov/pmc/articles/PMC5168830/[8]

MEETINGS, PRESENTATIONS AND POSTERS

August 2021

CSHL Eukaryotic mRNA Processing 2021

CSHL — Virtual

- Poster presentation: "Massive parallel reporter assay decodes *CD19* alternative splicing in CART-19 therapy resistance"

July 2021

EI Long Read RNA Symposium

Earlham Institute — Virtual

- Talk: "Questionable junctions: Using direct RNASeq to identify RT artifacts"

May 2021

RNA 2021

RNA Society — Virtual

- Talk: "Massive parallel reporter assay decodes *CD19* alternative splicing in CART-19 therapy resistance"

April 2021

FOR2333 meeting

FOR2333 — Virtual

- Talk: "Massive parallel reporter assay decodes *CD19* alternative splicing in CART-19 therapy resistance"

April 2021

NCI RNA meeting 2021

NCI NIH — Virtual

- Poster presentation: "Massive parallel reporter assay decodes *CD19* alternative splicing in CART-19 therapy resistance"

October 2020

EMBL-EMBO Symposium The Complex Life of RNA

EMBL Heidelberg — Virtual

- Poster presentation: "Decoding alternative splicing in *CD19* exon 2 using a high-throughput mutagenesis screen"

May 2020

RNA 2020

RNA Society — Virtual

- Poster Presentation: "The patterns of *Alu* exonisation in human cancer"

September 2019

RNA Informatics Meeting

Wellcome Trust Conferences — Hixton, UK

- Poster Presentation and flashlightning talk - "The patterns of *Alu* exonisation in human cancers"

June 2019

RNA 2019

RNA Society — Krakow, Poland

- Poster presentation: "The patterns of *Alu* exonisation in human cancers"

May 2019

PacBio SMRT Leiden

Leiden University — Leiden, Netherlands

- Poster Presentation and flashlightning talk "Decoding the splicing regulatory decisions using high-throughput mutagenesis coupled with long-read sequencing"

April 2019

RMU-RNA Salon

Frankfurt, Germany

- Short Talk: "The patterns of *Alu* exonisation in human cancers"

October 2018

EMBL-EMBO Symposium The Complex Life of RNA

EMBL Heilderberg — Heidelberg, Germany

- Poster presentation: "The patterns of *Alu* exonisation in human cancers"

April 2018

LCG European Symposium

UNAM Campus Paris — Paris, France

- Short Talk: "Analysis of the cis-regulatory landscape controlling *RON* splicing"

August 2017

Otto Warburg International Summer School and Research Symposium on RNA regulation and non-coding RNA function

CAS-MPG Partner Institute for Computational Biology — Shanghai, China

- Poster presentation: "Analysis of the cis-regulatory landscape controlling *RON* splicing". Best poster award.

June 2017

Gene Regulation by the Numbers

Institute of Molecular Biology, Mainz — Mainz, Germany

- Poster presentation: "Analysis of the cis-regulatory landscape controlling *RON* splicing"

April 2016

Undergraduate Research Symposium

University of Nevada, Reno — Reno, NV, USA

- Short Talk and Poster Presentation: "Accumulation of CircRNAs in the aging mouse brain"

February 2016

Keystone Symposium in Non Coding RNA and Enhancers

Santa Fe, NM, USA

- Poster presentation: "CircRNA accumulation in the aging mouse brain" with colleague Hannah Gruner.

INVITED TALKS

October 2021

Penn RNA Group

University of Pennsylvania — Virtual

- Talk: "Building blocks of immune escape: exons, introns, exitrons, and falsitrons"

September 2021

UNR Neuro-CMB Seminar

University of Nevada, Reno — Virtual

- Talk: "Decoding *CD19* splicing regulatory networks"

TEACHING EXPERIENCE

2016

Presentation on CRISPR-Cas9 technology to high school students

Youth Science Institute at UC Davis's Tahoe Environmental Research Center — Incline Village, NV

2015

Human Genomics Course (GEN_2015)

Undergraduate Program in Genomic Sciences — UNAM, Cuernavaca, Mexico

2021 **Co-organizer of Public Journal Club of Computational Biology**
Virtual

2021 **Representative of IMB at RNA Collaborative Seminar Series**
Virtual

- Together with other 22 institutions. From May 2021 also main coordinator of the Discord Server for the RCC.

2014 **Co-organizer of Seminar on Paleogenomics**
Cuernavaca, Mexico | Virtual